PSL
UNIVERSITÉ PARIS

THÈSE DE DOCTORAT

DE L'UNIVERSITÉ PSL

Préparée à MINES ParisTech

Towards a precise description of the grain boundary mobility and energy for their numerical integration in finite element modeling of recrystallization and grain growth mechanisms.

Soutenue par

Brayan David MURGAS PORTILLA

Le 07 avril, 2022

École doctorale n°264

ED SFA

Spécialité

Mécanique Numérique et Matériaux

Composition du jury :

Laurent Delannay Prof., UCL, Belgium	Referee
Łukas MADEJ Prof., AGH University of Science and Technology, Poland	Referee
Roland Logé Prof., EPFL, Switzerland	Examiner
Somnath GHOSH Michael G. Callas Chair Professor, Johns Hopkins University, USA	Examiner
Carl E. Krill III Prof., Ulm University, Germany	Examiner
Baptiste FLIPON Dr. Research Engineer, PSL MINES Paristech, France	Examiner
Pascal de MICHELI Dr. Research Engineer, Transvalor SA, France	Invited member
Nathalie BOZZOLO Prof., PSL MINES Paristech, France	Co-Supervisor
Marc BERNACKI Prof., PSL MINES Paristech, France	Supervisor

Aknowledgements

I have to confess that I was a little frightened and excited at the beginning of my Ph.D. It was a new field (Computational Metallurgy), and I had a lot of things to learn. Thanks to the guidance of Nathalie and Marc, I could finish this project. Thanks for sharing your experience and knowledge with me during these three and a half years. Thanks for your patience, teaching me to question everything and see the concepts practically. However, as Yoda [1] said: *Much to learn you still have. My old padawan. This is just the beginning.* I hope we can work together again and continue new research projects. I wish you the best in your lives and your projects.

I express my gratitude to the jury members: prof. Delannay, prof. Madej, prof. Logé, prof. Ghosh, prof. Carl Krill, Dr. Flipon, Dr. de Micheli, prof. Nathalie and prof. Marc.

I want to thank my mother for her mentorship and for supporting me in every project of my life. You've taught me to be strong, determined and kind. I got the desire and joy of learning from her. She bought four encyclopedias for my brother and me when we were kids, she made us read it every Saturday and Sunday morning and managed to instill lectures in our lives. I also thank my family, especially Nico, Angie, Edward, Pocho, Sebas, Yan, Tatiana and Cristhian. I have shared many adventures and learned a lot during my whole life with you.

It was a pleasure to be a member of the MSR team. I want to thank Sebastian (I always have something to learn from you), Karen (for your good vibe), Ludovic (for being my gym trainer), Julien, Baptiste (thanks for the byke and your constructive comments), Alexis, Illusca, Matheus, Arthur, Oswaldo, Diego and Victor. Thanks for all the burgers, dart games and the coffee breaks. You are all such good scientists. Also, to my other colleagues from Cemef, Mines ParisTech. Special thanks to Marie-Françoise, Florence, Suzanne, Gilbert and Cyrille, who were always in service to everyone at any moment.

I want to extend my gratitude to my high school teachers Dora (philosophy), Aparicio and Roberto (graphic and mechanical design), Socorro (maths), and Nixon (physics) from Instituto Tecnológico Salesiano Eloy Valenzuela; you gave me a guide during adolescence. To my teachers from Universidad Industrial de

[1] Yoda=Marc, Nathalie. Padawan=Me.

Santander. And my teachers from l'École Nationale d'Ingénieurs de Metz, Albert Tidu, and Stéphane Berbenni, who are such an inspiring teachers and scientists.

To my friends in Colombia that were inspiring Chapi, Manotas, Saul, Moi, Jhon, Favio, Gordillo, Motta, Daniel Pulido, Roger, Coste Pit, Juan Camilo, Sergio, el Pinchi, Maria la madre, Julian, Paula, Yuli, and Mario, for the parties, soccer matches, Halo, UNO, and PS1 games, los asaditos.

I'll keep Nice and the Alpes in my heart. What can I say, it's a little paradise! Thanks to the SPOC cycling team for teaching me how to pedal and showing me the beauty of Nice and the Alpes. Thanks Marcel for the beautiful byke I inherited from you. Life made me know really special and kind people, thank you Thierry, Isabelle, Gilbert, Martine, Alice, Denis and Welcome.

Joshua and prof. S. Ghosh, thank you a lot for your patience.

Thanks to Julia and her family, you have been supportive during these redaction months, also provided me with apricot and tomato jam. Julia, thanks for being so kind and inspiring and giving the spark of joy and peace. For every kilometer, we have traversed and the ones that are coming. Je t'aime de tout mon coeur.

This work is dedicated to my grandfather Pedro (alias el patillon or el narcorellenero [2]). Even if he didn't know and understand what I was doing in France, he was really proud of me. I will never forget that night joking around at Barrancas, la Guajira. You will be in my heart; I love you.

I extended a little this section but it's a nice opportunity to show you my gratitude. You all have been an important milestone in my life. Thank you.

[2]He used to sell blood sausages, named morcillas or rellenas in Colombia, at Agustin Codazzi.

Introduction

Thermodynamics and *Kinetics* are two fundamental topics in materials science. The study of thermodynamics provides information about a system at equilibrium; its extrapolation, under the assumption of local equilibrium, provides the basis for kinetic theories. Additionally, kinetics study the evolution of systems out of equilibrium involving changes in the microstructure, shape, volume or surface and/or composition. Determining the kinetics of recovery, grain growth, recrystallization, solidification and other metallurgical mechanisms is necessary to predict material properties but remains a very complex topic.

Metals, ceramics, rocks and ice are polycrystalline materials, it means that they are composed of crystals, also called grains. The evolution of the crystals during annealing plays an important role in the final properties of the material. Grain boundaries (GB) are surface defects, their velocity v produced under a driving pressure P is defined classically at the mesoscopic scale by the well known equation $v = \mu P$ where μ is an intrinsic property called GB mobility [1].

In the context of grain growth, the evolution of GB is driven by the reduction of interfacial energy, and GB velocity is classically described, at the mesoscopic scale, by the curvature flow driving pressure $P = -\gamma\kappa$ where γ, is the GB energy, and κ, the mean curvature (i.e., the trace of the curvature tensor in 3D). The kinetic equation $v = -\mu\gamma\kappa$ is a simplification of lower scale phenomena in constant discussions [2,3]. In this case, it constitutes at the polycrystalline scale, and in metal forming a state-of-the-art accepted physical framework.

GB energy and mobility are two intrinsic properties, the anisotropic behaviour of these two properties has been early reported by Smith in 1948 [4] and Kohara in 1958 [5]. During recrystallization and grain growth, the crystals evolve in exotic ways and complex microstructures can be formed, e.g. with the presence of twins. By now the definition of mobility is often approximated using an Arrhenius equation whereas parameters such as structure and composition can have an impact on it.

In the discussion of whether this kinetic equation is a reasonable approximation [6] and whether the reduced mobility ($\mu\gamma$ product) can really be considered as defined by temperature and crystallographic properties of the interface as misorientation and inclination, there is no clear and univocal answer today. First of all, the answer at the scale of a few interfaces and at the homogenized polycrystal scale can be contradictory as to the statistical effects. Moreover, a bias

in the reduced mobility field discussion today lies in the real capacity of full-field methods to take into account a reduced mobility appropriately defined in the 5D GB space $\mathcal{B}$, defined by the misorientation and inclination in representative 2D or 3D simulations. As detailed in this thesis, such a capacity is typically unclear in the current state-of-the-art. Thus, the discussion between experimental data and anisotropic full-field simulations is to be treated with extreme caution.

If numerical modeling by considering heterogeneous values of GB mobility and GB energy remains a complex discussion, it has in fact been widely studied at the polycrystalline scale with a large variety of numerical approaches: multi phase-field [7–9], Monte Carlo [10, 11], molecular dynamics [12], oriented tessellation updating method [13], vertex [14], front-tracking Lagrangian or Eulerian formulations in a finite element (FE) context [15–17], and level-set (LS) [18–20], to cite some examples. The first models proposed in the literature define the GB mobility and energy as constants, called isotropic, [7, 10, 18, 21, 22]. The models evolved in order to reproduce more complex microstructures or local heterogeneities. Heterogeneous models were proposed, in which each boundary has its own energy and mobility [11, 19, 20, 23–30]. For instance, every grain could be related with an orientation, thus the mobility and energy can be computed from a model describing their disorientation dependence [8, 20], but just one parameter from the five describing the GB space is considered. Finally, general frameworks in which the five parameters are discussed have been proposed, and these models could be categorized as fully anisotropic [20, 31, 32].

The comprehensive understanding of GBs and the *process-microstructure* relationship is crucial and complex. The origin of this complexity is in the one hand due to the passage from the GB space to a scalar value, $\mathcal{B} \rightarrow \mathbb{R}^+$. On the other hand, the mechanisms governing the GB motion extend across multiple length and time scales. As such, experimental and computational studies must be carried out together. In addition to the enrichment of numerical approaches, several studies were carried out in order to compute GB properties. For instance, recent studies have shown the relation between the GB structure and GB energy of bicrystals [33, 34]. The knowledge of the bicrystal relation is an important contribution to the study of GB motion and GG. However, little is known about the effect of GB properties anisotropy on the statistical behavior of microstructures [35]. It has been shown that the surface tension is not the only force controlling GB motion during grain growth, as GBs evolve two additional parameters may be taken into account. First, a torque term is generated by the anisotropic nature of GB energy. Second, as GB evolve they can create stresses in the surrounding area leading to additional driving pressures [36, 37].

The experimental techniques and numerical approaches to estimate GB properties are essential to the understanding of microstructure evolution. To ensure all these parameters work and are reliable for simulating microstructure evolution under real thermomechanical processes, the latter should be mimicked in laboratory scale experiments to carefully assess evolution kinetics and their dependence

on thermomechanical parameters.

Annealing phenomena and recrystallization is the aim of the DIGIMU® software developed by the Digimu consortium, Transvalor company and CEMEF. The Digimu consortium is composed of several partners: Safran, Aubert & Duval, Framatone, CEA, Timet, ArcelorMittal, Constelium and Ascometal. The purpose of the DIGIMU consortium is to develop new global Finite Element (FE) schemes to simulate microstructural evolutions during metal forming processes. The efficient treatment of the migrating interfaces carries a great importance because the prediction of microstructures in those simulations is based on the relation $v = \mu P$, one could thus say that the physics of the problem is contained in the definition of the *mobility* and the net *driving pressure*. DIGIMU® integrates 2D and 3D tools for the modeling of polycrystalline microstructures including GB motion due to grain growth, recrystallization (static, dynamic and post-dynamic), and Smith-Zener pinning by second phase particles. DIGIMU® also includes annealing phenomena such as recovery, crystal plasticity and work-hardening to model hot deformation.

In this PhD work, an enrichment of the FE tools in terms of GB anisotropy will be introduced. The methodology introduced here are composed by numerical developments to include the anisotropy of GB properties and experimental tests to measure GB properties and compare the numerical results to experimental data. The main goal of this work is to end up with more physical models. The work presented in Chapter 3 have been published [38] and the work presented in Chapter 4 is under review.

The main concepts introduced in Chapter 1 are used in the manuscript. This chapter is focused on the state-of-the-art concerning the concept of boundary mobility and its role on the migration of boundaries. In the first section the polycrystal is defined, also migration mechanisms of boundaries are presented. Secondly, the first experimental results to estimate values of GB mobility for high purity materials and low purity materials are presented, this section is finished with a discussion concerning the limitations of the GB migration equation.

In Chapter 2, the existing *full field* methods at the mesoscopic scale are briefly reviewed. This includes multi phase-field, Monte Carlo, cellular automata, molecular dynamics, vertex, front-tracking Lagrangian or Eulerian formulations in a finite element (FE) context, and level-set (LS).

In Chapter 3, several FE-LS formulations are compared using heterogeneous GB mobility and energy that depend on the GB disorientation. GG simulation of a model system including one triple junction and in a polycrystalline microstructure are performed in 2D and 3D. This section is necessary in order to choose a FE-LS formulation for further modeling GG in more realistic microstructures.

In Chapter 4, the Isotropic and Anisotropic FS-LS are used to model GG in a 316L stainless steel. Two types of GB network are considered, first, twin boundaries are excluded and then considering all the boundaries (with twin boundaries).

Also, two kinds of microstructures are considered, one generated statistically from grain size distributions, and the other being a digital twin created from EBSD data. Regarding GB properties, GB energy is defined either as heterogeneous or anisotropic, and GB mobility is defined as heterogeneous.

In Chapter 5, the perspectives and general conclusions of this work are presented. Some preliminary results of some perspectives are also detailed.

Oral and written communications

This research work has lead or contributed to the following written and oral communications.

Articles

- Brayan Murgas, Baptiste Flipon, Nathalie Bozzolo and Marc Bernacki. Level-Set modeling of grain growth in 316L stainless steel under different different assumptions regarding grain boundary properties. arXiv preprint and submitted to Materials.

  https://arxiv.org/abs/2202.04930

- Sebastian Florez, Karen Alvarado, Brayan Murgas, Nathalie Bozzolo, Dominique Chatain, Carl E. Krill, Mingyan Wang, Gregory S. Rohrer and Marc Bernacki. Statistical behaviour of interfaces subjected to curvature flow and torque effects applied to microstructural evolutions. Acta Materialia, 222(8), 2021.

  DOI:10.1016/j.actamat.2021.117459

- Sebastian Florez, Julien Fausty, Karen Alvarado, Brayan Murgas, and Marc Bernacki. A 2D Front-Tracking Lagrangian Model for the Modeling of Anisotropic Grain Growth. Materials, 14(15), 2021.

  DOI:10.3390/ma14154219

- Brayan Murgas, Sebastian Florez, Nathalie Bozzolo, Julien Fausty, and Marc Bernacki. Comparative study and limits of different level-set formulations for the modeling of anisotropic grain growth. Materials, 14(14), 2021.

  DOI:10.3390/ma14143883

- Sebastian Florez, Julien Fausty, Karen Alvarado, Brayan Murgas and Marc Bernacki. Parallelization of an efficient 2D-Lagrangian model for massive multi-domain simulations. Modelling and Simulation in Materials Science and Engineering 29(6), 2021.

  DOI:10.1088/1361-651X/ac0ae7

- Baptiste Flipon, Victor Grand, Brayan Murgas, Alexis Gaillac, Alexis Nicolaÿ, Nathalie Bozzolo and Marc Bernacki. Grain size characterization in metallic alloys using different microscopy and post-processing techniques. Materials Characterization 174(9), 2021.

  DOI:10.1016/j.matchar.2021.110977

- Julien Fausty, Brayan Murgas, Sebastian Florez, Nathalie Bozzolo and Marc Bernacki. A new analytical test case for the anisotropic grain growth problem - first calculations with a Finite Element Level Set model. Applied Mathematical Modelling 93(5), 2020.

  DOI: 10.1016/j.apm.2020.11.035

Posters

- Brayan Murgas, Julien Fausty, Nathalie Bozzolo and Marc Bernacki. Accounting for grain boundary mobility heterogeneity. Métallurgie quel avenir. Nancy, France. May 2019.

Presentations

- Brayan Murgas, Julien Fausty, Sebastian Florez, Baptiste Flipon, Nathalie Bozzolo and Marc Bernacki. Anisotropic grain growth modeling using a Level-Set Finite Element formulation. WCCM-Eccomas Congress, Virtual Congress. January 2021.

Awards

- Excellence price from Université Côte D'Azur. December 2021.

- 1st place in the Arts and Science contest. Special mention of the jury - World Congress on Computational Mechanics - European Community on Computational Methods in Applied Sciences (WCCM-ECCOMAS). January 2021.

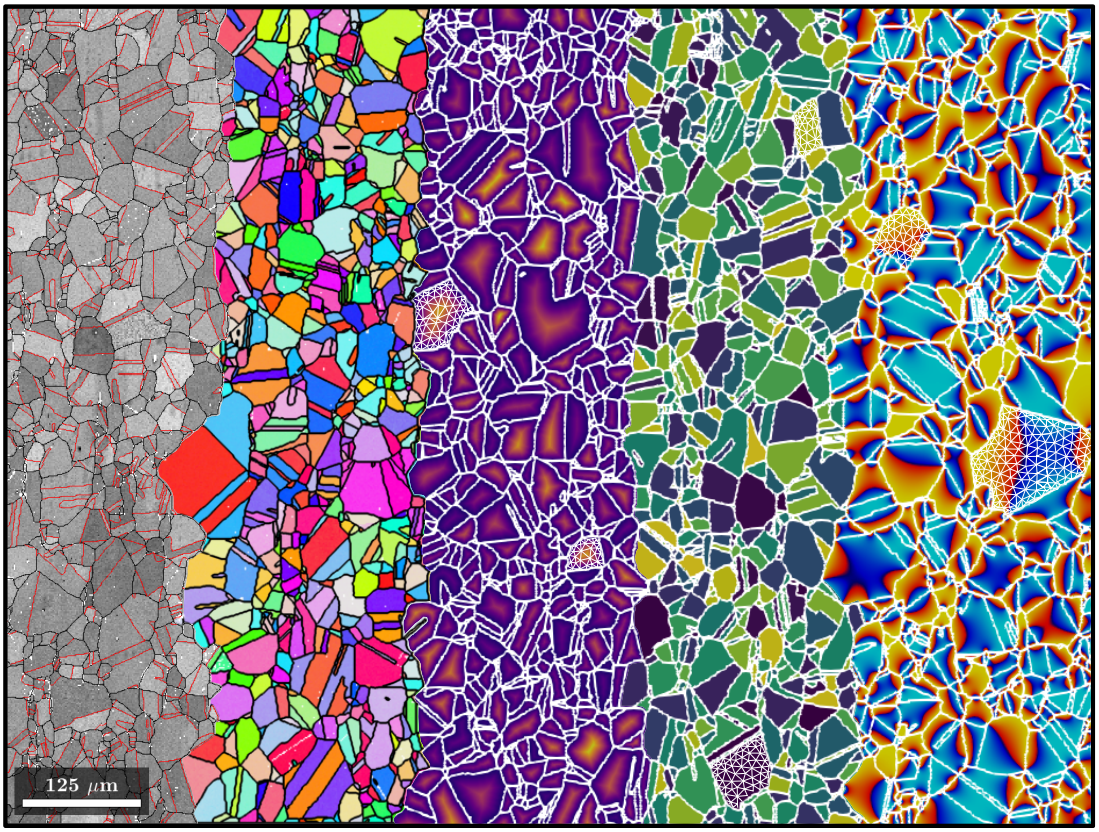

Figure 1: L'immersion. Image available online at Flickr (https://flic.kr/p/2kG66Pr, Uploaded on March 1, 2021) licensed under CC BY 2.0 (https://creativecommons.org/licenses/by/2.0/, Uploaded on March 1, 2021). Title: L'immersion. Author: Brayan Murgas.

Contents

Chapter 1

Definition of grain boundary mobility and limits of the migration equation $v = \mu P$ in polycrystalline materials

Studies of grain growth (GG) and recrystallization (ReX) have been carried out in order to notably comprehend the mechanisms responsible for the migration of GBs. Experiments were initially performed using bicrystals and tricrystals. However, the individual effect of the GB mobility and GB energy was not known. Thanks to new experimental and numerical techniques the study of each GB property is possible. Hence, new models of GB properties and mechanisms have been discovered.

This chapter is focused on the state of the art concerning the concept of GB mobility and its role on GB migration. In the first section the polycrystal, GB and their migration are presented. Secondly, existing experimental results of the state of the art are presented for low and high purity materials, the limitations of the GB migration equation are also discussed.

1.1 The polycrystal and motion of GBs

Most of the inorganic solids are polycrystalline, those materials are formed of crystals of different size, orientation and/or nature. The properties of the materials could be defined using the characteristics of crystals, for example the Hall-Petch equation relates the yield stress with the grain size [39]. The fundamental definitions used throughout the text are discussed here. Also, diffusion and GB movement equations are shown in order to reveal their resemblance.

1.1.1 The crystal lattice and its defects

A perfect crystal is a solid composed of atoms, ions or molecules highly arranged in patterns repeated periodically [40]. In metals the points of a lattice space may be the position of atoms. The atoms are arranged in a basic structure that is repeated, thus every lattice point has the same number of neighboring atoms. There are 14 space-lattice called the Bravais lattices [41] divided into seven families: triclinic, monoclinic, orthorhombic, tetragonal, rhombohedral, hexagonal and cubic. The most common Bravais lattices of the cubic system are the primitive cubic, body centered cubic (bcc) and face centered cubic (fcc), see Figure 1.1. As the lattice is repeated periodically the Miller notation is used because it easily provides the orientation of crystal planes and directions [42].

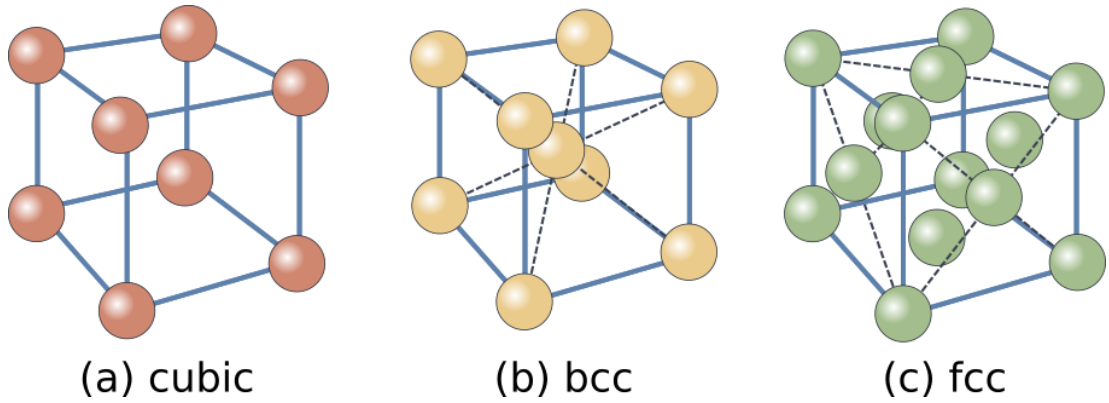

Figure 1.1: (a) Cubic (b) fcc and (c) bcc Bravais lattices.

In some applications, perfect monocrystals are of prime importance for their creep properties (e.g., turbine blade), and it requires complex and expensive manufacturing processes. Most common metallic parts have defects that change the structure of the material and their arrangement are responsible of the properties of the material. Defects types can be classified into point (0D), linear (1D), planar (2D) and volume (3D) defects. Vacancies, interstitial, substitutional atoms are point defects, dislocations are 1D defects, grain/phase interfaces, and stacking faults are 2D defects, and pores, cracks are 3D defects [43].

The characteristics and properties of defects are complex and have been widely studied. First, defects can interact, for instance, in irradiated materials GBs can act as sink or source of defect points [44], also dislocations interact with GBs [45]. Second, they can change as a function of the material composition; a recent study using atomic scale characterization has for example revealed a range of defect patterns of a binary Pt-Au model alloy [46]. Figure 1.2 reveals the relation between chemistry segregation and defect type [46]. More details about lattice defects can be found in [43, 47, 48].

This PhD thesis is focused on the study of GBs (2D defects). In the next section the different terms to define GB structure are presented.

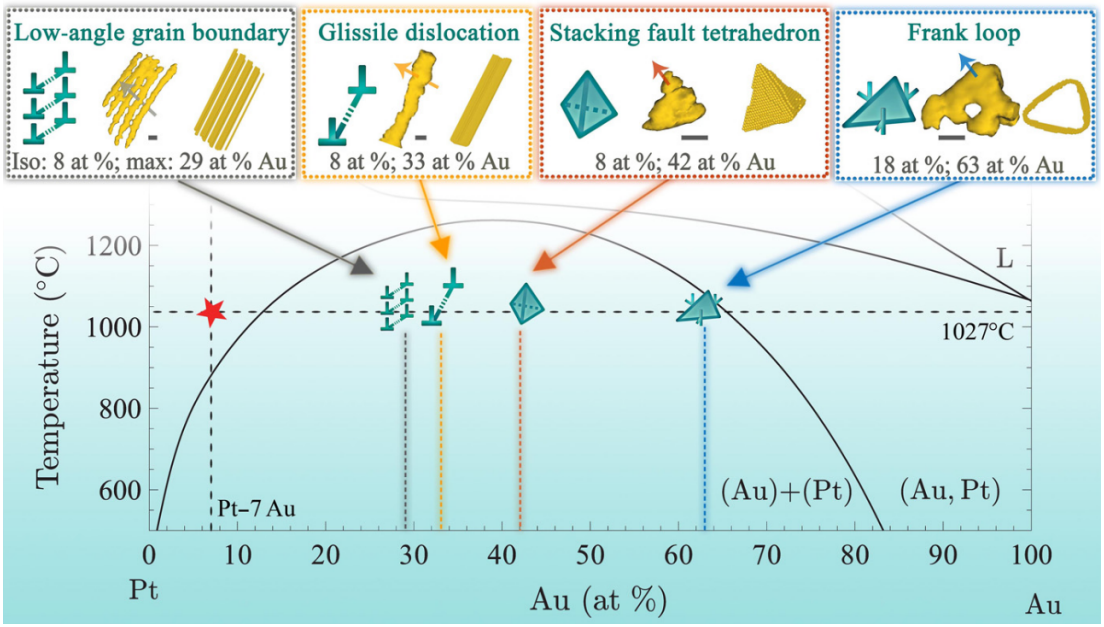

Figure 1.2: Cross-correlative study of a Pt-7 atomic (at) % Au thin film specimen annealed at 1300 K for 15 min. Each panel shows an atome probe tomography reconstruction (middle) of each observed defect type, corresponding defect symbols (left), and a diffusive molecular dynamics simulation result (right) in the colored boxes. The numbers in each box are the Au at % isosurface (Iso) values for imaging (left) and maximum (max) solute at % near the defects (right). The red star marks the bulk alloy composition. Image reproduced from [46].

1.1.2 Crystallographic definitions

In addition to point and linear defects inside a crystal, most crystalline materials are composed of many crystals formed during solidification or under the influence of a thermomechanical load. Figure 1.3 shows a simulation of solidification followed by grain growth using solid seeds with random orientation and GB anisotropy. Let us consider a domain Ω, of space-dimension d, filled by n grains $G_i \in \Omega$, being open spaces of Ω and defining the set $\mathcal{G} = \{G_i, i = 1, \ldots, N_G\}$ with N_G the number of grains. The crystals or *grains* inside a polycrystal have different orientation (O_i) but can also differ in terms of chemical composition, shape, volume, etc.

Two neighboring grains G_i and G_j constitute a GB B_{ij}, and the whole set of boundaries form the GB network Γ. In three dimensions (3D), eight parameters are necessary to describe the GB: the misorientation between the adjacent crystals may be defined by three parameters, e.g. the Euler angles φ_1, Φ and φ_2, the GB plane requires two parameters to define its unitary normal $\vec{n} = (n_1, n_2, n_3)$ and the translation vector $\vec{t} = (t_1, t_2, t_3)$. The knowledge of the GB structure is then very complex and it may be described mesoscopically in mathematical terms. At the mesoscopic scale, a GB is considered as a sharp interface and the

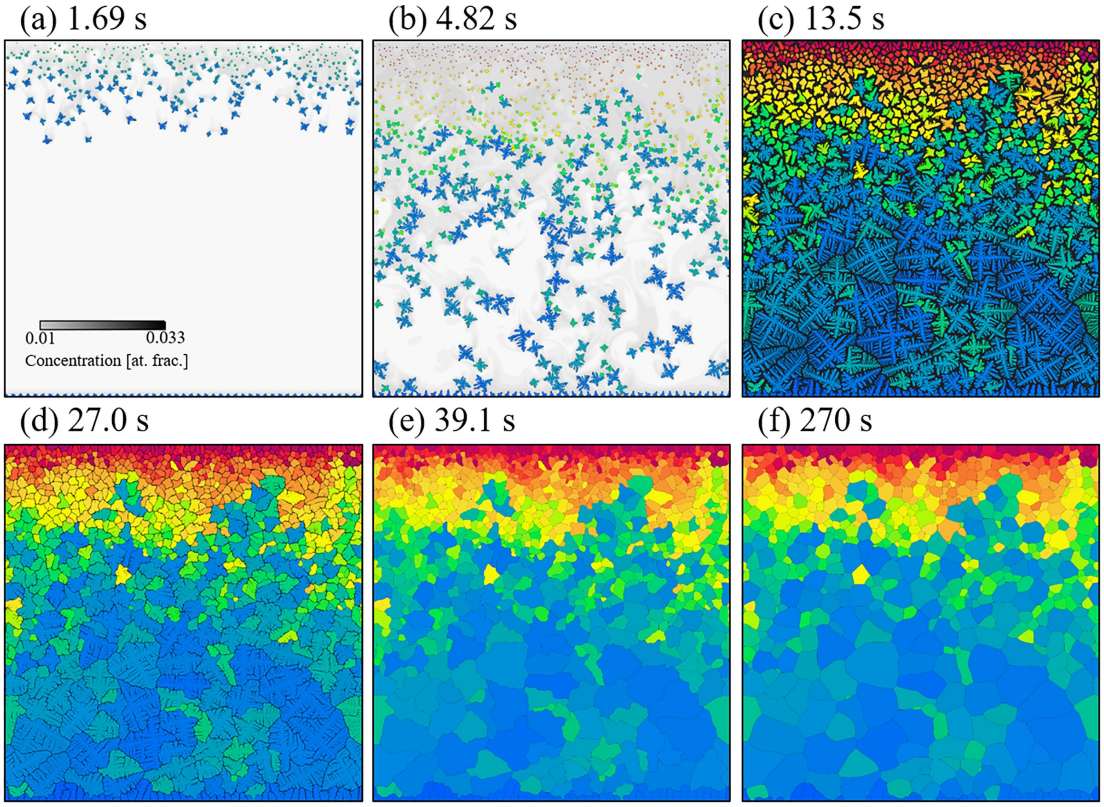

Figure 1.3: Snapshots during polycrystalline solidification with showering and subsequent grain growth. The gray and color scales indicate the solute concentration in liquid and solid grain number, respectively. Simulation perfomed using a Multi Phase Field Lattice Boltzmann model. Image from [49].

translation vector is not taken into account. Finally at the mesoscopic scale, a GB is classically described in a 5D space. The 3 crystallographic properties describing the orientation relationship between two neighboring grains, O_i and O_j, can be described by the misorientation matrix $M_{ij} = O_j O_i^{-1}$, see Figure 1.4. As such, at the mesoscopic scale the GB may be characterized by a tuple:

$$B_{ij} = (M_{ij}, n_{ij}).$$

Parameterization of rotation matrices

Grain orientation and GB misorientation are rotation matrices. One can describe rotations using different parameterization, such as the Rodrigues parameters, axis-angle, Euler angles, quaternions, rotation vector, Miller indices, to name a few. The following definitions of rotation matrix can be found in detail in [50]. The Rodrigues parameters are expressed, using the Einstein notation, via the entries of the rotation matrix as:

$$r_i = \frac{1}{2}\varepsilon_{ijk} R_{jk} = -\frac{1}{1 + O_{ll}}\varepsilon_{ijk} O_{jk}, \tag{1.1}$$

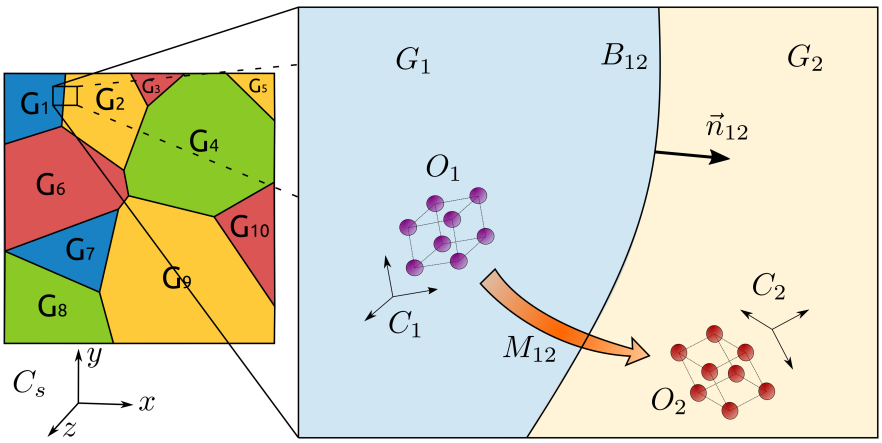

Figure 1.4: Scheme depicting one GB and its parameters. Image available online at Flickr (https://flic.kr/p/2m5JQkz, Uploaded on June 15, 2021) licensed under CC BY 2.0 (https://creativecommons.org/licenses/by/2.0/, Uploaded on June 15, 2021). Title: 10GGBParam. Author: Brayan Murgas.

where ε_{ijk} is the permutation symbol, $R = (I+O)^{-1}(I-O)$ is an antisymmetric (skew-symmetric) matrix representation of the orthogonal rotation matrix O. Here the identity rotation is given by $r_i = 0$. The inverse relation is:

$$O_{ij} = \frac{1}{1 + r_l r_l}((1 - r_k r_k)\delta_{ij} + 2r_i r_j - 2\varepsilon_{ijk} r_k), \tag{1.2}$$

where δ_{ij} is the Kronecker delta.

A more intuitive way to represent rotations is via the axis-angle parameterization. Here a rotation matrix is represented through a rotation angle θ around an axis $\vec{a}$, i.e., $O = (\vec{a}, \theta)$, being θ the magnitude that *represents* the rotation. The rotation angle is defined as

$$2cos\theta = O_{mm} - 1. \tag{1.3}$$

And the unit vector of the rotation axis a_i is defined as

$$a_i = \frac{-1}{(3 - O_{lm}O_{ml})^{1/2}} \varepsilon_{ijk} O_{jk}, \tag{1.4}$$

this expression is valid if the trace $O_{mm} = tr(O) \neq -1$ or 3. Finally, the relation between $(\vec{a}, \theta)$ and O is

$$O_{ij} = \delta_{ij} cos\theta + a_i a_j (1 - cos\theta) - sin\theta \varepsilon_{ijk} a_k, \tag{1.5}$$

this equation can be obtained substituting $r_i = a_i tan(\theta/2)$ in Equation 1.2. It is important to be aware that there is no unique rotation axis for half turns or null rotations. Also, one can obtain the same angle θ for different rotation axis $\vec{a}$ because of crystal symmetry.

A more classical parameterization of matrix orientation is done through the use of Euler angles. The rotation matrix is composed of three rotation matrices, where each rotation matrix $O(\vec{n}, \omega)$ corresponds to a rotation around $\vec{n}$ by the angle ω. The orientation matrix is composed of three matrices $O(e_3, \varphi_1)$, $O(e_1, \phi)$ and $O(e_3, \varphi_2)$, where φ_1, ϕ and φ_2 are the Euler angles, one can see that two rotations are done around the z axis and other around the x axis. The individual rotation matrices are defined as

$$O(e_3, \varphi_1) = \begin{bmatrix} cos\varphi_1 & sin\varphi_1 & 0 \\ -sin\varphi_1 & cos\varphi_1 & 0 \\ 0 & 0 & 1 \end{bmatrix}, \tag{1.6}$$

$$O(e_1, \phi) = \begin{bmatrix} 1 & 0 & 0 \\ 0 & cos\phi & sin\phi \\ 0 & -sin\phi & cos\phi \end{bmatrix}, \tag{1.7}$$

and

$$O(e_3, \varphi_2) = \begin{bmatrix} cos\varphi_2 & sin\varphi_2 & 0 \\ -sin\varphi_2 & cos\varphi_2 & 0 \\ 0 & 0 & 1 \end{bmatrix}. \tag{1.8}$$

Hence, the orientation matrix is defined as $O(\varphi_1, \phi, \varphi_2) = O(e_3, \varphi_2)O(e_1, \phi)O(e_3, \varphi_1)$ or may be redefined in its explicit form as

$$O(\varphi_1, \phi, \varphi_2) = \begin{bmatrix} cos\varphi_1 cos\varphi_2 - sin\varphi_1 sin\varphi_2 cos\phi & sin\varphi_1 cos\varphi_2 + cos\varphi_1 sin\varphi_2 cos\phi & sin\varphi_2 sin\phi \\ -cos\varphi_1 sin\varphi_2 - sin\varphi_1 cos\varphi_2 cos\phi & -sin\varphi_1 sin\varphi_2 + cos\varphi_1 cos\varphi_2 cos\phi & cos\varphi_2 sin\phi \\ sin\varphi_1 sin\phi & -cos\varphi_1 sin\phi & cos\phi \end{bmatrix}, \tag{1.9}$$

Euler angles are frequently used in texture analysis but the information can remain limited.

Quaternions are also important in the description of rotations. The advantage of quaternions over the other parameterization is that one can perform algebraic operations easier. Quaternions algebra can be derived from the Clifford algebra ($\mathcal{C}_2$ group) [50]. Let e_μ, $\{\mu = 0, 1, 2, 3\}$, be the orthonormal basis of a four dimensional vector space over real numbers. A quaternion is defined as $q = q^\mu e_\mu$, where q^μ are real numbers, for simplicity this definition is representated as $a + b\mathbf{i} + c\mathbf{j} + d\mathbf{k}$, where $\mathbf{i}, \mathbf{j}, \mathbf{k}$ are the basic quaternions, the coefficient e_0 is the *scalar part* and $q^0 = a$, $q^1 = b$, $q^2 = c$ and $q^3 = d$. A quaternion for which is norm $|q| = (q^\mu q^\mu)^{0.5} = 1$ is called a *unit quaternion*. Unit quaternions represent rotations, the relation between quaternion components and the rotation matrix components are

$$O_{ij} = ((q^0)^2 - q^k q^k)\delta_{ij} + 2q^i q^j - 2\varepsilon_{ijk} q^0 q^k \tag{1.10}$$

or in its explicit form as

$$O = \begin{bmatrix} (q^0)^2 + (q^1)^2 - (q^2)^2 - (q^3)^2 & 2(q^1q^2 - q^0q^3) & 2(q^1q^3 + q^0q^2) \\ 2(q^1q^2 + q^0q^3) & (q^0)^2 - (q^1)^2 + (q^2)^2 - (q^3)^2 & 2(q^2q^3 - q^0q^1) \\ 2(q^1q^3 - q^0q^2) & 2(q^2q^3 + q^0q^1) & (q^0)^2 - (q^1)^2 - (q^2)^2 + (q^3)^2 \end{bmatrix}, \quad (1.11)$$

and the inverse relation

$$q^i = \mp \frac{\varepsilon_{ijk} O_{jk}}{2(O_{ll} + 1)^{1/2}}. \quad (1.12)$$

Finally, quaternions are related to the rotation axis a_i, rotation angles θ, and Rodrigues parameters r_i, respectively as

$$a_i = \frac{q^0 q^i}{(q^0 q^0 (q^k q^k))^{1/2}} \text{ for } q^0 q^k \neq 0 \text{ and } a_i = q^i \text{ for } q^0 = 0, \quad (1.13)$$

$$q^0 = \pm cos(\theta/2) \text{ and } q^i = \pm sin(\theta/2) a_i, \quad (1.14)$$

and

$$r_i = \frac{q^i}{q^0}, q^0 \neq 0. \quad (1.15)$$

Miller indices are frequently used for texture and orientation analysis. In mathematical terms the lattice is defined by a set of vectors determined by linear combinations of the form $u^i a_i$, where u^i are integers, a_i are linear independent vectors and $i = 1, 2, 3$. If one defines a crystallographic metric as $g_{ij} = a_i a_j$, its contravariant g^{ij} is determined by $g^{ij} g_{jk} = \delta^i_k$. Miller (plane) indices and (Miller) direction indices are respectively covariant coordinates with co-prime integer values and contravariant coordinates of lattice vectors. In practice, Miller indices, $(hkl)[uvw]$, specifies direction cosines of crystals parallel to a given plane and a given direction of the sample frame. To obtain the crystallographic plane (hkl) one has to identify the plane intercepts on the x,y,z axes, specifies the intercepts in fractional coordinates, and finally, takes the reciprocals of the fractional intercepts. The crystallographic direction $[uvw]$ represents a vector passing from the origin to a lattice point $\vec{r}$, where its components $u = r_1, v = r_2, w = r_3$ are the crystallographic direction. If r_1, r_2, r_3 have fractions the components must be multiplied by their common denominator. The relation between the orientation matrix and Miller indices is

$$O((hkl)[uvw]) = \begin{bmatrix} b_1 & t_1 & n_1 \\ b_2 & t_2 & n_2 \\ b_3 & t_3 & n_3 \end{bmatrix}, \quad (1.16)$$

with

$$\vec{n} = \frac{(h, k, l)}{(h^2 + k^2 + l^2)^{1/2}}, \quad \vec{b} = \frac{(u, v, w)}{(u^2 + v^2 + w^2)^{1/2}}, \text{ and } \vec{t} = \frac{\vec{n} \times \vec{b}}{|\vec{n} \times \vec{b}|}. \quad (1.17)$$

Due to the symmetry of crystals, Miller indices are generalized to plane and direction groups using the following notation $\{hkl\}<uvw>$.

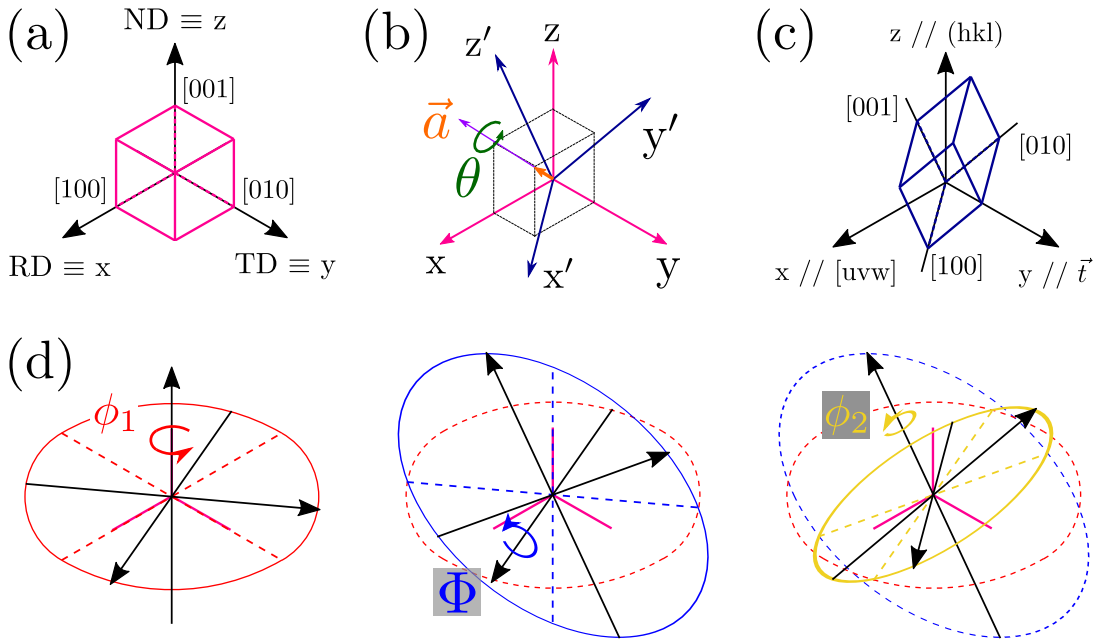

Figure 1.5: Representation of a rotation. ND, RD and TD are the normal, rolling and transverse directions. (a) Initial lattice with axes ([100],[010],[001]) parallel to the reference (sample) axes (x,y,z). (b) Rotation from the reference axes (x,y,z) to the new axes (x′,y′,z′) represented by the axis-angle ($\vec{a}$,θ) parameterization. (c) Representation of the rotation using the Miller indices, (hkl) is normal to the z (ND) axis and [uvw] is parallel to the x (RD) axis. (d) Representation of the sequence of rotations $O(e_3, \phi_1)$ (Red), $O(e_1, \Phi)$ (Blue), and $O(e_3, \phi_2)$ (Yellow) that defines the rotation matrix and the Euler angles. The reference axes are colored in magenta.

For instance, in Section 3.3.2 the two fixed Euler angles were $\phi_1 = 35°$ and $\Phi = 45°$ which are typical from the Brass Texture $(110)[\bar{1}12]$ with Euler angles ($\phi_1 = 35°$,$\Phi = 45°$,$\phi_1 = 0°$).

Classification of grain boundaries

Misorientation is frequently parameterized with the Rodrigues vector, unit quaternions or the axis-angle set. Rodrigues vectors and the axis-angle set are useful for representing GBs, and quaternions are used to perform efficient computations. The equations presented before are valid but symmetry must be applied in both sides of the GB, i.e., $M_{ij} = (S_c O_j)(S_c O_i)^{-1}$, where S_c is the symmetry operator. Hence, it exists equivalent misorientations without any physical difference, for instance, for the cubic system there are 24 independent operators that correspond to 24x24x2=1152 equivalent misorientations.

Due to the number of equivalent misorientations, it is necessary to limit the rotation space such that there is an unique misorientation. This limited region is known as asymmetric domain, asymmetric unit, asymmetric region, symmetrically equivalent area, fundamental zone or Mackenzie cell [50]. The Rodrigues (Rodrigues-Frank) space is the more natural representation of the Fundamental Zone [51]. The Rodrigues parameters, r_i, may be expressed as a function of the disorientation θ and the rotation axis a_i as

$$r_i = tan(\theta/2)a_i. \tag{1.18}$$

being the three components of this vector the basis of the Rodrigues space. The fundamental zone for cubic lattices with no sample symmetries is a truncated cube, see Figure 1.6. The distance from the origin to the octagonal and triangular facets are normal to the <100> axis ($\theta_{max<100>} = 45°$, $r_{i,max} = tan(\pi/8)$), and the <111> axis ($\theta_{max<111>} = 60°$, $|r_i| = tan(\pi/6)$), respectively. The maximum angle is realized at the corners with $\theta = 62.8°$. Thus, the Rodrigues parameters (r_1, r_2, r_3) correspond to the axis $([100], [010], [001])$. Figures 1.6 also shows the fundamental zone of the cubic-cubic symmetry that has the shape of a truncated pyramid and is known as the Mackenzie cell.

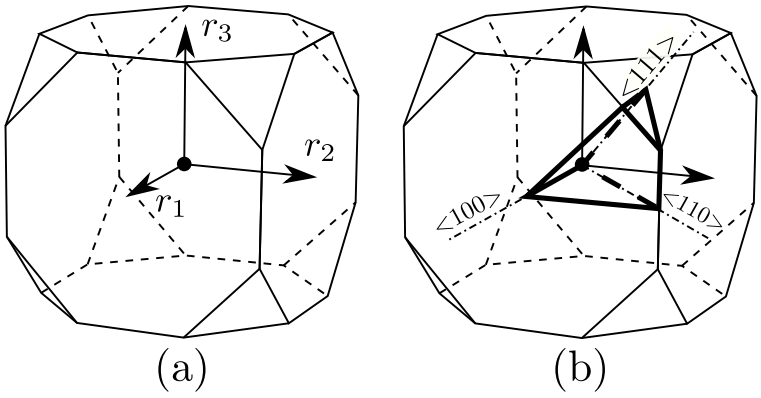

Figure 1.6: Orientation spaces in the Rodrigues space for cubic lattices. (a) Cubic-Triclinic (O, C_1) symmetry. (b) Cubic-cubic (O, O) symmetry. Reproduced from [51].

The misorientation is frequently defined in terms of the axis-angle set i.e., $M_{ij} = (\theta, \vec{a})$. In the computations, one normally takes the minimum rotation angle, called *disorientation*, obtained with Equation 1.3. Using this representation, two important types of GBs are classically identified as a function of the disorientation: **High Angle Grain Boundaries** (HAGB) and **Low Angle Grain Boundaries** (LAGB). With a disorientation transition from LAGB to HAGB which is frequently set as $10° < \theta < 15°$.

Furthermore, if we take into account the misorientation axis, one can define two important types of GBs: twist and tilt boundaries presented in Figure 1.7. At particular disorientations, the lattices of the two adjacent grains contain a

common sublattice that forms a periodic atomic structure. This concept is known as *coincidence sublattices* or *coincidence site lattices* (CSL) [50]. CSL are identified using Σ, where the value of Σ is the ratio between the number of lattice points in the CSL and the number of lattice points of the original lattice. This fit between the two crystal lattices is sometimes related to special GB properties such as low energy configurations [1]. Some examples of Σ CSL boundaries used in this work are listed in table 1.1.

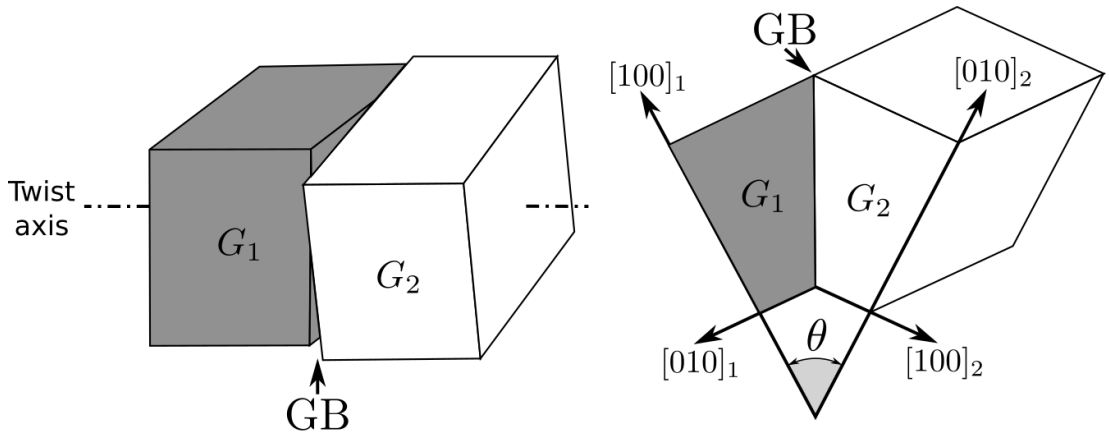

(a) Twist boundary (b) Symmetrical tilt boundary

Figure 1.7: (a) Boundary plane perpendicular to the rotation axis, (b) boundary plane parallel to the rotation axis. Reproduced from [52].

Table 1.1: Σ CSL orientation relationship for cubic lattice. The CSL is specified by a rotation angle around a rotation axis.

Σ	**Disorientation** θ	**Axis** $\vec{a}$	**Type**
1	0.0°		
3	60.0°	< 111 >	Tilt
3	70.53°	< 110 >	Twist
5	36.86°	< 100 >	Tilt
5	53.13°	< 100 >	Tilt
7	38.21°	< 111 >	Tilt
9	38.94°	< 110 >	Twist
11	50.47°	< 110 >	Tilt

Figure 1.8 shows the GB sets <100>, <110> and <111>. The volume is another view of the fundamental zone in Rodrigues space shown in Figure 1.6. The 5D nature of the GB can be represented by a point corresponding to the misorientation and a unit vector corresponding to the GB normal. For instance, violet Σ3 twin boundary is a pure twist 60° [111] GB, its normal is aligned to the black line representing the <111> sets.

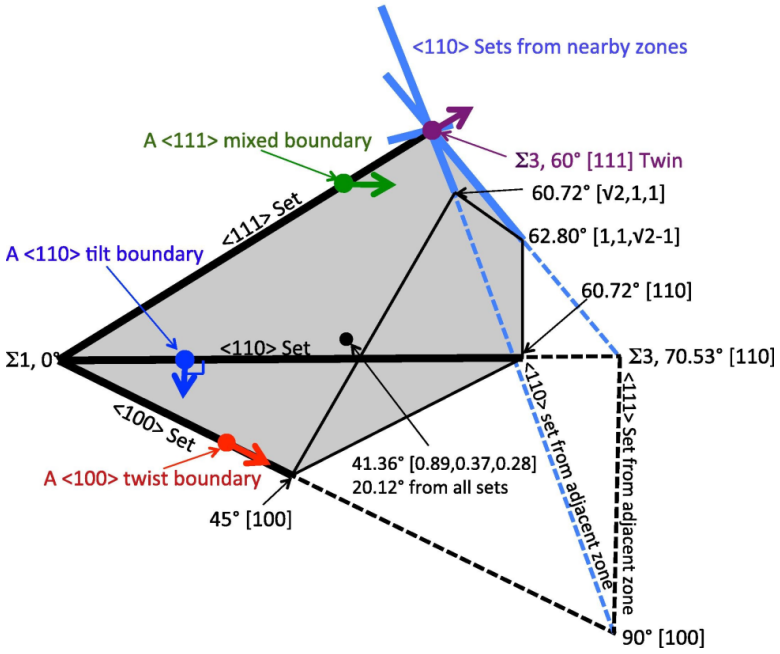

Figure 1.8: Geometry of an arbitrary GB in the 5D space can be represented as a point in Rodrigues space (Misorientation) with an attached unit vector (GB normal). The GB sets lie along the thick black and blue lines. The most remote point from the scaffolding sets is shown near the center of the fundamental zone. Reproduced from [34].

Other classifications of GBs are used in the literature, in [53] GBs are classified into three broad categories: *singular*, *vicinal* and *general*. In [52], GBs are classified into two groups: *special* and *random* GBs. Singular or special GBs correspond to CSL. Vicinal GBs have a misorientation near to a CSL. Finally, general or random GBs are other boundaries.

The GB space $\mathcal{B}$ parameterized by the misorientation and the normal direction is illustrated in Figure 1.4. The two quantities of interest, the GB energy, γ, and the GB mobility, μ, are maps from $\mathcal{B}$ to $\mathbb{R}^+$.

1.1.3 Motion of GBs

The motion of interfaces generally tend to decrease the total free energy G per unit volume (V). The driving pressure P is defined as

$$P = -\frac{dG}{dV}. \tag{1.19}$$

Motion of interfaces may be *conservative* or *non-conservative* [54]. Non-conservative motion involves long-range diffusion, examples are phase change, diffusional creep and sintering of polycrystalline materials [53]. In this work conservative motion is of interest. Conservative motion occurs when the atomic

fraction of each component in the adjoining crystals are the same (equal composition). This motion occurs under quasi-steady conditions and could involve atom jumps (short-range diffusion), for example the thermally activated motion of GBs during grain growth. The mechanisms of motion depend on the thermal activation required and the type of interface. Table 1.2 summarizes some of these mechanisms.

Table 1.2: Motion mechanisms of sharp (narrow) GBs, from [53].

Mechanism	**Type of GB**
Glissile motion of interfacial dislocations	LAGB; singular and vicinal HAGB; martensitic interfaces
Glide and climb of interfacial dislocations	LAGB; Singular or vicinal CSL HAGB
Shuffling motion of pure steps	Singular or vicinal CSL HAGB
Uncorrelated atom shuffling	General GBs; general heterophase GBs
Uncorrelated diffusional transport	General GBs; general heterophase GBs

GB motion could be seen as a generation and destruction of lattice sites at the interface. Motion could be reduced to jump of atoms across the GB that generates motion. Assuming a narrow GB, the atoms cross the boundary by atomic jump with frequency Υ. If the boundary displacement is the diameter of an atom b_a, the GB velocity can be defined as [52]:

$$v = b_a(\Upsilon^+ - \Upsilon^-) = b_a\left(\nu_+ exp\Big(-\frac{Q_m^+}{kT}\Big) - \nu_- exp\Big(-\frac{Q_m^- + Pb_a^3}{kT}\Big)\right), \tag{1.20}$$

where Υ^+ and Υ^- are the jump frequencies of atoms in both directions, ν the attack frequency, Q_m the migration free energy, k the Boltzmann constant, T the absolute temperature, P the net driving pressure and Pb_a^3 is the free energy gained when an atom is attached to the growing grain ($\Omega_a = b_a^3$ the atom volume). Assuming $\nu_+ = \nu_- = \nu_D$ (where ν_D is the Debye frequency) and same free energy in both directions $Q_m^- = Q_m^+ = Q_m$ the velocity may be simplified as:

$$v = b_a \nu_D exp\Big(-\frac{Q_m}{kT}\Big)\Big(1 - exp\Big(\frac{Pb_a^3}{kT}\Big)\Big), \tag{1.21}$$

if $Pb_a^3 \ll kT$ $(T \geq 0.3T_m)$

$$exp\Big(-\frac{Pb_a^3}{kT}\Big) \approx 1 - \frac{Pb_a^3}{kT}, \tag{1.22}$$

which gives a simplified equation for the velocity of a GB

$$v = \frac{b_a^4 \nu_D}{kT} exp\Big(-\frac{Q_m}{kT}\Big) \times P, \tag{1.23}$$

this model is simple and could be refined, one could, for example, integrate the influence of vacancies or solute atoms.

In a more general form, GB velocity may be defined, in the unitary normal direction to the GB ($\vec{n}$), as the product of the GB mobility and the sum of driving pressures $P = \sum P_i$:

$$\vec{v} = \mu P \vec{n}, \tag{1.24}$$

the units for the velocity, mobility and driving pressure are $\left[\frac{m}{s}\right]$, $\left[\frac{m^4}{J \cdot s}\right]$ $\left(\left[\frac{m}{s \cdot Pa}\right]\right)$ and $\left[\frac{J}{m^3}\right]$ $\left(\left[\frac{N}{m^2}\right]\right)$, respectively. Sources of driving pressures are of different nature (Table 1.3), and theoretically any gradient of intensive quantities (electric potential, interfacial energy, magnetic field, electric field, concentration, etc) could be a driving pressure, as in the diffusion of species where conjugate forces generate the fluxes. The mobility described in Equation 1.23 by $\mu = \frac{b_a^4 \nu_D}{kT} exp\Big(-\frac{Q_m}{kT}\Big)$ is often simplified at the mesoscopic scale and in hot metal forming context through an Arrhenius law (thermally activated):

$$\mu = \mu_0 \ exp\Big(-\frac{Q}{RT}\Big), \tag{1.25}$$

where μ_0 is a constant preexponential factor, Q the activation energy, $T\,[K]$ the absolute temperature and R the universal gas constant.

Indeed, in practice the migration of grain boundaries as a function of atom jumps using Equation 1.23 is difficult to identify. Thus at the polycrystalline scale, and because the considered T range are often not very wide, rough approximations of Equation 1.23 are classically considered through assuming a constant value of μ_0 or only as a function of the temperature.

Generally during recrystallization, the two main driving pressures are due to capillarity effects P_c and the difference in stored energy during plastic deformation P_e, the total pressure is $P = P_c + P_e$. P_c and P_e are defined classically as [1]:

$$P_c = -\gamma\kappa, \tag{1.26}$$

and

$$P_e = [\![E]\!] = \tau[\![\rho]\!], \tag{1.27}$$

where γ is the grain boundary energy, κ is the local mean curvature and $[\![E]\!]$ is the jump of stored energy through the grain boundary. Figure 1.9 illustrates a scheme

of the driving pressures directions, a negative driving pressure reduces the GB size while a positive one increases it. P_c points to the center of curvature of the GB, and P_e points toward the grain with higher stored energy. At the mesoscopic scale dislocations can be described in terms of density and not individually as in the case of dislocation dynamics, therefore the stored energy can be approximated as $E = \tau \times \rho$ where the energy per unit dislocation line, τ, is approximated through the relation $\frac{Gb^2}{2}$, where G and b are respectively the shear modulus and the Burgers vector. As summarized in table 1.3 other driving pressures may be present during recrystallization but the driving pressure due to the capillarity and the difference in the stored energy are two or more orders of magnitude higher in the context of hot metal forming and when solid/solid phase transformations are not involved.

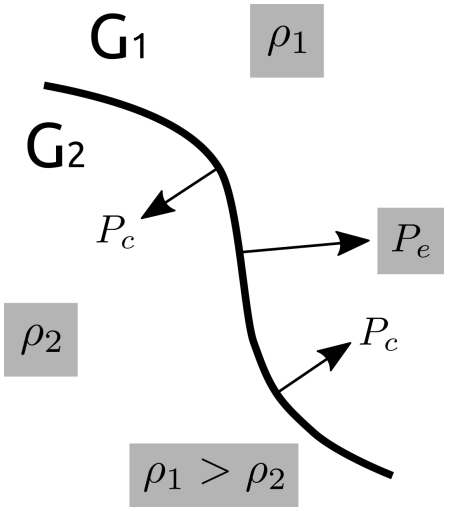

Figure 1.9: Representation of the driving pressures between two grains G_1 and G_1. The driving pressure produced by capillarity P_c tends to flatten the GB. The driving pressure produced by stored energy P_e points toward the grain with higher dislocation density ρ, this driving pressure tends to decrease the total stored energy of the system. P_c direction can change along the GB. ρ is the dislocation density which defines the stored energy.

Source and equation	**Parameters**	**Estimated P [MPa]**
Chemical driving force $P = R(T_1 - T_0)c_0 ln\|c_0\|$	c_0: concentration, maximum solubility at T_0; $T_1(T_0)$: annealing temperature	$\sim 6e2$
Stored deformation energy $P = \frac{1}{2}\rho G b^2$	ρ: dislocation density; $\frac{Gb^2}{2}$: linear dislocation energy	~ 10
Grain boundary energy (Capillarity) $P = -\gamma\kappa$	γ: grain boundary energy; κ: grain boundary curvature	~ 0.01
Magnetic field $P = \frac{\mu_0 H^2 \Delta\chi}{2}(cos^2(\Theta_1) - cos^2(\Theta_2))$	H: Magnetic field magnitude; $\Delta\chi$: difference of magnetic susceptibilities; Θ: magnetic field direction	$\sim 3.5e-04$
Elastic energy $P = \frac{\tau^2}{2}\left(\frac{1}{E_1} - \frac{1}{E_2}\right)$	τ: elastic stress; E_1, E_2: elastic moduli of neighboring grains	$\sim 2.5e-04$
Temperature gradient $P = \frac{\Delta S 2\lambda grad(T)}{\Omega_a}$	ΔS: entropy difference between adjacent grains; T: temperature gradient; 2λ: grain boundary thickness; Ω_a: molar volume	$\sim 4e-05$

Table 1.3: Examples of driving pressure (in $[MPa]$) for GB migration, from [52].

1.2 Experimental Results

Generally speaking, experimental results homogenized at the mesoscopic scale are consistent with Equation 1.24. Nevertheless, in certain cases the relation is not strictly verified and large variations of this kinetic equation can be seen at the GB scale. Measurements of the mobility are difficult because of the number of parameters affecting it [52]. Also, the developments of predictive models for the mobility of boundaries are complex because of the symmetries of the crystals adjoining the boundary and the arrangement of the atoms in the boundary [1]. When studying GB motion, one has to make two crucial decisions: choose a sample geometry and the driving pressure(s) involved to estimate the GB properties. Not all the driving pressures are easy to produce in a laboratory. The driving pressure used in the experiments is chosen based on its reproducibility, magnitude, stability, and the possibility to control, e.g., using a magnetic field. During GG experiments, GB normal velocity is defined as:

$$v = -\mu\gamma\kappa, \tag{1.28}$$

this equation is a simplification of a more complex equation involving the GB stiffness tensor $\Gamma(\vec{n})$, i.e., $\vec{v} = -\mu\Gamma(\vec{n}) : \mathbb{K}\vec{n}$, where $\Gamma(n) = \gamma + \nabla_n\nabla_n\gamma$, $\mathbb{K}$ is the curvature tensor, and ∇_n the surface gradient. The main issues about the GG experimental results are that the anisotropy of the GB energy is generally neglected: $\Gamma(\vec{n})$ is systematically simplified to γ due to the difficulty to evaluate $\Gamma(\vec{n})$. Finally, μ and γ cannot be dissociated, appearing through the product $\mu\gamma$ (sometimes called reduced mobility) which often leads to inconsistencies in the literature where the real behavior of μ is frequently confused with that of $\mu\gamma$.

A way to dissociate μ from γ can be to use an additional driving pressure. Most of the studies are performed using deformed samples involving P_c and P_e, thus, the GB velocity is defined as:

$$\vec{v} = \mu(-\gamma\kappa + [\![E]\!])\vec{n}. \tag{1.29}$$

It must be highlighted that in this equation, κ and $[\![E]\!]$ are signed scalar quantities depending on the local GB characteristics and the local direction of the dislocation density jump across the GB, see Figure 1.9. The driving pressure produced by the stored energy is uncertain because of its difficulty to be measured and its non-homogeneity. However, it has been frequently studied due to its importance in industrial processes.

The aim of the next section is to define the parameters affecting the mobility and the limits of the Equation 1.25 represented by nonlinearities in Arrhenius plots and changes in the activation energy based on experimental evidences. The GB mobility sigmoidal model is introduced, this model is based on experimental observations and is frequently used in mesoscopic simulations to define GB mobility as a function of the disorientation, $\mu(\theta)$. These results are part of the first experimental studies realized to study GB mobility.

1.2.1 Crystal arrangements

The measurements of GB mobility are mostly carried out in subgrains [55–58] and bicrystal [59–65] arrangements, Figure 1.10 illustrates some of the geometries used. Polycrystalline arrangements take into account the effect of neighboring crystals and multiple junctions, thus, correlation between mobility and temperature, pressure, impurity, grain boundary structure, the study of atomic mechanisms and other specific parameters is difficult to obtain for a particular GB. On the other hand, bicrystal specimens provide data for a specific GB with a define misorientation and are reproducible but they are difficult to manufacture.

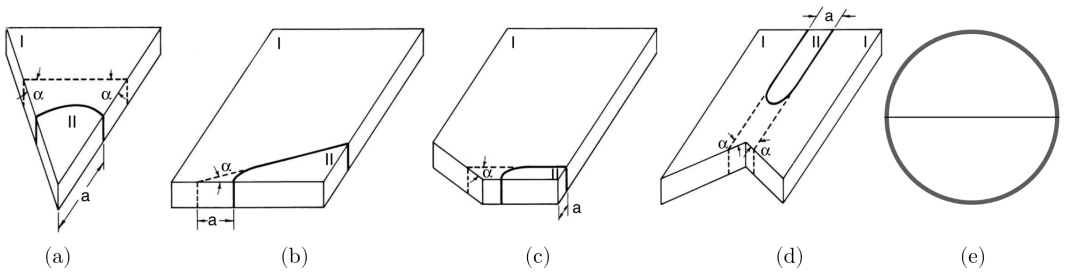

Figure 1.10: Crystalline arrangements. (a) Wedge technique, (b) reversed capillary technique, (c) quarter loop technique, (d) half-loop technique, (e) Crystal used in [55], the line in the center represents a scratch, subgrain growth is perpendicular to the scratch. From [52].

The use of bicrystals was one of the first methodologies used to estimate the reduced mobility [52, 59–66]. The first estimations of GB reduced mobility ($\mu\gamma$) were computed using the wedge technique, reverse capillary technique or quarter loop (QL) technique. The main advantage is the reproducibility of results. However, this relies on the accuracy of the sample fabrication. Such crystal arrangement requires the use of two (or three) single crystal seeds cut specifically to create a specific misorientation of the bicrystal (tricrystal). The seeds are then connected to a polycrystal using local melting and are grown by directional melting (see [66] for more details). Hence, several defects can be induced, for instance, porosities during the melting/solidification stage, cracks during the solidification or even recrystallization nucleation due to work-hardening after cutting the sample.

Each crystal arrangement has its advantages and disadvantages to estimate the mobility parameters, crystal arrangements that isolate the migration of the GB are preferred. GB reduced mobility is calculated from the evolution of geometrical data: the position of GB tip is followed and its velocity is estimated. Finally, the driving pressure is estimated as $P = \gamma\kappa$, this pressure is different for the wedge, reversed capillary, QL and half loop (HL) techniques. Hence, the GB reduced mobility is estimated as $\mu\gamma = v/\kappa$. The driving pressure using the wedge

geometry (Figure 1.10a) is computed as:

$$P = \frac{\gamma}{R} = \frac{\gamma}{a}, \tag{1.30}$$

where a is the distance from the edge of the sample to the GB and R the radius of the GB, see Figure 1.10a. The main advantage of the methodology is the simple description of the driving pressure and its disadvantage is that the driving pressure increases as the GB evolves. At the beginning the driving pressure is small and the external pressures, i.e., grooving, can easily modify the GB motion until the external forces are overcome. For that reason, the driving pressure can be underestimated and so the reduced mobility overestimated.

The reversed-capillary method was firstly proposed by Sun and Bauer [67]. The magnitude of the driving pressure can be modified changing the angle α, see Figure 1.10b and the relation for the driving pressure is given by

$$P = \frac{\gamma}{R} = \frac{\gamma}{a} f(\alpha), \tag{1.31}$$

with $f(\alpha)$ an amplification factor. The main disadvantage of the wedge (Figure 1.10a) and reversed-capillary (Figure 1.10b) geometries is the lack of steady state velocity, which was solved using the QL and HL techniques [61].

The QL (Figure 1.10c) and HL (Figure 1.10d) techniques are characterized by both a transitory movement and a steady state movement. At the steady state the GB moves as a whole with an *average* driving pressure defined for the QL and HL respectively as

$$P_{QL} = \frac{\gamma}{a} \text{ and } P_{HL} = \frac{2\gamma}{a}. \tag{1.32}$$

Overall, the best bicrystal techniques are the QL and HL because the grooving is minimized and they can be extended to triple junctions. We have to keep in mind that the estimated values of reduced mobility are average for the considered misorientation because the dependence on the GB inclination is neglected (See a numerical example in Appendix A.1). Also, the GB energy, γ, is unknown. Thus, the effects of both GB mobility and energy, are measured simultaneously through the reduced mobility.

Finally, Humphreys and colleagues [55,57,68] used single crystals of Al under the assumption of a driving pressure provided by the subgrains following the relation $P = \frac{c\gamma}{L}$, with c a constant equal to 1 or 2 and the GB energy, γ, is defined using the Read-Shockley model [69] and L the mean linear subgrain intercept. For HAGB, in addition to the pressure provided by the subgrains, a retarding pressure is taken into account, its value is given by the relation $P_c = \frac{2\gamma_{max}}{R}$ where γ_{max} is the GB energy of HAGBs assumed as constant and R is the equivalent radius of the grain. As it was mentioned before, the value of the driving pressure is averaged and is affected by the measurement errors. In the following subsections, experimental results are presented. A significant part of these results was obtained using bicrystal samples, a simplified view of the capillarity pressure and

by frequently substituting the notion of reduced mobility for that of GB mobility. Additionally, thermal grooving affects the motion of GBs, and it affects the actual identified value of grain boundary mobility. Thus, these existing results discussed here must be handled with caution.

1.2.2 Mobility regimes

Following discussions proposed in [1], mobility of grain boundaries is often divided into regions depending on the disorientation, θ. Four regions are identified as shown in Figure 1.11. Table 1.4 presents the main characteristics of regions **A**, **B**, **C1** and **C2**. The doted lines in Figure 1.11 indicate insufficient experimental data of region **A**.

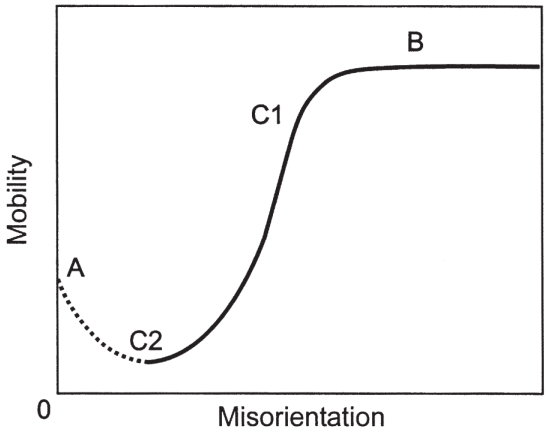

Figure 1.11: Schematic diagram of the regions of GB mobility as a function of the disorientation. From [1].

1.2.3 Experimental evidence of the sigmoidal model

Knowledge of migration of LAGB is of great importance during recovery and continuous dynamic recrystallization. Boundary structure of LAGBs is composed of dislocation arrays. Motion of LAGBs consists in a collective movement of individual dislocations produced by shear stress. In [71–75], GB motion is studied under mechanical stress and it has been shown that the mobility seems dependent on the misorientation angle. Figure 1.12 illustrates the effect of misorientation angle on the GB velocity under a constant stress of symmetrical tilt boundaries in Zinc, this figure illustrates the region **A** reported in Figure 1.11 but few experimental studies are available in the literature for $\theta < 1°$. Also, for low values of θ, we may not talk about a GB but more of a dislocation arrangement. It must be highlighted that Figure 1.12 reports a tendency of v but it is assumed that μ have the same tendency because it follows Equation 1.24 with a driving pressure

Table 1.4: Main characteristics of the regions shown in Figure 1.11. C, c_j, b, and D_S are respectively a constant, the concentration of jogs, the Burgers vector and the coefficient of self-diffusion.

Region	**Disorientation** $\theta\,[^\circ]$	**GB mobility** $(\mu(\theta))$	**Mechanism**
A	$\theta \to 0$	$\mu = \frac{c_j b^2}{4c_1\theta}\frac{D_S}{kT}$	Dislocation climb and glide [70]
C2	$2-5$	$\mu = Cb\frac{D_S}{kT}$	Dominant mechanisms not clear, it may be related to the movement of dislocations [1]
C1	$5-15$	$\mu \propto \theta$	Atoms transfer (Analogous to the diffusion through a membrane of thickness h)
B	$\theta > 15$	μ independent of θ, equation 1.23	Atom jumps across the boundary

defined in a particular form:

$$P = 2\tau_{xy} sin\frac{\theta}{2}, \tag{1.33}$$

where τ_{xy} is a constant shear stress. This result also illustrates that the GB mobility definition ($\mu = \vec{v}/P$) can often be experiment or model dependent which, somewhere, complexify the global discussion concerning the effective parameter impacting the GB mobility.

Other studies of GB motion under the influence of a shear stress were carried out by Gorkaya et. al [65, 72–75]. Experiments of tilt boundaries in high purity aluminum have shown a transition of the GB mobility at $\theta \approx 13.6^\circ$ at 573 and 873 $[K]$ ($0.61T_m$ and $0.93T_m$), see Figure 1.13. At 873 $[K]$, the mobility of LAGB is higher than the mobility of HAGB. In [72] the activation energy, Q, obtained from the two different tilt boundaries (<112> and <111>) are similar. In [72], the authors have also exhibited a difference of the activation energy between LAGBs and a HAGBs, Q_{LAGB} =123.5 $[kJ/mol]$ and Q_{HAGB} =81.05 $[kJ/mol]$. In [72], Q_{LAGB} and Q_{HAGB} are similar to the activation energy of self-diffusion in aluminum and grain boundary diffusion, respectively.

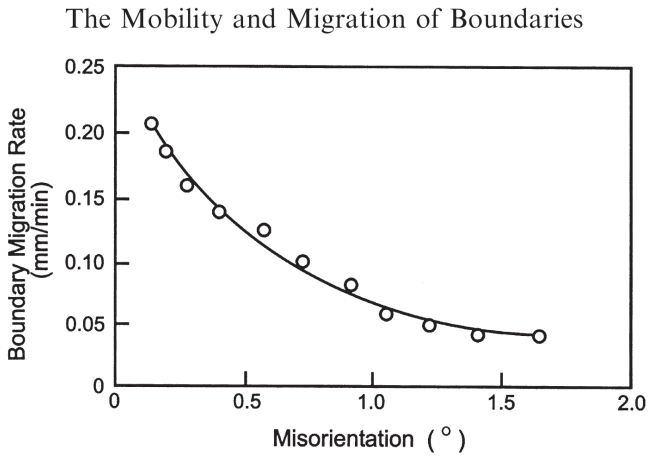

Figure 1.12: GB velocity of symmetrical tilt boundaries at $350°C$ under a constant stress of $63.4\,[kPa]$ in Zinc as a function of disorientation. Taken from [1] from the work of [71].

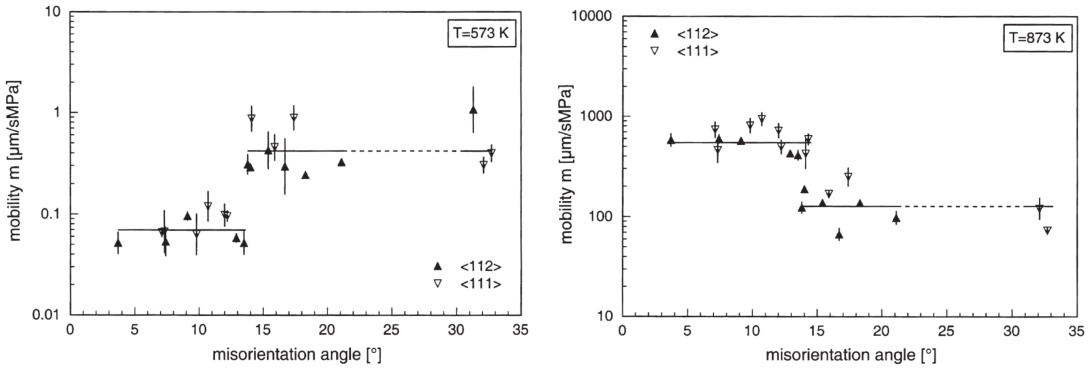

(a) (b)

Figure 1.13: Dependence of the grain boundary mobility on the misorientation angle of symmetrical planar <112> and <111> tilt boundaries under the influence of stress of high purity aluminum at (a) $573\,[K]$ and (b) $873\,[K]$. From [72].

In [65], motion of curved and planar tilt boundaries are compared, the driving force of the planar GB is defined by Equation(1.33) and regarding the curved GBs the authors used the QL technique, the driving pressure is defined as $P = \gamma/a$ leading to

$$v = -\frac{\mu\gamma}{a}, \tag{1.34}$$

with a the width of the QL bicrystal, see Figure 1.10. The authors found different migration mechanisms for planar and curved GBs based on the behavior of the activation energy and a different dependence of the activation energy on the GB disorientation. These results however neglected the anisotropic nature of γ and took it as a constant, $\gamma = \gamma_{max}$. In [2], a new equation of GB migration was proposed under the assumption that GB migration is controlled by the motion of linear defects, thus the driving pressure is divided into a driving pressure

associated with shear stress and the second is associated with surface energy reduction in the system, i.e., capillarity.

Humphreys et al. carried out several studies using aluminum alloys. The authors have shown one of the first EBSD in-situ techniques that allow the tracking of crystals and opened a new way to study the evolution of microstructures. However, one issue is encountered: how recrystallization was induced, for instance, the surface is abraded [68] or a scratch is done in the middle of the sample [55], hence the experiments are hard to reproduce. Even so, they reported the mobility dependence on the misorientation angle of region **C2**, see Figure 1.14. Also, the data fit the power law $\mu_0 = k\theta^C$ ($k = 3\times10^{-6}\,[m^4/Js]$ and $C = 5.18$) represented by a solid line [68].

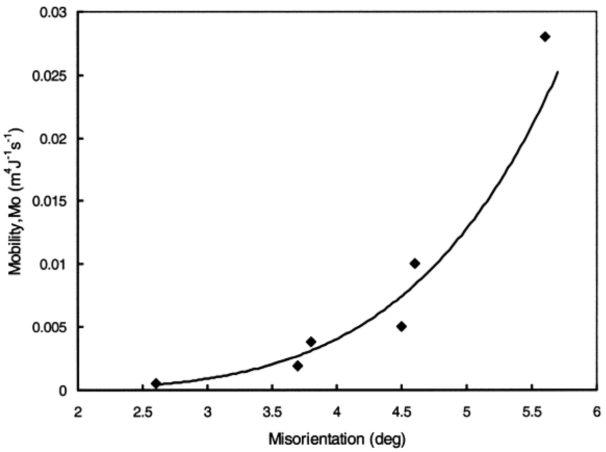

Figure 1.14: Effect of the average grain disorientation on the mobility of LAGB using high purity $Al - 0.005\%Si$ alloy at $300°C$. From [68].

Some characteristics of LAGB have been reported by Bauer et. al [59, 67]. The measurements were performed using the reversed capillary technique. GB mobility measurements are indirect using the expression $a^2/f(\alpha) = 2\mu\gamma t$ where a is the wedge displacement of the hyperbolic GB generated by capillary forces, t the annealing time and $f(\alpha)$ is a parameter related to the geometry of the GB. K is a normalized parameter, it may also be defined as a *pseudo reduced mobility*:

$$K = 2\mu\gamma f(\alpha). \tag{1.35}$$

It means that these results are related to the tip of the GB. Thus, the GB is subjected to surface grooving, and once again, its change in normal direction is neglected. On the other hand, the driving pressure is not constant. Figures 1.15a and 1.15b show the GB mobility and activation energy dependence on disorientation for sodium chloride and copper, one can see that $Q_{LAGB} > Q_{HAGB}$. The same tendencies are depicted in Figure 1.13b. Also, the activation energy of LAGB of copper $Q_{Cu,LAGB}$ is close to the activation energy in self diffusion and $Q_{NaCl,LAGB}$ is close to the diffusion of Cl^- in $NaCl$.

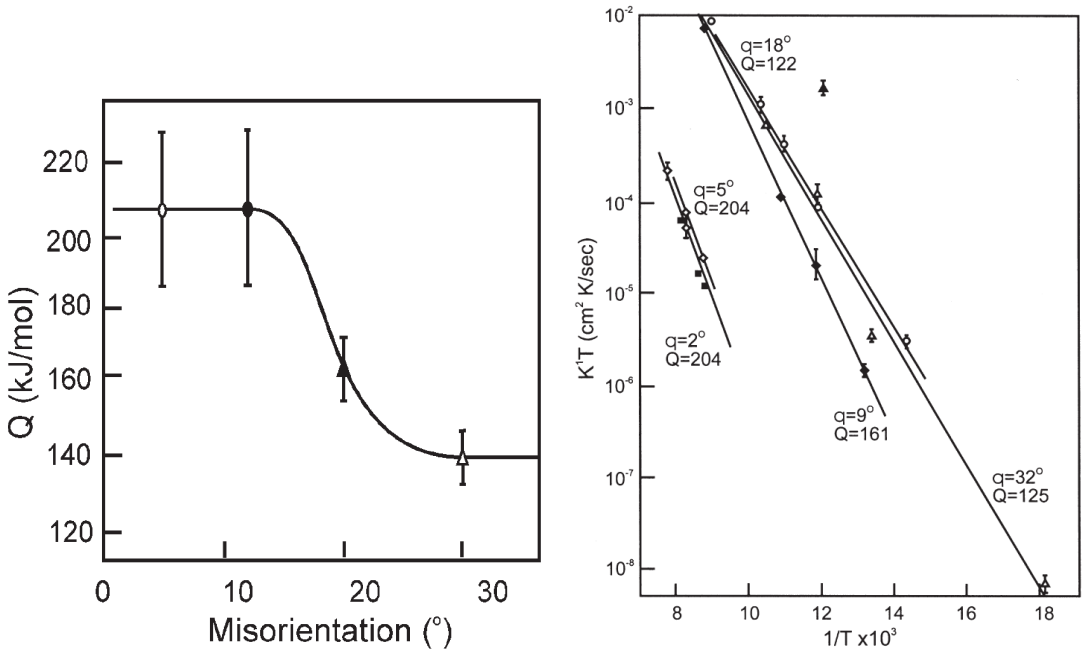

(a) (b)

Figure 1.15: (a) Variation of the activation energy with misorientation angles around the axis <100> of NaCl bicrystals, from [67]. (b) Variation of the reduced mobility K' with temperature and the misorientation angle for high purity copper. The unit of the activation energy Q are $[kJ/mol]$, from [59]. Both experiments were carried out using the reversed capillary technique.

Several investigations of boundary mobility in aluminum have been reported [56, 68, 76]. In [56], the annealing behavior of cube-oriented crystals is studied (Figure 1.16a). It was found, for different temperatures, that the mobility increases with misorientation and reaches a plateau which is consistent with regions **C1** and **B** as illustrated in Figure 1.11. For these two regions, a sigmoidal empirical relation between μ and θ has been proposed and is classically used [77]:

$$\mu = \mu_{max}\left(1 - exp\left(-B\left(\frac{\theta}{\theta_0}\right)^A\right)\right), \tag{1.36}$$

where μ_{max} is the mobility of HAGB (supposed to be constant), θ_0 the misorientation angle when the boundary could be defined as $HAGB$ and two constants A and B; in [68] $A = 4$ and $B = 5$. Equation 1.36 may be redefined in order to introduce the effect of the temperature as a result of the difference between the activation energies of LAGB and HAGB as seen in Figures 1.15a and 1.16b using a sigmoidal relation.

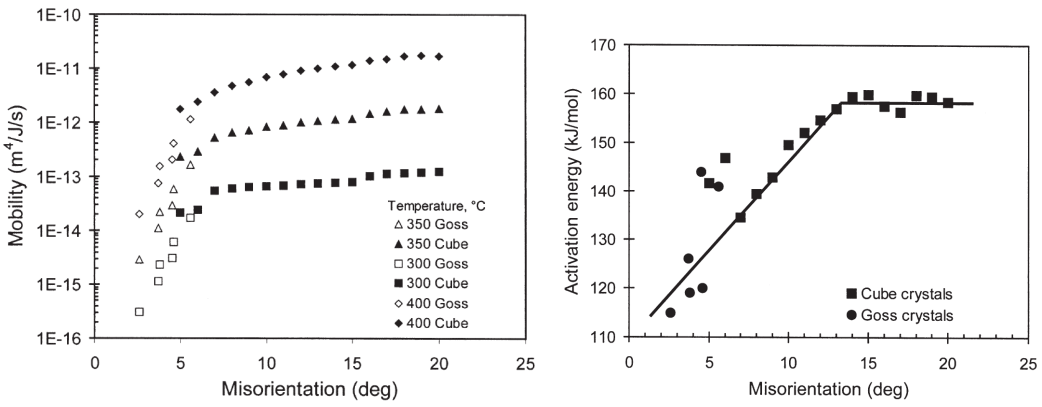

(a) (b)

Figure 1.16: (a) Variation of the mobility with temperature and the misorientation angle for $Al - 0.05\%Si$. Combined results of subgrain growth in crystals of Goss and Cube orientation. From [1]. (b) Effect of the misorientation angle on the activation energies (Q) in $Al - 0.05\%Si$ measured from subgrain growth. From [56]. Both experiments were carried out using the single crystal technique.

These results show the experimental framework of the model frequently used to describe GB mobility in mesoscopic models of GG and ReX. However, they are based on 2D data, GB energy is assumed to be isotropic and the GB stiffness tensor is neglected. New methodologies to estimate GB mobility have emerged and intend to give a better insight of the GB properties and motion mechanisms. In the next two subsections, additional results are presented and the limitations of the classical mesoscopic GB migration equation (Equation 1.24) are discussed.

1.2.4 Limitations and transitions: Non-continuous Arrhenius plots and different disorientation dependence

HAGB have been studied in more details than LAGB. The effect of temperature, misorientation, boundary plane, impurities and point defects must be studied to understand the grain boundary migration in more complex materials such as alloys with the aim to take them into account in the numerical description of GBs at the mesoscopic scale.

The effect of temperature

As seen above, the activation energy gives an idea about the thermally activated atomic processes. Constant activation energies over a temperature range as seen in Figure 1.15b are typical of high purity materials. In alloys and low purity materials, transition temperatures are important and should be taken into account leading to different activation energies depending on the temperature ranges [61, 78, 79].

- **Change in the boundary structure:** Rutter and Aust [78] have shown the temperature and misorientation angle dependence of the activation energy in bicrystals of high purity lead for <100> tilt boundaries. Activation energies in CSL boundaries are lower due to a change in the structure and/or the presence of impurities. Activation energy changes were also exhibited by Maksimova et al. [61] for boundaries within 1° of the Σ17 (28°) in 99.9999% purity Tin. Figure 1.17 shows a drop in mobility around the Σ17 boundary while increasing the temperature. The change in the activation energy at high temperatures is explained by the authors as resulting from a grain boundary structure change, within the temperature range used in their experiments where diffusion coefficients of boundaries are similar to that of liquids, between $0.94T_m$ and $0.98T_m$.

- **Change in the mechanisms of boundary migration:** Several experiments in pure lead and zinc at elevated temperatures ($T > 0.7T_m$) have shown a transition regime to low or zero activation energy, this transformation may be related to an evolution from a diffusion mechanism to a cooperative atomic shuffle [1].

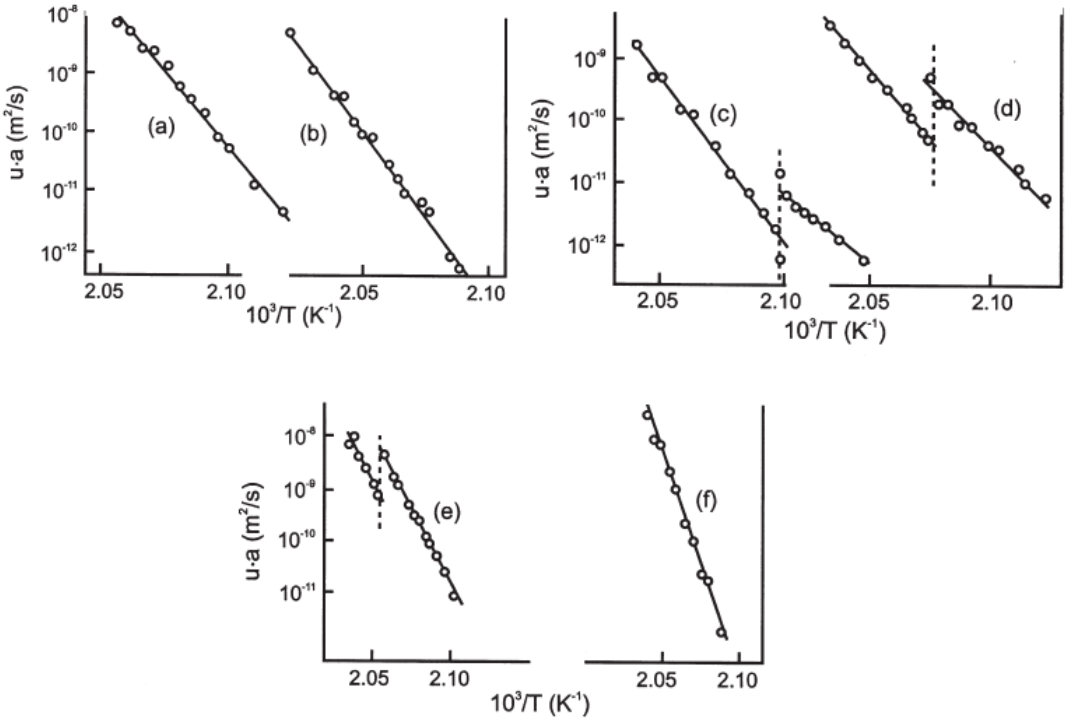

Figure 1.17: Discontinuity in the migration of boundaries under capillary driving pressure. Temperature dependence of the <001> tilt boundary migration rate in Tin using a constant driving force. Boundaries within ≈ 1° of the Σ17 boundary: (a) 26°, (b) 26.5°, (c) 27°, (d) 27.7°, (e) 28.2° and (f) 29.5°, from [61].

The effect of the GB misorientation

Several authors have found that crystals grow rapidly when having boundaries with certain disorientation. Kronberg and Wilson [80] postulated that it exists a relation between fast growing and the structure of the involved boundaries, i.e., special boundaries. Humphreys and Huang carried out investigations in aluminum [55] using a cylindrical crystal depicted in Figure 1.10 and a scratch to induce recrystallization. Figure 1.18 shows the effect of both misorientation angle and the angle from the <111> axis on the GB migration velocity. As one can see, the beginning of Figure 1.18a shows a similar tendency of the sigmoidal model but after 40°, the grain relative velocity decreases. However, it is important to point out that the authors analyzed the movement of GBs in 2D. Also, the stored energy is approximated as

$$E_D = \frac{2\gamma_{max}\dfrac{\bar{\theta}_G}{\theta_0}\left(1 - ln\dfrac{\bar{\theta}_G}{\theta_0}\right)}{\bar{L}}, \tag{1.37}$$

where $\bar{L}$ is the mean linear grain intercept, $\bar{\theta}_G$ the mean grain disorientation and γ_{max} the GB energy of HAGBs.

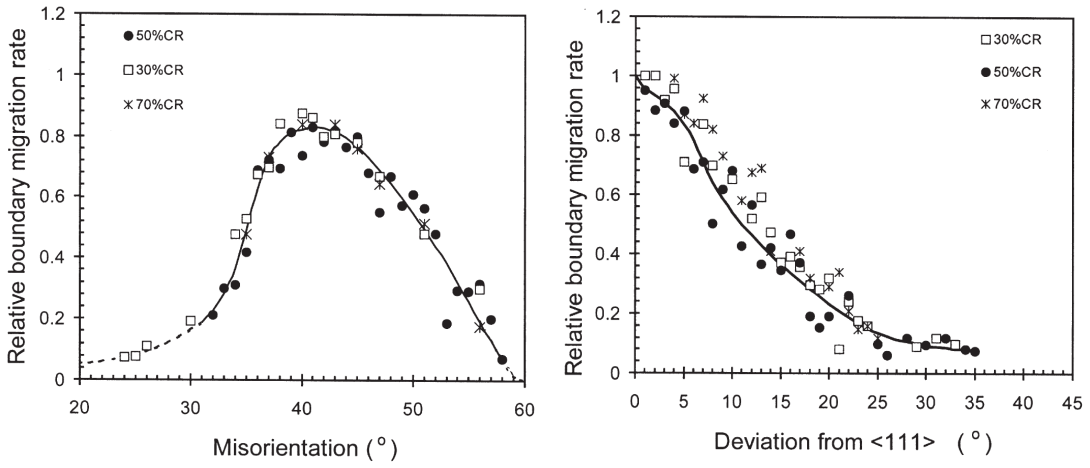

(a) (b)

Figure 1.18: Relative boundary migration rates in a deformed single-phase Al-Si alloy using the single crystal technique. (a) Relative migration variation with misorientation angle. (b) Relative migration variation with deviation from a <111> axis. From [55].

Another example where the sigmoidal model of GB mobility seems not representative anymore is frequently found in materials with high impurity levels. Shvindlerman and colleagues carried out experiments in aluminum at different percentages of purity of tilt boundaries. Figures 1.19a and 1.19b show the effect of the disorientation on the reduced mobility and the activation energy. The

advantage of these experiments, using capillarity driving pressures, is to study particular bicrystal configurations. Figure 1.19a shows a peak at $\theta = 38.2°$ ($\Sigma 7$ twin boundary (TB)) and a transition at $\theta = 40.5$ °. The two disorientations have two different values of activation energy, also, the reduced mobility of <111> tilt boundaries of 40.5° is higher at elevated temperatures whereas at low temperatures the reduced mobility of 38.2° is higher. This transition of the dominant disorientation may be related to grain boundary structure change and solute drag as seen in Figure 1.19b where the activation energy is lower near CSL configurations.

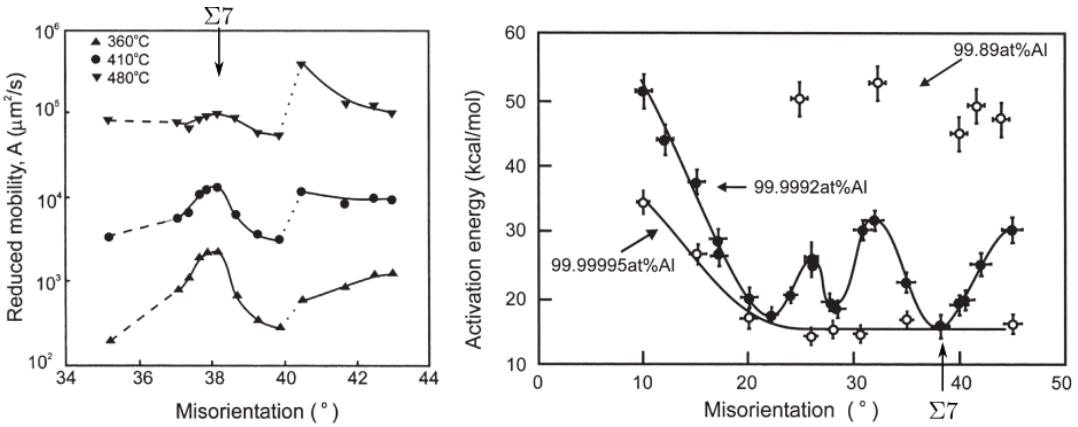

(a) (b)

Figure 1.19: (a) Effect of temperature and disorientation on the reduced mobility of <111> tilt boundaries in 99.999%Al determined by curvature driven grain growth. From [81]. (b) Disorientation and purity dependence of the activation energy for migration of different purity of <100> tilt boundaries in aluminum. From [82].

Experimental investigations [56, 81] have reported a relation between the activation energy Q and the preexponential term μ_0 summarized in Equation 1.38. α and β are constant for a similar type of boundaries (tilt or twist). This relation is known as *the compensation effect*, observed in thermally activated processes like grain boundary diffusion or grain boundary migration, and is defined as:

$$Q = \alpha ln|\mu_0| + \beta. \tag{1.38}$$

The compensation temperature $T_c = \frac{\alpha}{k}$ highlights two regions: above T_c, the higher is μ_0 the higher is Q as shown in Figure 1.19a, while for $T < T_c$ the higher is μ_0 the lower is Q.

These results reveal a complex behavior of GB motion as a function of solute concentration and temperature which makes the study of GBs more complex. To the author's knowledge, this kind of study has never been done in steels or other alloys, this is discussed in the following section (Section 1.2.5).

The effect of the boundary plane

GB plane effect on the GB mobility has also been reported [1,5]. Twist boundaries can grow slower than tilt boundaries as seen in Figure 1.20, which is a clear evidence of oriented growth.

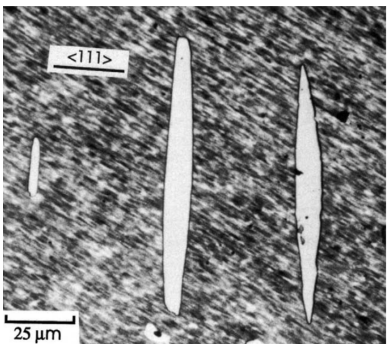

Figure 1.20: Optical micrograph of lenticular grains, viewed edge-on in a recrystallizing single crystal of $Al-0.05\%Si$. The broad face is parallel to the rotation axis, i.e. tilt boundary. From [83].

1.2.5 The effect of impurities and point defects

Until now, experimental results of high purity materials have been shown. In real materials, impurities and solutes must be taken into account in order to enhance the description of GB properties. The GB mobility can be decomposed into intrinsic and the extrinsic components, denoted as μ_i and μ_e (also called "solute atom drag mobility"), respectively [54,59]. Results shown in the previous sections represent the intrinsic mobility when the impurities do not affect the values of the mobility and the Arrhenius plot of equation 1.25 is globally verified.

Effect of solute concentration

The velocity of a GB is affected by the presence of impurities or solutes that produce a drag pressure $P_d = P_d(v, C, T)$, where C is the solute concentration [54]. In order to find the relation between the GB velocity $v(p, C, T)$ and its interaction with the solutes, the applied pressure P is approximated to the sum of the drag pressure P_d and the intrinsic pressure P_i (i.e. the driving pressure that would move the boundary at the same velocity v without impurities):

$$P(v, C, T) = P_i(v, T) + P_d(v, C, T) \ . \tag{1.39}$$

If equation 1.39 is multiplied by v, it could be seen as the energy dissipated by the intrinsic migration and the drag effect

$$Pv = P_i v + P_d v \ . \tag{1.40}$$

Finally, dividing equation 1.39 by v, a relation between the mobility and its components μ_i and μ_e can be expressed as

$$\frac{1}{\mu} = \frac{1}{\mu_i} + \frac{1}{\mu_e}. \tag{1.41}$$

In addition to the GB mobility dependence on impurity species, concentration and distribution, P depends on GB pinning, surface drag and thermal grooving at free surfaces. Figure 1.21 shows two different regimes in function of the concentration of Mg and Cu solute atoms in Al: at **high concentration** the GB mobility is low and at **low concentration** the GB mobility is higher and does not vary strongly with concentration. Figure 1.21a shows that at high concentration the solute *atmosphere* affects the GB migration whereas in the high GB mobility regime the GB is not affected by the solutes. In addition, the nature of the solute atom alters the transition of the two velocity regimes (see Figure 1.21a) and the activation energy transition as shown in Figures 1.21b and 1.21c.

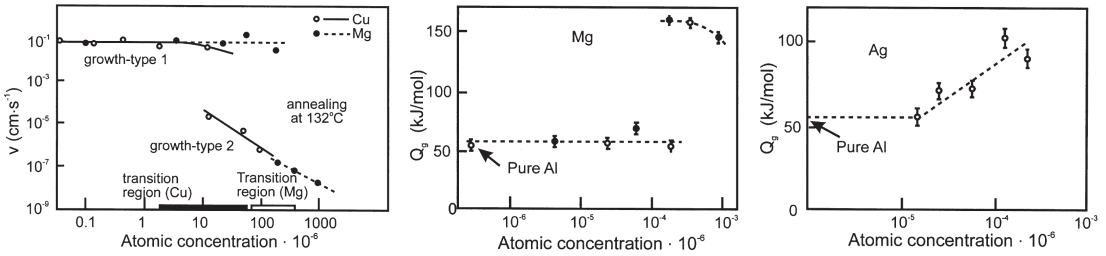

(a) Effect of Cu and Mg on v. (b) Effect of Mg on Q. (c) Effect of Ag on Q.

Figure 1.21: Effect of impurities on the growth of new grains in deformed aluminum. From [84].

Combined effect of temperature and solute concentration

The effect of temperature is indirectly linked to the activation energy Q. Here the term *apparent activation energy* is used because it may not correspond to only one physical mechanism. In Figure 1.22a, a peak is found at high temperatures for GB mobility in Au with 20 ppm Fe, the apparent activation energy is lower and the GB mobility increases abruptly. In other cases, a peak is found depending on the concentration of the solute atom as seen in Figure 1.22b for aluminum. This transition is due to the interaction between the solutes and the GB, this interaction could be explained using the concept of GB adsorption and could be divided into four segments. The first is characterized by Q independent of the concentration C. The second is characterized by an increase of Q with increasing C. The third is characterized by a decrease of Q, this means that not all the solute atoms moves within the boundary. Finally the GB adsorption is saturated and Q remains constant.

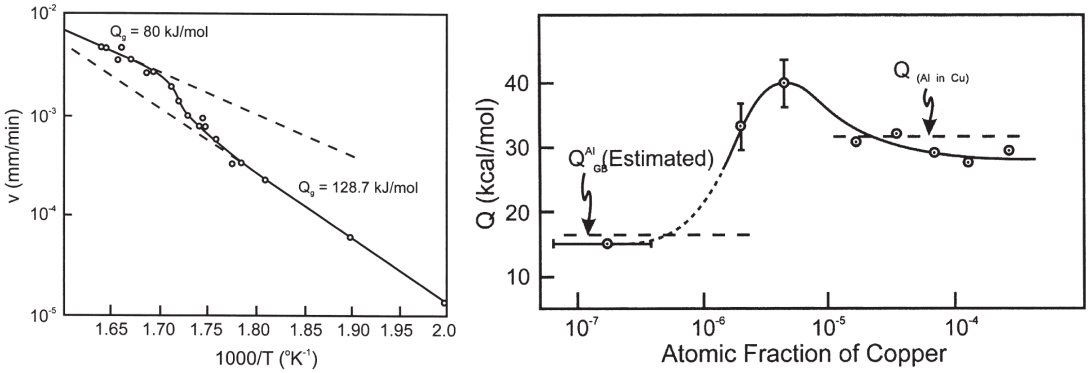

(a) (b)

Figure 1.22: Effect of temperature on grain boundary migration. (a) Effect of the temperature on the migration velocity of a 30° <111> tilt boundary in gold with 20 ppm Fe. From [1] according to the work of [85]. (b) Effect of Cu on the activation energy of boundary migration in aluminum. From [1] according to the work of [86].

Combined effect of solute concentration, orientation and temperature

As it has been shown, GB mobility and structure are related. Random and special GBs dependence on the solute concentration differs. Both types of GBs have similar mobilities at low concentrations but when the concentration increased random GBs change more drastically as seen in Figure 1.23. The effect of the disorientation on the activation energy and the reduced mobility of tilt boundaries is shown in Figures 1.19a and 1.19b. In both figures, for a certain amount of solute concentration, the GB mobility reaches a peak at disorientation near the Σ5 CSL site. Nevertheless, this behavior is not general for all impurity levels. In Figure 1.19b, for aluminum of 99.99995% purity, the activation energy does not fluctuate and for aluminum of 99.89% purity the disorientation effect on the activation energy is lower. The peaks at the CSL disorientation may be link to a less constraint GB structure where atoms could diffuse along or across the GBs.

The temperature effect on the mobility of grain boundaries also seems more complex than generally considered. Experiments of <100> tilt boundaries on aluminum [82] and lead [78] have reported the combined effect of temperature and misorientation as seen in Figure 1.24. At high temperatures the boundary velocity tends to be constant for HAGBs, this may be due to the detachment of the solute atmosphere from the boundary.

These results confirm the GB mobility dependence on the disorientation (and more generally on misorientation) under the influence of impurities or solute atoms. Also, the effect of the solute concentration depends on the temperature. Point defects have been investigated but their interpretation is more difficult because they interact with linear and superficial defects. Also, it has been reported that point defects accelerate the diffusion and migration of boundaries (in accordance with theories of diffusion [53]).

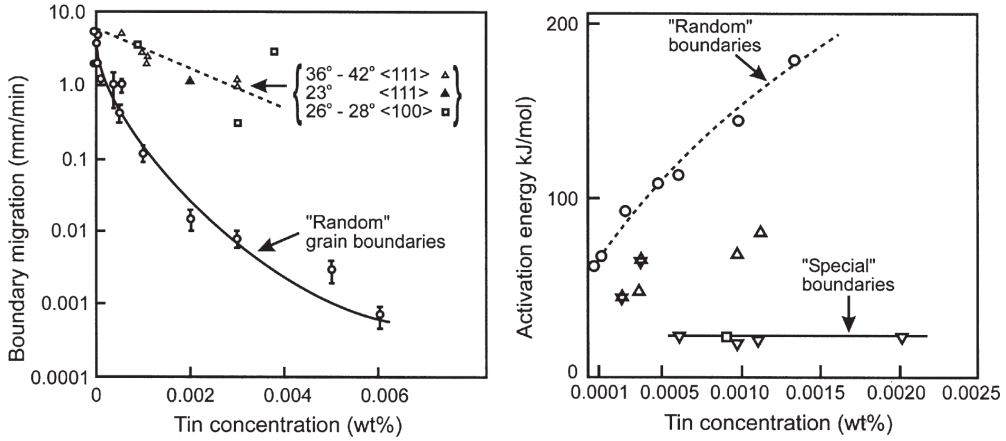

(a) (b)

Figure 1.23: Effect of tin on (a) the rate of grain boundary migration at 30° and (b) the activation energy of random and special boundaries in lead. From [87,88].

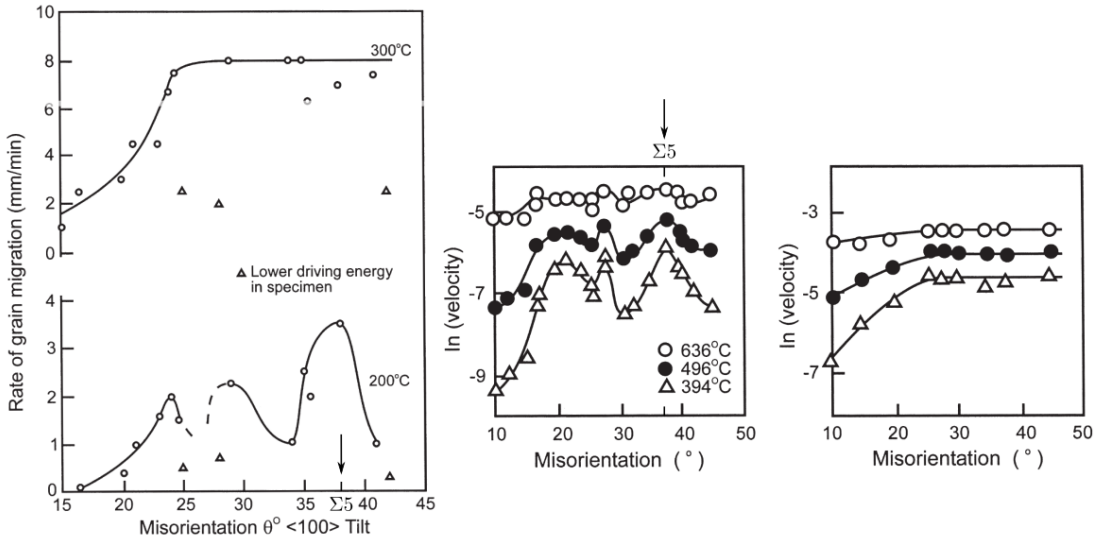

(a) (b) (c)

Figure 1.24: (a) The effect of temperature and misorientation angle on the velocity of $< 100 >$ tilt boundaries in lead, Image from [1] according to the work of [78]. The effect of temperature and misorientation angle on the mobility of $< 100 >$ tilt boundaries of 99.9992% Al (b) and 99.99995% Al (c), image from [1] according to the work of [82].

1.3 New methodologies to estimate the GB mobility

As the computational tools evolved, GB *mobility and energy* could then be estimated separately using Molecular Dynamics [58, 89–91]. However, the time and length scales are very short compared to those of real annealing phenomena such as recrystallization and grain growth. Another methodology has been used for estimating *GB reduced mobility values*, mixing both experiments and simulations and reverse engineering, thus the time and length restrictions are overcome [92–96].

In the following subsections, some examples of the aforementioned methodologies are presented.

1.3.1 3D estimation of GB reduced mobility values of polycrystals using synchrotron and tomography analysis

3D visualization of microstructures allows to study the evolution of microstructures in a more realistic way. 3D visualization have been carried out using micro-focused high-energy X-rays [97], synchrotron radiation X-ray diffraction contrast tomography (SR-DCT) [92], atom probe tomography (APT) [98], optical microscopy or SEM combined with serial sectionning or focused ion beam (FIB) [99]. Among those 3D characterization techniques, only the first one is non-destructive and allows for measuring the GB position at different stages of the evolution. Based on SR-DCT, laboratory X-ray diffraction contrast tomography (LabDCT) has been further developed and relatively large samples can be studied with an acceptable accuracy (SR-DCT: grain size resolution (diameter): 5 μm, GB spatial resolution: 1.5 μm and angular resolution: 0.1°; LabDCT: grain size resolution (diameter): 7.6 μm, GB spatial resolution: 1.9 μm and angular resolution: 0.1°) [95]. Thus, it became possible to study the influence of GB crystallographic parameters and also the interaction between GBs in 4D. Using this technique, GB properties are computed using reverse engineering: GB are characterized experimentally, the initial microstructure is immersed in a digital twin microstructure, the heat treatment is simulated and GB properties of individual GBs are fitted in order to obtain a similar microstructure evolution [92–95].

The 3D data acquisition combines absorption contrast tomography to obtain the phase topography and diffraction-based tomography to obtain the crystal orientations and stress state. After acquisition, data are processed through the following steps:

- Segmentation and indexing of diffraction spots,
- Reconstruction and segmentation of individual grains,
- Assembly of grains into the sample volume.

Hence, the experimental set of grains $\mathcal{G}^{exp}$ is obtained. The fitting approach consists in comparing the evolution of the numerical ($\mathcal{G}^{sim}$) and experimental set

of grains. In [92, 93, 96], numerical simulations are performed using the phase field method [100]. At $t = 0$ s, the experimental microstructure is reconstructed such that $\mathcal{G}^{exp}(t_0) = \mathcal{G}^{sim}(t_0)$. The optimization step aims to find the set of reduced mobility values $\boldsymbol{\mu\gamma} = \{\mu\gamma_{11}, \mu\gamma_{12}, \cdots, \mu\gamma_{nn}\}$ to minimize the cost function $f_{cost}(t, \boldsymbol{\mu\gamma}) = \sum_{ij} f_{ij}^{cost}$. In [92, 93], the authors proposed to consider a cost function for each grain boundary B_{ij}

$$f_{ij}^{cost}(\phi_i^{sim}, \phi_i^{exp}, \phi_j^{sim}, \phi_j^{exp}) = \int_{B_{ij}} (\phi_i^{sim}(\mu\gamma_{ij}) - \phi_i^{exp})^2 + (\phi_j^{sim}(\mu\gamma_{ij}) - \phi_j^{exp})^2 dx, \tag{1.42}$$

where ϕ are the distance functions from the experiments and simulations. The initial reduced mobility is estimated using the same methodology presented in Chapter 4 to compute an average reduced mobility value ($\boldsymbol{\mu\gamma} = \overline{\mu\gamma}$), then GB properties are fitted in order to match the experimental microstructure. Figure 1.25 shows a comparison between the experimental and numerical data from [93]. Even with the average initial reduced mobility value most of the GBs are alike in 2D and 3D. In [93], the GB reduced mobility values show no correlation with the GB crystallographic parameters. Two GBs with the same misorientation and similar GB morphology can have different values of the GB reduced mobility. These results may arise from the fact that the heterogeneity of the GB reduced mobility is not properly described and the effect of the GB inclination and torque terms (GB stiffness tensor) are neglected, hence, the GB reduced mobility may be seen as an average value for a given misorientation.

These results are really interesting and open a new way to study microstructures in 3D with high resolution (in Figures 1.25 and 1.26, grain orientation and GB positions were mapped with resolution of 0.1° and 1.5-3 μm, respectively) and capturing the 5D nature of GBs. However, the GB mobility cannot be dissociated from the GB energy, this may be the reason to not have a clear relation between GB reduced mobility and its crystallography. Another advantage of this technique is that it opens the possibility of studying the GB stiffness tensor in real microstructures.

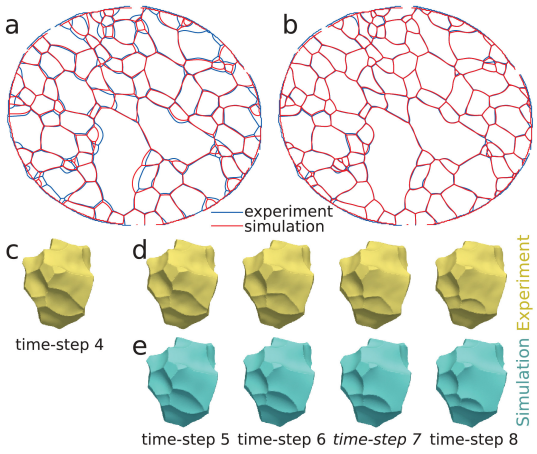

Figure 1.25: Comparison of experimental and simulated GBs in pure iron annealed at 700°C for 30 minutes. The annealing step is 5 minutes. (a) Comparison of a 2D section of the 3D microstructure obtained after simulating GG with the initial average reduced mobility. (b) The same as (a) but using fitted reduced mobility values. (c) One grain at time step 4. (d) Experimental and (e) numerical evolution of one grain using the fitted reduced mobility values. Figure from [93].

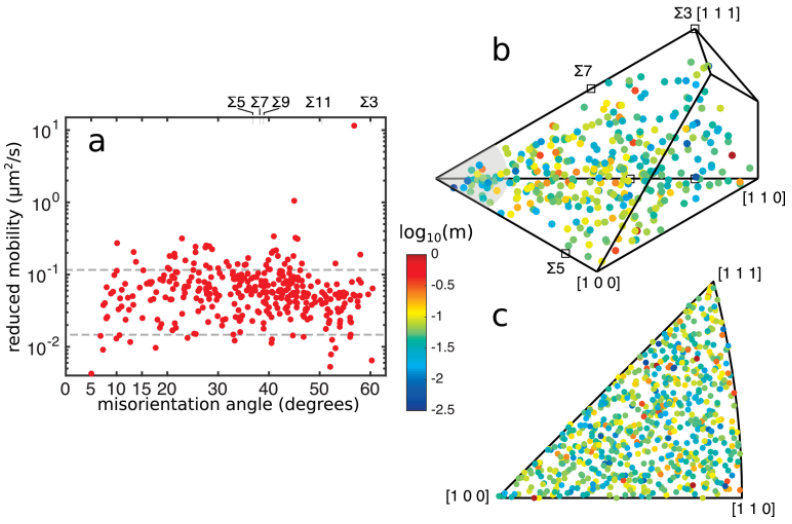

Figure 1.26: Fitted GB reduced mobility values of 344 GBs in iron as a function of (a) disorientation, (b) misorientation (in the Rodrigues-Frank space) and (c) GB inclination. Figure from [93].

1.3.2 Estimation of GB mobility using molecular dynamics

Molecular dynamics (MD) is one of the most effective simulations tools to investigate the behavior of materials at the atomic scale. The main limitations of MD simulations are the time and length scales, for that reason most of the simulations in polycrystalline microstructures are limited to some µm and ns. Most of the MD studies are then focused on few GBs, and also there are no studies on polycrystals with thousands of grains. Thanks to current developments on this domain, this issue could be overcome in a near future [101].

The motion of atoms is governed by the Newton's equation of motion

$$m_a \vec{a}_a = \vec{f}_a, \quad \forall \vec{r}_a \in \Omega \tag{1.43}$$

where m_a, $\vec{a}_a$ and $\vec{f}_a$ are the mass, the acceleration and the force vector on the atom a. The LAMMPS code [102], which is one of the most used MD code, solves this equation using the velocity-Verlet time integration scheme.

The appearance of Molecular Dynamics provided new methods to estimate GB properties allowing to overcome the difficulty of manufacturing crystals. This approach has been applied to different geometries such as the shrinking circle (sphere) [103,104], the HL geometry presented above [105,106], bi/tricrystals with planar GBs [58, 89–91, 107–113] and polycrystals [12, 114]. The first estimations of GB mobility were carried out using the HL geometry but two problems arose from those simulations: the GB reduced mobility is average and isotropic.

A flat GB was considered by Janssens et al. to overcome the issue of the GB anisotropy and concentrate the study on a specific misorientation [89]. Most of the MD calculations of GB mobility performed so far are based on this methodology [58, 89–91]. The authors proposed an orientation-dependent artificial potential $u_\xi(\vec{r}_i)$ where $\vec{r}_i$ is the position vector of atom i. This artificial force induces the motion of GBs as it occurs when stored energy differences exist between grains, with one grain containing stored energy being consumed by the other with lower energy. This methodology can be used to model flat or curved GBs and the simulations are carried out during short MD times.

The well-known surveys carried out by Olmsted et al. used Janssens' methodology [89] and the embedded atom method (EAM) to study GB mobility in pure nickel [90]. The authors found different effect of many variables on the GB mobility. Figure 1.27 shows the value of GB mobility as a function of the disorientation for different types of GB (special and general GBs), one can see that the sigmoidal model described above does not describe the dependence on the disorientation. The main reason for this difference is the simplification of the GB description (5D space) to a simple angle, the disorientation. In [58], the authors showed a complex dependence of GB mobility on temperature using MD. Ni GBs have shown different behaviors in terms of GB mobility: traditional thermally activated, non-thermally activated, mixed modes and boundaries that cannot be classified.

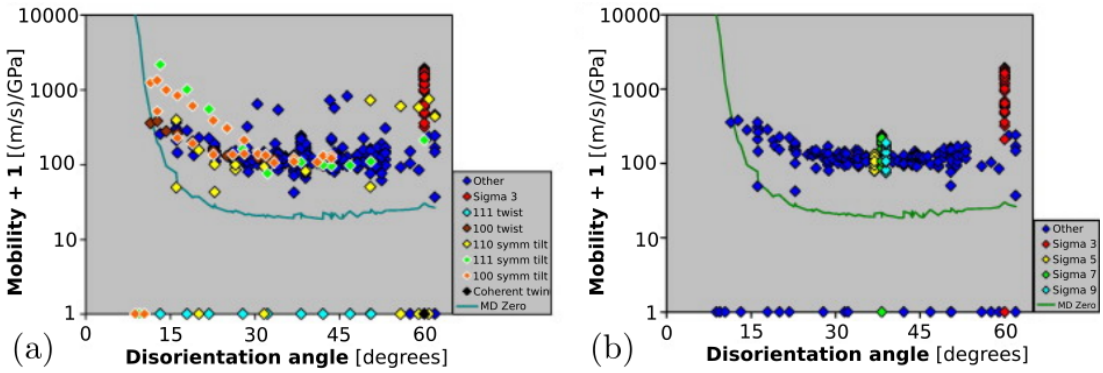

Figure 1.27: GB mobility as a function of disorientation for EAM Ni at 1400K (a) for 388 GBs and (b) for 285 GBs with low shear-coupled motion. The symbols represent the GB type. The solid line is the GB mobility resolution limit of the MD simulations in terms of relative shear. Image from [90].

As a matter of fact, the real crystallographic dependency of the GB mobility is more complex, in [104] the authors used the data from [90] and showed the dependency of the Σ3 twin boundary on the misorientation. Figure 1.28 shows the GB mobility of the Σ3 twin boundary as a function of the GB inclination. Comparing Figures 1.27 and 1.28, one can see that the disorientation is not a variable that can fully describe the crystallographic dependence of the GB mobility.

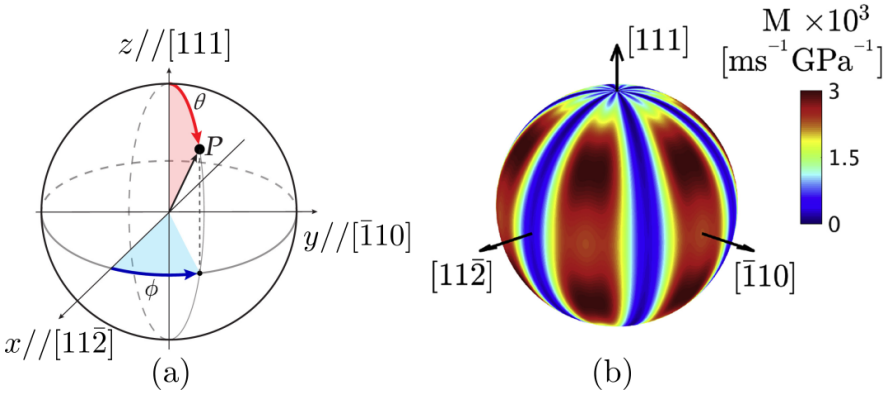

Figure 1.28: GB mobility as a function of the GB inclination for Σ3 TB using the functional fit $\mu(\theta,\phi)$ = 1.527 - 0.535 cos(2θ) - 0.361 cos(4θ) - 0.976 cos(6ϕ) + 0.410 cos(6ϕ) cos(2θ) + 0.359 cos(6ϕ) cos(4θ) - 0.392 cos(12ϕ) and with data coming from [90]. Image from [104].

Thanks to the recent MD results and the recent developments of GB metrics [115–121], analytical models have been proposed to define the GB energy landscape in the 5D GB space [34]. MD simulations allow to study GB properties that remained poorly known, but with limits in time and length scales. The time scale is classically limited to some *ns*. Moreover, the length scale is

limited to a few nanometers and very few studies have been carried out on polycrystals [12, 114]. Several methods have been developed to extend the MD time scale, for instance, the collective variable-driven hyperdynamics [101], but these methods are still in development.

Even if MD studies can give a detailed idea of the behavior of GB properties, one must keep in mind that these results remain also numerical estimations, and the results in alloys, steels, or other polycrystalline materials with more than one element in their composition may be different due to the effect of impurities, driving pressures or interactions with other GBs. Nevertheless, the observations of MD results can give an idea of the behavior of GBs that can be used for enriching mesoscopic models of GG and ReX.

1.4 Disconnection models and mobility tensor

As shown before, several experimental results have shown a good fit between μ vs T using the Arrhenius equation. However, some experimental results exhibited transitions at given temperatures (see Figure 1.17) and molecular dynamic simulations [58, 90, 122] have revealed atypical behaviors where GBs are immobile, anti-thermal, thermally activated, thermally damped, T-independent or mixed . Additionally, we have seen that GB velocity is sensitive to the crystallography, composition and driving pressures. The limits of the classical GB motion equation $\vec{v} = \mu P \vec{n}$ is then more and more discussed, at yet at the GB interface scale. New models of GB motion have emerged via line defects known as disconnections [54, 123]. GB disconnections may be defined by a Burgers vector $\vec{b}$ and a step height h. Hence, different modes of steps and dislocation motion produce an enhanced spectrum of GB migration mechanisms.

In [124–127], GB mobility has been presented as a non-intrinsic property that depends on the driving pressure. With this in mind, in [128], GB mobility has been redefined as a 3×3 tensor with a new coordinate system such that the GB normal is parallel to the e_1 axis and its first component μ_{11} represents the classical GB mobility defined in Equation 1.24. μ_{1j} $(j \neq 1)$ and μ_{ij} $(i, j \neq 1)$ represents the shear coupling and GB sliding, respectively. Thus, the GB mobility tensor links the velocity to the vectorial net driving pressure (P_i) through a matrix product (written here using the Einstein summation notation):

$$v_i = \mu_{ij} P_j, \tag{1.44}$$

where $P_j = -\partial G / \partial u_j$ and $v_i = \dot{u}_i$ with $u_i = (u_1, u_2, u_3)$ being the generalized displacement. One may redefine Equation 1.44 explicitly as:

$$\begin{pmatrix} v_1 \\ v_2 \\ v_3 \end{pmatrix} = \begin{bmatrix} \mu_{11} & \mu_{12} & \mu_{13} \\ \mu_{21} & \mu_{22} & \mu_{23} \\ \mu_{31} & \mu_{32} & \mu_{33} \end{bmatrix} \begin{pmatrix} P_1 = P \\ P_2 = \sigma_{12} = \tau_{12} \\ P_3 = \sigma_{13} = \tau_{13} \end{pmatrix} \tag{1.45}$$

where τ_{12} and τ_{13} are shear stresses applied along the e_2 and e_3 directions which define the GB plane. Continuum disconnection models are presented in more detail in the next chapter.

1.5 Summary and discussion

GB migration has been presented, this literature review was focused on the grain boundary mobility and the parameters affecting it. Firstly, the definitions used throughout the text and the motion of GBs were presented: lattice, defects, GB structure, types of GBs, motion of GBs and driving pressures. Secondly, experimental results have shown that the behavior of high purity metals follow the sigmoidal model being functions of the disorientation, θ. Finally, MD results and a new model based on disconnections using a tensorial GB mobility was briefly presented.

Most of the experimental results focused on a specific type of GBs using bicrystals or tricrystals. Experimental data is usually compared to the following equation $\mu = \mu_0 exp(-Q/RT)$. Using Arrhenius plots, the activation energy, Q, can tehn be estimated but, in fact, GB mobility depends also on the misorientation, impurity concentration or GB type. For high purity materials, the Arrhenius plot is linear which means the presence of a unique mechanism of GB motion. Additionally, the results with high purity materials revealed a sigmoidal model that can be used to relate disorientation and GB mobility.

However, experimental results become more complex when the material gains in impurities or is composed of more than two elements. The problem with the Arrhenius equation is that it does not work all the time (see Figures 1.17 and 1.22). All those effects may be linked to the GB structure: first, at high temperatures the GB structure can change and the migration mechanism as well; second, at certain temperatures the effect of impurities is more pronounced resulting in activation energies or mobilities oscillating as the misorientation angle increases. At low temperatures solute atoms do not diffuse easily and at certain misorientation angles, the GB structure captures the solute atoms in the boundaries and the GB mobility is then reduced.

The experimental results have shown the complexity of GB motion. One major issue is generally the simplification to 2D analysis instead of 3D, meaning that some information are neglected. Thanks to MD simulations, the GB mobility was estimated as a function of the GB inclination for general and special GBs, thus completing the 5D space, but these results haven't been, at yet, confirmed experimentally. GB mobility is then a very complex topic, intensively studied in the state of the art, with sometimes contradictory conclusions.

This work is composed of an experimental and numerical part. In the next chapter, the literature review is completed with the introduction of different numerical approaches used to model grain growth at the mesoscopic scale that account for anisotropic/heterogeneous GB properties. Special attention is given

to the framework used during this work combining Finite Element (FE) methods and Level Set (LS) functions.

1.6 Résumé en Français du Chapitre 1

Ce chapitre présente les bases théoriques et concepts importants utilisés tout au long de ce texte. Il est divisé en différentes parties décrivant: les concepts du polycrystal et de migration des joints de grains, les résultats expérimentaux de l'état de l'art pour estimer la mobilité des joints de grains et finalement, l'introduction du concept des disconnections.

La mobilité est souvent décrite comme thermiquement activée avec un modèle de type Arrhenius. La base expérimentale du modèle Sigmoidal est également présentée. Ce modèle est fréquemment utilisé pour décrire la mobilité en fonction de la désorientation dans les calculs à champs complets à l'échelle mésoscopique. Les limites de l'équation d'Arrhenius sont mises en évidence. Elles sont notamment liées à l'effet de la composition chimique, de la température, du changement de type de joint de grains ou de changements de mécanismes de migration.

Chapter 2

Accounting for anisotropic grain boundary properties using different numerical methods at the mesoscopic scale

GG modeling has been widely studied at the mesoscopic scale with a large variety of numerical approaches: multi phase-field [7–9], Monte Carlo [10,11], orientated tessellation updating method [13], vertex [14], front-tracking Lagrangian or Eulerian formulations in a FE context [15–17] and FE-LS [18–20], to cite some examples. Most of the models are based on (or verify) the classical velocity equation given by Equation 1.24.

One can classify the full-field approaches with respect to the definition of GB properties. The first models proposed in the literature defined GB properties as constants, carrying the name of *Isotropic*, [7, 10, 18, 21, 22, 129], this category shows good agreement in terms of mean quantities and distributions, nevertheless, they are restrictive in terms of the grains morphology and texture predictions. The models evolved in order to reproduce more complex microstructures or local heterogeneities, such as twin boundaries. *Heterogeneous* models were proposed, in which each GB has its own energy and mobility [11, 19, 20, 23–30, 130–133]. In general, every grain is related with an orientation, thus the mobility and energy can be computed in terms of the disorientation [8,20]. Finally, general frameworks in which the five parameters, misorientation and inclination are discussed, have been proposed, these models could be categorized as *fully anisotropic* [31,32,134].

This chapter aims to show the implementation of heterogeneous or anisotropic GB properties in the aforementioned approaches, and also, to discuss their advantages and disadvantages. First, the Vertex, Phase Field, Monte Carlo and Cellular Automata approaches are presented, including the details about the introduction of heterogeneous or anisotropic GB properties. Finally, the Finite-Element Level-Set (FE-LS) formulations used along this work are presented.

A part of the work presented in this chapter has been published in [134, 135].

2.1 Full Field modeling approaches

2.1.1 Monte Carlo

The first Monte Carlo (MC) mesoscale approach for microstructure evolution was proposed in 1984 by M. P. Anderson et al. in [21]. As for CA approaches, the microstructure is represented into a regular lattice. Each lattice site is defined by an orientation O_i in the form of an integer between 1 and Q. The GB are defined using the edges between two lattice sites of different orientation. GB energy is classically defined from the following Hamiltonian:

$$E = \sum_i E_i = \sum_i \sum_j^{nn} -J(\delta_{O_i O_j} - 1), \tag{2.1}$$

where $\delta_{O_i O_j}$ is the Kronecker delta symbol and the summation is carried out for all nearest neighbors (nn) sites j of site i. J is added to the system's energy every time two consecutive sites are different. Finally, the kinetics of the GB is obtained by the integration of an MC approach over the domain: A lattice site i is chosen randomly, then a new trial orientation O_i^* is selected randomly, such that, $O_i^* = \{1, \cdots, Q | O_i^* \neq O_i\}$. A transition probability is computed using the Metropolis method and the classical choice is given by the following function:

$$P = \begin{cases} exp(-\Delta E/kT) & \Delta E > 0, \\ 1 & \Delta E \leq 0 \end{cases}, \tag{2.2}$$

where ΔE is the change of energy caused by the trial orientation O_i^*. If $\Delta E \leq 0$, the transition is applied, while for $\Delta E > 0$ the probability to change the orientation is given by $exp(-\Delta E/kT)$. The time definition of a MC simulation is called *Monte Carlo Step*. It is related to N reorientation attempts, where N is the total number of lattice sites. It means that if one site lattice is chosen several times in one MC step, not all the lattice sites may be tested.

Heterogeneous GB energy was considered in [136] one year after the first MC applications concerning GG modeling [21] completing a series of articles called *Computer Simulation of Grain Growth*. As the grains are identified by their orientation, the authors defined the GB energy as a function of the GB disorientation:

$$E_i = \sum_j^{nn} \gamma(\theta), \tag{2.3}$$

where E_i is defined as an "anisotropy" potential. The authors tested three different forms of γ as a function of the disorientation, one of them is of the Read-Shockley form [69]. Regarding the heterogeneity of GB mobility in [11, 137], the

authors used the definition of the Hamiltonian defined in Equation. 2.3 and they proposed the following equation concerning the transition probability:

$$P = \begin{cases} \dfrac{\mu(\theta)\gamma(\theta)}{\mu_{max}\gamma_{max}} exp(-\Delta E/kT) & \Delta E > 0, \\ \dfrac{\mu(\theta)\gamma(\theta)}{\mu_{max}\gamma_{max}} & \Delta E \leq 0. \end{cases}, \tag{2.4}$$

2.1.2 Cellular automata

Cellular Automata (CA) models are based on the use of regular grids. The four main ingredients of the CA approach are:

- the definition of the cell geometry,
- the number and kind of states,
- the definition of neighboring cells, and
- the transition rules.

The first application of CA models of ReX was proposed by Hasselbarth in 1991 [138]. In 1996, the idea of Hasselbarth was combined with the Monte Carlo (MC) methodology to model GG [139]. In [139], the von Neumann's definition of neighbors is used and the state of the cell is defined by its orientation ranging from 1 to Q_s. By using the example given in Figure 2.1, the transition of the central cell "a" is determined by:

- The state of the cells b, c, d, e (If three of them has the same state as a, the cell a does not change).
- The cell must overcome the energy barrier to change of state. The probability of successful transition could be defined as $P = exp\,(-\Delta E/kT)$, where $\Delta E = E - E_B$, E_B is the energy barrier and E is the local energy.
- Grain boundary energy is homogeneous.

The physics of the CA approach is encapsulated in the definition of the energy barrier and transition rules. For instance, in [132, 133, 140], heterogeneous GB properties were defined within the probability function using an activation energy and GB mobility that could depend on the disorientation as:

$$P = \frac{\mu(\theta)}{\mu_{max}} \frac{\sum P_i}{P_{max}} exp\left(-\frac{E(\theta) - E_B}{kT}\right). \tag{2.5}$$

where $\sum P_i$ is the net driving pressure. For the case of pure GG, $\sum P_i = P_c = -\gamma\kappa$ and the heterogeneity of GB energy can be considered. The effect of the

inclination is not discussed in the literature due to the definition of GBs (as borders of regular grids).

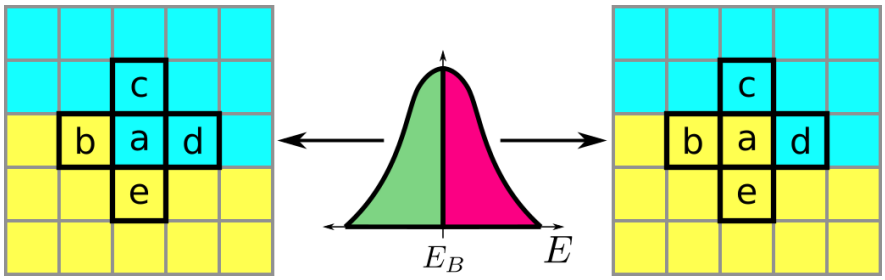

Figure 2.1: Energy barrier between two states (yellow and cyan). The center cell "a" changes from its initial state (cyan) to the neighboring state (yellow) if it overcomes the energy barrier, E_b. The Von Neumann's definition of neighbor cells is used.

2.1.3 Vertex

This approach consists in representing GBs and multiple junctions as continuous interfaces divided by a successive number of nodes called vertex. In the literature, one can find implicit or explicit formulations to calculate the velocity of the nodes. The early developments of vertex models were proposed in [141] for simulations of growth in two-dimensional soap froths. Based on the topological operations presented in [141], Soares et al. presented the first vertex model of GG in [142] based on a thermodynamic formulation that separates the effect of faces, edges and vertices. Under the assumption of having straight edges, the authors proposed the following GB motion equation :

$$\vec{v}_j = \mu_j \sum \vec{\varepsilon}_i, \tag{2.6}$$

where $\vec{v}_j$ and μ_j are the velocity and mobility of a vertex j, and $\vec{\varepsilon}_i$ the line tensions acting at this vertex. This model was firstly proposed as isotropic, i.e., $\mu_j = \mu$ and $|\vec{\varepsilon}_i| = \varepsilon$ are constant.

In [143], Kawasaki et al. proposed an implicit formulation based on a dissipative equation of motion defined as

$$\frac{\partial R_R}{\partial \vec{v}} = -\frac{\partial \nu}{\partial \vec{r}}\,, \tag{2.7}$$

where R_R represents the Rayleigh dissipation function and ν the potential function. The following vertex equation of motion was derived

$$\frac{1}{3}\sum \frac{|\vec{r}_{(ij)}|}{\mu_{(ij)}}\vec{n}_{(ij)} \times \vec{n}_{(ij)} \cdot \left(\vec{v}_i + \frac{1}{2}\vec{v}_j\right) = -\sum \gamma_{(ij)}\frac{\vec{r}_{(ij)}}{|\vec{r}_{(ij)}|} = -\sum \gamma_{(ij)}\vec{t}_{(ij)}, \tag{2.8}$$

where $\vec{r}_{(ij)}$ is the vector $\vec{r}_i - \vec{r}_j$, $\vec{r}_i$ is the position of the vertex i. $\vec{n}_{(ij)}$, $\gamma_{(ij)}$ and $\mu_{(ij)}$ are respectively the normal unit vector, the boundary energy and the mobility of

the boundary segment delimited by vertices i and j. $\vec{v}_i$ is the unknown velocity of vertex i, $\vec{t}_{(tj)} = \vec{r}_{(ij)}/|\vec{r}_{(ij)}|$ is a unit vector and the summation is carried out for each vertex j connected to a given vertex i. In Equation 2.8, the left-hand side defines the anisotropic nature of GB properties. In contrast, the central and right-hand sides define its heterogeneous nature. For instance, GB properties of a set of edges (ij) between two grains could be defined as disorientation dependent: $\mu_{(ij)}(\theta)$ or $\gamma_{(ij)}(\theta)$. Even if the proposed formulation by Kawasaki et al. could handle anisotropy, the authors proposed a more straightforward formulation known as **model II**:

$$\frac{1}{6\mu}\left(\sum|\vec{r}_{(ij)}|\right)\vec{v}_i = -\gamma\sum\vec{t}_{(ij)}, \tag{2.9}$$

with μ and γ being homogeneous-isotropic properties.

Triple junctions are singular points where no misorientation or normal direction could be defined directly. In [144, 145], the authors estimated a "triple junction mobility", which is different from the GB interfaces mobility that form the junction. In order to reproduce this effect, the vertex approach was enhanced adding the following term to R_R:

$$R_{TJ} = \sum^{N_{TJ}} \frac{\vec{v}_i^{\,2}}{\mu_{TJ}}, \quad n = 1, \cdots, N_{TJ} \tag{2.10}$$

where N_{TJ} and μ_{TJ} are the number of triple junctions and their mobility [146,147]. L. A. Barrales Mora introduced an anisotropic vertex formulation where both the effect of the misorientation and normal direction are taken into account [14]. In general a velocity is calculated in every vertex and its position is updated with the following explicit Euler scheme:

$$\vec{r}_i(t+\Delta t) = \vec{r}_i(t) + \vec{v}_i(t)\Delta t, \tag{2.11}$$

with Δt the time step. The vertex approach is flexible and has shown a relative easiness to handle anisotropy and heterogeneity [14]. Nevertheless, the main difficulty is to handle topological events, which become more complex in 3D. Moreover, intragranular fields (such as stored energy) cannot be predicted and taken into account into driving pressures. Mixed vertex simulations have emerged in order to add intragranular fields and describe other mechanisms.

Vertex-FE approach

This method was proposed recently and combines vertex and FE approaches in order to define GBs and their migration, known as *To Real Motion (TRM)* algorithm [17]. The approach maintains the discretization inside the grains using an evolving triangular mesh, thus, the discretization will remain valid for FE calculations as illustrated in Figure 2.2. In that way, crystal plasticity or recrystallization can be implemented [148].

In [135], GB velocity to model anisotropic GG is derived from the model proposed in [17] using the TRM approach and the model proposed by L. A.

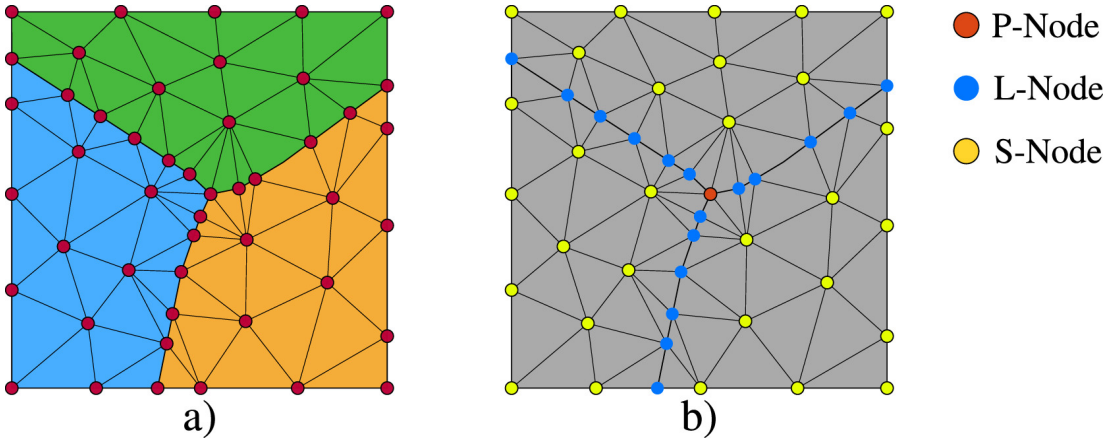

Figure 2.2: Example of he nodal geometric tagging performed on a body fitted mesh in the TRM algorithm. a) Considered grain topology. b) Resulting nodal tagging. Image from [17].S-, L- and P-Nodes are surface, linear and point nodes in 2D.

Barrales in [14]:

$$\vec{v_i} = \mu(\theta)_i \left(-\gamma(\theta)_i \kappa_i \vec{n}_i + \frac{\sum_j T_{ij} \vec{n}_{ij}}{c^{-1} \sum_j |\overline{N_i N_j}|} \right), \tag{2.12}$$

where T_{ij} is a torque term, $\vec{n}_{ij}$ is the normal of the segment $|N_i \bar{N_j}|$ and c is the number of connections of the multiple junction. One can note the effect of heterogeneity in terms of disorientation in $\mu(\theta)_i$ and $\gamma(\theta)_i$, and the effect of the anisotropy in the term $\frac{\sum_j T_{ij} \vec{n}_{ij}}{c^{-1} \sum_j |\overline{N_i N_j}|}$. This method has several advantages: first, the method reduces the CPU time compare to classical FE approaches, and second, the method is highly flexible thanks to the different definitions of the GB velocity. However, it remains limited, at yet, to 2D modeling.

Vertex-Monte Carlo approach

A different methodology is found in [149], the authors coupled the Vertex and Monte Carlo methods to describe recrystallization. The model induces GB motion through Monte Carlo steps. At each step, a triple junction is chosen randomly and its position is changed randomly within a radius δ_r. The energy of the triple junction m is computed as

$$G_m = \sum_n \left(\gamma(\theta)_{(mn)} \vec{t}_{(mn)} + E_{(mn)} A_{(mn)} \right), \tag{2.13}$$

where n describes the triple junctions connected to m, $E_{(mn)}$ is the stored energy and $A_{(mn)}$ the grain surface of the grains between the two triple junctions m and n. This model have been presented with heterogeneous GB mobility and energy as functions of the disorientation, $\gamma(\theta)_{(mn)}$ and $\mu(\theta)_{(mn)}$.

Finally, the energy evolution between the steps t and $t+1$ is:

$$\Delta G_m = G_m^{t+1} - G_m^t, \tag{2.14}$$

and the transition probability is defined as:

$$P = \begin{cases} \dfrac{\mu(\theta)}{\mu_{max}} exp(-\Delta G_m/kT) & \Delta G_m > 0, \\ \dfrac{\mu(\theta)}{\mu_{max}} & \Delta G_m \leq 0\ . \end{cases} \tag{2.15}$$

The main advantage of this approach is that the resolution of large equation systems is avoided, but as the MC approach, the time step used in this method has no direct physical meaning.

2.1.4 Phase field

The Phase Field (PF) method has gained a lot of popularity and is used in numerous applications, from crack propagation to dislocation dynamics [150]. The approach is based on the diffuse-interface description developed by Cahn and Hilliard [100] and applied in the context of microstructural evolution such as multiphase evolution or grain growth [151,152]. The microstructure is defined using a set of field variables. The set of variables is divided in two main groups: conserved (c_i) and non-conserved (η_i). Hence, the evolution of a given state of variables (i.e., the microstructure) is defined by the minimization of the total free energy which is defined by

$$F = \int_v \Big(f(c_1, c_2, \cdots, c_n, \eta_1, \eta_2, \cdots, \eta_p) + \sum_{i=1}^{n} \alpha_i (\nabla c_i)^2 + \\ + \sum_{i=1}^{3}\sum_{j=1}^{3}\sum_{k=1}^{p} \beta_{ij} \nabla_i \eta_k \nabla_j \eta_k \Big) dV, \tag{2.16}$$

where f is the local free energy, and α_i and β_{ij} are gradient energy coefficients. The temporal evolution of F is described by the Cahn-Hilliard nonlinear diffusion equation [153]:

$$\frac{\partial c_i}{\partial t} + \nabla M_{ij} \nabla \frac{\partial F}{\partial c_j} = 0,$$

and the time dependent Ginzburg-Landau equation [154]:

$$\frac{\partial \eta_j}{\partial t} + L_{jk} \frac{\partial F}{\partial \eta_k} = 0,$$

where L and M are related to the dissipation of energy of the system.

The first PF based model of GG was proposed by Chen et al. in [155–157]. This model, also known as Continuum Field, employed the following free energy density

$$f = \sum_{i=1}^{p} \left[-\frac{k_\alpha}{2}\eta_i^2 + \frac{k_\beta}{4}\eta_i \right] + k_\gamma \sum_{i=1}^{p}\sum_{j>1}^{p} \eta_i^2\eta_j^2, \tag{2.17}$$

k_α, k_β and k_γ being phenomenological parameters. The total free energy of the system is

$$F = \int_v \left[f(\eta_1, \eta_2, \cdots, \eta_p) + \sum_{i=1}^{p} \frac{\beta}{2}(\nabla\eta_i)^2 \right] dV, \tag{2.18}$$

where $\beta_{ij} = \delta_{ij}\beta/2$. If Equation 2.17 is replaced in Equation 2.18 the kinetic equation may be redefined as

$$\frac{\partial\eta_i}{\partial t} = -L_i \left[k_\alpha\eta_i + k_\beta\eta_i + 2k_\gamma\eta_i \sum_{j\neq i}^{p} \eta_j^2 - \beta\nabla^2\eta_i \right], \quad i = 1, 2, \cdots, p, \tag{2.19}$$

if the cross terms of the dissipation energy parameter are ignored (i.e., $L_{jk} = L_j$). The Continuum Field approach has been modified and other PF formulations can be found in the literature: Multi-phase field [158], Anti-symmetric MPF [159] and Generalized MPF [160] can be cited. A comparison of different PF approaches is presented in [161, 162].

The PF approach has been widely enriched in order to deal with heterogeneity and anisotropy. In general, the effect of disorientation and inclination are directly attributed to the terms $k_\gamma(\theta, \vec{n})$, $\beta(\theta, \vec{n})$ and $L(\theta, \vec{n})$, being $\beta(\theta, \vec{n})$ and $L(\theta, \vec{n})$ proportional to the GB energy γ and mobility μ, respectively [8, 31, 131, 163]. Other possibility could be to define the free energy density with an anisotropy coefficient, $f_a = X(\theta, \vec{n})f$ [163], where $X(\theta, \vec{n})$ encapsulates the effect of the disorientation and inclination.

2.1.5 Level-Set

The LS method is a flexible tool initially developed by Osher and Sethian [164] to describe curvature flow of interfaces, enhanced later for evolving multiple junctions [165, 166], and considered in recrystallization and grain growth problems in [167, 168]. The principle for modeling polycrystals is the following: the grain interfaces are defined through scalar fields called LS functions ϕ in the space Ω and more precisely by the zero-isovalue of the ϕ functions. LS functions to the interfaces are classically initialized as the sign Euclidean distance functions to these interfaces:

$$\begin{cases} \phi(X) = \pm d(X, \Gamma), & X \in \Omega, \quad \Gamma = \partial G \\ \phi(X \in \Omega) = 0 & \rightleftharpoons \quad X \in \Gamma. \end{cases} \tag{2.20}$$

with d the Euclidean distance and ϕ generally defined as positive inside the grain and negative outside. The dynamics of the interface is studied by following the

evolution of the LS field. The interface may be subjected to an arbitrary velocity field $\vec{v}$ and its movement can be simulated by solving the transport equation:

$$\frac{\partial \phi}{\partial t} + \vec{v} \cdot \vec{\nabla} \phi = 0. \tag{2.21}$$

The flexibility of this method lies in the ability to take into account different physical phenomena encapsulated in the velocity field. This equation is solved to describe the movement of every grain. When the number of grains increases one may use a graph coloring/recoloring strategy [169] in order to limit drastically the number of involved LS functions $\Phi = \{\phi_i, i = 1, \ldots, N\}$ with $N \ll N_G$ being N the number of LS functions. Additionally, two more treatments are necessary. Firstly, the LS functions are reinitialized at each time step to keep the metric property of a distance function:

$$\|\nabla \phi\| = 1. \tag{2.22}$$

Indeed, after the transport resolution, the LS functions is no longer a distance function, hence, the initial metric can be restored solving Equation 2.22. In the proposed numerical framework, the algorithm developed in [170] is used. Secondly, the evolution may not preserve the impenetrability constraints of the LS functions leading to overlaps and voids between grain interfaces. These events are corrected after solving the transport equation by resolving Equation 2.23 as proposed in [165] and classically used in LS framework [168, 171].

$$\phi_i(X) = \frac{1}{2}\left[\phi_i(X) - \max_{j \neq i} \phi_j(X)\right], \quad \forall i = \{1, \ldots, N\}. \tag{2.23}$$

Several formulations using the LS framework exist in the literature. The initial GG formulation uses a homogeneous grain boundary energy and mobility [18], the velocity field is thus defined as :

$$\vec{v} = \mu P \vec{n} = -\mu \gamma \kappa \vec{n}, \tag{2.24}$$

with $P = -\gamma\kappa$ the capillarity pressure and n the outward unitary normal to the interface. When dealing with recrystallization, supplemental terms could be added to the velocity as proposed in [18]. If ϕ is defined as positive inside the grain and remains a distance function (by verifying Equation 2.22), the mean curvature and the normal may be defined as:

$$\kappa = -\Delta \phi, \quad \vec{n} = -\vec{\nabla} \phi, \tag{2.25}$$

then the velocity in Equation 2.24 may also be defined as:

$$\vec{v} = -\mu \gamma \Delta \phi \vec{\nabla} \phi. \tag{2.26}$$

The first application with pseudo heterogeneous GB properties using a LS framework was proposed by Mießen et al. [19]. The authors modified Equation 2.24 such that γ is a function of the disorientation and $\mu = 1/\gamma(\theta)$. In other words, the effect of heterogeneity is avoided and the formulation remains Isotropic. The new differential equation to transport the distance functions is similar to the heat equation and is defined as:

$$\frac{\partial d}{\partial t} - \Delta d = 0. \tag{2.27}$$

It means that the GB velocity is defined by the relation $\vec{v} = -\kappa\vec{n}$. The new differential equation has an analytical solution given by

$$G(X,t) = \frac{1}{(4\pi t)^{1/2}} exp\left(\frac{-|x|^2}{4\pi}\right), \tag{2.28}$$

known as the Gaussian kernel. Hence the evolution of the distance function for a grain k can be reduced to the convolution equation below

$$d_k(X, t + \Delta t) = G(X, t = \Delta t) * d_k(X, t), \tag{2.29}$$

and it does not require the computation of the curvature. The authors also defined different triple junction mobility. In general the authors observed convergence of the grain growth rate towards the von Neumann-Mullins law [172].

In [32] the authors proposed an anisotropic formulation using LS functions and solved Equation 2.21 using Finite Difference. GB energy is anisotropic, $\gamma(M)$, and its effect is introduced in the definition of the GB velocity:

$$\vec{v} = -\mu\vec{\nabla}\left(\gamma(M)\vec{\nabla}\phi\right)\vec{n}, \tag{2.30}$$

the origin of Equation 2.30 in [32] is not specified but the term $\vec{\nabla}\left(\gamma\vec{\nabla}\phi\right) = \vec{\nabla}\gamma\vec{\nabla}\phi + \gamma\Delta\phi$ is similar to the one proposed earlier by Fausty et al. in [25]. The main innovation in [32] was the use of the code GB5DOF [34] to describe the anisotropy of GB energy, for bicrystals and tricrystals.

2.1.6 Level-Set Finite-Element formulations

When looking to the evolution of the FE-LS framework for GG, four main formulations have been proposed in the state of the art. In the first one, an Isotropic formulation is considered by introducing Equation 2.26 into Equation 2.21, thus the Isotropic transport equation may be defined as a pure diffusive problem with $\mu\gamma$ only temperature dependent [18]:

$$\frac{\partial \phi}{\partial t} - \mu\gamma\Delta\phi = 0. \tag{2.31}$$

This formulation has shown good agreement with experimental data regarding GG predictions concerning the mean grain size and even the grain size distribution (GSD) [169, 173, 174]. However, this approach is limited to reproduce complex grain morphology (non-equiaxed ones), described special GBs and to respect textures. This formulation could be slightly modified in a second one with the introduction of heterogeneous GB properties leading to a Heterogeneous formulation:

$$\frac{\partial \phi}{\partial t} - \mu(\theta)\gamma(\theta)\Delta\phi = 0. \tag{2.32}$$

With this formulation, it is expected to obtain more physical grain shapes. Indeed, some GBs can evolve faster thanks to higher GB reduced mobility values, and triple junctions may have different dihedral angles thanks to different GB energy values. This strategy which is classically used in full-field formulations (not only in LS ones) can lead to confusion when it is named as "heterogeneous". Indeed, *stricto sensu*, the heterogeneity shape of μ and γ can lead to additional terms in the driving pressure of the kinetic equation (Equation 2.24) but also in the weak formulation derived to solve the GB motion. However, the term "heterogeneous" will be used in the following to distinguish this formulation from the purely isotropic model.

Such discussion is described in [25] where an additional term capturing the local heterogeneity of the multiple junctions is added to the velocity equation such that:

$$\vec{v} = \mu(\vec{\nabla}(\theta)\gamma \cdot \vec{\nabla}\phi - \gamma(\theta)\Delta\phi)\vec{\nabla}\phi. \tag{2.33}$$

Inserting this term into the transport equation (Equation 2.21) leads to the, hereafter called, "Heterogeneous with Gradient" formulation [25]:

$$\frac{\partial \phi}{\partial t} + \mu\vec{\nabla}\gamma(\theta) \cdot \vec{\nabla}\phi - \mu\gamma(\theta)\Delta\phi = 0. \tag{2.34}$$

The introduction of the term $\vec{\nabla}\gamma(\theta) \cdot \vec{n}$ only acts at multiple junctions because these are the only places where this term does not vanish. This formulation is equivalent to the Isotropic one if no heterogeneity is added. This formulation has been used to model triple junctions [25] and polycrystalline microstructures with different models of heterogeneous GB energy [20].

Finally, in [134, 175], works in which I participated, a new relation for the velocity was developed using thermodynamics and differential geometry. The five crystalline parameters are taken into account with an intrinsic torque term, which leads to (see Equation (2.43) in [175]):

$$\frac{\partial \phi}{\partial t} - \mu\left(\frac{\partial^2\gamma(\theta,\vec{n})}{\partial\tilde{\nabla}_\alpha\phi\partial\tilde{\nabla}_\beta\phi} + \gamma(\theta,\vec{n})m^{\alpha\beta}\right)\tilde{\nabla}_\alpha\tilde{\nabla}_\beta\phi + \mu P^{\alpha\beta}\tilde{\nabla}_\beta\gamma(\theta,\vec{n})\tilde{\nabla}_\alpha\phi = 0, \tag{2.35}$$

where $m^{\alpha\beta}$ is the metric with components α and β of a Riemannian n-manifold, with n the dimension of the space, and $\tilde{\nabla}$ the Levi-Civita connection. This equation may be redefined using a flat metric and tensor notations as:

$$\frac{\partial \phi}{\partial t} - \mu \left(\frac{\partial^2 \gamma(\theta, \vec{n})}{\partial \vec{n} \partial \vec{n}} + \gamma(\theta, \vec{n}) \mathbb{I} \right) : \mathbb{K} + \mu \mathbb{P} \vec{\nabla} \gamma(\theta, \vec{n}) \cdot \vec{\nabla} \phi = 0, \tag{2.36}$$

and also written as:

$$\frac{\partial \phi}{\partial t} - \mu \left(\vec{\nabla}_{\vec{n}} \vec{\nabla}_{\vec{n}} \gamma(\theta, \vec{n}) + \gamma(\theta, \vec{n}) \mathbb{I} \right) : \mathbb{K} + \mu \vec{\nabla}_{\vec{n}} \gamma(\theta, \vec{n}) \cdot \vec{\nabla} \phi = 0, \tag{2.37}$$

where $\mathbb{I}$ is the unitary matrix, $\mathbb{P} = \mathbb{I} - \vec{n} \otimes \vec{n}$ is the tangential projection tensor, and therefore, $\vec{\nabla}_{\vec{n}} \gamma = \mathbb{P} \vec{\nabla} \gamma$ with $\vec{\nabla}_{\vec{n}}$, the surface gradient on the unit sphere of interface normal $\vec{n}$, $\mathbb{K} = \vec{\nabla} \vec{n} = \vec{\nabla} \vec{\nabla} \phi$, is the curvature tensor. In Equation 2.35, the term $P^{\alpha\beta} \tilde{\nabla}_\beta \gamma \tilde{\nabla}_\alpha \phi$ and its equivalent $\mathbb{P} \vec{\nabla} \gamma \cdot \vec{\nabla} \phi$ in Equation 2.36, i.e., $\vec{\nabla}_n \gamma \cdot \vec{\nabla} \phi$, should be null in the grain interfaces. However, the front-capturing nature of the LS approach, which requires to solve Equation (2.36) not only at the GB network but also in its vicinity, needs to consider this term, which could be non-null around the GB interfaces. This stabilization term is then totally correlated to the front-capturing nature of the LS approach and not derived from the GG driving pressure. The resulting tensorial diffusion term, $D = \vec{\nabla}_{\vec{n}} \vec{\nabla}_{\vec{n}} \gamma + \gamma \mathbb{I}$ [134,175], is also well-known as the GB stiffness tensor $\Gamma(M, \vec{n})$ in [104,176]. With this formulation, the 5D-GB space $\mathcal{B}$ is fully described and is referred to as "Anisotropic-5". In [134], this formulation was only considered for a bicrystal using a mathematical function to describe the effect of the GB inclination on the GB energy, $\gamma(\vec{n})$.

If the torque term is neglected in Equation 2.36, the formulation could be simplified as:

$$\frac{\partial \phi}{\partial t} + \mu \mathbb{P} \vec{\nabla} \gamma(\theta) \cdot \vec{\nabla} \phi - \mu \gamma(\theta) \Delta \phi = 0. \tag{2.38}$$

This equation is hereafter called "Anisotropic" and is not equivalent to the "Heterogeneous with Gradient" formulation (Equation 2.34).

2.2 Disconnection-based formulations

Disconnection based models are new alternatives to model GB motion. The models have shown a good accuracy and continuous models have been proposed for GBs, triple junctions and polycrystals [2, 114, 127, 177–182]. This section is mainly focused on the works on the GB mobility tensor proposed by K. Chen et al. [128] and two consecutive articles presented by J. Han, D. Srolovitz and M. Salvalaglio where a disconnection-based continuum model is presented and used in a PF approach [180, 181].

In [128], the authors performed MD simulations on a $\Sigma 7$ [111] $(12\bar{3})$ symmetric tilt GB in copper to study the behavior of the GB mobility tensor (See section

1.4). They demonstrated that the components of the GB mobility tensor are non-zero. Figure 2.3 shows the temperature dependence of the GB mobility components. The components can vary by several orders of magnitude with

$$\mu_{11} > \mu_{1i} > \mu_{22} > \mu_{33},\ i = 1, 2, 3. \tag{2.39}$$

The dashed lines are fitted using a disconnection statistical model of the GB mobility tensor [128]:

$$\mu_{ij} = \frac{f_0 L^2}{k_B T} \sum_m H_i^{(m)} H_j^{(m)} exp(-Q^{(m)}/k_B T), \tag{2.40}$$

where the superscript m represents the disconnection mode, f_0 is the attempt frequency, L is the GB width (cell distance), $Q^{(m)}$ is the activation energy and $H_i \equiv (h, b_2, b_3)$ is a vector defined by the disconnection step h and the components of the burgers vector parallel to the GB plane, b_2 and b_3.

From Figure 2.3 one can see the different temperature dependences of the GB mobility components. The components μ_{11}, μ_{22} and μ_{12} follow an antithermal behavior dominated by the prefactor $1/T$. While the components μ_{33}, μ_{23} and μ_{13} follow an Arrhenius law linked to the $exp(-Q^{(m)}/k_B T)$ factor. Experimental results frequently show the temperature dependence of GB mobility fitted by an Arrhenius relation $\mu_{11} \propto \mu_0 exp(-Q/k_B T)$, but for this particular case ($\Sigma 7$ [111] $(12\bar{3})$ symmetric tilt GB in copper) $\mu_{11} \propto 1/T$.

In this type of model, the temperature dependence is determined by the disconnection activation energy $Q^{(m)}$ and the number of disconnection modes activated during GB migration. For instance, in Figure 2.3 the activation energy for the components μ_{33}, μ_{23} and μ_{13} is $Q^{(1)} \approx 2eV$. On the other hand, the components μ_{11}, μ_{22} and μ_{12} have two modes $Q^{(1)} \approx 0eV$ and $Q^{(2)} \approx 0.2eV$. Additionally, the bicrystallography which is classically defined by the tuple (M,n) is now defined by one or multiple disconnection modes by the tuple $(\vec{b}_m, h_m)$. These results are similar to those presented in [58] where different temperature relations for μ can be found. It is necessary to point out that even if these results show different tendencies of GB mobility, they need to be confirmed by experimental results which may explain the non-linearity of the Arrhenius plots presented in section 1.2.4.

In [128], the authors have also shown results for 2D polycrystalline cases. If GB migration and shear are not coupled, one can obtain a simplified kinetic equation from the classical GB motion equation (Equation 1.24): $R^2 - R_0^2 = 2\mu_{11} g\gamma t$, where R is the equivalent grain radius, $g = n/6 - 1$ is a factor that describes grain topology and n the number of edges. When GB shear is coupled, Equation 1.45 may be redefined as

$$\begin{pmatrix} \dot{R} \\ -\dot{\tau} R/G \end{pmatrix} = \begin{bmatrix} \mu_{11} & \mu_{12} \\ \mu_{21} & \mu_{22} \end{bmatrix} \begin{pmatrix} g\gamma/R \\ \tau \end{pmatrix}, \tag{2.41}$$

where τ is the shear stress and the dot notation represents time derivative. An equivalent simplified kinetic equation is defined as $R^2 - R_0^2 = 2\tilde{\mu} g\gamma t$, where the effective GB mobility of the polycrystal is defined as $\tilde{\mu} = |\mu_{ij}|/\mu_{22} = \mu_{11} - \mu_{12}^2/\mu_{22}$.

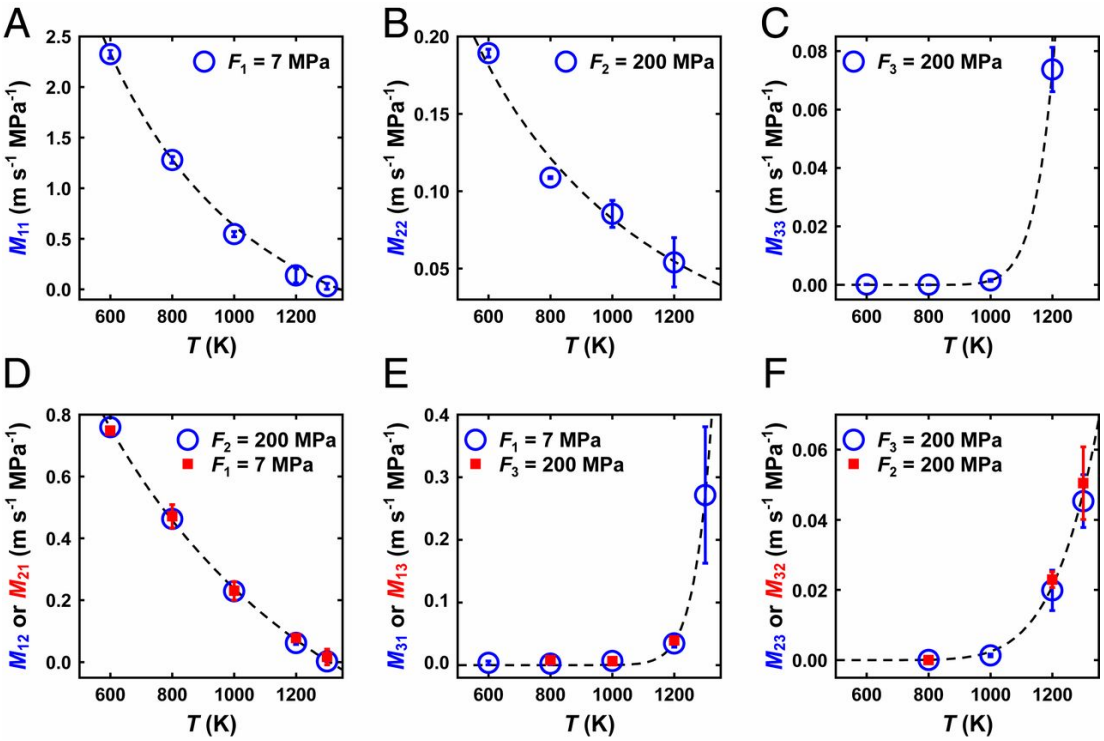

Figure 2.3: Temperature dependence of the GB mobility components (A) μ_{11}, (B) μ_{22}, (C) μ_{33}, (D) μ_{12}, (E) μ_{13} and (F) μ_{23} of a $\Sigma 7$ [111] $(12\bar{3})$ symmetric tilt GB in copper (error bars indicate the range of the simulation results). The data points represent the MD results, and the dashed lines are fits of the data to Equation 2.40 for a single disconnection mode. For the off-diagonal components of $\mu_{ij} (i \neq j)$, two sets of data points (blue circles and red squares) are shown. Image from [128].

These results show a reduction of the GB mobility if shear is considered, $\tilde{\mu} < \mu_{11}$. Additionally, the behavior of the apparent GB mobility $\tilde{\mu}$ depends on the temperature dependence of its components $d\mu_{11}/dT$ and $d(\mu_{12}^2/\mu_{22})/dT$. The fact that most of the experimental results follow an Arrhenius equation means that the components are dominated by the exponential factor $\mu_{11} - \mu_{12}^2/\mu_{22} \propto \mu_0 exp(-Q/k_B T)$. To conclude, one can keep in mind that the component μ_{11} can dominate among the GB mobility tensor components for a large range of temperature, hence, the classical GB migration equation can be accepted. However, in some cases, the shear coupled migration and the GB mobility tensor should be considered in order to correctly describe the GBs evolution.

2.2.1 Phase Field Disconnections

After the series of papers describing GB migration via disconnections, four recent papers presented continuum models using the Phase field approach [178, 180–182]. This extension is important in order to predict the different behaviors of

GB migration through disconnections in mesoscopic simulations. The first PF implementation was presented by B. Runnels in [178]. Eventually, J. Han et al. presented two consecutive papers with a detailed explanation of disconnection mediated GB motion [180] and its extension to large scale simulations [181].

In [180], the authors derived the GB motion equations under the influence of different driving pressures. The migration equation developed using disconnections is defined using the Einstein notation as:

$$v_i = \mu_{ij} P_j = (\Gamma_s \kappa + \tau \Lambda + \psi) \mu_{ij} n_j, \tag{2.42}$$

where Γ_s is a scalar representation of the GB stiffness tensor defined using disconnections, κ the mean curvature, $\tau = \tau_{disc} + \tau_{ext}$ the shear stress separated into contributions from the external shear stress τ_{ext} and the stress generated by the disconnections along the interface τ_{disc}, ψ accounts for the chemical potential jump and Λ is a factor that correlates the shear coupling generated in different directions. The crystallography in Equation 2.42 is present intrinsically in the terms μ_{ij}, Γ and Λ which are defined via disconnections. From Equation 2.42 one can obtain the classical GB migration equation of GG ($v_i = -\mu\gamma\kappa n_i$) under the following conditions: disconnections are represented by steps (i.e., the Burgers vector is zero), μ and γ are isotropic and $\psi = 0$.

In [180], disconnection movement is dominated by glide in two directions, thus:

$$\Lambda \equiv \beta^{(2)} - \beta^{(1)} = \frac{b^{(2)}}{h^{(2)}} - \frac{b^{(1)}}{h^{(1)}}, \tag{2.43}$$

where $\beta \equiv \dfrac{b}{h}$ is the shear coupling factor characterized by the step h and the Burgers vector b, and the superscripts (1) and (2) are equivalent to the $R(1)$ and $R(2)$ disconnections of the reference interfaces that are parallel to the x-plane and y-plane. The shear coupling β is less effective at high temperatures, thus, $\Lambda \to 0$ [128]. Also, in some cases the shear coupling in the two directions is equivalent $\beta^{(2)} = \beta^{(1)}$, hence $\Lambda = 0$. It means that the difference between disconnection-based formulations and classical formulations presented in section 2.1 is notable in particular cases where the factor Λ is high enough.

From the Anisotropic LS-FE formulation (Equation 2.36), GB velocity can be expressed using the Einstein summation notation as:

$$v_i = \left(\mathbb{P}_{kj} \gamma_{,j} n_k - \Gamma_{mn} \mathbb{K}_{mn}\right) \mu n_i, \tag{2.44}$$

where $\gamma_{,j}$ is the GB energy gradient. If the chemical potential in Equation 2.42 is neglected, the GB motion equation via disconnections may be redefined as:

$$v_i = (\Gamma_s \kappa + \tau \Lambda) \mu_{ij} n_j, \tag{2.45}$$

the differences between Equations 2.44 and 2.45 lies in the definition of the GB mobility, the definition of the GB stiffness tensor, and the presence of the projected GB energy gradient in Equation 2.44 and the shear coupled migration term $\tau\Lambda$ in Equation 2.45 which could be easily added to the FE-LS approach.

2.3 Summary and discussion

The classical kinetic equation ($v = \mu P$) is a simplification of lower scale phenomena [2,3] but it constitutes at the polycrystalline scale and in metal forming state-of-the-art an accepted physical framework. One must keep in mind two main questions: Is this kinetic equation is a reasonable approximation [6]? Is the reduced mobility ($\mu\gamma$ product) only defined by the temperature and macroscopic properties of the interface as misorientation and inclination? A clear and univocal answer seems complicated today. A bias in the reduced mobility field discussion lies today in the real capacity of full-field methods to take into account a reduced mobility defined properly in the 5D space defined by the misorientation and inclination.

The majority of the methods can deal with heterogeneous GB properties (3-parameters) using phenomenological models that describe GB properties as a function of the disorientation θ, but the misorientation axis and inclination dependence are not frequently studied. The effect of the GB normal has been studied using Vertex, Phase Field and Level-Set approaches due to the smooth representation of GBs. On the other hand, GBs using CA and MC approaches are stepped and the effect of the GB normal is not studied. However, a different type of model was developed using the kinetic Monte Carlo method [127,183,184]. The main difference is that the classical migration equation is not used anymore but the motion of GBs is controlled by the formation and motion of disconnections [179].

One can find some weaknesses in the use of the term "anisotropy". In the literature heterogeneous values of GB properties have been often categorized as anisotropic. For instance, in [8, 13, 28, 30, 185] heterogeneous GB energy and a constant GB mobility are considered to model polycrystal evolution during GG, and the models are categorized as anisotropic even if it is assumed that the GB energy does not depend on the GB normal and the GB mobility is homogeneous. Another example is found in [32], the proposed LS formulation in context of regular grids includes the effect of anisotropic GB energy using both the effect of the misorientation and the inclination in a GB energy gradient. However, the GB energy dependence on the normal direction is defined without inquiring if additional torque terms are needed and the GB mobility is homogeneous.

Most of the full-field models at the mesoscopic scale cannot deal with the whole description of the GB space (5D). During this PhD thesis, the FE-LS approach has been used and enhanced. The mean reason why LS framework was adopted in this work is its ability to simulate concomitant mechanisms even in context of large deformations. This aspect is essential if one want to model realistic thermomechanical paths in metal forming. In the next chapter, existing LS formulations are discussed and also extended to consider a full anisotropic formulation.

2.4 Résumé en Français du Chapitre 2

Ce chapitre est dédié à l'introduction des différentes méthodes à champ complet utilisées en modélisation de la recristallisation et de la croissance de grains. Par ailleurs, leurs extensions afin de considérer des propriétés de joints de grains hétérogènes et anisotropes ont été présentées.

Chapter 3

Comparative study of different finite element level-set formulations for the modeling of anisotropic grain growth

Due to the wide variety of formulations, this chapter aims to compare four different formulations within a FE-LS approach, the former is the **Isotropic** formulation frequently used in different contexts such as GG, recrystallization, GG with second phase particles [167–169,174,186]. The second one is a simple extension of the isotropic formulation by considering non-homogeneous values of the GB reduced mobility, i.e., **Heterogeneous** formulation. The third formulation was firstly proposed in [25] and extended to polycrystals using different mathematical models of GB energy in [20], i.e., **Heterogeneous with Gradient** formulation. The last formulation is based on a more robust thermodynamics and differential geometry framework but was only applied, at yet, to a bicrystal-like geometry [134], i.e., **Anisotropic** formulation.

One of the perspectives of this work is to criticize and validate these existing formulations but also to consider the enrichment of GB mobility in FE-LS framework. In section 3.2, simulation results are compared with analytical solutions in the context of simple triple junction geometries. In section 3.3, polycrystalline simulations are studied. Mean values and statistical quantities are compared with two different initial textures and using heterogeneous GB energy and mobility. Section 3.4 is dedicated to the inclination dependence discussions studying the movement of triple junctions and bicrystals. Extension to 3D discussions will conclude this chapter.

A part of the results presented in this chapter were published in [38].

3.1 Level-Set Finite-Element formulations

Four different formulations will be studied. The strong formulations used in this work are the ones defined by Equations 2.31, 2.32, 2.34, 2.36 and 2.38. Moreover, the effect of the heterogeneous GB mobility is defined as a *GB mobility gradient* in the weak formulation of the Heterogeneous with Gradient and Anisotropic formulations. The weak formulations of Equations 2.31, 2.32, 2.34, 2.36 and 2.38, with $\varphi \in H_0^1(\Omega)$ are respectively

$$\int_\Omega \frac{\partial \phi}{\partial t}\varphi d\Omega + \int_\Omega \mu\gamma\vec{\nabla}\varphi\cdot\vec{\nabla}\phi d\Omega - \int_{\partial\Omega}\mu\gamma\varphi\vec{\nabla}\phi\cdot\vec{n}d(\partial\Omega) = 0, \tag{3.1}$$

$$\int_\Omega \frac{\partial \phi}{\partial t}\varphi d\Omega + \int_\Omega \mu(\theta)\gamma(\theta)\vec{\nabla}\varphi\cdot\vec{\nabla}\phi d\Omega - \int_{\partial\Omega}\mu(\theta)\gamma(\theta)\varphi\vec{\nabla}\phi\cdot\vec{n}d(\partial\Omega) = 0, \tag{3.2}$$

$$\begin{aligned}\int_\Omega \frac{\partial \phi}{\partial t}\varphi d\Omega + \int_\Omega \mu(\theta)\gamma(\theta)\vec{\nabla}\varphi\cdot\vec{\nabla}\phi d\Omega - \int_{\partial\Omega}\mu(\theta)\gamma(\theta)\varphi\vec{\nabla}\phi\cdot\vec{n}d(\partial\Omega)+\\ +2\int_\Omega \mu(\theta)\vec{\nabla}\gamma(\theta)\cdot\vec{\nabla}\phi\varphi d\Omega + \int_\Omega \gamma(\theta)\vec{\nabla}\mu(\theta)\cdot\vec{\nabla}\phi\varphi d\Omega = 0,\end{aligned} \tag{3.3}$$

$$\begin{aligned}\int_\Omega \frac{\partial \phi}{\partial t}\varphi d\Omega + \int_\Omega \mu(\theta)D(M,\vec{n})\vec{\nabla}\varphi\cdot\vec{\nabla}\phi d\Omega+\\ \int_\Omega \mu(\theta)(\mathbb{P}\cdot\vec{\nabla}\gamma(M,\vec{n}) + \vec{\nabla}D(M,\vec{n}))\varphi\vec{\nabla}\phi d\Omega + \int_\Omega \vec{\nabla}\mu(\theta)D(M,\vec{n})\cdot\vec{\nabla}\phi\varphi d\Omega = 0,\end{aligned} \tag{3.4}$$

and

$$\begin{aligned}\int_\Omega \frac{\partial \phi}{\partial t}\varphi d\Omega + \int_\Omega \mu(\theta)\gamma(M,\vec{n})\vec{\nabla}\varphi\cdot\vec{\nabla}\phi d\Omega - \int_{\partial\Omega}\mu(\theta)\gamma(M,\vec{n})\varphi\vec{\nabla}\phi\cdot\vec{n}d(\partial\Omega)+\\ \int_\Omega \mu(\theta)(\mathbb{P}\cdot\vec{\nabla}\gamma(M,\vec{n}) + \vec{\nabla}\gamma(M,\vec{n}))\varphi\vec{\nabla}\phi d\Omega + \int_\Omega \gamma(M,\vec{n})\vec{\nabla}\mu(\theta)\cdot\vec{\nabla}\phi\varphi d\Omega = 0.\end{aligned} \tag{3.5}$$

More details about the construction of $D(M,\vec{n})$ could be found in Section 5.2.2. All the formulations presented here are equivalent if the properties are homogeneous but the main question remains to test their real capacity concerning the fact to take into account the GB crystallography in the description of μ and γ. The advantage of the Heterogeneous with Gradient and Anisotropic formulations is the ability to take into account the change of boundary type in multiple junctions.

In the next sections a comparative study is presented. It must be highlighted that the formulations proposed in Equation 3.3 and Equation 3.4 are more general than those proposed in [25] and [134], respectively, as μ is here considered also as heterogeneous (function of θ: $\mu(\theta)$). Also, GB energy is better described using

the anisotropic model of GB energy (function of $M(\theta, \vec{a})$ and $\vec{n}$: $\gamma(M(\theta, \vec{a}), \vec{n})$) called GB5DOF [34]. Thus, the GB energy is a function of the misorientation and the inclination as $\gamma(M, \vec{n})$.

The "Isotropic", "Heterogeneous", "Heterogeneous with Gradient", "Anisotropic-5" and "Anisotropic" formulations will be referred, in the following, as Iso, Het, HetGrad, Aniso5 and Aniso. The next table is a summary of the five FE-LS formulations used in this work as a function of the GB crystallographic properties $B = (M(\theta, \vec{a}), \vec{n})$.

Summary of FE-LS formulations

Iso	:	$\vec{v} = -\mu\gamma\kappa\vec{n}$
Het	:	$\vec{v} = -\mu(\theta)\gamma(\theta)\kappa\vec{n}$
HetGrad	:	$\vec{v} = \mu(\theta)(\vec{\nabla}\gamma(\theta) \cdot \vec{n} - \gamma(\theta)\kappa)\vec{n}$
Aniso	:	$\vec{v} = \mu(\theta)\left(\mathbb{P}(\nabla\gamma(B), \vec{n}) - \gamma(B)\kappa\right)\vec{n}$
Aniso5	:	$\vec{v} = \mu(\theta)\left(\mathbb{P}(\nabla\gamma(B), \vec{n}) - \left(\gamma(B)\mathbb{I} + \frac{\partial^2\gamma(B)}{\partial\vec{n}\partial\vec{n}}\right) : \mathbb{K}\right)\vec{n}$

In practical terms both μ and γ could be functions of B but little information of $\mu(\vec{n})$ is known. In section 5.2.2, a case with both anisotropic GB mobility and GB energy ($\mu(M, \vec{n})$,$\gamma(M, \vec{n})$) will be presented.

3.2 The Grim Reaper case

In this section, simulation results obtained with the Het, HetGrad and Aniso formulations are compared for a triple junction microstructure in 2D. This geometry is chosen because analytical relations are available for the comparison of triple junction velocities and angles depending on the $\mu\gamma$ values. The simulations presented here were carried out with unstructured triangular meshes, a P1 interpolation, and using an implicit backward Euler time scheme for the time discretization. The system is assembled using typical P1 FE elements with a Streamline Upwind Petrov–Galerkin (SUPG) stabilization for the convective term [187]. The boundary conditions (BCs) are classical null von Neumann BCs applied to all of the LS functions. This choice imposes the orthogonality between the LS functions and the boundary domain (each plane of the boundary domain can be seen as a symmetric plane). By considering a minimal and maximal mesh size (respectively h_{min} and h_{max}), an optimized anisotropic remeshing strategy developed by Bernacki et al. [186, 188], used in the DIGIMU® software [189] and

illustrated in Figure 3.1, is adopted here. The mesh is finely and anisotropically refined close to the interfaces ($\phi < \phi_{min}$) and becomes isotropic when $\phi > \phi_{max}$, with a linear evolution of the normal mesh size between ϕ_{min} and ϕ_{max}. A homogeneous tangential mesh size ($h_t = h_{max}$) is considered everywhere and the normal mesh size is then defined as:

$$\begin{cases} h_n = h_{min}, & \phi < \phi_{min}, \\ h_n = m(\phi - \phi_{min}) + h_{min}, & m = \dfrac{h_{max} - h_{min}}{\phi_{max} - \phi_{min}} \quad \phi_{min} \leq \phi \leq \phi_{max}, \\ h_n = h_t = h_{max}, & \phi > \phi_{max}. \end{cases} \tag{3.6}$$

By generalizing this approach at the multiple junctions, a fine isotropic ($h_n = h_t = h_{min}$) remeshing is automatically performed (see [186] for more details). During grain boundary migration, thanks to a topological mesher/remesher, anisotropic remeshing operations are performed periodically to follow the grain interfaces. Typically, a remeshing operation is considered each time a LS is about to leave the fine mesh area set by ϕ_{min}.

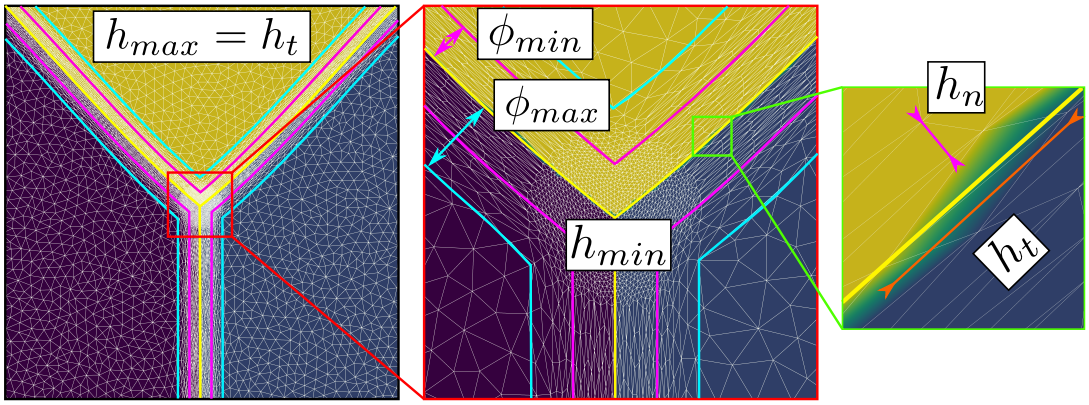

Figure 3.1: Illustration of the anisotropic mesh refinement [188, 190].

3.2.1 Description of the test case

The case presented here is described in [7], a well known case for heterogeneous triple junction, called "Grim Reaper" due to its particular profile. The authors developed a stationary solution of a symmetric triple junction. The initial microstructure is a dimensionless T-shape triple junction with three phases and unitary dimensions $L_x = 1$ and $L_y = 3$ (see Figure 3.2). This geometry was chosen because after a transient-state, a quasi-steady-state is reached, where analytical relations, depending on the reduced mobility, are available for the triple junction velocity and equilibrium angles.

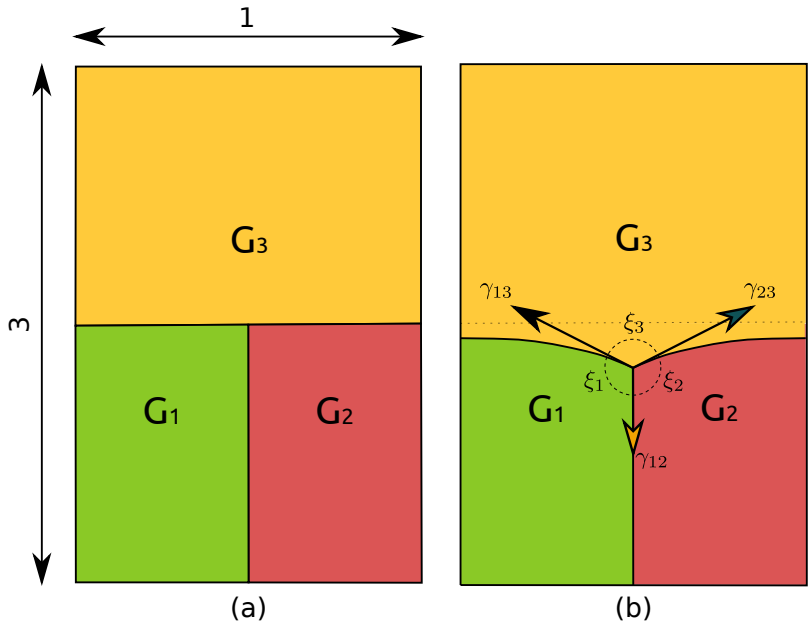

Figure 3.2: T-shape triple junction (a) and quasi steady state of the triple junction showing the dihedral angles and GB energies (b).

When the quasi-steady-state is reached, the triple junction moves with a constant velocity towards the bottom of the domain, with a stable triple junction profile which respects the conditions imposed by the Herring's equation [191]:

$$\sum_{j>i} \gamma_{ij} \vec{\tau}_{ij} + \frac{\partial \gamma_{ij}}{\partial \vec{\tau}_{ij}} = 0, \tag{3.7}$$

where γ_{ij} is the GB energy and $\vec{\tau}_{ij}$ are the inward pointing tangent vectors of the three boundaries at the triple junction. In the present example, the grain boundary energy is constant per interface ($\gamma(\theta)$) and the above equation may as well be expressed by the Young's law (no torque terms):

$$\sum_{j>i} \gamma_{ij} \vec{\tau}_{ij} = 0, \tag{3.8}$$

which may be expressed in terms of the angles ξ_i of the grain i, through the Young's equilibrium (see Figure 3.2):

$$\frac{sin\xi_1}{\gamma_{23}} = \frac{sin\xi_2}{\gamma_{13}} = \frac{sin\xi_3}{\gamma_{12}}. \tag{3.9}$$

By considering an axially symmetric configuration where $\gamma_{13} = \gamma_{23} = \gamma_{top}$ and $\gamma_{12} = \gamma_{bot}$, and by defining the ratio of grain boundary energies as $r = \frac{\gamma_{top}}{\gamma_{bot}}$, an analytical value for the angle ξ_3 can be obtained:

$$\xi_3^{ana} = 2arccos\left(\frac{1}{2r}\right). \tag{3.10}$$

Moreover, the stationary transported profile takes the form of the "Grim Reaper" profile, defined as:

$$\begin{cases} y(x,t) = g(x) + v_{TJ}^{ana} t \\ g(x) = -\dfrac{\mu\gamma_{top}}{v_{TJ}^{ana}} ln\left(cos\left(\dfrac{v_{TJ}^{ana}}{\mu\gamma_{top}} x\right)\right) + y_0 \end{cases} \tag{3.11}$$

where v_{TJ}^{ana} is the magnitude of the stationary velocity, y_0 is the initial y-value, and (x, y) are the Cartesian coordinates. By using Neumann boundary conditions, the stationary velocity could be related to the x-size of the domain:

$$v_{TJ}^{ana} = -\frac{2\mu\gamma_{top}}{L_x}\left(\frac{\pi}{2} - \frac{\xi_3^{ana}}{2}\right). \tag{3.12}$$

In order to focus on a considerable level of heterogeneity in the system, r is initially fixed as equal to 10 ($\gamma_{top} = 1$ and $\gamma_{bot} = 0.1$), and μ is defined as unitary. Several simulations were carried out and compared with the analytical values of $\xi_3^{ana} = 174.27°$ and $v_{TJ}^{ana} = -0.100042$. These variables are computed as follows:

- The velocity of the triple junction is computed using the relation $v_{TJ} = \left(y_{TJ}^{t+\Delta t} - y_{TJ}^{t}\right)/\Delta t$, where y_{TJ}^{t} is the y-position of the triple point at time t and Δt is the time step.
- The dihedral angles are computed using the methodology presented in [25]: one may define, at each time, a circle of radius ε with circumference $\mathcal{C}_\varepsilon$, and divide it into arcs which pass through grain G_i with length $\mathcal{L}_\varepsilon^i$. The angle of the arc, ξ_i, could be approximated thanks to the relation $\xi_i = 2\pi\mathcal{L}_\varepsilon^i/\mathcal{C}_\varepsilon$.

Hence, these variables are affected by the spatial discretization of the domain and the choice of ε, which must be close enough to the multiple junction while containing a sufficient number of finite elements, as illustrated in Figure 3.3, where different values of ε are tested. Here, the value $\varepsilon = 0.05$ is adopted. v_{TJ} and ξ_i are compared using relative errors which are defined as:

$$e_X = \left|\frac{X^{ana} - X}{X^{ana}}\right|,$$

where X^{ana} is the analytical value of the variable to be compared. Another discussed quantity is the interfacial energy, calculated using:

$$E_\Gamma = \sum_i \sum_{e\in\mathcal{T}} \frac{1}{2}\gamma l_e(\phi_i), \tag{3.13}$$

where $\mathcal{T}$ is the set of all elements in the FE mesh, l_e is the length of the zero iso-value existing in the element e, and i refers to the number of LS functions, and the $\frac{1}{2}$ is necessary due to the duplicity of the LS functions in the interfaces

defining a grain boundary. This variable is frequently studied and it may be seen as an energetic measure of how quickly the system reaches equilibrium.

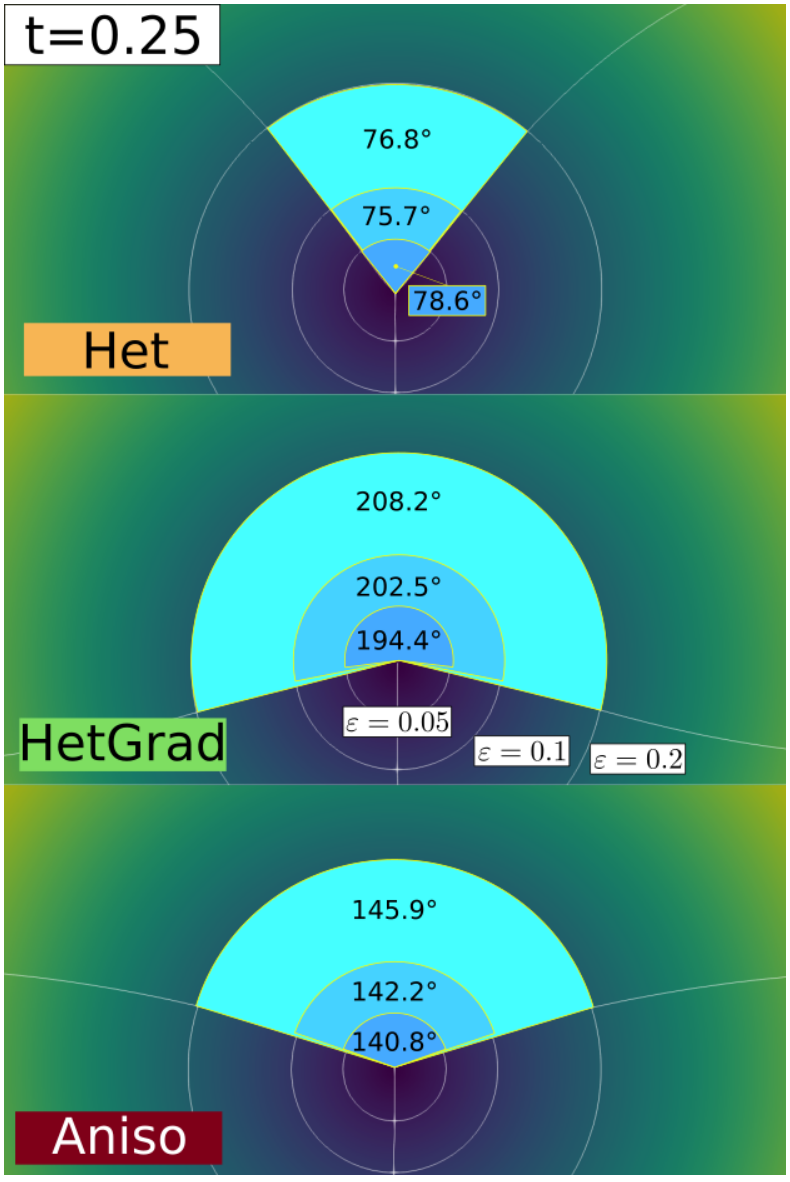

Figure 3.3: The triple junction at $t = 0.25$ using $h_{min} = 5\times10^{-4}$, $\Delta t = 1\times10^{-5}$. The three white circles represent the radius $\varepsilon = \{0.05, 0.1, 0.2\}$ used to compute the top dihedral angle. One can see the impact of the curved interfaces around the triple junctions in the ξ_3 estimation. In the following, the value $\varepsilon = 0.05$ is adopted.

3.2.2 Results and analysis

First, a sensibility analysis for the three formulations was carried out. The values of mesh size and time step used here are: $h_{max} = h_t = 1 \times 10^{-2}$, $h_{min} = \{5 \times 10^{-4},\ 1 \times 10^{-3},\ 5 \times 10^{-3},\ 1 \times 10^{-2}\}$ and $\Delta t = \{1 \times 10^{-5},\ 5 \times 10^{-5},\ 1 \times 10^{-4},\ 5 \times 10^{-4}\}$. For all the cases, Φ_{min} and Φ_{max} are fixed respectively to 1×10^{-2} and 2×10^{-2}. Figure 3.3 shows, for the different formulations, the triple junctions at $t = 0.25$ using $h_{min} = 5 \times 10^{-4}$ and $\Delta t = 1 \times 10^{-5}$. One dihedral angle is depicted for different values of ε. In the following, $\xi_3^{h_{min}[k],\Delta t[k]}$ is used to define the converged value of the ξ_3 angle for the k-th value of the h_{min} and Δt datasets. Indeed, if the results described in Figures 3.4–3.6 principally aim to compare the simulations with the quasi-steady-state analytical values, it is also interesting to discuss the obtained converged value of v_{TJ} as a function of the converged value of ξ_3 (i.e., if Equation (3.12) is respected for these values).

Figure 3.4 illustrates the evolution of E_Γ, ξ_3, and v_{TJ} using the Het formulation. Two stages appear in E_Γ, whereby it initially increases before decreasing. The results illustrate the fact that the approach seems not to converge, in time and space, towards the analytical solutions. However, in terms of the dihedral angle, the results converge towards $\xi_3^{h_{min}[0],\Delta t[0]}$, and the triple junction velocity converges toward the corresponding velocity $v_{TJ}^{ana(h_{min}[0],\Delta t[0])}$ (following Equation (3.12)). The movement of the Het formulation is mostly influenced by the curvature of the interface, as exposed in Section 3.1, and one has to keep in mind that there are no additional terms that could influence the movement of the interfaces. These results illustrate that the Het formulation, by considering heterogenous values of reduced mobility and the multiple junction treatment defined by Equation 2.23, without re-discussing the capillarity driving pressure used in the kinetic equations, is definitively not a good option when a convective/diffusive formulation is solved to model the GG mechanism.

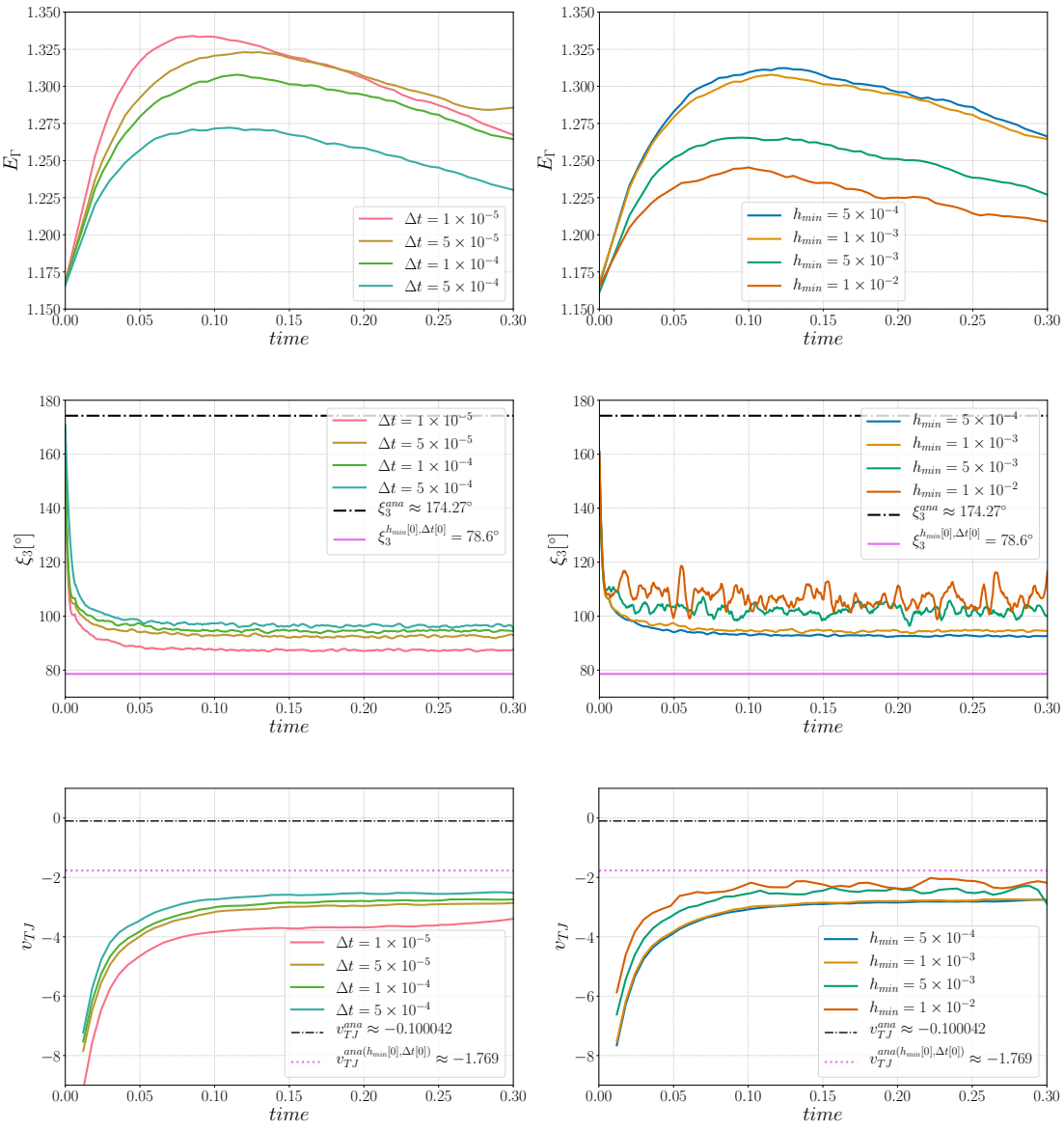

Figure 3.4: Sensibility analysis for the Het formulation in (**left**) time for $h_{min} = 1 \times 10^{-3}$ and in (**right**) h_{min} size for $\Delta t = 1 \times 10^{-4}$: (**top**) interfacial energy sensibility, (**middle**) triple junction angle, ξ_3, sensibility analysis, and (**bottom**) triple junction velocity, v_{TJ}, sensibility analysis.

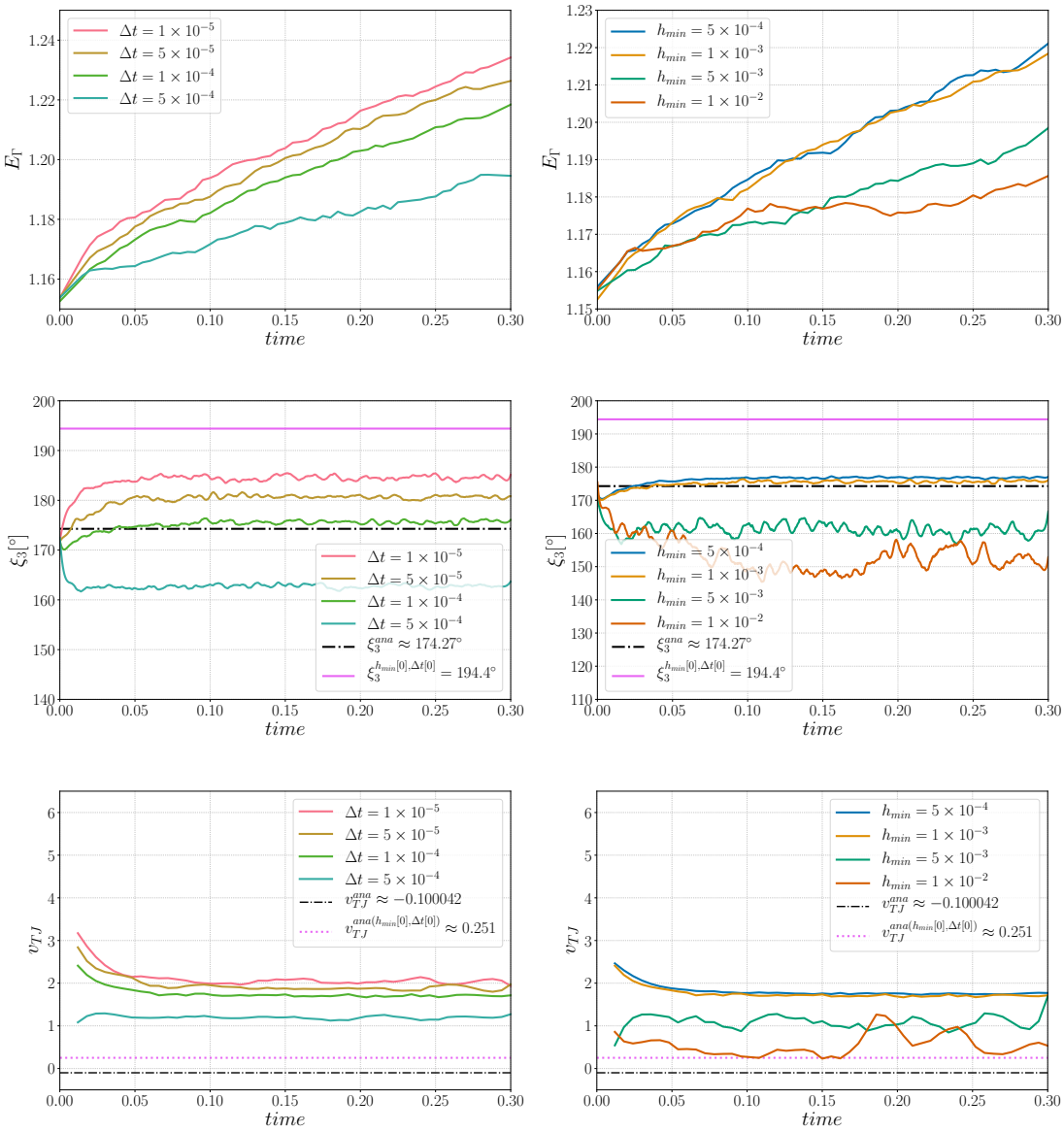

Figure 3.5: Sensibility analysis for the HetGrad formulation in (**left**) time for $h_{min} = 1 \times 10^{-3}$ and in (**right**) h_{min} size for $\Delta t = 1 \times 10^{-4}$: (**top**) interfacial energy sensibility, (**middle**) triple junction angle, ξ_3, sensibility analysis, and (**bottom**) triple junction velocity, v_{TJ}, sensibility analysis.

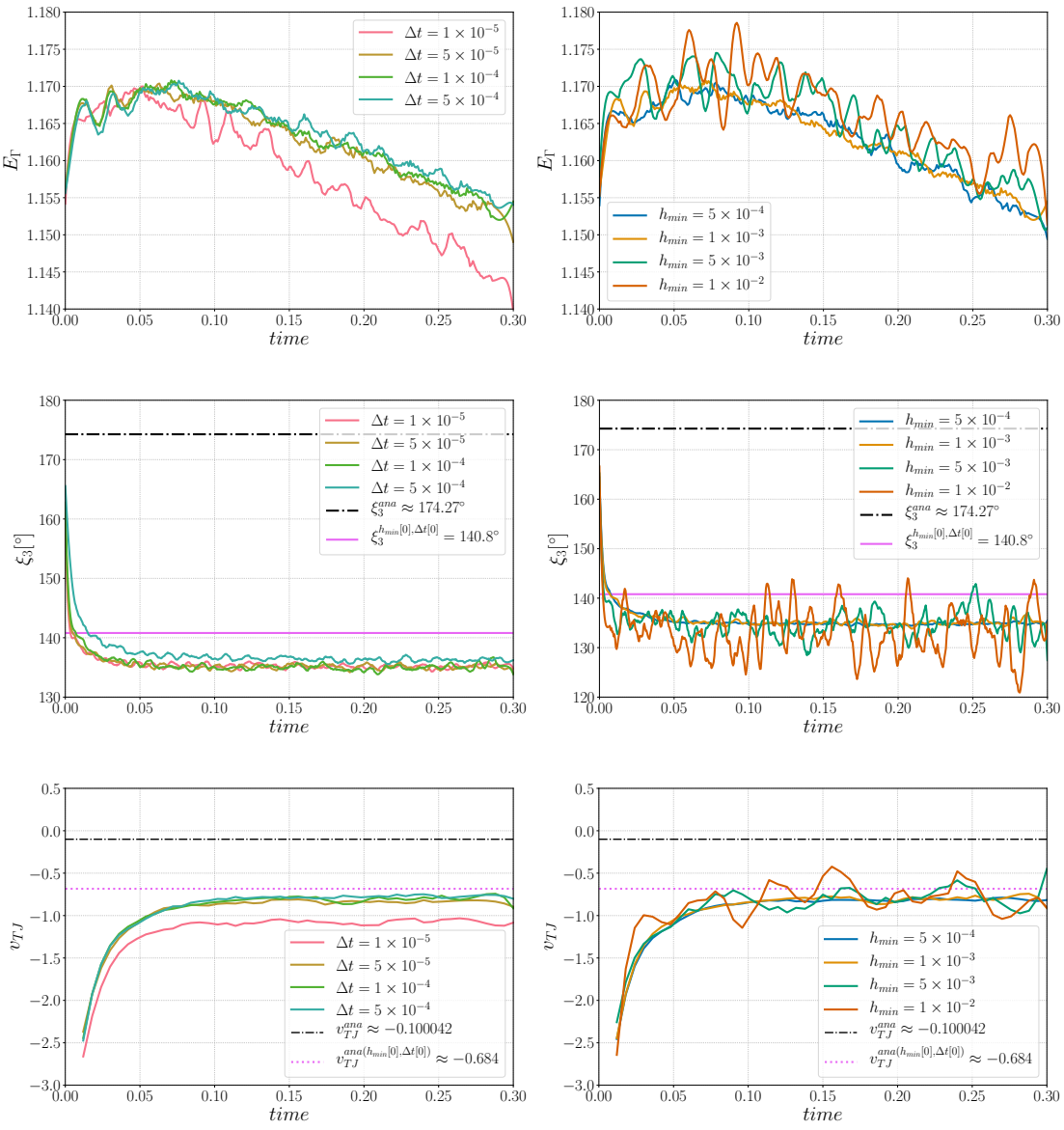

Figure 3.6: Sensibility analysis for the Aniso formulation in (**left**) time for $h_{min} = 1 \times 10^{-3}$ and in (**right**) h_{min} size for $\Delta t = 1 \times 10^{-4}$: (**top**) interfacial energy sensibility, (**middle**) triple junction angle, ξ_3, sensibility analysis, and (**bottom**) triple junction velocity, v_{TJ}, sensibility analysis.

The evolution of the HetGrad formulation is quite different, the interface evolves in the opposite direction (see Figure 3.7) which explains that E_Γ increases during the simulation (see Figure 3.5). An explanation of this evolution comes from the presence of the grain boundary energy gradient, $\nabla\gamma$, in the triple junction. The main purpose of this gradient is the correction of the triple junction dihedral angles and velocity. In Figure 3.5, one can see that ξ_3 is closer to its analytical value and that it also converges towards $\xi_3^{h_{min}[0],\Delta t[0]}$. Nevertheless, $\nabla\gamma$

also changes the kinetics of the interface because it is present along the interface and exerts a force that overcomes the effect of the curvature and generates a movement in the opposite direction. Regarding the velocity, it does not converge towards the analytical value v_{TJ}^{ana}, nor the correlated value $v_{TJ}^{ana(h_{min}[0],\Delta t[0])}$.

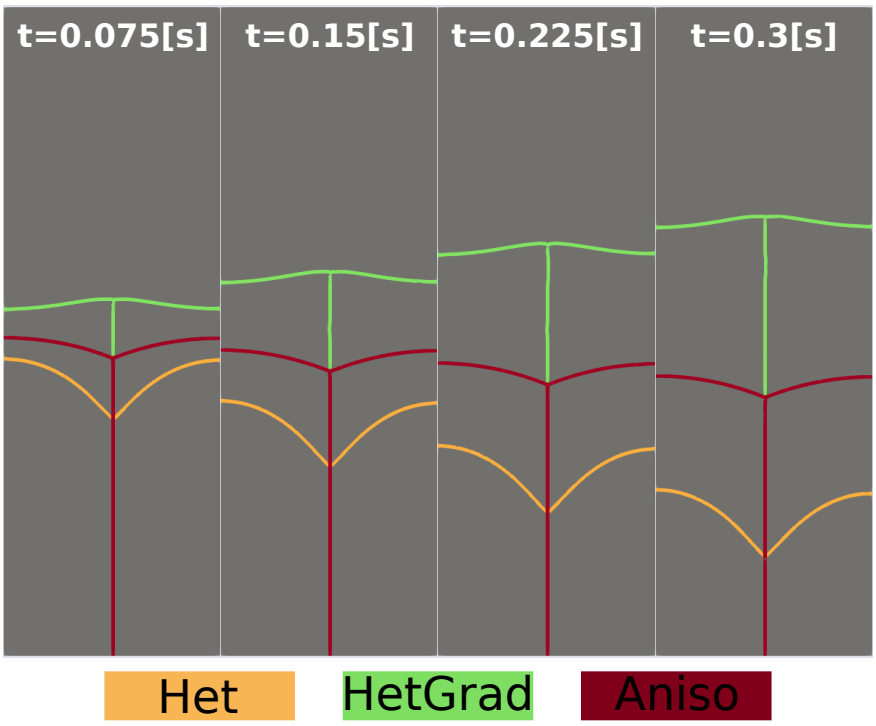

Figure 3.7: Evolution of the interfaces at different time steps of the three models.

The Aniso formulation has an additional term, the projection tensor $\mathbb{P}$, which takes into account the tangential changes of $\nabla\gamma$. Thanks to this term, the interface evolves in the right direction, with a minimization of the boundary energy. From the evolution of ξ_3 and v_{TJ}, one can see that the simulation converges in time and space. Even if the values of ξ_3 do not precisely fit the analytical value, they converge towards $\xi_3^{h_{min}[0],\Delta t[0]}$. Moreover, the converged value of velocity is around $v_{TJ}^{ana(h_{min}[0],\Delta t[0])}$, meaning that the kinetics and topology of the triple junction are well-correlated through Equation (3.12).

The evolution of the triple junction profile using the Het, HetGrad, and Aniso formulations is illustrated in Figure 3.7. Both the Het and Aniso formulations produced the Grim Reaper profile, while the profile produced by the HetGrad formulation evolves in the opposite direction. This is reflected in the values of the triple junction velocity shown in Figure 3.8c. From the comparison of the interfacial energy evolution (Figure 3.8a) and of the velocities (Figure 3.8c), one can see that the Aniso formulation has the best energetic behavior and a better approximation of the triple junction velocity. However, the best approximation of dihedral angles is obtained with the HetGrad formulation (Figure 3.8b).

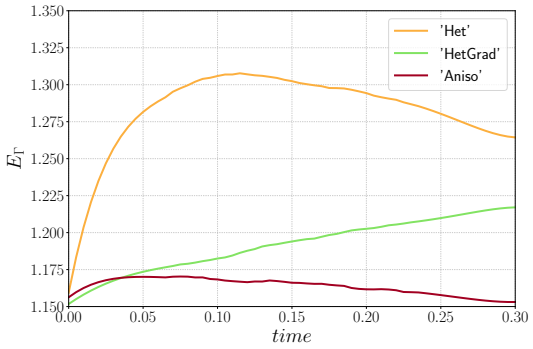

(a) $E_\Gamma(t)$

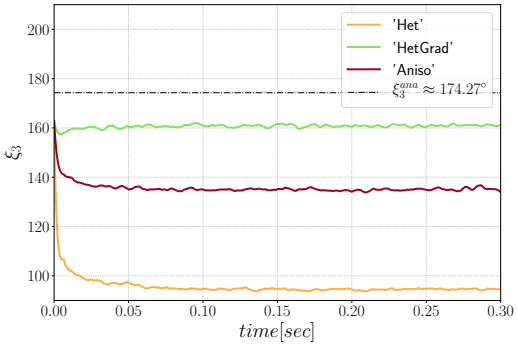

(b) $\xi_3(t)$

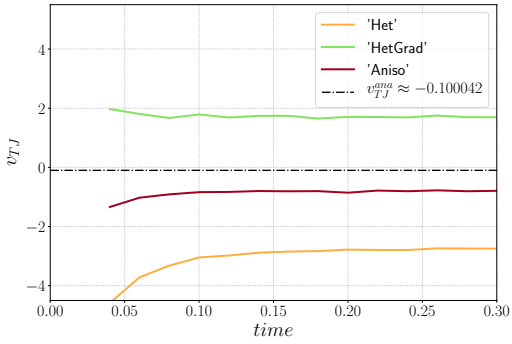

(c) $v_{TJ}(t)$

Figure 3.8: Time series of E_Γ, ξ_3 and v_{TJ} for the three formulations.

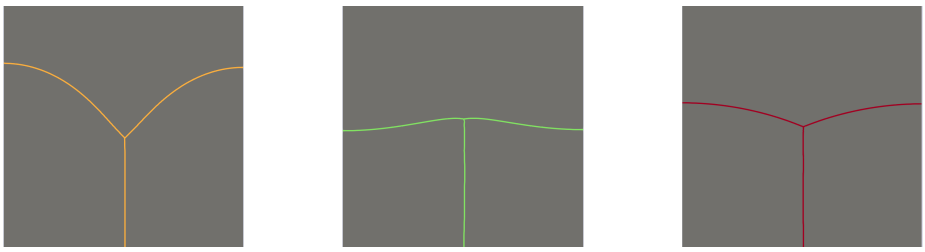

(a) Het (b) HetGrad (c) Aniso

Figure 3.9: Detail of the triple junction at $t = 0.3$.

The level of anisotropy defined here is high ($r = 10$), and this order of value has also been discussed in the literature [25, 29, 162] and remains necessary to discuss realistic polycrystal aggregates (coherent twin energy, for example). In Figure 3.10, the effect of the anisotropy level (r value) on the top dihedral angle and the triple junction velocity is illustrated. We have carried out simulations using $h = 1 \times 10^{-3}$, $\Delta t = 1 \times 10^{-4}$ and $r \in \{0.55,\ 0.625,\ 0.714,\ 0.833,\ 1.0,\ 1.25,\ 1.66,\ 2.5,\ 5,\ 10\}$, which are equivalent to $\gamma_{bot} \in \{1.8,\ 1.6,\ 1.4,\ 1.2,\ 1.0,\ 0.8,\ 0.6,\ 0.4,\ 0.2,\ 0.1\}$. These results allow us to conclude that the Het methodology is not adapted whatever the r value. Interestingly, the HetGrad formulation seems very good for ξ_3 and v_{TJ} for $r < 1.5$, but the migration direction ends up being reversed for higher r values, while keeping an excellent profile for the equilibrium angles. Finally, if the angle respect is slightly worse for the Aniso formulation, the respect of the triple junction speed is much better as soon as $r > 1$. In Figure 3.10b, the three additional dashed lines represent the expected velocity for the ξ_3 values obtained after reaching equilibrium, as illustrated in Figure 3.10a using Equation 3.12. One can see that the Het and HetGrad formulations correlate ξ_3 and v_{TJ} for $r < 1$. On the other hand, the Aniso formulation correlates ξ_3 and v_{TJ} for every r value. A good correlation could be advantageous if one wants to perform more realistic simulations where correct kinetics and topology of the microstructure are of significant importance.

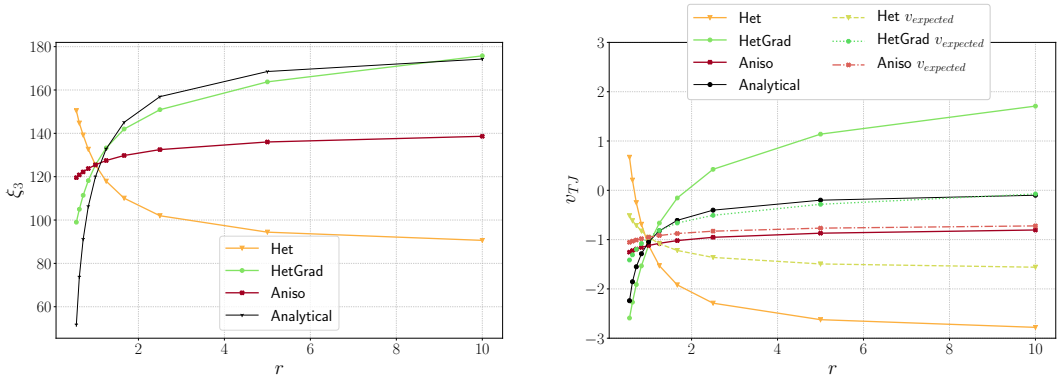

(a) ξ_3 (b) v_{TJ}

Figure 3.10: Variation of triple junction characteristics as a function of r using the Het, HetGrad, and Aniso formulations, and the 1×3 domain. $h = 1 \times 10^{-3}$ and $\Delta t = 1 \times 10^{-4}$.

Effect of the mesh and domain size

The simulations presented above were carried out with an unstructured static mesh (StaticMesh) and a body fitted remeshing technique (Fitz) [192] and then compared to the results obtained using the remeshing technique presented before (Remesh) [186, 188]. The mesh size around the triple junction is the same for the three cases. First the same domain with $L_x = 1$ and $L_y = 3$ is used, Figure 3.12 and Figure 3.11 show the value of the dihedral angle and the velocity after the

triple junction reaches an stationary state. One can see that the difference between the three cases is small regarding ξ_3, also the case using the static mesh is slightly closer to the analytical values. On the other hand, the values of v_{TJ} show a similar tendency using the Aniso and HetGrad formulation.

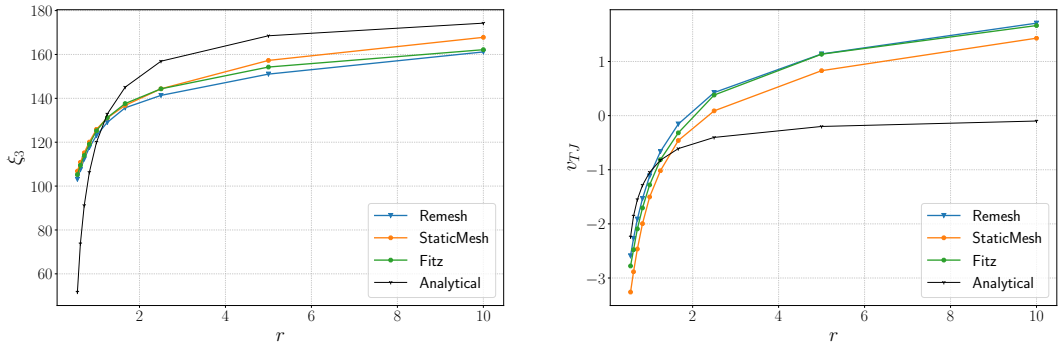

(a) ξ_3 (b) v_{TJ}

Figure 3.11: Variation of triple junction characteristics as a function of r using the HetGrad formulation and the 1x3 domain.

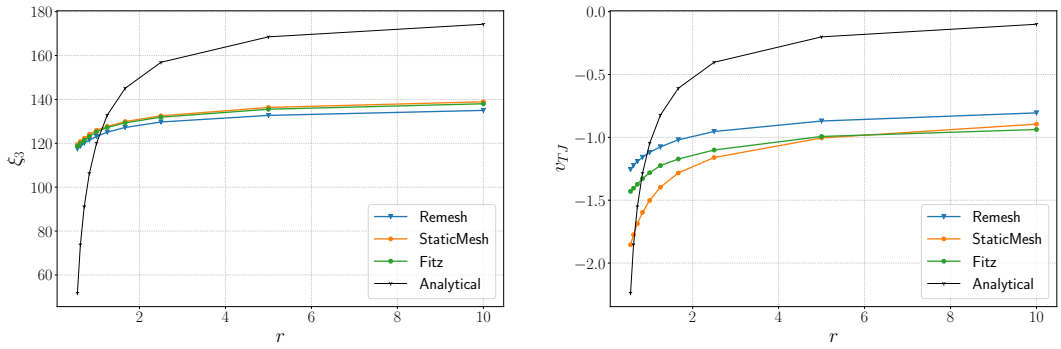

(a) ξ_3 (b) v_{TJ}

Figure 3.12: Variation of triple junction characteristics as a function of r using the Aniso formulation and the 1x3 domain.

If the domain is bigger, similar results are found, the HetGrad formulation has a better approximation of the dihedral angle and also evolves in the wrong direction for $r > 2$. On the other hand, the Aniso formulation has a better approximation of the junction velocity.

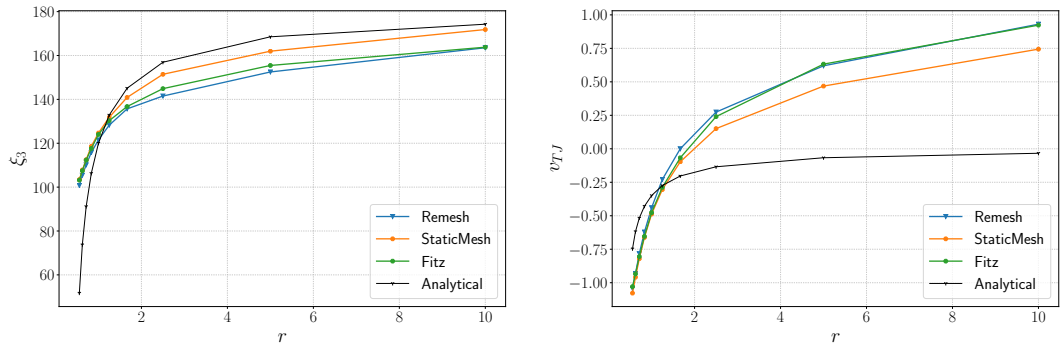

(a) ξ_3 (b) v_{TJ}

Figure 3.13: Variation of triple junction characteristics as a function of r using the HetGrad formulation and the 3x3 domain.

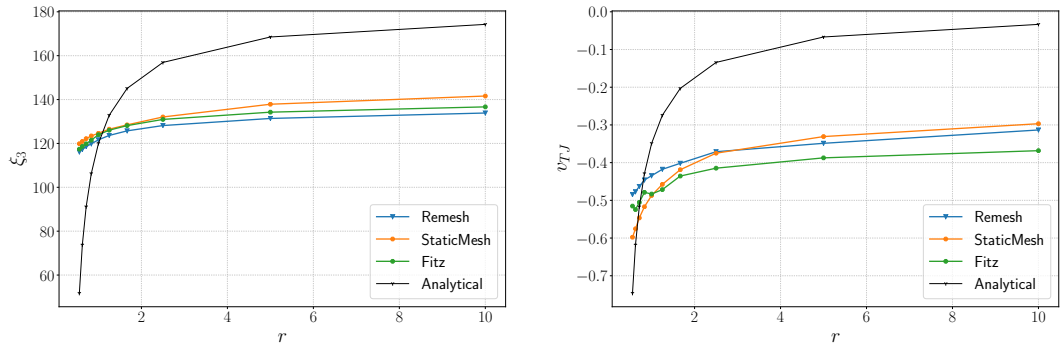

(a) ξ_3 (b) v_{TJ}

Figure 3.14: Variation of triple junction characteristics as a function of r using the Aniso formulation and the 3x3 domain.

Effect of the Boundary Conditions

In [25], the authors proposed the HetGrad formulation and performed several simulations for different values of r. The authors compared the dihedral angles against the analytical Grim Reaper values, see Equation 3.10, and found a very good estimation of the dihedral angles. A triangular domain was used with an initial triple junction equilibrium at 120° and Dirichlet boundary conditions (fixing the GB in the border domain). In other words, a final configuration respecting the Young's equilibrium is attained without the possibility to describe the transient state with an analytical solution. In order to study the Aniso formulation behavior, the same case is presented here. An isotropic mesh is used with a local adaptation around the triple junction where the mesh is refined in a circle of radius $\varepsilon = 0.05$, allowing the simulation to be more computationally efficient in terms of CPU time and memory storage. Figure 3.15 illustrates the mesh around

the triple junction, where one can see the change of the mesh size close to the triple junction.

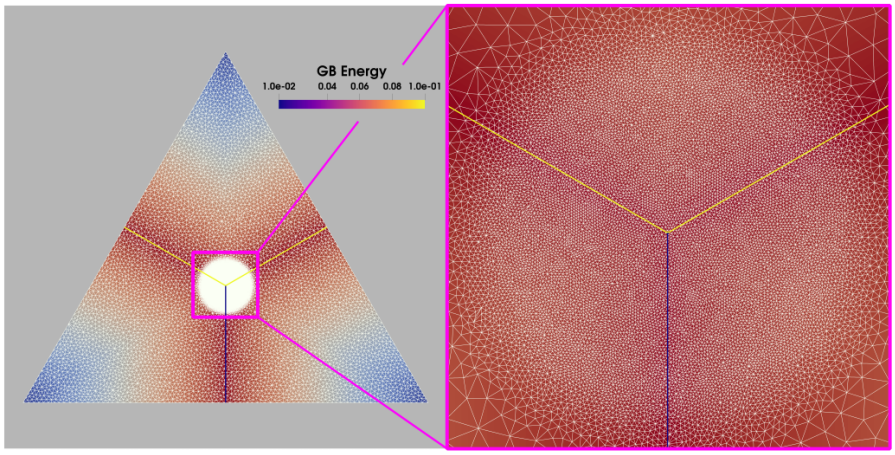

Figure 3.15: Initial configuration of the triangular case with a refined isotropic mesh around the triple junction and a coarse mesh outside the triple junction with $r = 10$.

Multiple simulations were carried in order to study the effect of r. The constant parameters are the GB mobility $\mu = 1$, the GB energy of the top interfaces $\gamma_{top} = 0.1$, the mesh size at the triple junction $h_{TJ} = 0.001$, the mesh size outside the triple junction $h = 0.01$, and the time step $\Delta t = 1 \times 10^{-4}$. As for the case presented before, the GB energy of the bottom interface is changed to obtain $r \in \{0.55,\ 0.625,\ 0.714,\ 0.833,\ 1.0,\ 1.25,\ 1.66,\ 2.5,\ 5,\ 10\}$ ($\gamma_{bot} \in \{0.18,\ 0.16,\ 0.14,\ 0.12,\ 0.1,\ 0.08,\ 0.06,\ 0.04,\ 0.02,\ 0.01\}$). In Figure 3.16, one can see the same tendencies as in Figure 3.10, with the HetGrad formulation being the best option in terms of dihedral angles' prediction.

Figure 3.17 shows the interface evolution with $r = 10$. The evolution is similar for the Grim Reaper example in Figure 3.7. The Het and Aniso formulations exhibit a Grim Reaper-like profile, while the HetGrad formulation evolves in the upward direction. This may seem wrong, however, for this particular geometry an upward movement is expected for $r > 1$ in order to match the analytical angles and as the initial angles are fixed to 120°. Thus, one can say that the interface obtained with the Het formulation evolves in the wrong direction. On the other hand, the movement obtained by the HetGrad formulation exaggerates the expected displacements and the interface is highly curved. Another illustration of the interface movement is shown in Figure 3.18 for $r = 1.66$, where the HetGrad and Aniso formulations have a correct evolution of the interface and the dihedral angle is closer to the analytical value, as shown in Figure 3.16.

In Figure 3.19, one can see the evolution of E_Γ. The trends are similar to the previous test case. The HetGrad and Aniso formulations have a better energetic behavior, and the Aniso formulation remains the best option for high anisotropy levels.

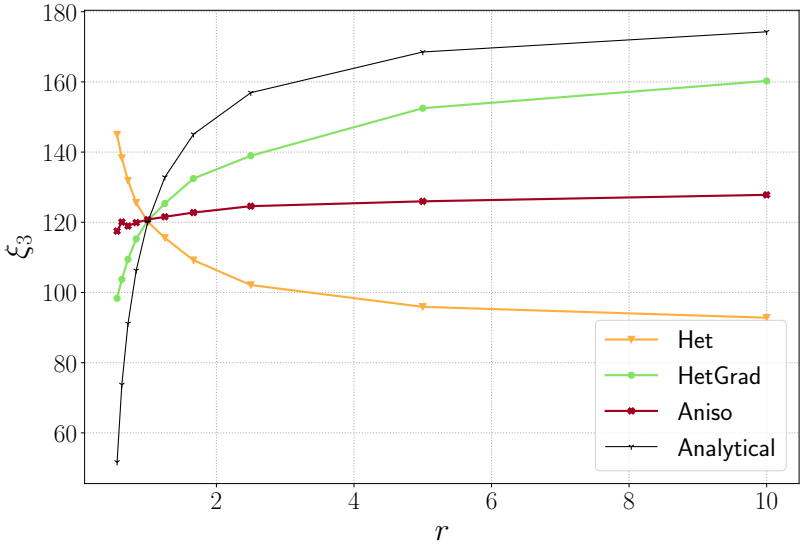

Figure 3.16: Triangular case with Dirichlet boundary conditions: variation of the triple junction top dihedral angle ξ_3 as a function of r using the Het, HetGrad, and Aniso formulations.

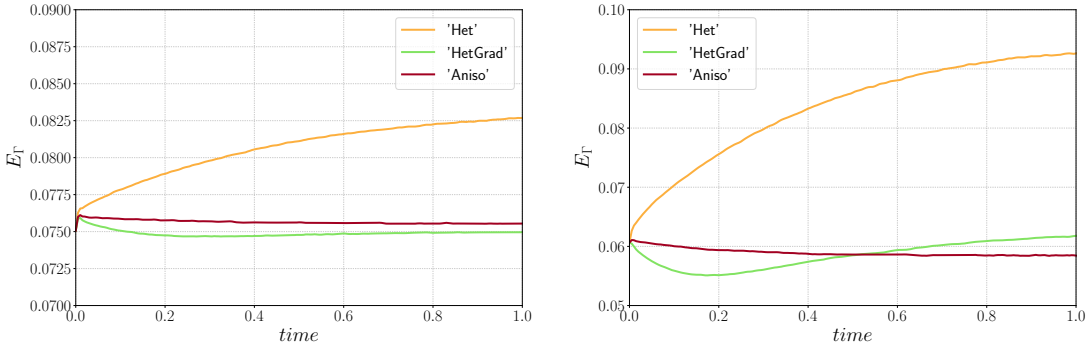

(a) $r = 1.66$ (b) $r = 10$

Figure 3.19: Variation of the interfacial energy, E_Γ, using two different values of r.

These results highlight that the Aniso formulation seems to be the more physical model for a triple junction regarding the velocity of the triple junction and the interfacial energy. Additionally, it also represents the dihedral angles correctly for a wide range of anisotropy levels. Nevertheless, this idea must be reinforced with large scale simulations of polycrystals which is the subject of the next section.

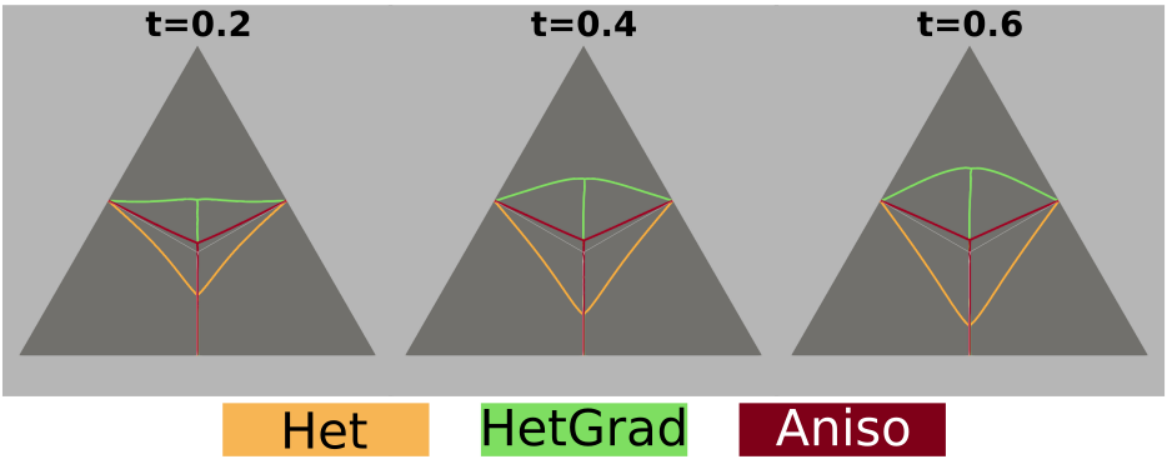

Figure 3.17: Interface evolution using the Het, Hetgrad, and Aniso formulations of the triple junction with $r = 10$.

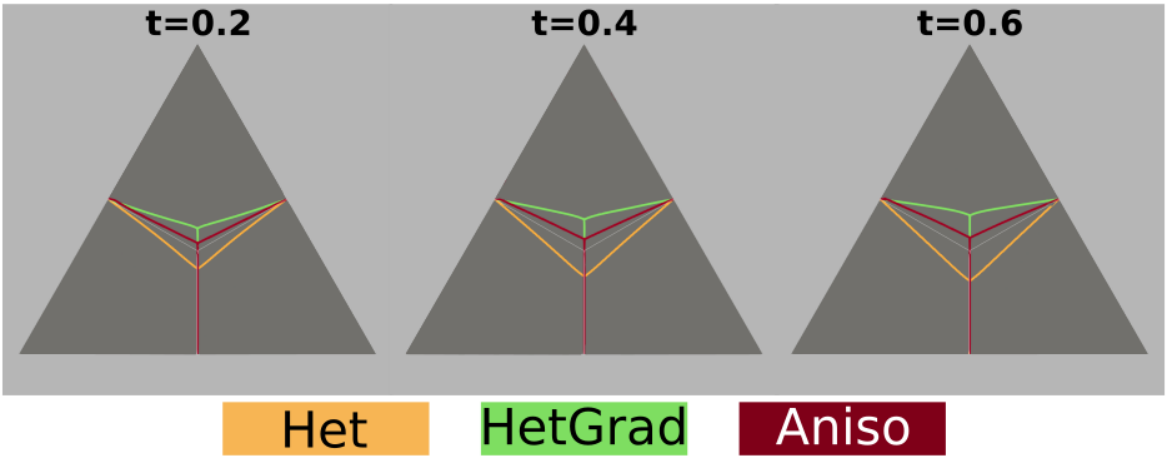

Figure 3.18: Interface evolution using the Het, Hetgrad, and Aniso formulations of the triple junction with $r = 1.66$.

3.3 Effect of the texture and heterogeneous GB properties during GG simulations of a polycrystalline microstructure

In this section, we study a representative GB network in 2D. Figure 3.20 exhibits the initial characteristics of the microstructure, it consists of a square domain with length $L = 1.6$ mm and 5000 grains generated using a Laguerre-Voronoi tessellation [193] based on an optimized sphere packing algorithm [194] with a log-normal distribution for the arithmetic mean grain size. The grain size, R, of each grain is defined as $\sqrt{S/\pi}$, with S as its surface (i.e., defined as the radius of the equivalent circular grain of the same surface). Anisotropic remeshing is used

following Equation 3.6 with a refinement close to the interface. The mesh size in the tangential direction (as well as far from the interface) is fixed at $h_t = 5\,\mu m$ and at $h_n = 1\,\mu m$ in the normal direction. The time step is fixed at $\Delta t = 10\,s$. This section is mainly devoted to studying the heterogeneity of both GB energy and mobility using the four introduced grain growth formulations. Finally, the same study is performed using a different texture.

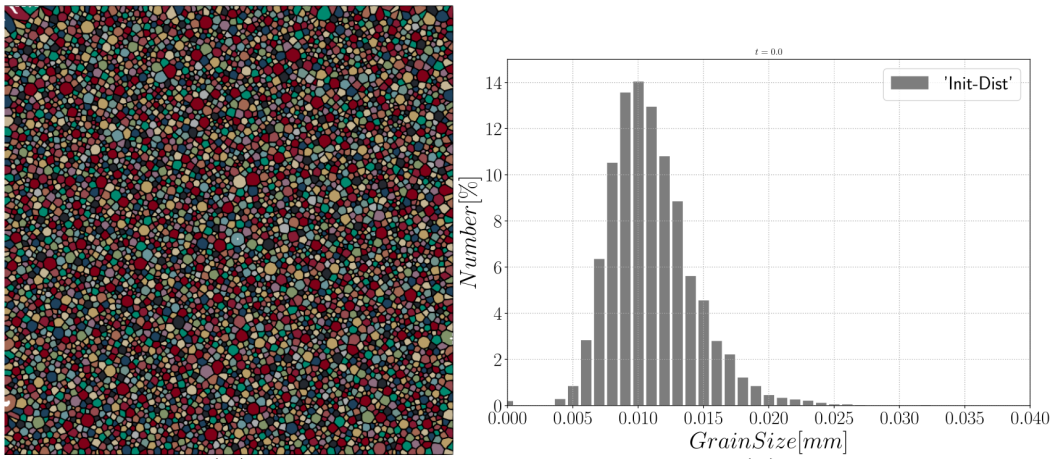

(a) (b)

Figure 3.20: Initial microstructure (a) with 5000 grains and its grain size distribution (b).

3.3.1 Effect of the heterogeneity

Here we use a misorientation dependent GB energy and mobility defined with a Read-Shockley (RS) function [69] and a Sigmoidal (S) function proposed by Humphreys in [77]:

$$\begin{cases} \gamma(\theta) = \gamma_{max} \frac{\theta}{\theta_0} \left(1 - ln\left(\frac{\theta}{\theta_0}\right)\right), \ \theta < \theta_0 \\ \gamma_{max}, \ \theta \geq \theta_0 \end{cases} \tag{3.14}$$

$$\mu(\theta) = \mu_{max} \left(1 - exp\left(-5\left(\frac{\theta}{\theta_0}\right)^4\right)\right), \tag{3.15}$$

where θ is the disorientation, μ_{max} and γ_{max} are the maximal GB mobility and energy, respectively. $\theta_0 = 30°$ is the disorientation defining the transition from a low angle grain boundary (LAGB) to a high angle grain boundary (HAGB). θ_0 is normally considered to be between $15-20°$ but here this parameter is exaggerated to exacerbate the heterogeneity of the system. The maximal values for the GB properties are $\mu_{max} = 1.379 mm^4 J^{-1} s^{-1}$, and $\gamma_{max} = 6 \times 10^{-7} J mm^{-2}$, these

values were estimated using the same methodology as in [173] and are typical for a stainless steel.

Figure 3.21 shows the orientation field using the vector magnitude $O_G = \sqrt{\varphi_1^2 + \phi^2 + \varphi_2^2}$ where $(\varphi_1, \phi, \varphi_2)$ are the three Euler angles. The Euler angles defining the crystallographic orientations generated in this case are generated randomly, leading to a Mackenzie-like disorientation distribution function (DDF) [195]. As the Read-Shockley model is used to define γ, the GB energy distribution (GBED) is concentrated at high values as seen in Figure 3.22.

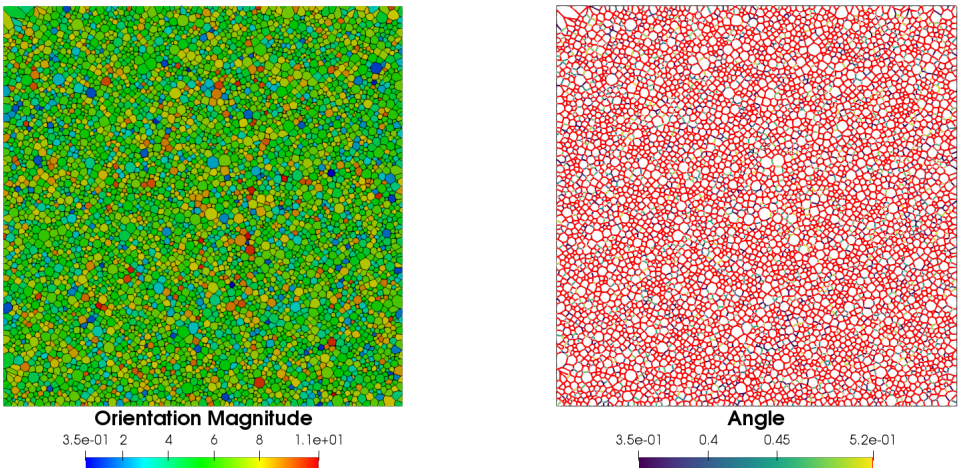

(a) Orientation (b) Disorientation

Figure 3.21: Initial crystallographic characteristics.

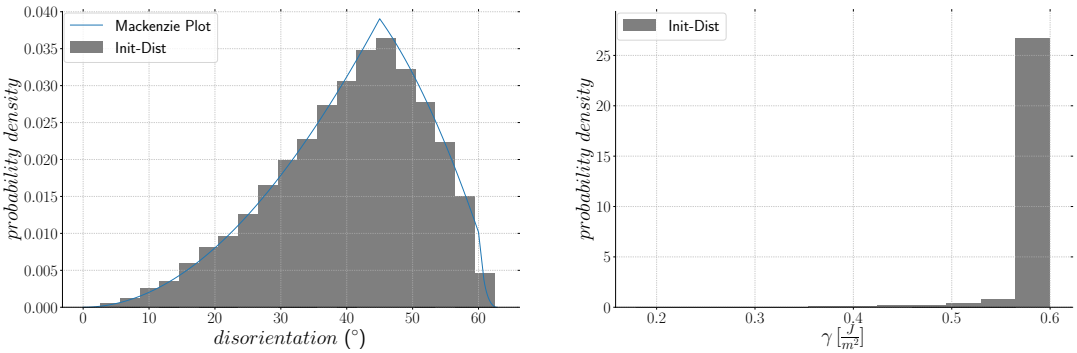

(a) Initial DDF (b) Initial GBED

Figure 3.22: Initial GB characteristics.

Heterogeneous grain boundary energy

In this section, GB energy is defined using Equation 3.14 and GB mobility is assumed isotropic. Hence, the Het, HetGrad, and Aniso formulations are presented as "Het(μ:Iso)", "HetGrad(μ:Iso)", and "Aniso(μ:Iso)". The results are summarized in Figures 3.23–3.25. First, it is noticeable that all the formulations have a similar evolution concerning the total grain boundary energy E_Γ, the number of grains N_g, and the mean grain size weighted by number $\bar{R}_{Nb[\%]}$ or by surface $\bar{R}_{S[\%]}$. Additionally, if the grain size distribution weighted by number is normalized (Figure 3.24), one can recognize that all the formulations have similar distributions and the minima have similar values with respect to the mean radius. Similar results for the "Iso" and "HetGrad" formulations with heterogeneous GB energy defined by the Read–Shockley model were already reported [20].

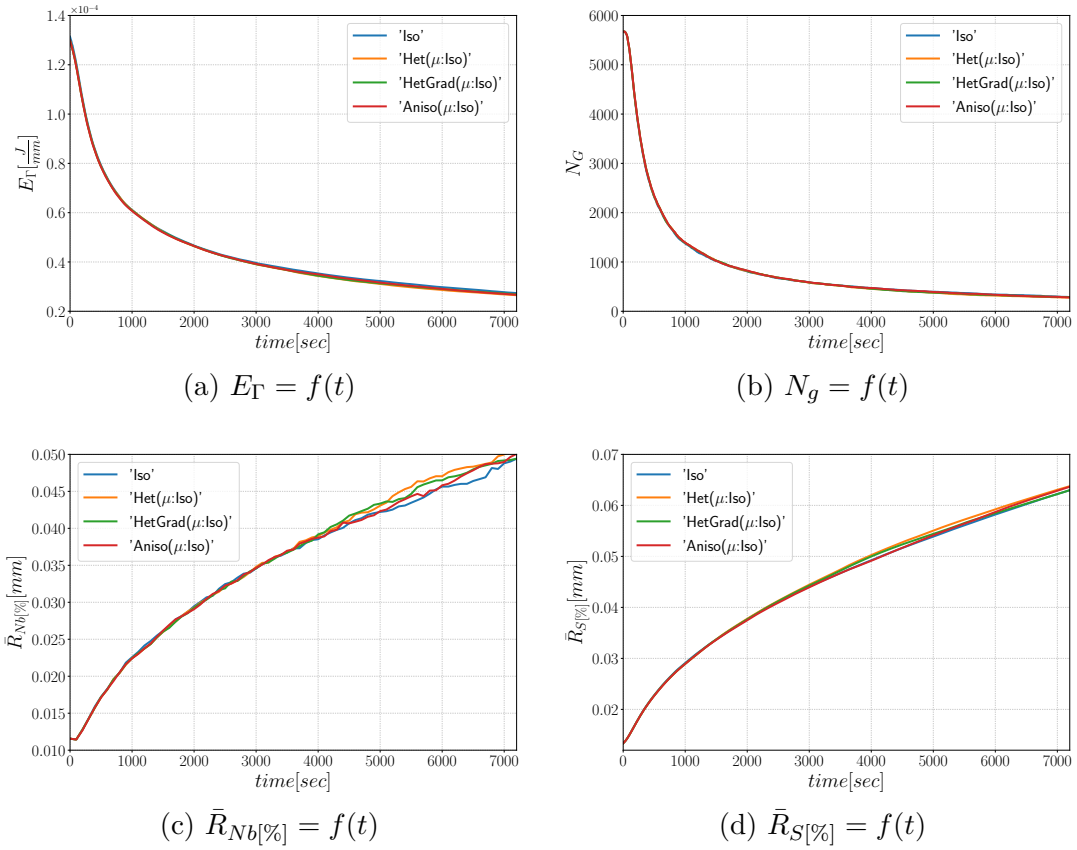

(a) $E_\Gamma = f(t)$ (b) $N_g = f(t)$

(c) $\bar{R}_{Nb[\%]} = f(t)$ (d) $\bar{R}_{S[\%]} = f(t)$

Figure 3.23: Mean values time evolution for the different formulations.

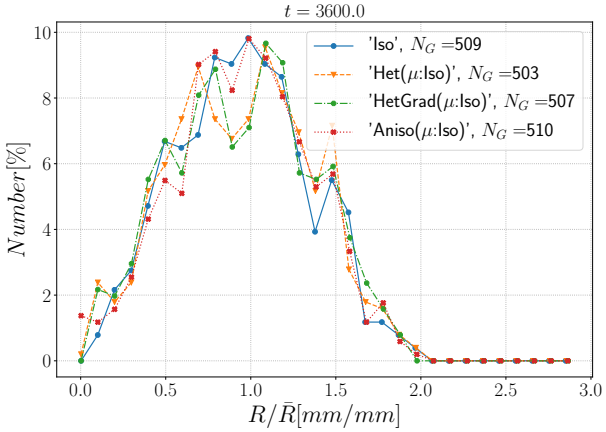

Figure 3.24: Grain radius distribution weighted by number at $t = 1h$.

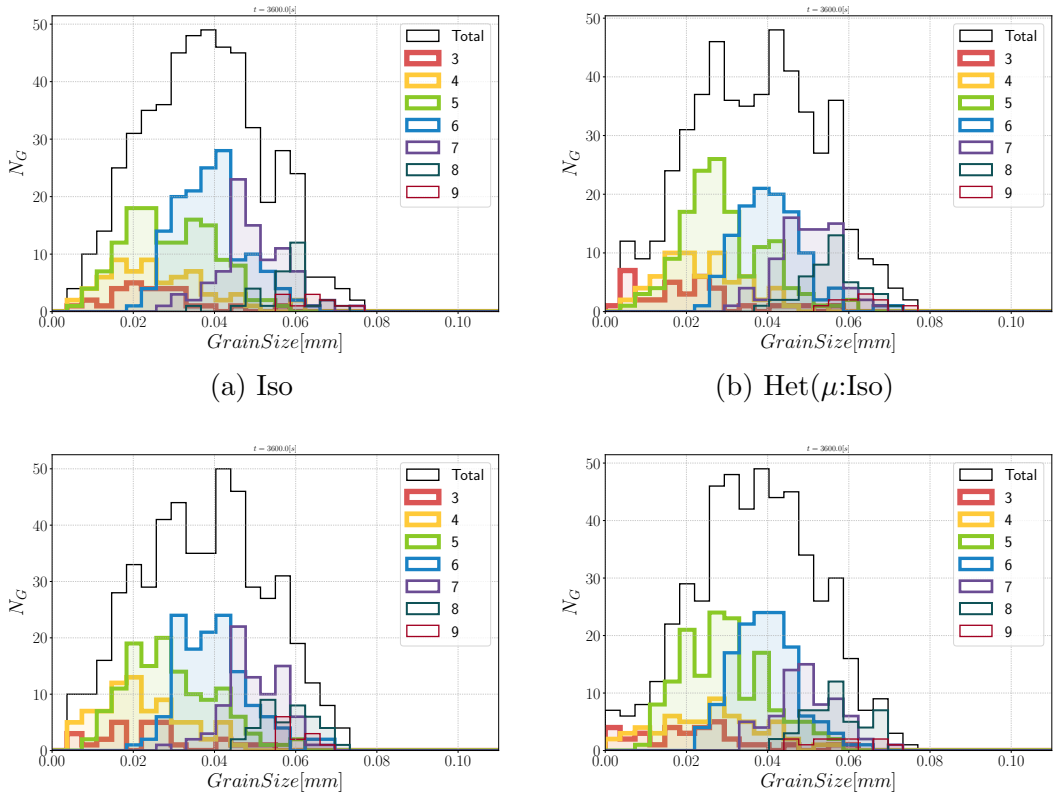

(a) Iso

(b) Het(μ:Iso)

(c) HetGrad(μ:Iso)

(d) Aniso(μ:Iso)

Figure 3.25: Grain size distribution and contributions from every group of grains with coordinance from 3 to 9 at $t = 1h$.

The slow evolution of the mean values has been reported as a consequence of little local heterogeneity produced by a Mackenzie-like DDF and/or a low value of θ_0 [30, 185, 196, 197]. If the DDF starts as a Mackenzie distribution, the value

of GB mobility and energy is focused at higher values, thus the microstructure cannot easily find a path to minimize its energy faster and the DDF changes slightly from its initial Mackenzie form. In other words, the initial configuration is almost isotropic. Slight differences can be observed after $t = 1$ h for the different formulations, which may be due to the low final number of grains ($N_G \approx 500$).

Regarding the morphology of the microstructures at $t = 1$ h, the grains are equiaxed. If we divide the total group of grains in classes divided by the number of neighbors (defined as the coordination number in the following), n, an interesting analysis regarding the morphology of grains could be performed. In Figure 3.25, the contribution of every class is depicted, and at $t = 0$ s, most of the grains verify $n = 5$. After one hour, one can directly appreciate that the class with $n = 6$ is the main class using the four formulations. This agrees with theoretical predictions of grain boundary motion with isotropic GB energy, which promotes triple junctions with dihedral angles near 120° [172]. This aspect again illustrates the limited impact of the considered anisotropy in this configuration.

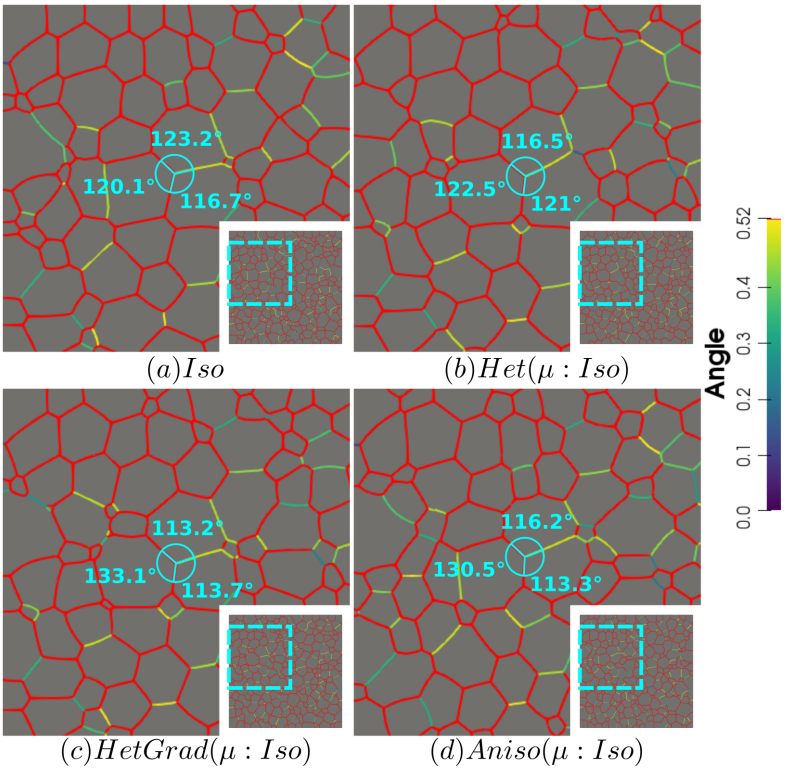

Figure 3.26: Disorientation of the boundaries using the four formulations with homogeneous grain boundary mobility at $t = 2h$, boundaries with a disorientation higher than 30° are colored in red. The triple junction presented with the dihedral angles is present during the whole simulation.

Heterogeneous grain boundary energy and mobility

In this section both GB energy and mobility are heterogeneous, respectively defined with Equations 3.14 and 3.15, for that reason the names introduced above are replaced by "Het(μ:S)", "HetGrad(μ:S)" and "Aniso(μ:S)". In order to compare the results presented above, the same initial microstructure and crystallographic orientations are used. The mean values evolution and distributions remain similar among the four formulations and keep similar values as presented before. The heterogeneous GB mobility may affect the morphology of the microstructure, due to a retarding effect from GBs with disorientation lower than θ_0. There is a resemblance between the four microstructures shown in Figure 3.27 showing mostly equiaxed grains. Two important aspects of these microstructures are that the microstructure obtained by the "Het" formulation is the most dissimilar with a lower number of GBs with disorientation inferior to θ_0. Second, the presence of low angle GBs ($\theta < 30°$) looks higher using the Anisotropic formulation. Nevertheless, this is not reflected in the interfacial energy nor the DDF (see Figure 3.28). Regarding the microstructure obtained with the Anisotropic formulation, the blue GBs with less than 12° looks like a sub-grain structure, this kind of structure has been found in other works using Phase Field formulations [8].

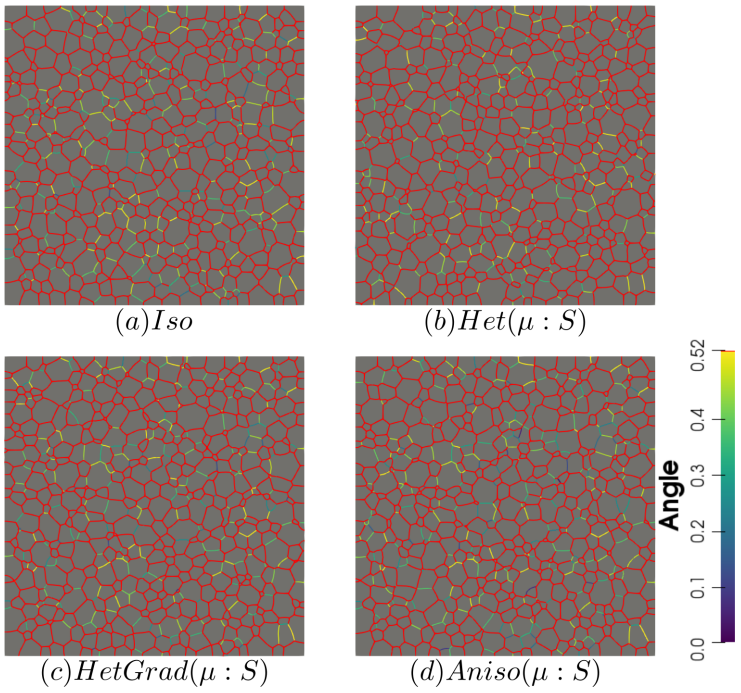

Figure 3.27: Disorientation of the boundaries using the four formulations with heterogeneous grain boundary mobility at $t = 1h$, boundaries with a disorientation higher than 30° are colored in red.

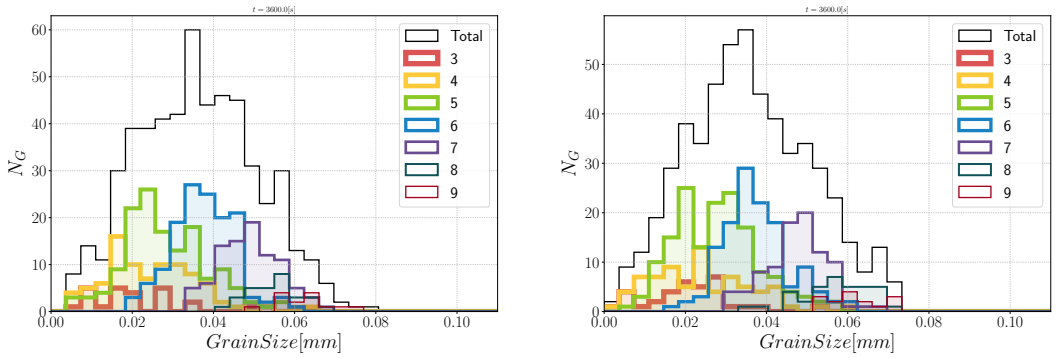

(a) HetGrad(μ:S) (b) Aniso(μ:S)

Figure 3.28: Grain size distribution and contributions from every group of grains with coordinance from 3 to 9 at $t = 1h$.

Finally, Figure 3.29 shows the disorientation distribution function using both an isotropic and heterogeneous mobility at $t = 1h$. As said before, the initial Mackenzie-type distribution evolves slowly, a slow preference of low angles GBs is found. Using heterogeneous mobility affect slightly the DDF, one can see that the Anisotropic formulation (Aniso(μ:S)) exacerbates low values of disorientation reflected in higher values in the distribution at $0 < \theta < 10°$. Due to the Mackenzie like DDF, the GB energy distribution is concentrated around γ_{max}, i.e, the level of anisotropy ($R = \gamma_{max}/\gamma_{min}$) is $R = 1$ leading to microstructures with triple junctions angles around 120° (see Figure 3.27), these results are in accordance with prior works [172, 196, 198].

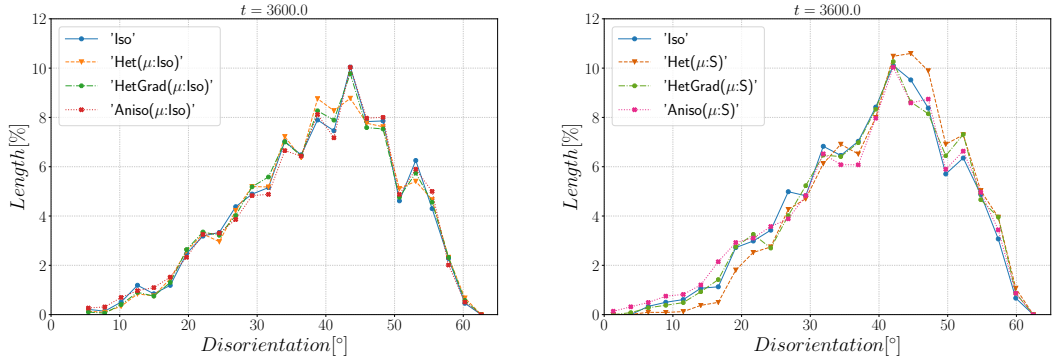

(a) μ isotropic (b) μ sigmoidal

Figure 3.29: Disorientation distribution function at $t = 1h$ using an isotropic (a) and a heterogeneous (b) mobility.

At this point one can see that for a non-texture material with an initial Mackenzie-like DDF the GB energy and mobility is similar to an Isotropic case. That is the fundamental reason of little difference among the formulations using

isotropic or heterogeneous GB mobility. The results exhibit similar evolution of mean values, distributions and morphology. In order to study the behavior of the different formulations for a wider spectrum of GB properties, the next section is devoted to study the effect of the texture using the four formulations with isotropic and heterogeneous GB mobility.

3.3.2 Effect of the texture

Here, the crystallographic orientations are defined differently: one Euler angle is generated randomly with a uniform distribution function and the two others are constants. As a result, the final disorientation distribution is more uniform, as seen in Figure 3.30. Properties are defined using Equations 3.14 and 3.15, and the transition disorientation angle is set to 30°, as previously used. The main effect of the wider resulting GBED is the increase of local anisotropy at triple junctions, as illustrated in Figure 3.30, compared to the previous test case (Mackenzie-like DDF).

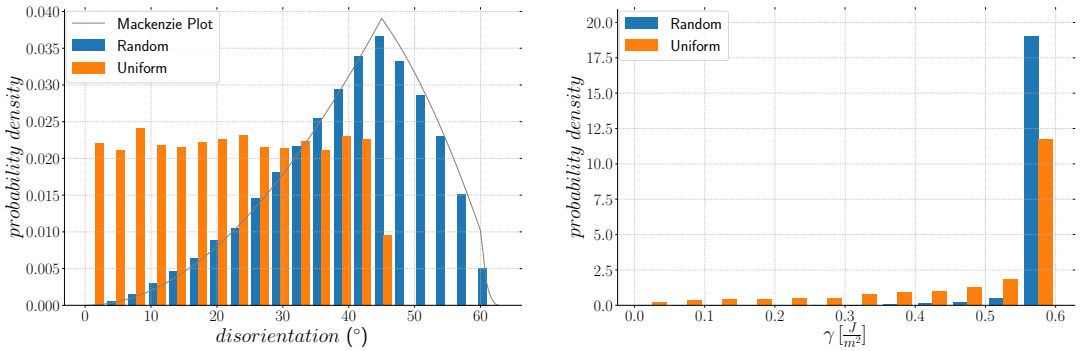

Figure 3.30: Comparison of GB distribution properties, (a) DDf and (b) GBED.

Heterogeneous grain boundary energy

The results described in Figure 3.31 illustrate that the Iso formulation predicts the fastest evolution. Additionally, one can see that the interfacial energy is better minimized using the Aniso formulation. From these results, one can infer that the isotropic formulation seems not adapted in this context. For a wider range of anisotropy levels, such as the one used in this test case, a particular coordination number with $n = 4, 5$ may be more present [172, 198]. However, the Iso formulation promotes equiaxed grains ($n = 6$). Once again, this tendency discredits the Isotropic approach for highly heterogeneous interfaces.

Regarding both heterogeneous formulations (Het and HetGrad), the evolution of mean values and distributions are similar, as illustrated in Figures 3.31 and 3.32. First, both predicted distributions have similar groups, with $n = 4, 5, 6$, and second, the predicted microstructures show mostly equiaxed grain with a similar distribution of GB disorientation. In Figure 3.33, one can see similar clusters of

GBs, with high values of disorientation depicted in red. From the morphology of GBs (Figure 3.33), the formulation that respects the most, on average, the triple junction angles is the Anisotropic one. This is illustrated in Figure 3.34, where the dihedral angles of a triple junction formed by GBs with low and high disorientation angles are shown. For this particular example, in Figure 3.34, blue and red boundaries have values of γ of about $0.25 \times 10^{-7} J \cdot mm^{-2}$ and $6 \times 10^{-7} J \cdot mm^{-2}$, respectively. One can estimate an approximated value of the dihedral angle opposite the blue interface using Equation 3.10, which is about 177°, with $r = 6/0.25 = 24$. The results described in Figures 3.31 and 3.35 show that while promoting a slower evolution of the microstructure, the Aniso (μ:Iso) formulation exhibits a better behaviour concerning the decreasing GB energy.

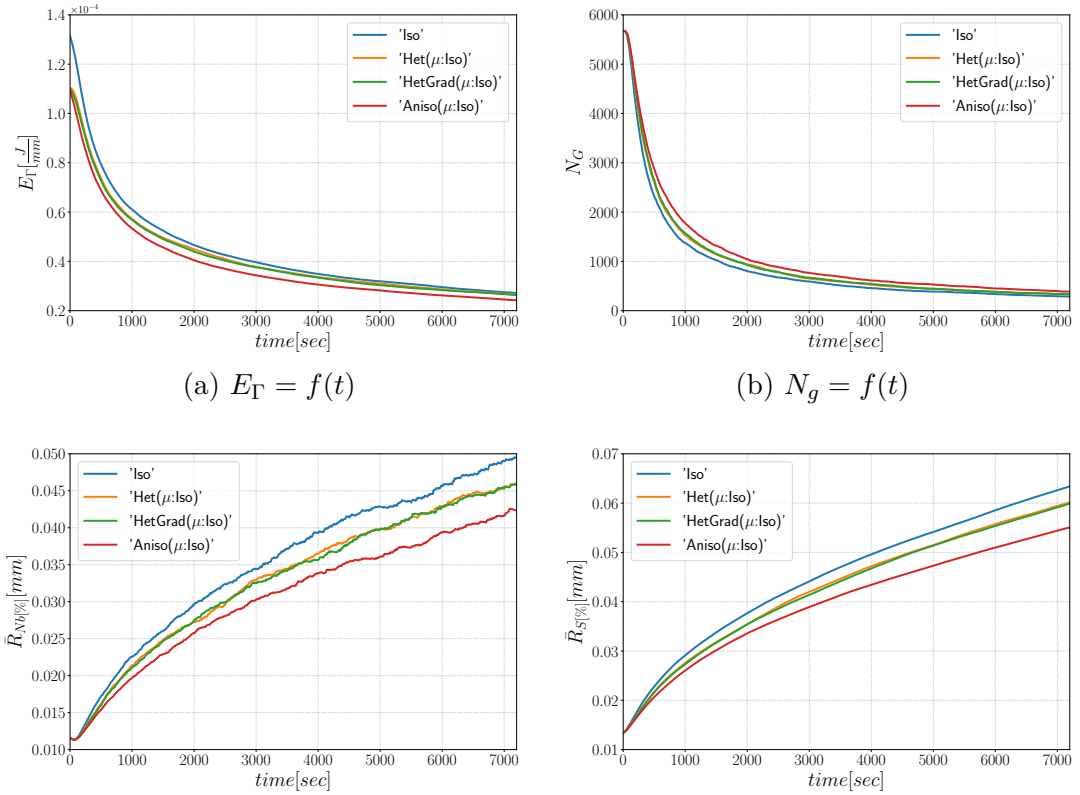

(a) $E_\Gamma = f(t)$ (b) $N_g = f(t)$

(c) $\bar{R}_{Nb[\%]} = f(t)$ (d) $\bar{R}_{S[\%]} = f(t)$

Figure 3.31: Mean values time evolution for the different formulations.

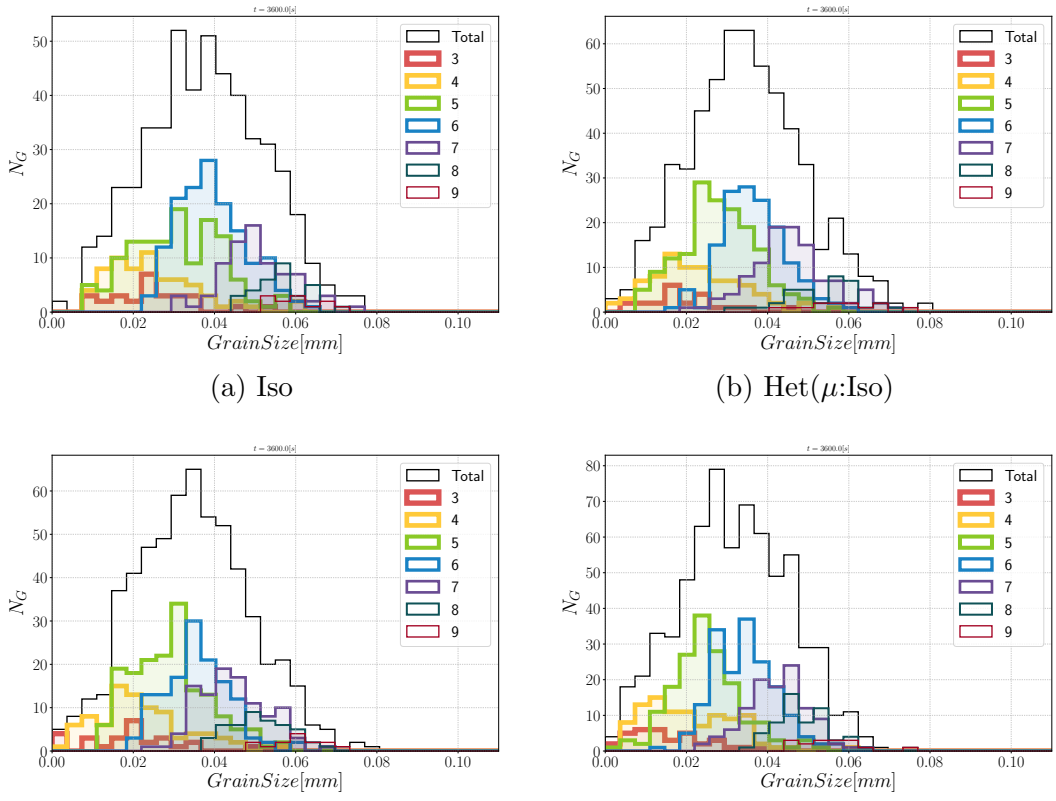

(a) Iso (b) Het(μ:Iso)

(c) HetGrad(μ:Iso) (d) Aniso(μ:Iso)

Figure 3.32: Equivalent radius distribution and contribution from every group of grains with coordinance from 3 to 9 at $t = 1h$.

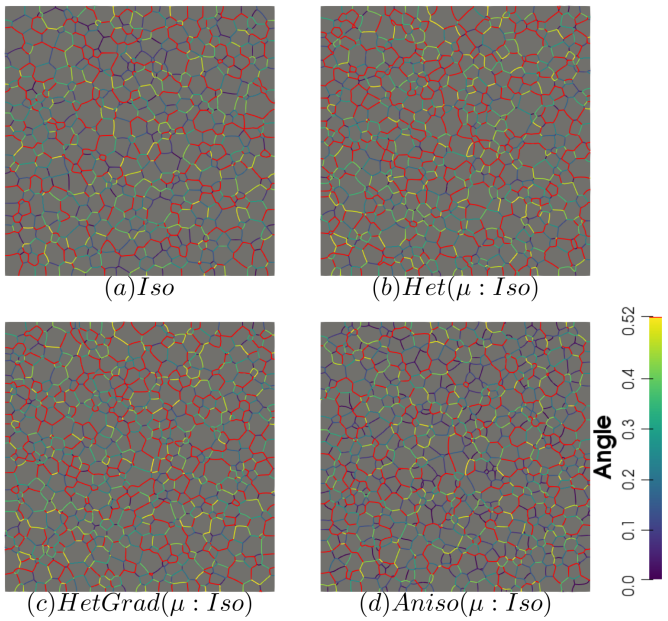

Figure 3.33: Disorientation of the boundaries using the four formulations with homogeneous grain boundary mobility at $t = 1h$, boundaries with a disorientation higher than 30° are colored in red.

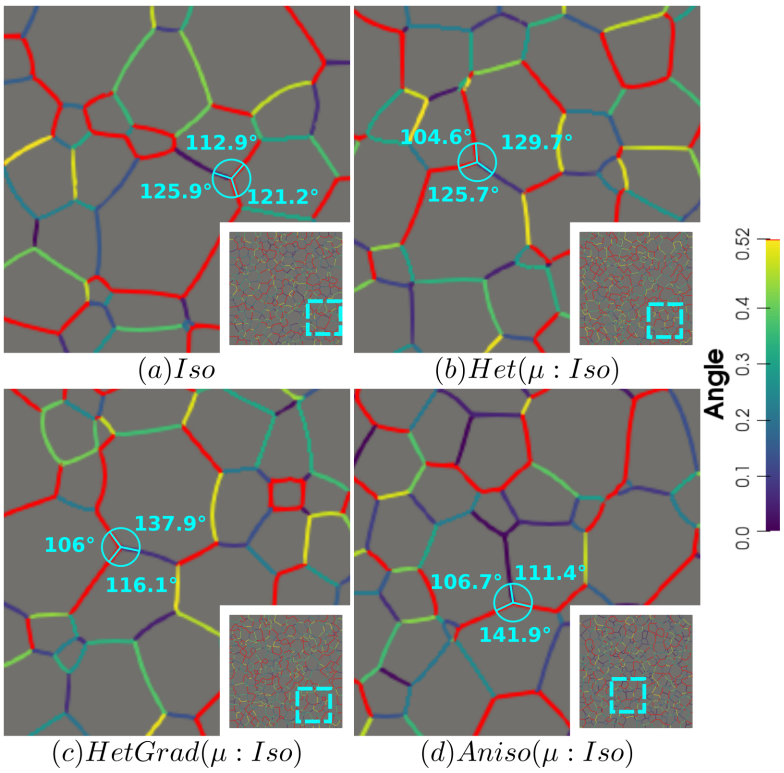

Figure 3.34: TJ dihedral angles among boundaries with high (red) and low (blue) GB energy. The disorientation of the boundaries is also depicted for the four formulations and homogeneous grain boundary mobility at $t = 2h$. Boundaries with a disorientation higher than 30° are colored in red.

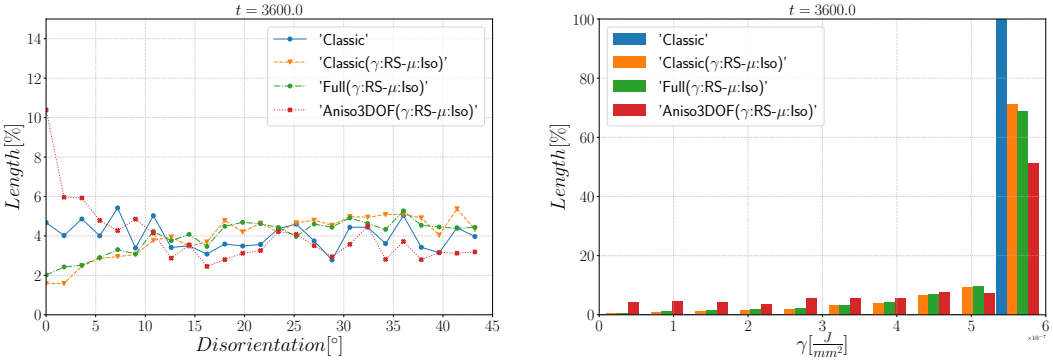

(a) Distribution of θ (b) Distribution of γ

Figure 3.35: Grain boundary characteristics distributions at $t = 1h$.

Heterogeneous grain boundary energy and mobility

If heterogeneous GB mobility is added, the evolution of the microstructures can vary significantly. The results presented in Figure 3.36 show two regimes for the

Het(μ:S) formulation. First, one can infer that the Het formulation have issues to reduce the interfacial energy and presents a peak which is the result of an evolution dominated by curvature flow without any effect of the heterogeneity. If we compare the results shown in Figures 3.31 and 3.36, one can see the retarding effect of using a heterogeneous GB mobility. This effect is more stronger on the HetGrad and Anisotropic formulations due to the gradients introduced by heterogeneous fields and is completely natural because technically the diffusivity is the scalar product $\gamma\mu$, so the effect of the crystallography is taken into account twice. Thus, the Isotropic case evolves faster than the other formulations.

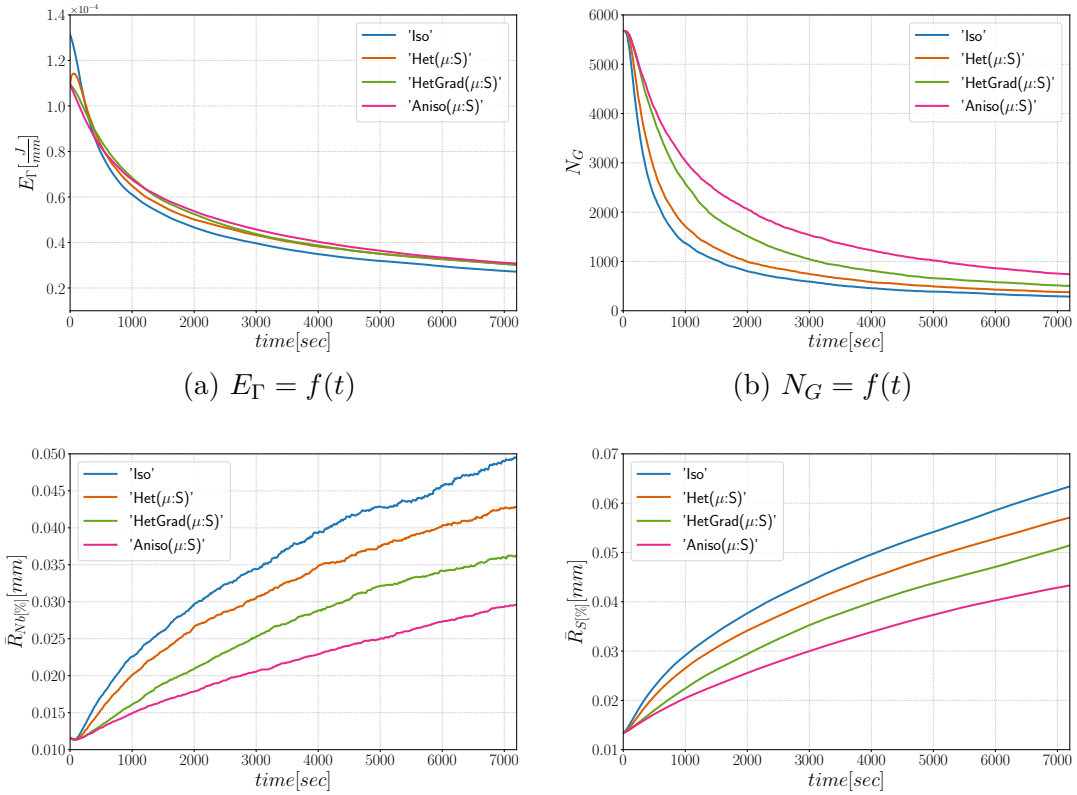

(a) $E_\Gamma = f(t)$ (b) $N_G = f(t)$

(c) $\bar{R}_{Nb[\%]} = f(t)$ (d) $\bar{R}_{S[\%]} = f(t)$

Figure 3.36: Mean values time evolution for the different formulations.

The results presented in Figure 3.37 and Figure 3.38 show that using the Het and HetGrad formulations the microstructure has more grains within the classes $n = 4$ and $n = 7$. On the other hand, the Anisotropic case didn't evolve enough to compare it to the other cases, one can see that the number of grains is around twice the number of grains of the other cases.

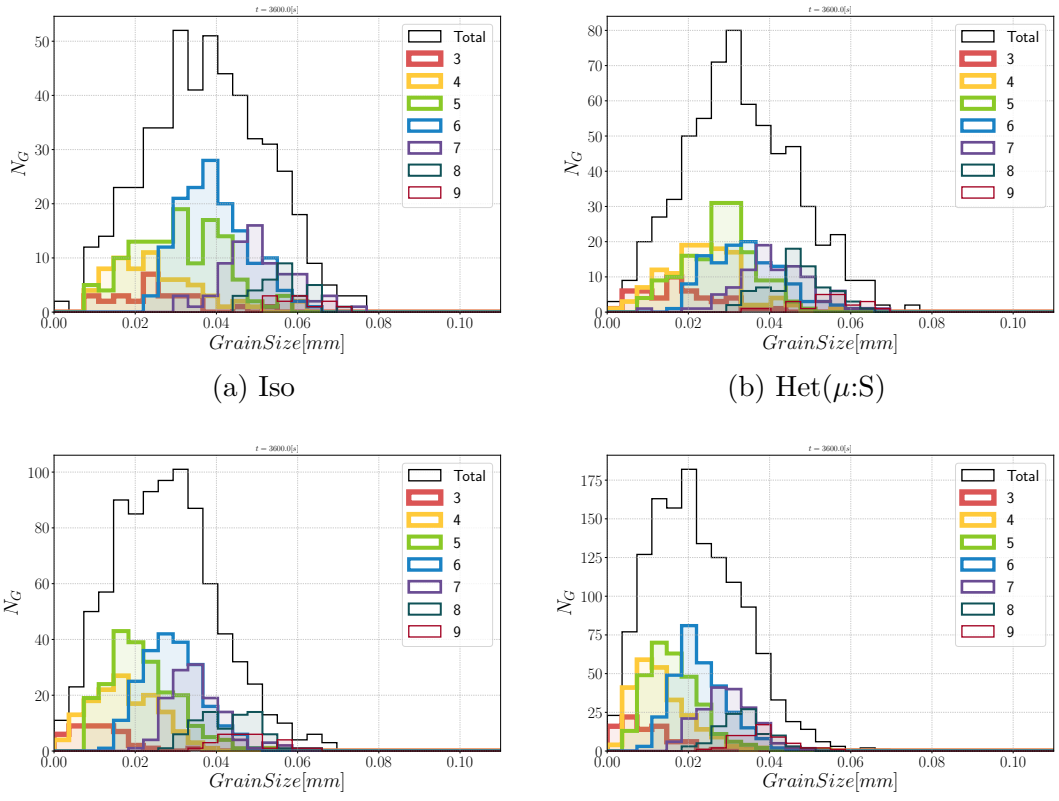

(a) Iso (b) Het(μ:S)

(c) HetGrad(μ:S) (d) Aniso(μ:S)

Figure 3.37: Equivalent radius distribution and contribution from every group of grains with coordinance from 3 to 9 at $t = 1h$.

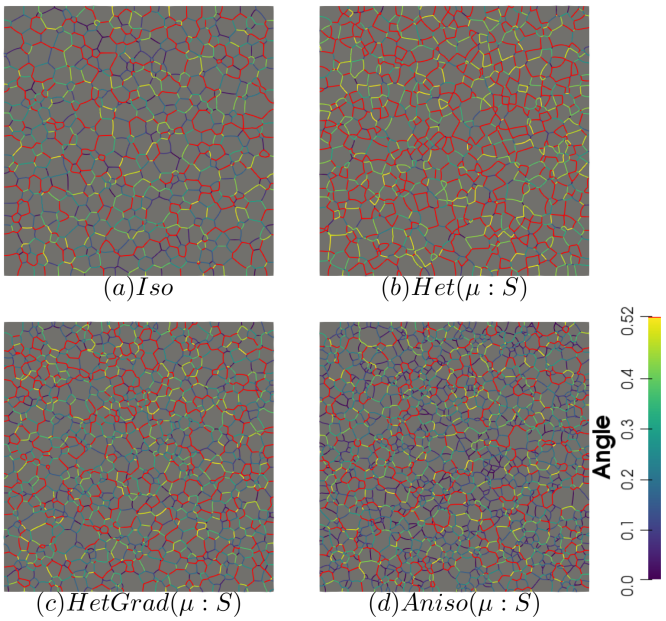

$(a) Iso$ $(b) Het(\mu : S)$

$(c) HetGrad(\mu : S)$ $(d) Aniso(\mu : S)$

Figure 3.38: Disorientation of the boundaries using the four formulations with heterogeneous grain boundary mobility at $t = 1h$, boundaries with a disorientation higher than 30° are colored in red.

Interestingly, the DDF of the Het formulation disagrees with the results presented in [185]. Here, the evolution of the DDF evolves in the opposite way to the expected results (see Figure 3.39). Indeed, the DDF tends to increase the percentage of interfaces with $\theta > \theta_0$ and decrease those with $\theta < \theta_0$, which clearly seems nonphysical. Moreover, the Iso and HetGrad formulations do not exacerbate a particular disorientation. Finally, the Anisotropic formulation seems to exhibit a more physical behavior by promoting a higher percentage of GBs with lower values of disorientation.

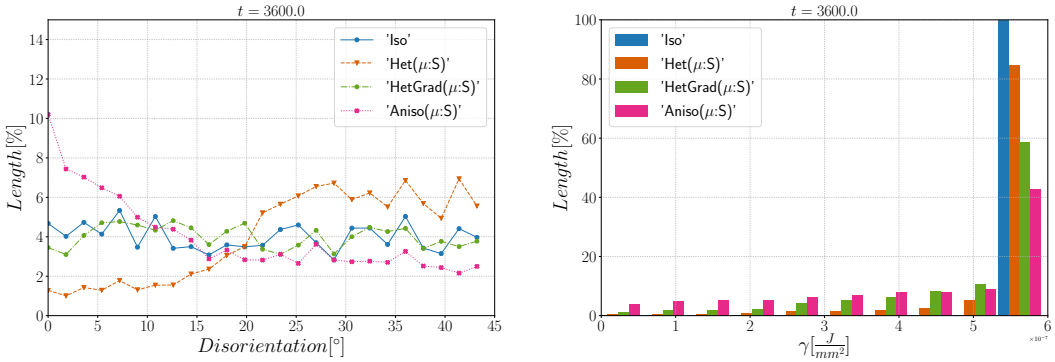

(a) Distribution of θ (b) Distribution of γ

Figure 3.39: Grain boundary characteristics distributions at $t = 1h$.

3.3.3 CPU Time

All the simulations presented here were performed on 20 cores with the same mesh size, $h_n = 1\mu m$ at the normal direction of the interface and $h_t = 5\mu m$ in the tangential direction of the interface and far from the interface. As expressed before, both heterogeneous formulations and the anisotropic formulation have additional terms which can be synonymous of more complex resolution. This aspect if not significant when moderated anisotropy is considered as illustrated by the first line of Table 3.1.

However, the CPU-Time changes importantly for the textured case presented above. The HetGrad and Aniso formulations take 2 and 4 additional hours, respectively, in comparison to the Isotropic formulation.

Table 3.1: CPU time in hours of the four formulations with heterogeneous GB energy and mobility.

Case	Iso	Het	HetGrad	Aniso
Random	5.4	5.5	5.5	5.6
Textured	5.4	5.5	7.3	9.4

3.4 Accounting for Misorientation and Inclination Dependence

The formulations presented above have dealt with heterogeneous GB properties. However, we know that the nature of the GB is described in a 5D space generated by the inclination and the misorientation. The effect of the normal direction has been described by Herring in [191] as a torque term. Hence, a triple junction should respect a condition frequently known as Herring's equation, i.e. Equation 3.7.

Due to the high dimensional space of GBs, many researchers have attempted to propose metrics that properly represent symmetries [115–121]. With these metrics, one can compare and compute the shortest paths (geodesics) between GBs. As the misorientation and the normal orientation and misorientation can change during the microstructure evolution due to grain rotation or grain disappearance/appearance, the evolution of the metric could reveal important information about the microstructure–property relationship. Recent works by Chesser et al. [199] and Francis et al. [200] have proposed new metrics using octonions, revealing good predictions of GB energy of the data published by Olmsted in [33].

To the authors' knowledge, the effect of the GB normal orientation is not clear, and more experimental, numerical, and theoretical works are needed. Here, we define the effect of the normal orientation using a model of GB energy proposed for fcc metals by Bulatov et al. [34] and available in the GB5DOF code. When γ is defined using the GB5DOF code, both the effect of the misorientation and inclination are taken into account using the crystallographic orientations of the two adjacent grains and the local coordinate system of the corresponding GB [34].

3.4.1 Triple Junction

This case concerns again a triple junction, as described by Figure 3.40. We performed simulations with a constant GB mobility set to $\mu = 1 \times 10^6\ mm^4 \cdot J^{-1} \cdot s^{-1}$, taken from [201], a domain of 1×1 mm^2, and a time step of $\Delta t = 5 \times 10^{-5}\ s$. The Aniso formulation is used by considering γ as only initially defined by the misorientation ($\gamma(M)$) and then also dependent on the inclination (obtained through the GB5DOF code and denoted as Aniso-GB5DOF, i.e., $\gamma(M, \vec{n})$). The Iso, Het, and HetGrad are not presented here because they evolve in the wrong direction (the expected movement should reduce the length of the interface between grain G_1 and G_2, depicted in yellow). The evolution of the interfaces shown in Figure 3.41 presents similar tendencies to the cases presented by Garcke in [202] and Hallberg in [32]. If both evolutions (without or with the inclination dependence) seem to promote similar triple junction evolution, the Aniso-GB5DOF case exhibits a much faster evolution, which illustrates the importance of accounting for the inclination in the reduced mobility description.

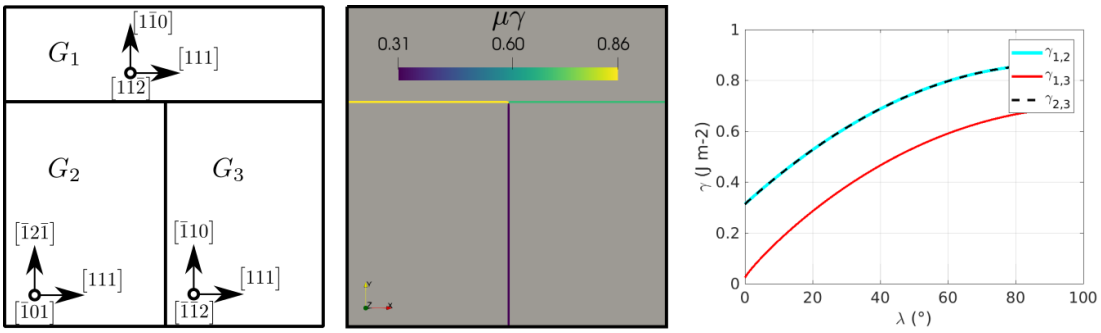

Figure 3.40: (**a**) Grain orientations, (**b**) initial reduced mobility [mm^2/s], (**c**) change of GB energy as a function of the GB inclination, λ, with respect to the x-axis, evaluated using the code GB5DOF [34].

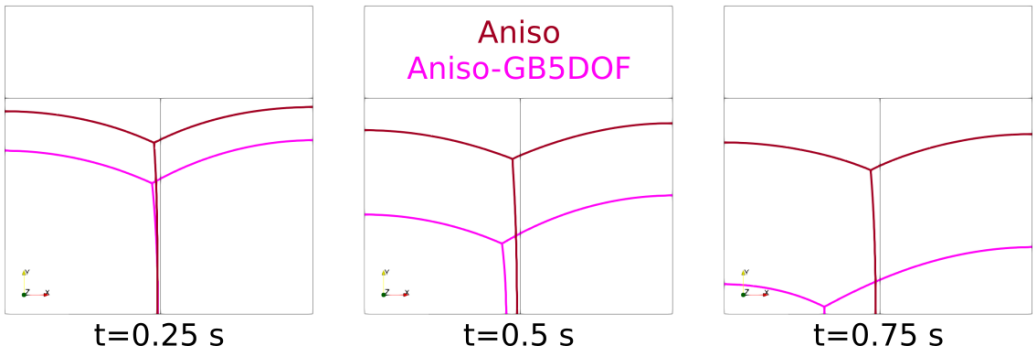

Figure 3.41: Interface evolution for three different times, $t = 0.25,\ 0.5,\ 0.75\ s$.

3.4.2 Coherent and Incoherent Twin Boundary

The main advantage of the GB5DOF code is that it is possible to characterize coherent and incoherent twin boundaries. These special GBs play an important role on polycrystalline microstructures, and their modeling is not frequently discussed at the mesoscopic scale. The next example was firstly proposed by Brown and Ghoniem in [203] and also reproduced at the mesoscopic scale in [32]. It consists of two grains composed of two coherent twin boundaries (CTB) and one incoherent boundary (ICB). Figure 3.42 shows the crystallographic orientation, the initial GB energy, and the variation of the GB energy as a function of the GB inclination. The Iso and Aniso formulations were used to model the GB movement. For the Aniso formulation, the GB5DOF code was used to compute the GB energy all along the simulation. On the other hand, the GB energy of the Iso case is constant and set to $\gamma = 0.65969\ J \cdot m^{-2}$. The evolution of the GB is shown in Figure 3.43. The time step was set to $\Delta t = 0.1\ ns$ and GB mobility was set to $\mu = 1.3 \times 10^7\ \mu m^4 \cdot J^{-1} \cdot ns^{-1}$ in order to reproduce the velocity of the ICB found by Brown and Ghoniem in [203], $v_{ICB} = 1.2\ m \cdot s^{-1}$. The movement

of the ICB should be uniform and it should respect the flatness of the CTB. The Aniso-GB5DOF simulation enables to respect the expected behavior.

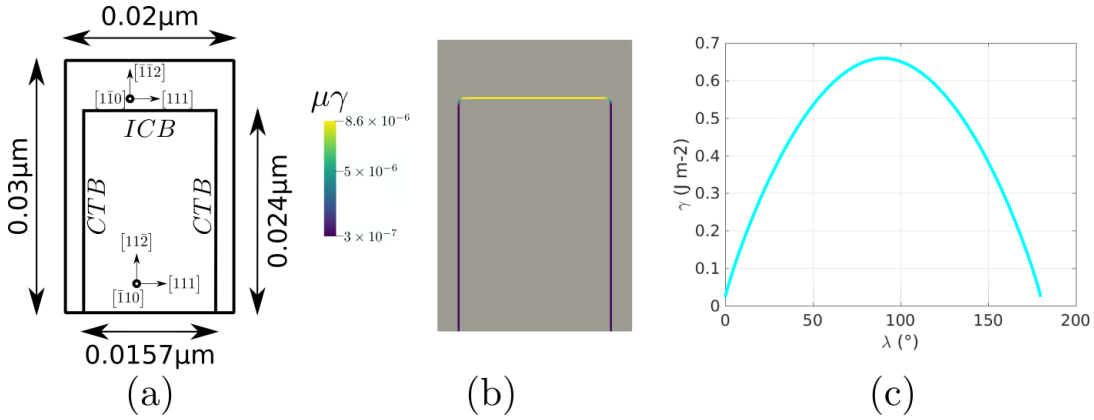

Figure 3.42: (**a**) Grain orientations, (**b**) initial reduced mobility [μ m^2/s], (**c**) change of GB energy as a function of the GB inclination, λ, with respect to the x-axis, evaluated using the GB5DOF code.

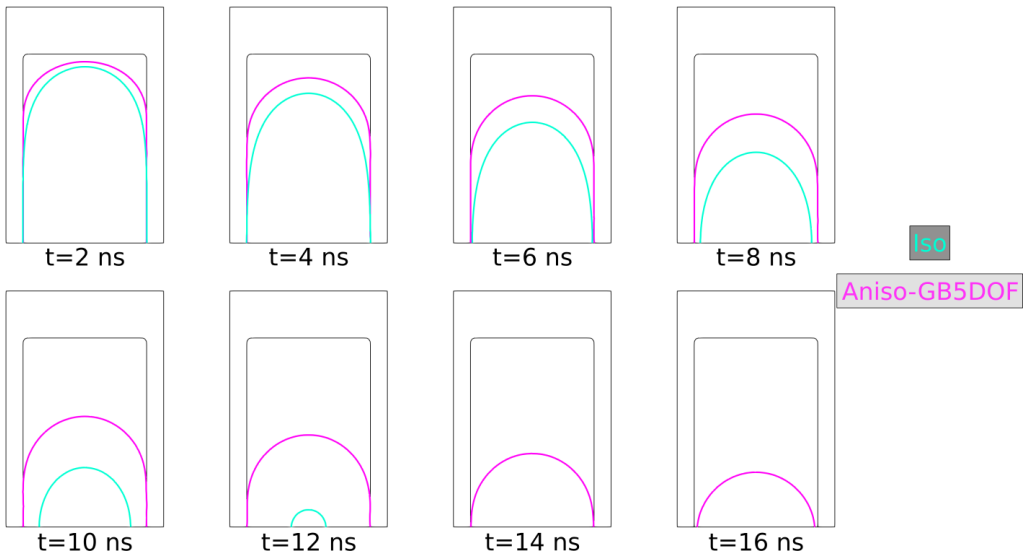

Figure 3.43: Interface evolution at different times, $t = \{2,\ 4,\ 6,\ 8,\ 10,\ 12,\ 14,\ 16\}$ ns.

3.5 Numerical implementation in 3D

2D simulations reveal important characteristics of the kinetics of microstructures. Nevertheless, more realistic microstructures need to be studied. To that end, 3D simulations are necessary because they reveal complex topological changes that are omitted in 2D simulations and in 3D, the inclination can be correctly

taken into account. In this section a 3D version of the Grim Reaper case and a polycrystalline case with 7100 initial grains are presented.

3.5.1 The Grim Reaper Case

The main difference with the 2D case is that the T junction is extruded and a boundary is added. This means that the two *triple lines* with an anisotropy level r are present. Figure 3.44 shows the initial configuration of the multiple junction. It is composed of 4 grains and 3 multiples lines from which two of them have a different value of r (colored in green). This example was proposed by Hallberg in [32] and remains dimensionless.

Dimensionless simulations are carried out using $\gamma_{top} = 1.0$, $\mu = 1.0$ and $r = \{10,\ 1.25,\ 0.55\}$. The $0.5 \times 0.5 \times 0.5$ domain is discretized with a non-structured static mesh with a size of $h = 0.01$. First, the evolution of the multiple junction with $r = 10$ is presented in Figure 3.45. Alike the 2D Grim Reaper case, the Het formulation is the fastest. The evolution of the triple junction obtained with the HetGrad formulation in 2D evolved in an opposite direction as it was expected for $r = 10$. Yet the 3D multiple junction evolves in the correct direction with a slight difference in the y-direction. Finally, the Aniso formulation evolves as expected. This simulation seems to be driven mostly by the curvature of the interfaces with a little effect of the gradients. Figure 3.46a shows the evolution of the interfaces

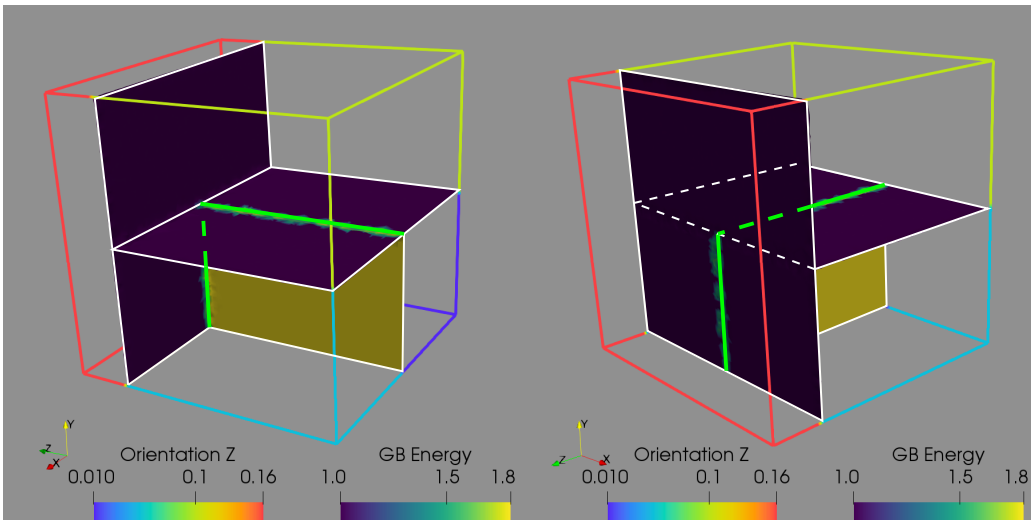

Figure 3.44: Multiple junction in 3D with two different points of view. The green lines depict the triple lines where the anisotropy level r is defined. The outline color corresponds to the z-Orientation of the grain.

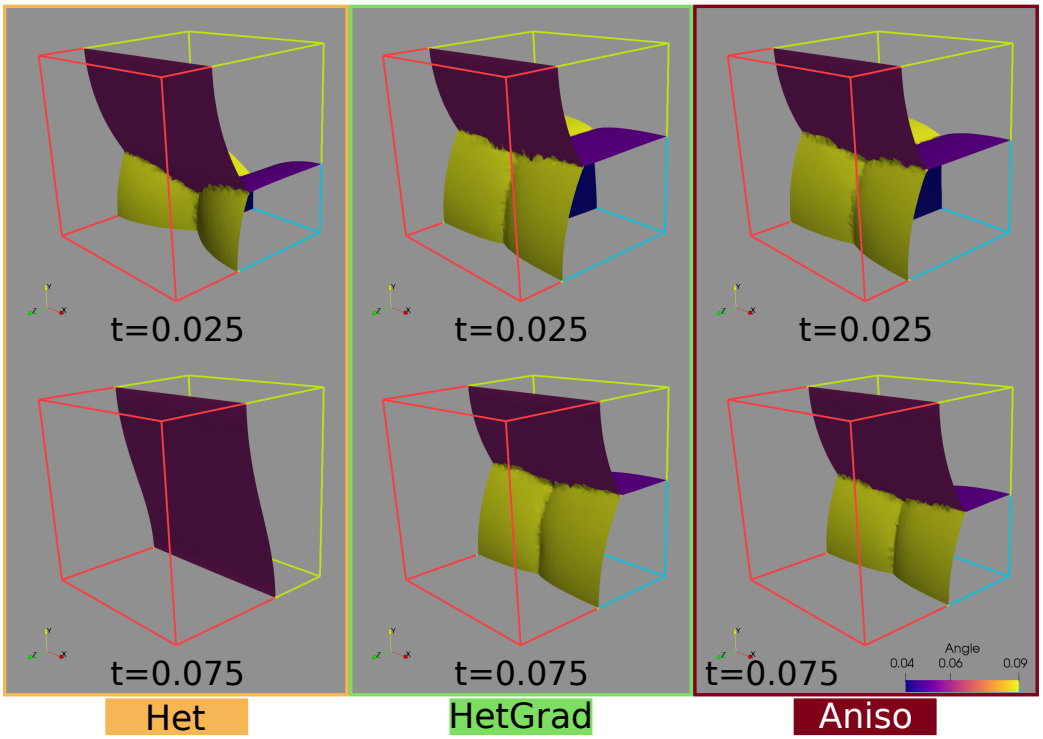

Figure 3.45: Multiple junction evolution in 3D, using the Het, Hetgrad and Aniso formulations with $r = 10$. The disorientation angles are shown for every interface at two different times $t = 0.025,\ 0.075$.

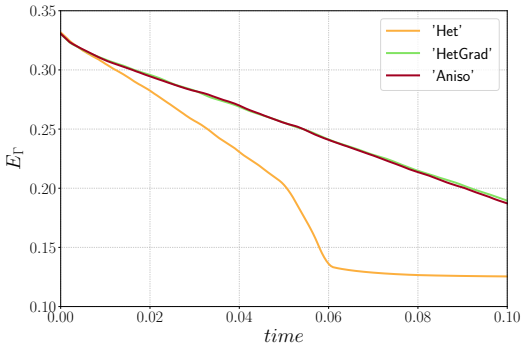

(a) $r = 10$

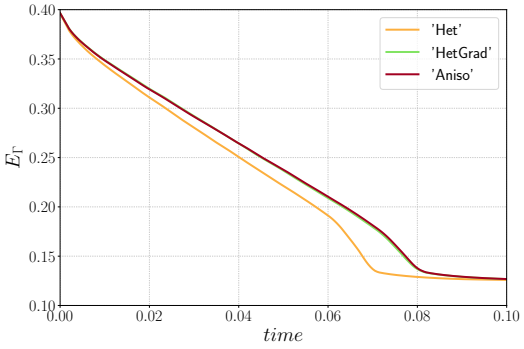

(b) $r = 1.25$

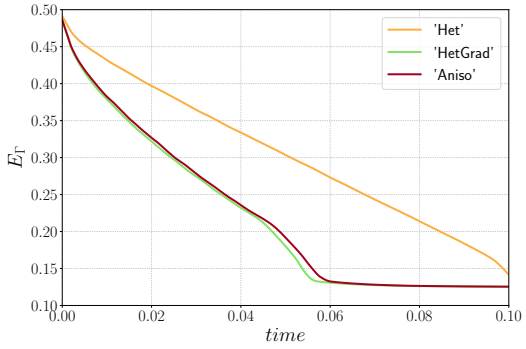

(c) $r = 0.55$

Figure 3.46: Time series of E_Γ using the three formulations with $a) r = 10$, $b) r = 1.25$ and $c) r = 0.55$.

3.5.2 Polycrystalline case with a strong texture

Figure 3.47 shows the initial microstructure employed to model 3D grain growth. The domain of size $0.1 \times 0.1 \times 0.1mm$ is discretized with a non-structured static mesh with a size of $h = 1\mu m$. The initial system consists of 7991 grains generated using a Laguerre-Voronoi tessellation [193] based on an optimized sphere packing algorithm [194] with a log-normal distribution for the arithmetic mean grain size ($\mu_{dist} = 0.003$ and $\sigma_{dist} = 0.0005$). The time step, maximal GB mobility, maximal GB energy and disorientation angle transition are set to $\Delta t = 10s$, $\mu_{max} = 1\ mm^4 \cdot J^{-1} \cdot s^{-1}$, $\gamma_{max} = 10^{-7}\ J \cdot mm^{-2}$ and $\theta_0 = 30°$. The orientation is generated as in Section 3.3.2: φ_2 is generated randomly using a uniform distribution and φ_1 and ϕ are constant.

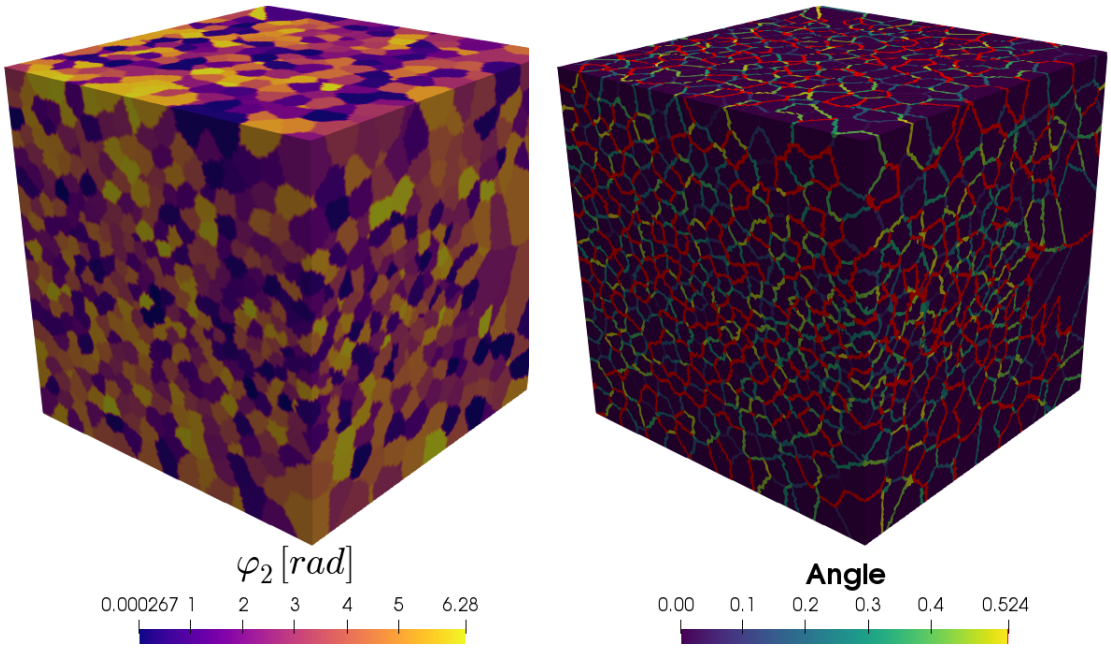

(a) Euler angle φ_2 (b) Disorientation angle

Figure 3.47: Initial microstructure characteristics. In (b) the red GBs have a disorientation angle higher than 30° (HAGBs).

Figure 3.48 shows the initial GB distributions, as exposed in the 2D cases, a DDF with a wider domain of disorientation produces a GBED with a bigger variation of GB energy and higher levels of anisotropy. The initial DDF is not as uniform as the one generated for the 2D case, see Figure 3.30, but the level of anisotropy is enough to expect different responses of the FE-LS formulations.

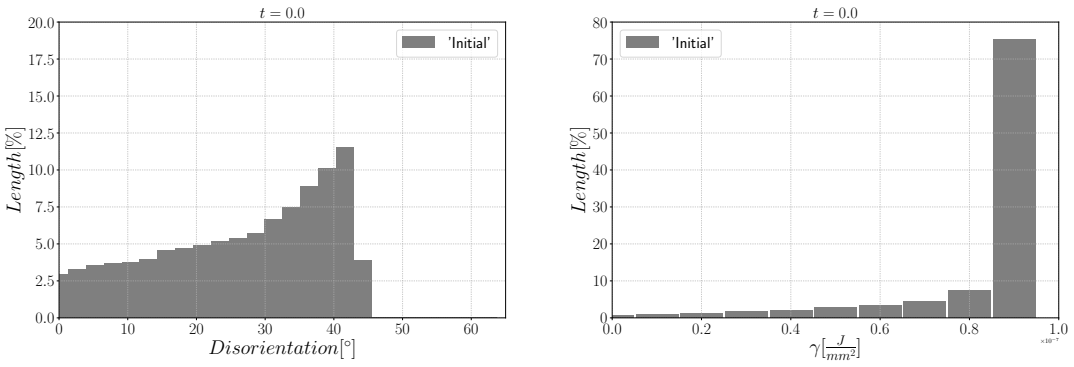

(a) Distribution of θ (b) Distribution of γ

Figure 3.48: Initial grain boundary characteristic distributions.

Heterogeneous grain boundary energy

The results described in Figure 3.49 are coherent to those exposed in the 2D case. First, the Iso formulation produces a faster evolution of the microstructure. Second, the interfacial energy is better minimized by the Anisotropic formulation. From Figures 3.50 and 3.51, one can see that the Anisotropic formulation allows the decreasing of the interfacial energy thanks to the creation and promotion of LAGBs colored in blue in Figure 3.51.

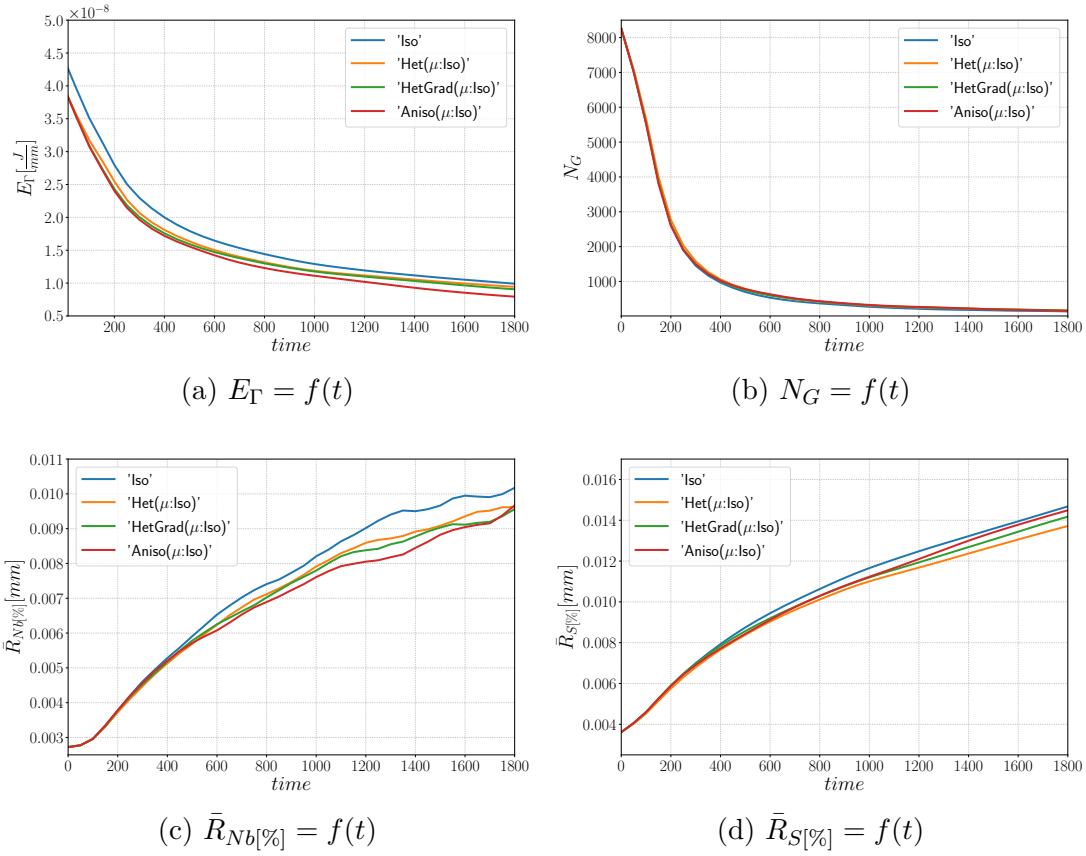

(a) $E_\Gamma = f(t)$ (b) $N_G = f(t)$

(c) $\bar{R}_{Nb[\%]} = f(t)$ (d) $\bar{R}_{S[\%]} = f(t)$

Figure 3.49: Mean values time evolution for the different formulations in 3D.

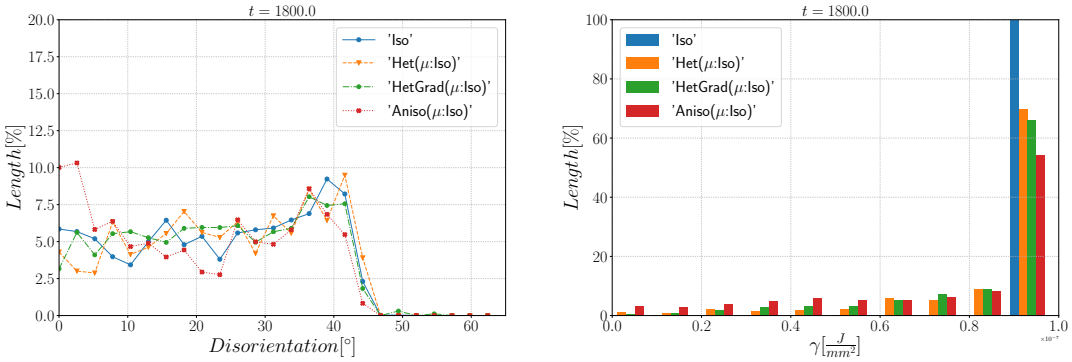

(a) Distribution of θ (b) Distribution of γ

Figure 3.50: Grain boundary characteristics distributions at $t = 30min$.

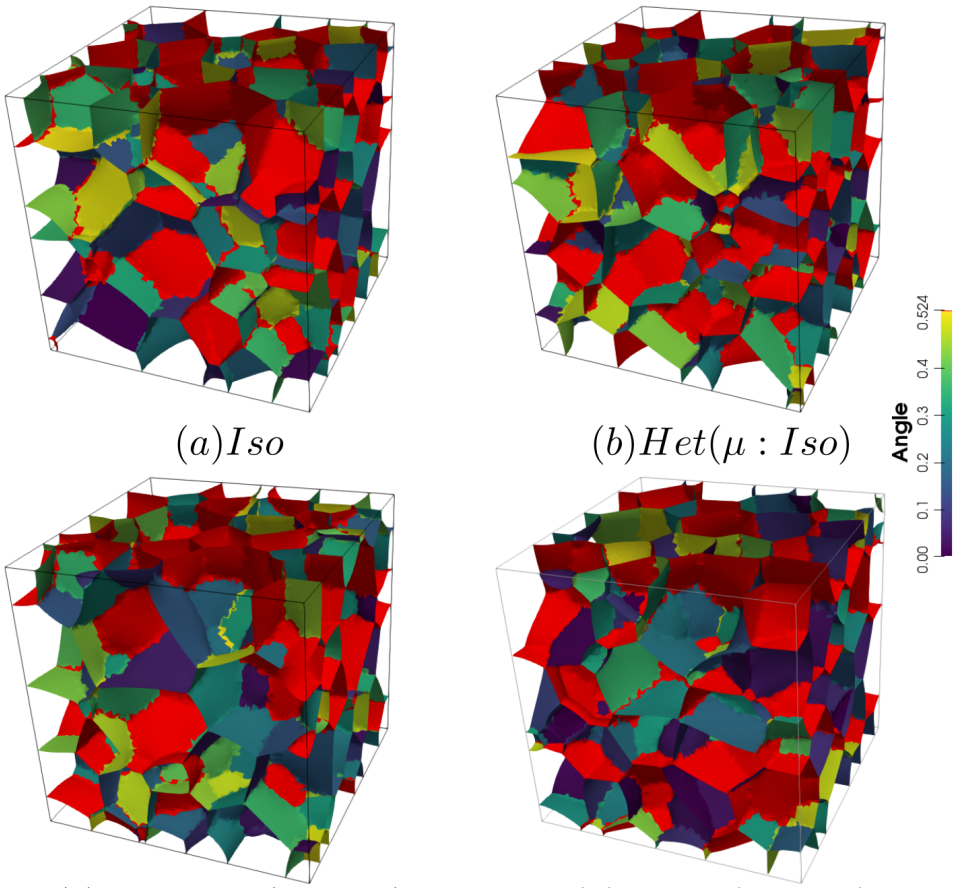

$(a) Iso$ $(b) Het(\mu : Iso)$

$(c) HetGrad(\mu : Iso)$ $(d) Aniso(\mu : Iso)$

Figure 3.51: Disorientation of the boundaries using the four formulations with isotropic grain boundary mobility at $t = 30min$, boundaries with a disorientation higher than 30° are colored in red.

Heterogeneous grain boundary energy and mobility

If the heterogeneity of GB mobility is added, the evolution of the microstructures are drastically modified. From Figure 3.52 the evolution of the grain size and the number of grains one can notice the slow evolution of the Het, Hetgrad and Aniso formulations. Also, the evolution of the interfacial energy does not present the peak near $t = 0s$. Interestingly, the DDF and the GBED produced by the Aniso formulation are in accordance with prior work [38, 185]. In Figures 3.53 and 3.54, the GBs with low disorientation angle are preferred by the Aniso formulation while the Iso, Het and HetGrad formulations do not exacerbate any particular disorientation.

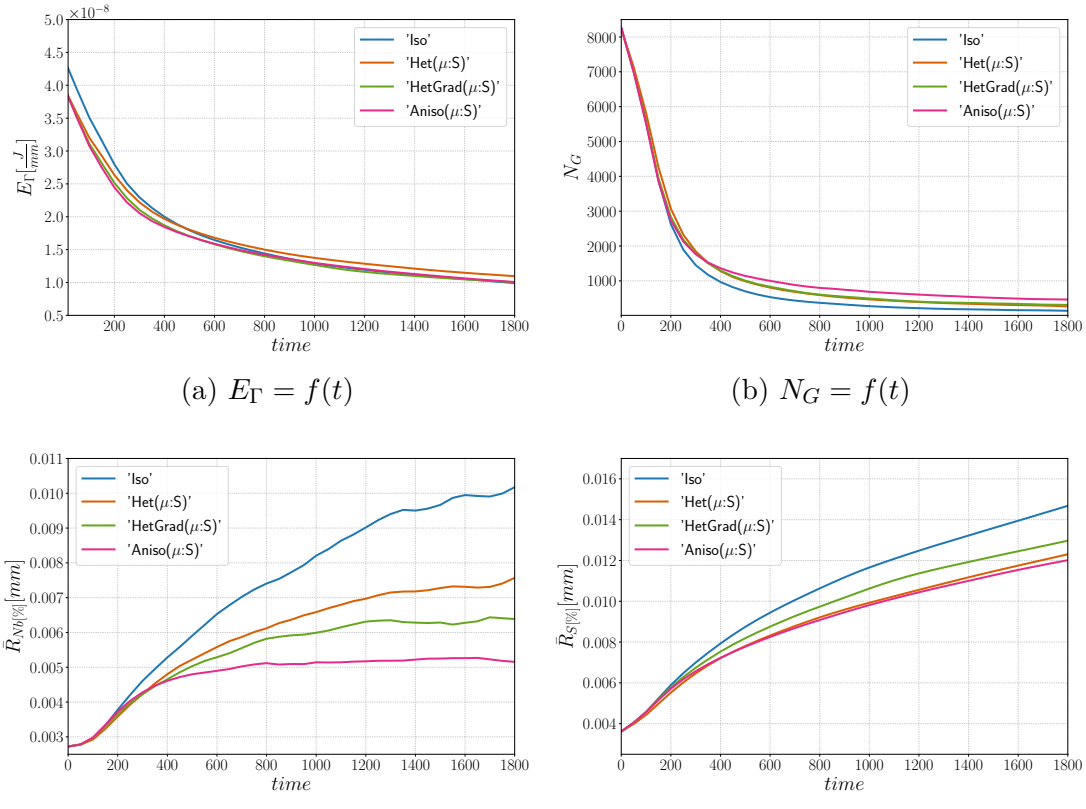

(a) $E_\Gamma = f(t)$ (b) $N_G = f(t)$

(c) $\bar{R}_{Nb[\%]} = f(t)$ (d) $\bar{R}_{S[\%]} = f(t)$

Figure 3.52: Mean values time evolution for the different formulations in 3D.

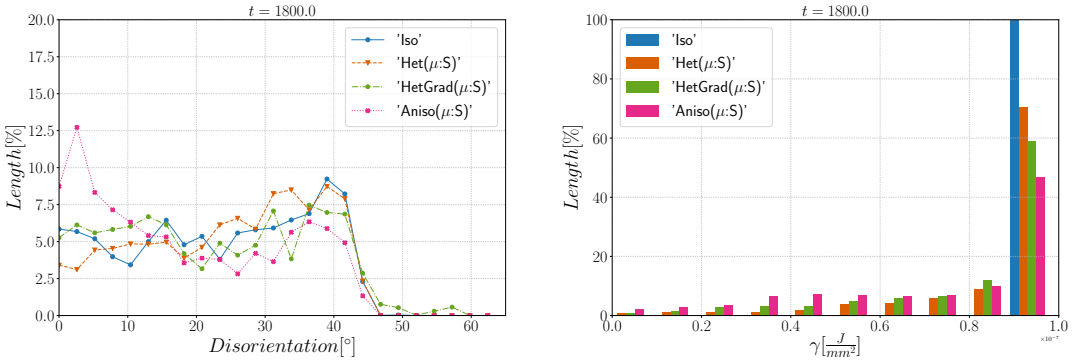

(a) Distribution of θ (b) Distribution of γ

Figure 3.53: Grain boundary characteristics distributions at $t = 30min$.

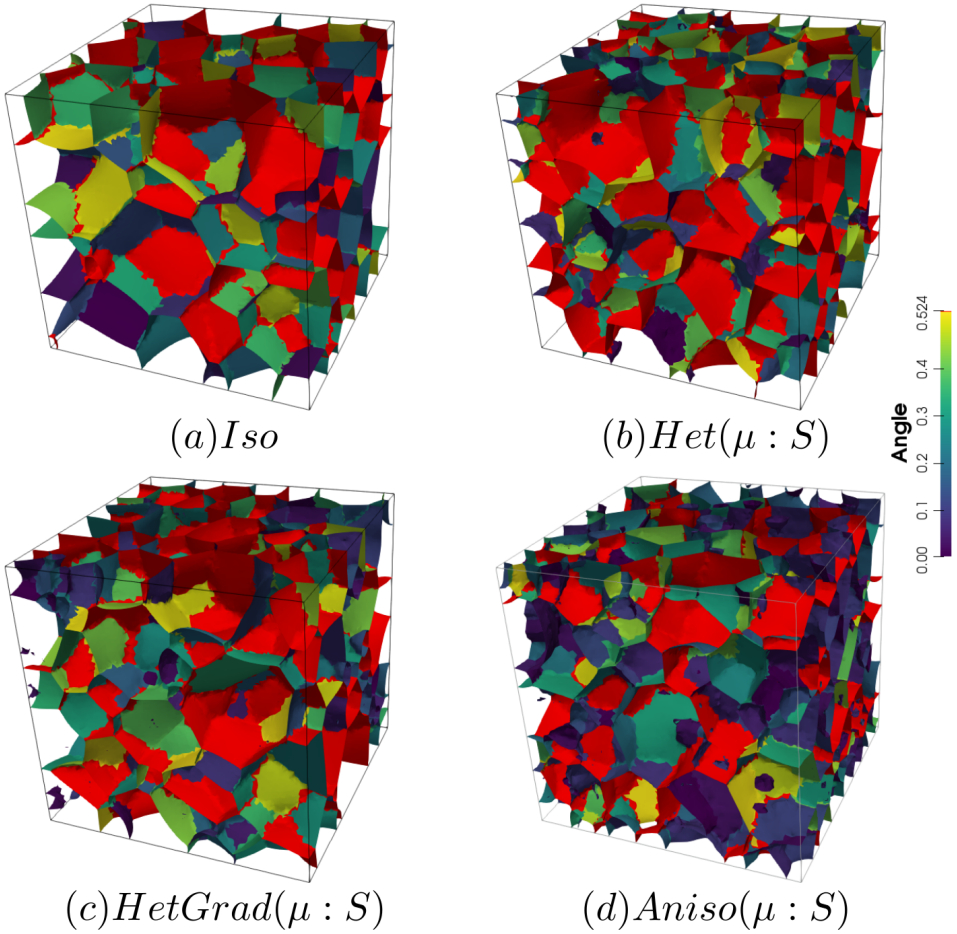

Figure 3.54: Disorientation of the boundaries using the four formulations with heterogeneous grain boundary mobility at $t = 30min$, boundaries with a disorientation higher than 30° are colored in red.

3.6 Conclusions

Different FE-LS formulations to simulate grain growth were presented and compared in this chapter. The isotropic formulation is able to reproduce mean grain size and grain size distribution evolutions when a moderated anisotropy is involved.

From the results presented using the triple junction cases, the Anisotropic formulation was the most accurate. The triple junction velocity predictions were the closest to the theoretical values while predicting accurate dihedral angles. In addition, the interfacial energy was always minimized and faster compared to the other approaches.

Additionally to these academic configurations, simulations using two different polycrystalline microstructures were performed. First, the initial orientations were generated using a uniform distribution, producing an initial Mackenzie-like disorientation distribution. Finally, another example with a textured orientation was considered. It was then illustrated that for a simple microstructure with initial random orientation, an isotropic formulation can be used, and that for a textured configuration, the Anisotropic formulation presents the best behavior in terms of grain morphology, DDF, and interfacial energy evolution predictions, while keeping a reasonable efficiency, compared to the isotropic formulation. The same results were obtained in 3D and the effect of the GB mobility looks to only modify the morphology of the grains.

The initial DDF and GBED are two important distributions that one has to analyze in order to choose a correct formulation. More importantly, the GBED and the GB energy values around multiple junctions are crucial to understand the anisotropic nature of microstructures. The next chapter is focused on the use of 2D experimental data of 316L stainless steel where different DDF are used. With the next results, we intend to validate the Anisotropic formulation as the best formulation to model anisotropic GG.

3.7 Résumé en Français du Chapitre 3

Ce chapitre s'est concentré sur la comparaison de quatre différentes formulations avec énergie et mobilité de joints de grain hétérogènes. Par ailleurs, l'ensemble des formalismes Éléments Finis hétérogènes ou anisotropes pour la description de γ ont été enrichis afin de pouvoir considerer une mobilité dependante de la désorientation.

Des cas académiques sur jonctions multiples ainsi que des cas plus réalistes sur polycristaux 2D et 3D sont considérés et discutés.

La formulation anisotrope présente les résultats physiques les plus réalistes mais il a également été montré que pour la prédiction de certains attributs et dans certaines configurations, la formulation isotrope pouvait être suffisante.

Chapter 4

Level-Set modeling of grain growth of 316L stainless steel using EBSD data.

In the previous chapter, academic triple junctions test cases and simplified polycrystalline microstructures were considered. The main conclusion was that the Isotropic formulation can reproduce mean values and distributions when the anisotropy level is moderated. However, when the anisotropy level increases, the Anisotropic formulation leads to more physical predictions in terms of grain morphology, global surface energy evolution and multiple junctions equilibrium. The goal of this chapter is to criticize the capacity of the Isotropic and Anisotropic formulations to model GG of a real material, 316L stainless steel, in terms of mean grain size, grain size distributions and mean GB properties. The effect of considering an initial microstructure using statistically representative Laguerre-Voronoï tessellation [193] or digital twin microstructures from EBSD data is compared. The effect of the GB energy definition is illustrated with two different frameworks: a 3-parameter one, well-known as the Read-Shockley formulation [69]; and a 5-parameter one using the the GB5DOF code proposed in [34]. The effect of the GB mobility description using an isotropic and a Sigmoidal model [77] is also discussed.

This chapter is organized as follows. First, in section 4.1, the FE-LS GB velocity formulations are presented briefly. The methodology to compute the GB reduced mobility from experimental data is presented in section 4.2. The results using the Isotropic and Anisotropic formulations are compared using statistically representative Laguerre-Voronoï tessellations (Section 4.3), immersed microstructures with heterogeneous GB properties (Section 4.4) and immersed microstructures with anisotropic GB energy using the GB5DOF code [34] (Section 4.5.1). Finally, a discussion about 3D uncertainties and their effect in the estimation of GB properties is presented.

This Chapter was partially submitted to publication in [204].

4.1 GB velocity formulation

The Isotropic and Anisotropic formulations were detailed in Section 3.1 but are briefly reminded in this section. The Isotropic formulation uses a homogeneous GB energy and mobility [18], the velocity field is thus defined as:

$$\vec{v} = -\mu\gamma\kappa\vec{n},$$

On the other hand, the Anisotropic formulation was developed using thermodynamics and differential geometry in [20, 175]. Both, the GB normal and misorientation are taken into account and an intrinsic torque term is present:

$$v = \mu(\theta)\left(\mathbb{P}\vec{\nabla}\gamma(M(\theta,\vec{a}),\vec{n})\cdot\vec{n} - \Gamma(M(\theta,\vec{a}),\vec{n}) : \mathbb{K}\right)\vec{n}.$$

In this study the torque term $\Gamma(M(\theta,\vec{a}),\vec{n}) = \vec{\nabla}_{\vec{n}}\vec{\nabla}_{\vec{n}}\gamma(M(\theta,\vec{a}),\vec{n}) + \gamma(M(\theta,\vec{a}),\vec{n})\mathbb{I}$ is neglected but the GB energy still depends on the GB misorientation and inclination, the kinetic equation could be simplified as:

$$v = \mu(\theta)(\mathbb{P}\vec{\nabla}\gamma(M(\theta,\vec{a}),\vec{n})\cdot\vec{n} - \gamma(M(\theta,\vec{a}),\vec{n})\kappa)\vec{n}.$$

The weak formulation of the Isotropic (Iso) and Anisotropic (Aniso) formulation are [38]

$$\int_\Omega \frac{\partial\phi}{\partial t}\varphi d\Omega + \int_\Omega \mu\gamma\vec{\nabla}\varphi\cdot\vec{\nabla}\phi d\Omega - \int_{\partial\Omega}\mu\gamma\varphi\vec{\nabla}\phi\cdot\vec{n}d(\partial\Omega) = 0,$$

and

$$\int_\Omega \frac{\partial\phi}{\partial t}\varphi d\Omega + \int_\Omega \mu(\theta)\gamma(M,n)\vec{\nabla}\varphi\cdot\vec{\nabla}\phi d\Omega - \int_{\partial\Omega}\mu(\theta)\gamma(M,n)\varphi\vec{\nabla}\phi\cdot\vec{n}d(\partial\Omega) + \int_\Omega \mu(\theta)(\mathbb{P}\cdot\vec{\nabla}\gamma(M,n) + \vec{\nabla}\gamma(M,n))\varphi\vec{\nabla}\phi d\Omega + \int_\Omega \gamma(M,n)\vec{\nabla}\mu(\theta)\cdot\vec{\nabla}\phi\varphi d\Omega = 0,$$

respectively.

If the properties are homogeneous both formulations are then equivalent. The main question remains the capability of these two numerical frameworks when the results are compared to experimental Electron Backscatter Diffraction (EBSD) data.

4.2 Parameters Identification

4.2.1 Microstructure characterization: EBSD

Electron Backscatter Diffraction (EBSD) provides the orientation maps for a given list of predefined materials. EBSD is used when aiming at quantifying microstructure characteristics such as texture, recrystallized fraction, grain size, GB disorientation, and GB length. The EBSD setup is the following. The sample is polished and placed in the SEM chamber. The sample is then tilted at 70° and the electron beam scans the surface of the sample over a regular grid with a fixed step size, see Figure 4.1. One can use square or hexagonal grids; in this work, a square grid is used.

EBSD maps are generated on a phosphor screen by backscatter diffraction. The diffraction presents a regular arrangement known as Kikuchi pattern [205] and which consists on a regular arrangement of parallel bands, see Figure 4.1. Every band fulfill the Bragg condition with respect to the atomic planes. The Kikuchi pattern is characteristic of the crystal structure and orientation in the indexed point. The crystal orientation and phase is determined for each point. In practice, data sets present non-indexed points that correspond to bad quality patterns.

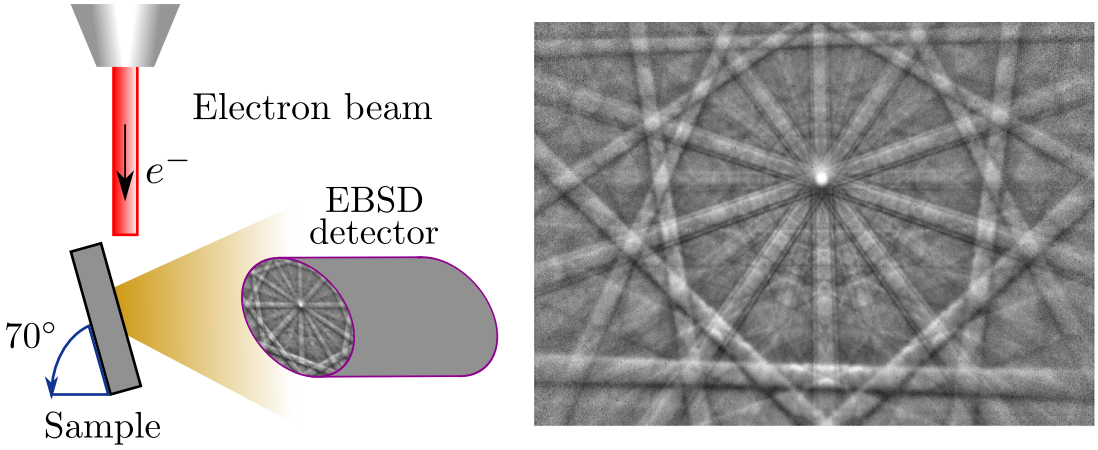

Figure 4.1: (a) Schematic of the EBSD geometry in a SEM showing the pole piece of the SEM, the electron beam, the tilted specimen, and the detector. (b) Experimental Kikuchi pattern showing the 10-fold rotation axis of AlCoNi, image from [206].

A TESCAN FERA 3 scanning electron microscope (SEM) is used to characterize the microstructure. It is equipped with several detectors including a Symmetry and C-Nano EBSD detectors. In this work the Symmetry EBSD detector was used. Post-processing was conducted using the MTEX toolbox in a Matlab environment [207].

4.2.2 Material characterisation

The chemical composition of the 316L stainless steel is reported in Table 4.1. The samples were machined in the form of rectangular parallelepipeds of $8.5mm \times 8.5mm \times 12mm$. The samples were then annealed at $1050°C$ during $30min$, $1h$ and $2h$. Afterwards, the samples were prepared for EBSD characterization. The preparation consisted of mechanical polishing, followed by fine polishing and finally electrolitic polishing, the details of the polishing are listed in Table 4.2.

Elem. Wgt%	Fe	Si	P	S	Cr	Mn	Ni	Mo	N
Min	bal.	-	-	-	16.0	-	10.0	2.0	-
Real	65.85	0.65	0.01	0.14	18.02	1.13	11.65	2.55	
Max	bal.	0.75	0.045	0.03	18.0	2.0	14.0	3.0	0.1

Table 4.1: Chemical composition of the 316L stainless steel (Weight percent).

Table 4.2: Polishing procedure applied to the 316L stainless steel samples. Plate and tower rate are the parameter of the used automatic polisher.

Abrasive	**time [s]**	**Plate [rpm]**	**Tower [rpm]**	**Force [dN]**
320 SiC paper	60	250	150	2.5
600 SiC paper	60	250	150	2.5
1200 SiC paper	60	250	150	2.5
2400 SiC paper	60	150	100	1
HSV - 3µm Diamond solution 0.12mL/8s	120	150	100	2
electrolytic polishing	30s	30V	Electrolyte A2 (Struers)	

Microstructures were analyzed at the center of the sample using a TESCAN FERA 3 Field Emission Gun Scanning Electron Microscope (FEGSEM), equipped with a Symmetry EBSD detector from the Oxford company. The EBSD map at $t = 0h$ has a size of 1.138 $mm \times 0.856$ mm and was acquired with a constant step size of 1.5 μm. The other three EBSD maps at $t = 30min$, $1h$, $2h$ have a size of 1.518 $mm \times 1.142$ mm and were acquired with a constant step size of 2 μm. Grain boundaries have a disorientation above 5 degrees ($\theta > 5°$) and $\Sigma 3$ twin boundaries have a misorientation axis <111> $\pm 5°$ and $\theta = 60 \pm 5°$.

The main properties of the initial microstructure are reported in Figure 4.2. Figure 4.2(b) illustrates the grain size and disorientation distribution ignoring $\Sigma 3$ twin boundaries (TB). The grain size is defined as an equivalent radius, $R = \sqrt{S/\pi}$, where S is the grain area. The microstructure consists in equiaxed grains with an arithmetic mean radius of 15 μm, and few bigger grains with a

radius around 60 μm. Additionally, the microstructure presents a Mackenzie-like disorientation distribution function (DDF) typical of random grain orientations. On the other hand, if $\Sigma 3$ TBs are considered, the DDF presents an additional sharp peak at a disorientation angle $\theta = 60°$, which come from the TBs and then constitute a strong source of anisotropy with regards to GB properties (see Figure 4.2(c)).

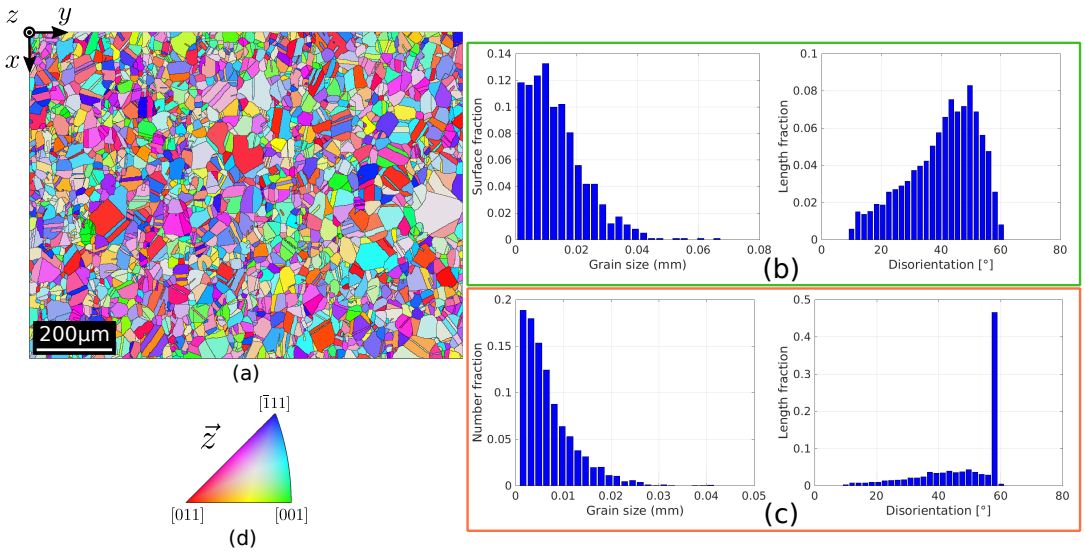

Figure 4.2: Initial microstructure properties determined by EBSD measurements. (a) IPF-z map. (b) Grain size distribution and DDF of grain boundaries excluding $\Sigma 3$ TBs. (c) Grain size distribution as measured in 2D sections and DDF of grain boundaries including $\Sigma 3$ TBs; the sharp peak on the DDF at 60° corresponds to $\Sigma 3$ TBs. (d) Standar triangle used to color the orientation maps IPF-Z (indicating which crystallographic direction is lying parallel to the direction perpendicular to the scanned section).

Figures 4.3, 4.4 and 4.5 show the band contrast maps and the grain size distributions at $t = 0s$, $30min$, $1h$, $2h$. Based on Figures 4.3 and 4.4, the evolution of the microstructure seems to mostly proceed by normal grain growth (NGG) but the surface grain size distribution shows that the microstrucuture has a bimodal population of grains (see Figure 4.5). However, some of the grains can reach an equivalent diameter above 0.1 mm, much larger than the average grain size.

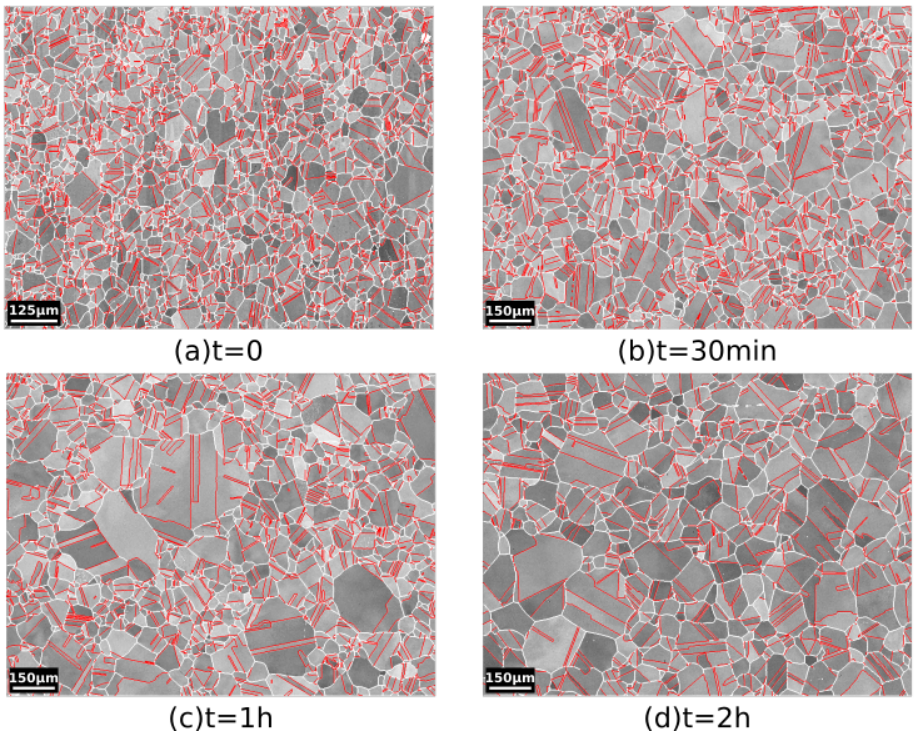

Figure 4.3: Annealing at $1050°C$: band contrast map of the microstructure of 316L steel at (a)t=0 s, (b)t=30 min, (c)t= 1 h, and (d)t= 2 h. Grain boundaries are depicted in white and Σ3 TBs in red.

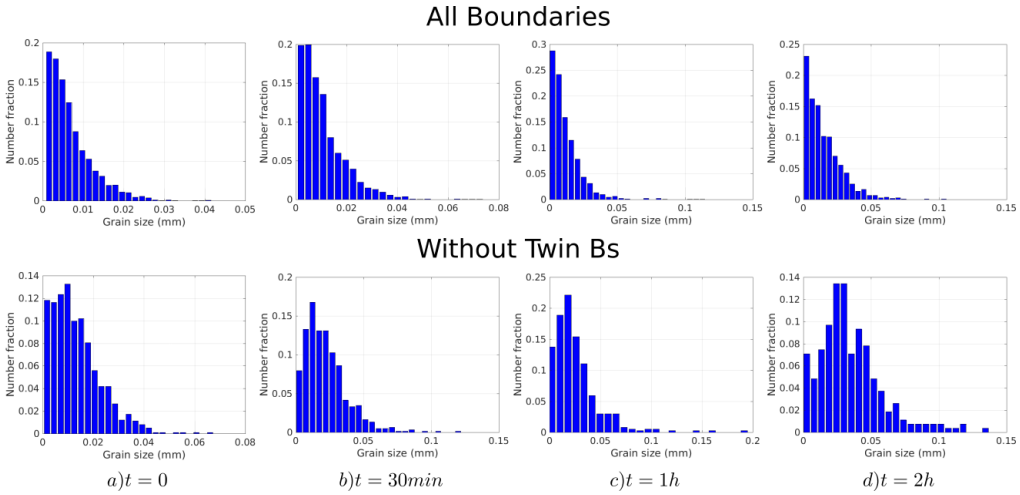

Figure 4.4: From left to right: evolution of the grain size histograms at t=0 s, t=30 min, t=1 h and t=2 h. Top: All boundaries are considered. Bottom: Σ3 twin boundaries are excluded.

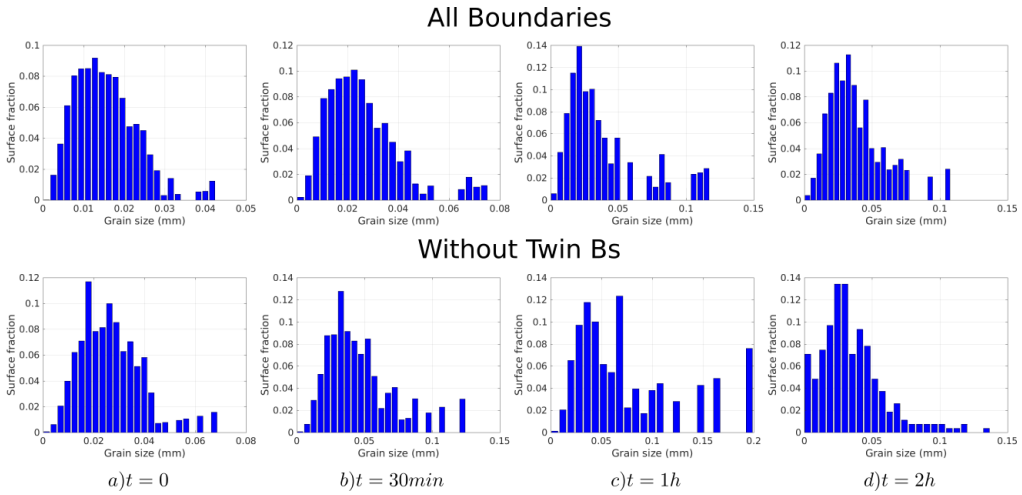

Figure 4.5: From left to right: evolution of the grain size histograms (in surface) at $t = 0s$, $t = 30min$, $t = 1h$ and $t = 2h$. Top: All boundaries are considered. Bottom: $\Sigma 3$ twin boundaries are excluded.

4.2.3 Estimation of the average grain boundary mobility based on the Burke and Turnbull GG method

In order to compute the average mobility necessary to run full-field simulations, the evolution of the arithmetic mean grain radius $\bar{R}_{Nb}$ must be known. Figure 4.6 shows the evolution of $\bar{R}_{Nb}$ as a function of the annealing time. Using the methodology discussed in [173, 208], one can obtain an average reduced mobility $\mu\gamma$ using the Burke and Turnbull model [209]. This model, where topological and neighboring effects are neglected, is based on five main assumptions: the driving pressure is proportional to the mean curvature, grains are equixaed, the GB mobility and energy are isotropic, the annealing temperature is constant and no second phase particles are present in the material. In this context, one can obtain a simplified equation describing the mean radius evolution:

$$\bar{R}_{Nb}(t)^2 - \bar{R}_{Nb}(t=0)^2 = \frac{1}{2}\mu\gamma t. \tag{4.1}$$

This methodology has been used in [173, 208, 210–212] assuming general grain boundaries with homogeneous GB energy and mobility. From the evolution of $\bar{R}_{Nb}$ in Figure 4.6 (excluding the $\Sigma 3$ TBs), one can then obtain a first approximation of the product $\mu\gamma$ for the general boundaries at $1050°C$. This approximation will be used for the $\mu\gamma$ definition in isotropic simulations. Nevertheless, as illustrated by the second orange curve in Figure 4.6, when $\Sigma 3$ TBs are considered in the analysis, grains are of course smaller, but they also grow much slower, with a direct impact on the apparent reduced mobility. This slow evolution can be produced by the strong anisotropy brought by special GBs in the global grain boundary network migration. Different ways to improve the description of the reduced mobility and their impacts in the results are discussed in the following.

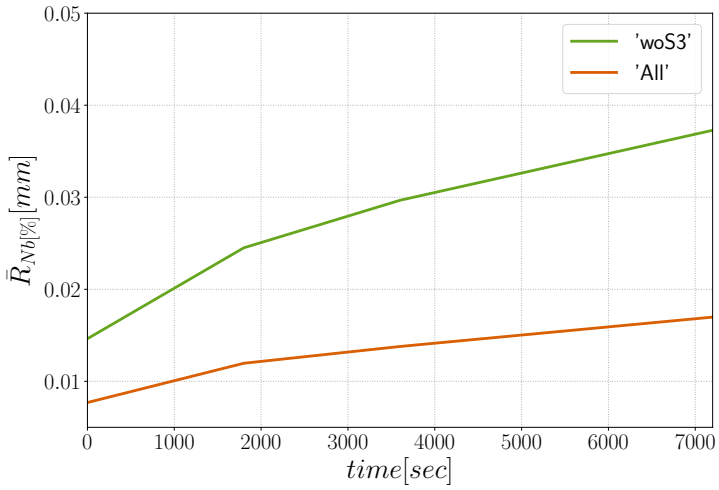

Figure 4.6: Mean grain radius evolution at $1050°C$ from experimental data measured in 2D sections by taking into account all boundaries (in orange) and without TBs (in green). The outer grains which share a boundary with the image borders are not taken into account in the analysis.

In the following sections, *general boundaries* make reference to the case without Σ3 TBs and the case with Σ3 is referred to as *all boundaries*.

4.3 Statistical cases

In this section, the 2D GB network is created from the initial experimental grain size distribution shown in Figure 4.7. The square domain has a length $L = 2.0mm$ and grains are generated using a Laguerre-Voronoi tessellation [193] based on an optimized sphere packing algorithm [194]. Anisotropic remeshing is used with a refinement close to the interfaces, the mesh size in the tangential direction (and far from the interface) is set to $h_{max} = 5\ \mu m$ and in the normal direction $h_{min} = 1\ \mu m$, with transition distances set to $\phi_{min} = 1.2\ \mu m$ and $\phi_{max} = 5\ \mu m$ (see [38, 186, 188] and Equation 3.6 for more details concerning the remeshing procedure and parameters). The time step is set to $\Delta t = 10\ s$. The orientation field was generated randomly from the grain orientations measured by EBSD in the initial microstructure (Figure 4.2a). The first part studies grain boundaries without Σ3 TB, (Section 4.3.1). In the second part, Σ3 TBs are included in the analysis, (Section 4.3.2).

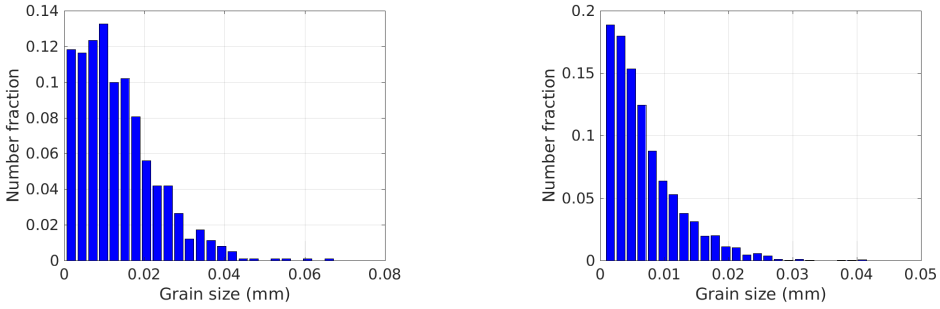

(a) Excluding TBs (b) Including TBs

Figure 4.7: Initial grain size distributions (a) excluding TBs and (b) all grain boundaries obtained from the initial EBSD map shown in Figure 4.2.

The interfacial energy and average GB properties are computed as

$$E_\Gamma = \frac{1}{2}\sum_i \sum_{e\in\mathcal{T}} l_e(\phi_i)\gamma_e \text{ and } \bar{x} = \frac{1}{2L_\Gamma}\sum_i \sum_{e\in\mathcal{T}} l_e(\phi_i)x_e, \tag{4.2}$$

where $\mathcal{T}$ is the set of elements in the FE mesh, l_e the length of the LS zero iso-values existing in the element e and i refers to the number of LS functions, L_Γ the total length of the GB network Γ, and x_e the GB property of the element e.

4.3.1 Statistical case with general boundaries

The first case with general boundaries is composed of $N_G = 4397$ initial grains. Figures 4.8a and 4.8b show the initial GB disorientation and the initial DDF distribution. Most of the interfaces have a disorientation higher than 15° due to the random generation of orientations that leads to a Mackenzie-like DDF, see Figure 4.8b.

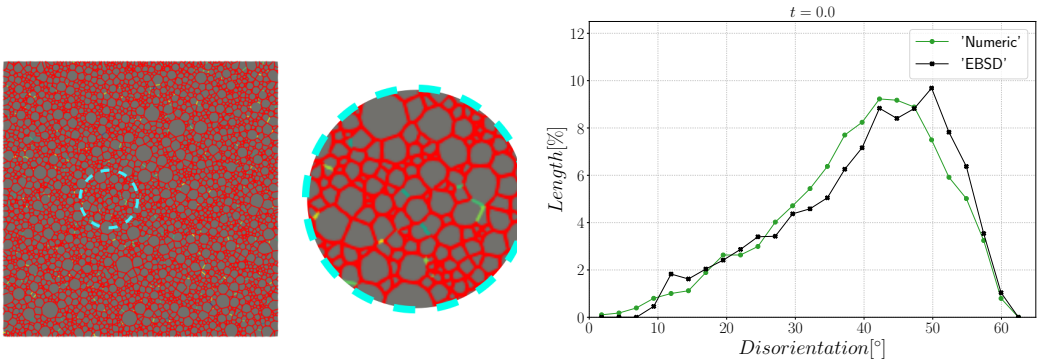

(a) Microstructure disorientation (b) DDF

Figure 4.8: Initial (a) microstructure disorientation with a cyan circle which represents the zone shown on the right and (b) the disorientation distribution.

The GB energy and mobility are then defined as being disorientation dependent, using a Read-Shockley (RS) [69] (see Equation 3.14) and a Sigmoidal (S) function [77] (see Equation 3.15). The transition disorientation from low angle GB (LAGB) to high angle GB (HAGB) is set to $\theta_0 = 15°$. The maximal value of GB energy is set to $\gamma_{max} = 6 \times 10^{-7} J \cdot mm^{-2}$ and are typical for stainless steel [111, 173]. The value of general HAGB mobility was computed using the methodology presented in section 4.2.3 and is fixed at $\mu_{max} = 0.476\ mm^4 \cdot J^{-1} \cdot s^{-1}$ for both Isotropic and Anisotropic formulations.

The simulations carried out using the Anisotropic formulation consider heterogeneous GB energy defined by Equation 3.14 and two descriptions of the mobility. If GB mobility is isotropic, the formulation is referred as "Aniso(μ:Iso)" and in the cases where GB mobility is heterogeneous (i.e. defined by Equation 3.15), the formulation is referred as "Aniso(μ:S)". Figure 4.9 shows the evolution of average quantities: normalized total GB energy $E_\Gamma / E_\Gamma(t = 0)$, normalized number of grains $N_G / N_G(t = 0)$, arithmetic mean grain radius $\bar{R}_{Nb}$, and normalized average GB disorientation $\bar{\theta} / \bar{\theta}(t = 0)$. One can see that the mean grain radius evolutions agree with the experimental data and that the evolution of the other mean values are close to each other when using the different formulations and present reasonable variations from the experimental data. As stated in [38], the effect of an heterogeneous GB mobility does not affect the evolution of the mean values and distributions when orientations are generated randomly and the DDF is similar to a Mackenzie distribution. On can see that the only mean value affected by the GB mobility is the average GB disorientation $\bar{\theta}$, being the "Aniso(μ:S)" formulation the one that is closer to the experimental evolution.

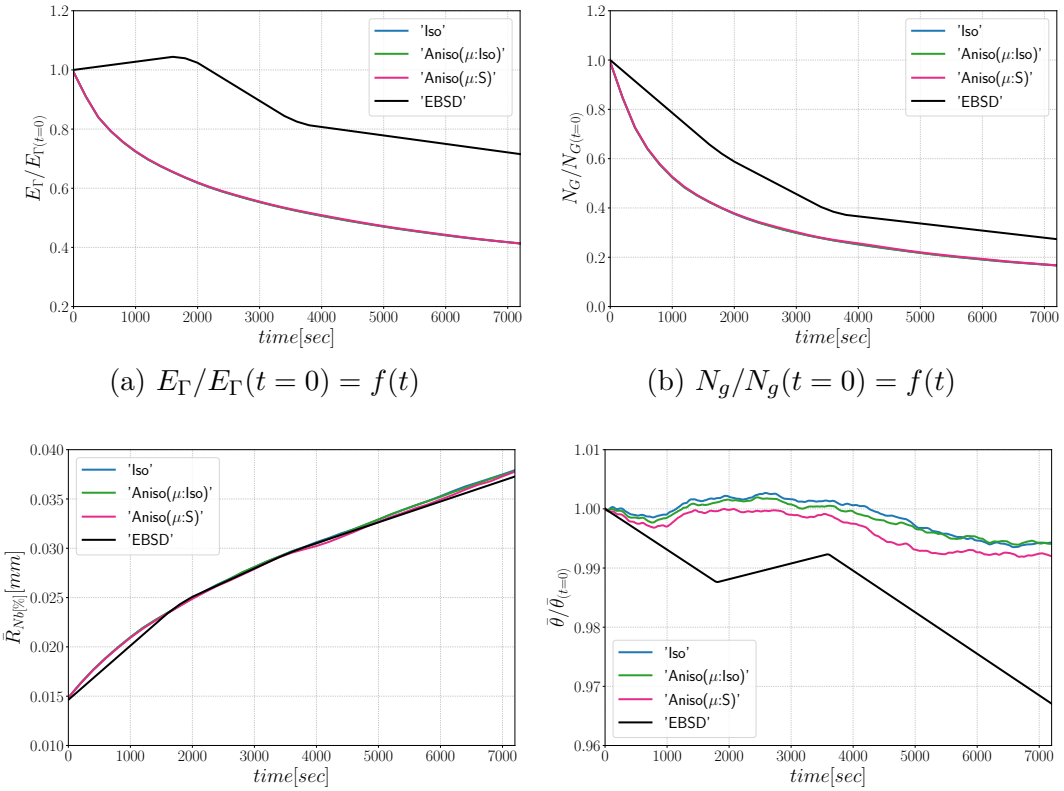

(a) $E_\Gamma/E_\Gamma(t=0) = f(t)$ (b) $N_g/N_g(t=0) = f(t)$

(c) $\bar{R}_{Nb[\%]} = f(t)$ (d) $\bar{\theta}/\bar{\theta}(t=0) = f(t)$

Figure 4.9: Mean values time evolution for the isotropic (Iso) formulation, anisotropic formulations with isotropic GB mobility (Aniso(μ:Iso)) and heterogeneous GB mobility (Aniso(μ:S)) and the experimental data (EBSD). Numerical results obtained from the initial microstructure shown in Figure 4.8a.

Figures 4.10 and 4.11, show a good match of GSD and DDF between simulation results and experimental data after one and two hours of annealing at 1050°C. One can see that the three cases are alike. The initial Mackenzie-like DDF evolves slowly for cases with random orientations and low anisotropy (as in [30, 38, 185, 196, 197]). Finally, in Figure 4.12, one can see the similarity between the microstructures obtained in the different simulations with most of the grains being equiaxed and few LAGBs.

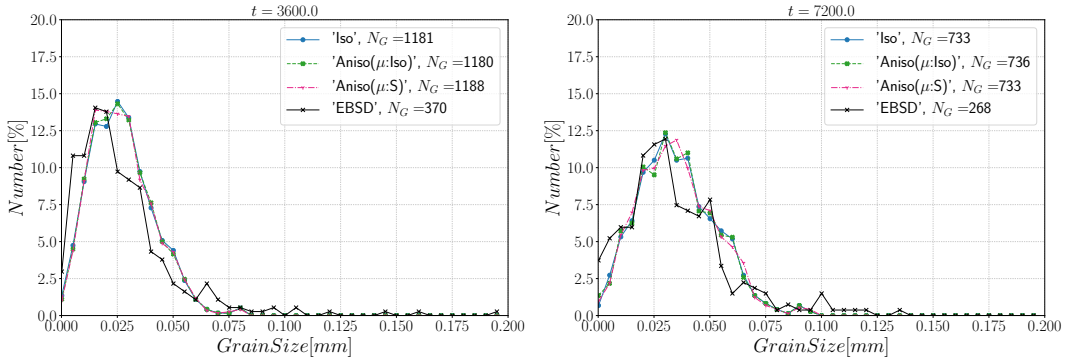

(a) $t = 1\ h$ (b) $t = 2\ h$

Figure 4.10: Grain Size Distributions obtained excluding TBs at (a) t=1h and (b) t=2h for the isotropic (Iso) formulation, anisotropic formulations with isotropic GB mobility (Aniso(μ:Iso)) and heterogeneous GB mobility (Aniso(μ:S)) and the experimental data (EBSD). N_G refers to the number.

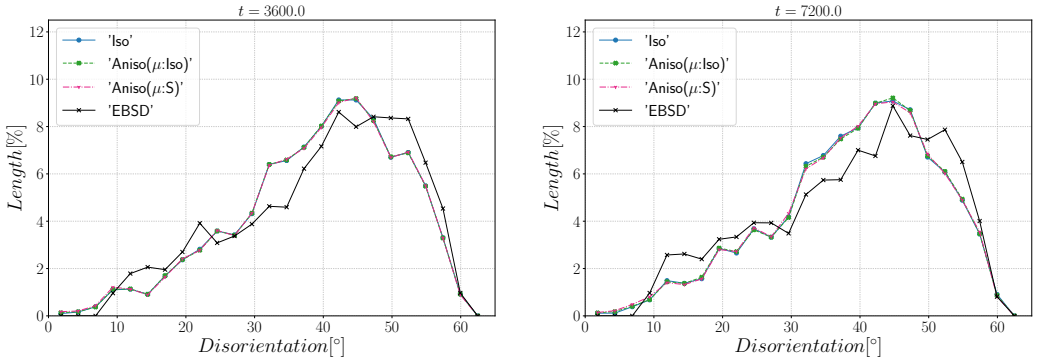

(a) $t = 1\ h$ (b) $t = 2\ h$

Figure 4.11: Disorientation Distribution obtained excluding TBs at (a) t=1h and (b) t=2h for the isotropic (Iso) formulation, anisotropic formulations with isotropic GB mobility (Aniso(μ:Iso)) and heterogeneous GB mobility (Aniso(μ:S)) and the experimental data (EBSD). The y-axis represents the GB length percentage.

The results presented here show that the evolution of an untextured polycrystal with an initial Mackenzie-like DDF could be simulated using an Isotropic formulation or an Anisotropic formulation with heterogeneous GB energy or both heterogeneous GB mobility and energy. This methodology has been used in different contexts under different annealing process [173,210–212] and with academic microstructures in [38]. In the next section, the same analysis is performed by considering the same domain but by introducing special grain boundaries through an update of the μ and γ fields.

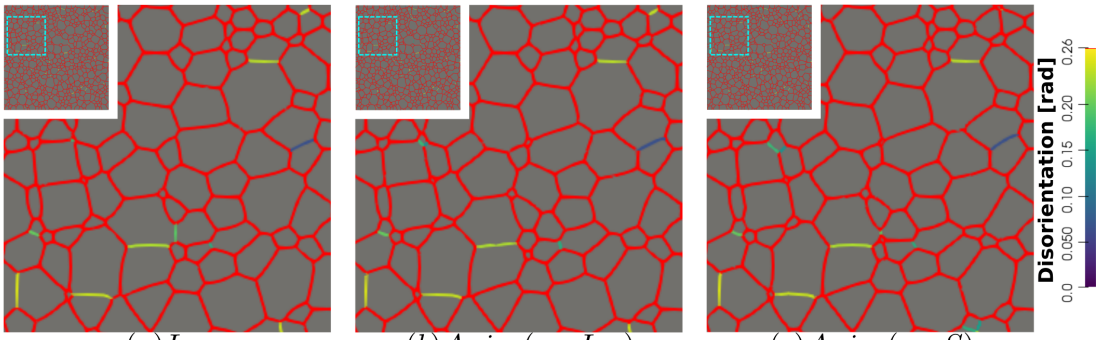

$(a) Iso$ $(b) Aniso(\mu : Iso)$ $(c) Aniso(\mu : S)$

Figure 4.12: Detail of the GB disorientation at $t = 2\ h$ in radians, GBs with a disorientation higher than 0.26 radians (15°) are colored in red: (a) Isotropic framework, (b) Anisotropic framework with γ function of θ (Equation 3.14) and μ constant, and (c) Anisotropic framework with γ and μ functions of θ through Equation 3.14 and Equation 3.15, respectively. Due to the few GBs with $\theta < 0.26$ just a square section at the top-left of the hole microstructure is shown.

4.3.2 Statistical case with an improved description of the γ and μ fields

The microstructure used in this section was generated using the same domain with $L = 2.0mm$ and the GSD shown in Figure 4.7b. The initial number of grains is $N_G = 14956$ and their orientation is also generated randomly from the EBSD orientations. The initial number of grains is more important comparatively to the previous test case as the GSD described in Figure 4.2(c - left side), where $\Sigma 3$ TBs are taken into account, is used to generate the Laguerre-Voronoï polycrystal.

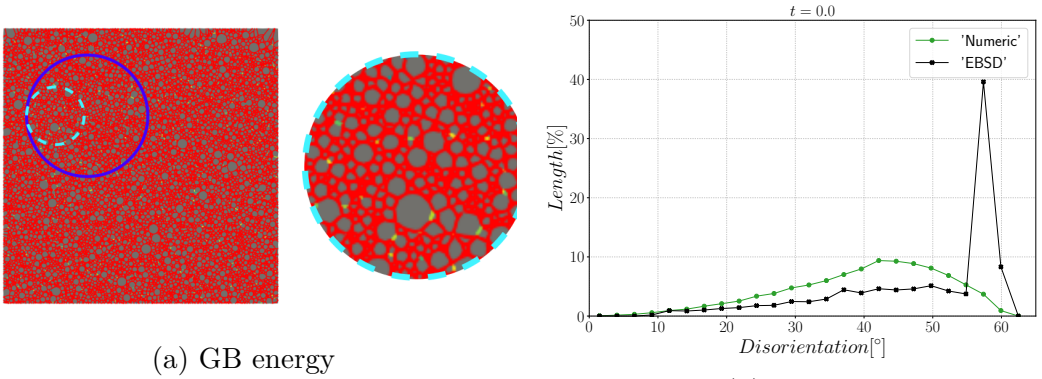

(a) GB energy

(b) DDF

Figure 4.13: Initial (a) microstructure disorientation with a cyan circle which represents the zone shown on the right and (b) the disorientation distribution. In (a), the blue circle shows the same zone as in Figure 4.17.

The same mesh and time step than the previous simulations are used in order

to be able to fairly compare the obtained results. In order to define the behavior of special GBs with properties close to Σ3 TBs, the μ and γ fields are updated as follow:

$$\begin{cases} \gamma(\theta) = \gamma_{max} \frac{\theta}{\theta_0} \left(1 - ln\left(\frac{\theta}{\theta_0}\right)\right), & \theta < \theta_0 \\ \gamma(\theta) = \gamma_{max}, & \theta_0 \leq \theta < \theta_{\Sigma 3} \\ \gamma(\theta) = \gamma_{max} * 0.1, & \theta \geq \theta_{\Sigma 3} \end{cases} \tag{4.3}$$

$$\begin{cases} \mu(\theta) = \mu_{max} \left(1 - exp\left(-5 \left(\frac{\theta}{\theta_0}\right)^4\right)\right), & \theta < \theta_{\Sigma 3} \\ \mu(\theta) = \mu_{max} * 0.1, & \theta \geq \theta_{\Sigma 3} \end{cases} \tag{4.4}$$

with $\theta_0 = 15°$ and $\theta_{\Sigma 3} = 60°$ and a value of GB energy and mobility set to $\gamma_{max} * 0.1$ and $\mu_{max} * 0.1$ for GBs with $\theta \geq \theta_{\Sigma 3}$. The value of μ_{max} is estimated using the evolution of $\bar{R}_{Nb[\%]}$ considering all GBs (see Figure 4.6). The estimated GB mobility is $\mu_{max} = 0.069\ mm^4 \cdot J^{-1} \cdot s^{-1}$, and is one order of magnitude lower from the GB mobility estimated without Σ3 TBs. The decrease of the GB mobility is proportional to the decrease of grain size (see Figure 4.6) due to the high number of TBs.

From the results shown in Figure 4.14, one can see that all formulations minimize the energy with the same efficiency (Figure 4.14a) and the microstructure evolve at a same rate leading to a good fit of mean grain size and number of grain evolutions comparatively to the experimental data. On the other hand, the Anisotropic formulation shows a better agreement in terms of mean disorientation evolution.

Figure 4.15 shows the evolution of the grain size distribution at $t = 1h$ and $2h$. GSDs present a good match (Figure 4.15) with small differences between the Iso and Anisotropic formulations. However the DDF predictions (Figure 4.16) are quite bad for all formulations even if the Anisotropic calculations tends to be better. This result can easily be explained by the use of statistics (GSD and orientations) from EBSD data which are not sufficient to accurately describe the real microstructure. First, the initial topology is simplified but above all, even if the orientation data come from the EBSD measurements, the resulting intial DDF is not accurate as a Mackenzie-like distribution is obtained as illustrated in Figure 4.13(b). Hence, the effect of heterogeneous GB energy and mobility anisotropy of the real microstructure are underestimated. A way of improvement of the proposed statistical generation methodology will be to modify the algorithm dedicated to the assignment of the orientation of each virtual grain by imposing also a better respect of the experimental DDF [213].

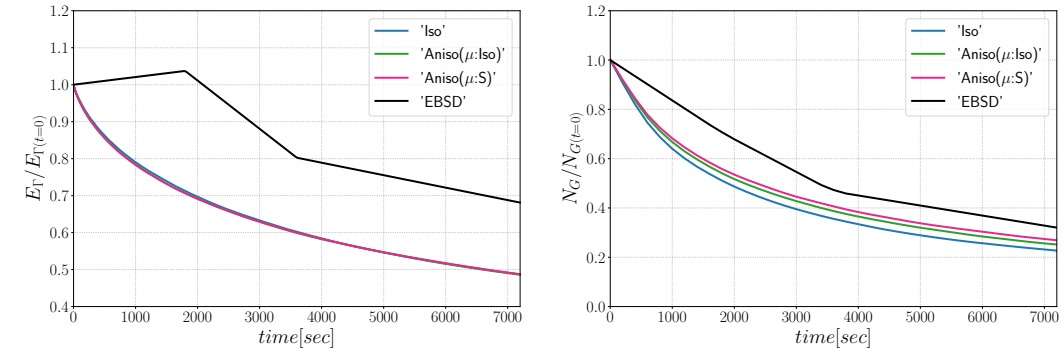

(a) $E_\Gamma/E_\Gamma(t=0) = f(t)$ (b) $N_g/N_g(t=0) = f(t)$

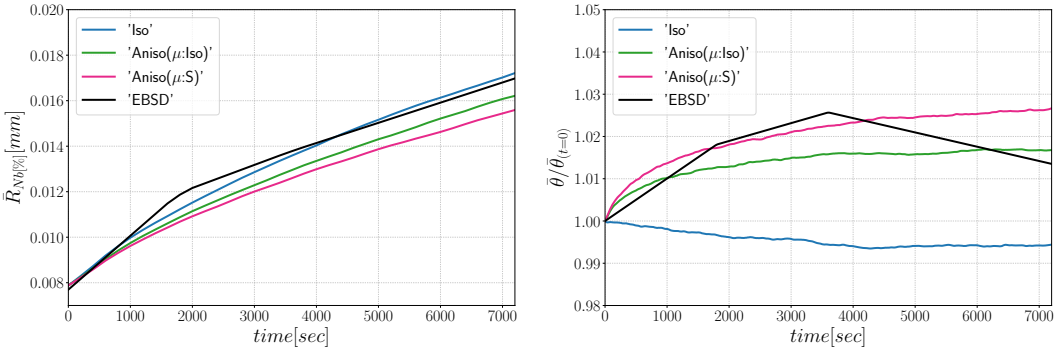

(c) $\bar{R}_{Nb[\%]} = f(t)$ (d) $\bar{\theta}/\bar{\theta}(t=0) = f(t)$

Figure 4.14: Mean values time evolution for the isotropic (Iso) formulation, anisotropic formulations with isotropic GB mobility (Aniso(μ:Iso)) and heterogeneous GB mobility (Aniso(μ:S)) and the experimental data (EBSD). Numerical results obtained from the initial microstructure shown in Figure 4.13a.

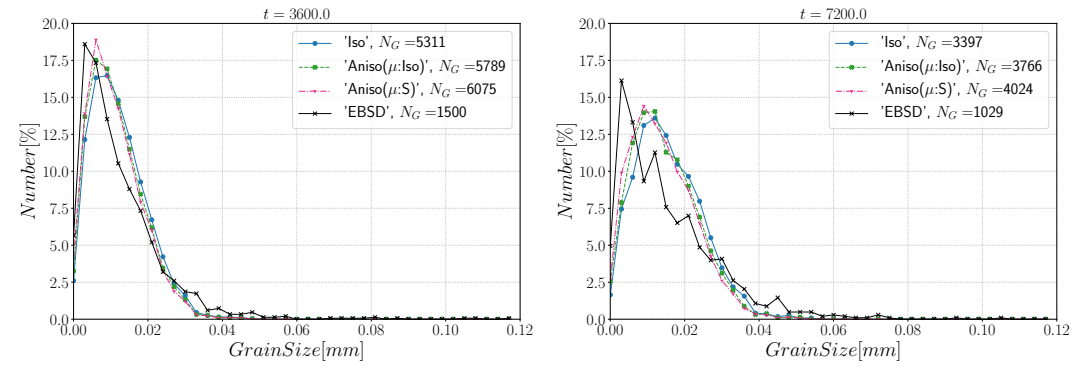

(a) $t = 1h$ (b) $t = 2h$

Figure 4.15: Grain Size Distributions obtained including TBs at (a) t=1h and (b) t=2h for the isotropic (Iso) formulation, anisotropic formulations with isotropic GB mobility (Aniso(μ:Iso)) and heterogeneous GB mobility (Aniso(μ:S)) and the experimental data (EBSD). N_G refers to the number of grains.

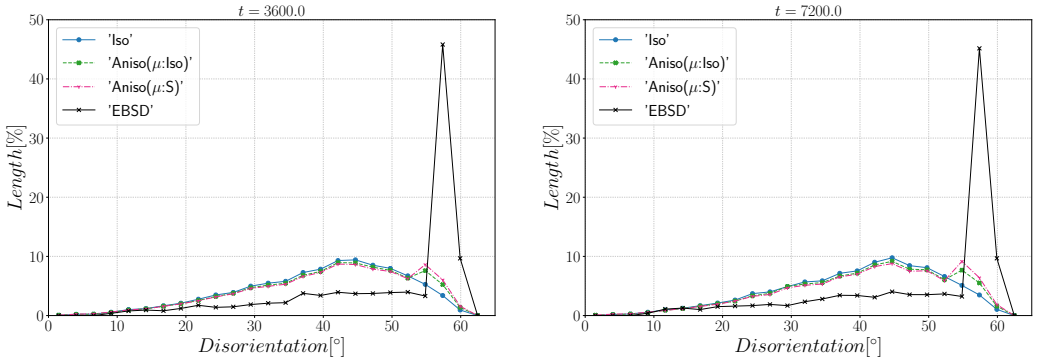

(a) $t = 1h$ (b) $t = 2h$

Figure 4.16: Disorientation Distribution obtained including TBs at (a) t=1h and (b) t=2h for the isotropic (Iso) formulation, anisotropic formulations with isotropic GB mobility (Aniso(μ:Iso)) and heterogeneous GB mobility (Aniso(μ:S)) and the experimental data (EBSD). The y-axis represents the GB length percentage.

The GB energy of the microstructure at $t = 2h$ is shown in Figure 4.17, a higher number of blue GBs, which correspond to TBs (low value of γ), is obtained using the Anisotropic formulations and the effect of heterogeneous GB mobility seems negligible.

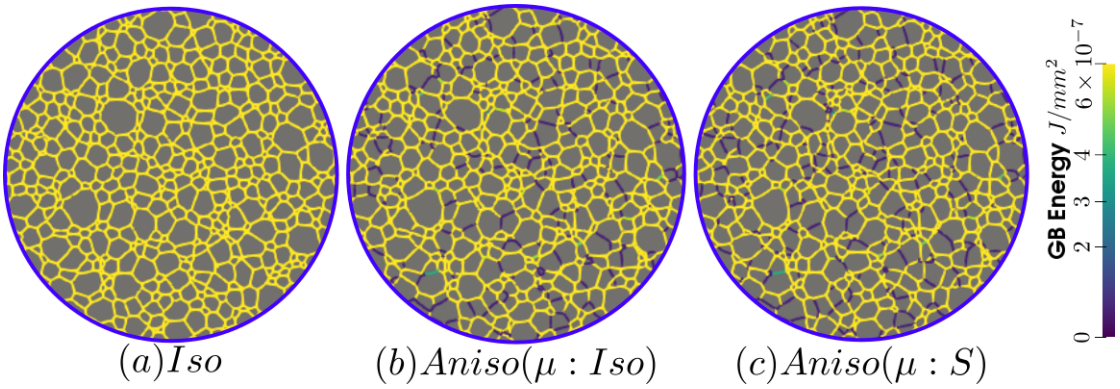

Figure 4.17: GB energy of the microstructure obtained with the (a) isotropic and anisotropic formulations using (b) isotropic GB mobility and (c) heterogeneous GB mobility at $t = 2\ h$ in the same zone shown in Figure 4.13a.

The next simulations are carried out by immersing the EBSD data in order to overcome the limits discussed above.

4.4 Immersion of EBSD data

In this section, a digital twin microstructure obtained by immersion of the EBSD map acquired on the initial microstructure (Figure 4.2) is discussed. Figure 4.18 shows the Band Contrast (BC) map of the microstructure and its numerical twin. The dimensions of the domain are $L_x = 0.856\ mm$ and $L_y = 1.138\ mm$ and contains 3472 crystallites. The time step is fixed at $\Delta t = 10\ s$ and the domain is discretized here using an unstructured static triangular mesh with a mesh size of $h = 1\ \mu m$. This microstructure is more appropriate to compare simulations and experimental data. The evolution of the numerical microstructure is compared to EBSD maps obtained at three different times: $t = 30min$, $1h$ and $2h$ (see Figure 4.3).

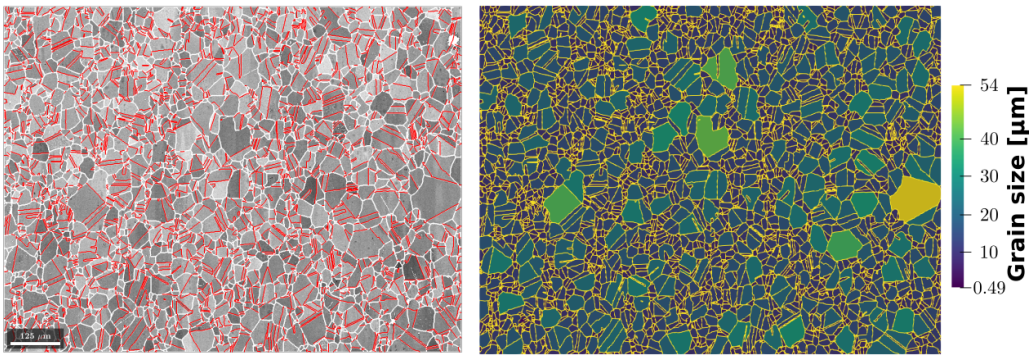

Figure 4.18: (left) EBSD band contrast map with GBs depicted in white and Σ3 TBs colored in red, and (right) its numerical microstructure displayed with a color code related to the grain size and GBs are colored in yellow. Here TBs are considered to calculate grain size, i.e., crystallite size.

GB energy and mobility are defined using Equations 4.3 and 4.4, respectively. The maximal value of GB energy is set to $\gamma_{max} = 6 \times 10^{-7}\ J \cdot mm^{-2}$ and the maximal value of GB mobility is set to fit the mean grain size evolution. The maximal value of GB mobility for the Aniso(μ:Iso) and Aniso(μ:S) formulations are $\mu_{max} = 0.146\ mm^4 \cdot J^{-1} \cdot s^{-1}$ and $\mu_{max} = 0.272\ mm^4 \cdot J^{-1} \cdot s^{-1}$ respectively. Regarding the isotropic formulation, the value of GB reduced mobility remains constant $\mu\gamma = 0.414 \times 10^{-7}\ mm^2 \cdot s^{-1}$. The changes in μ_{max} are due to the more complex geometry and the higher quantity of special boundaries that produce additional gradients of GB energy and GB mobility (see Equation 3.5). As stated before, the additional jump at $\theta_{\Sigma 3}$ is set to define special boundaries similar to Σ3 TBs. Figure 4.19 confirms the good match between the TBs colored in red in the EBSD band contrast map (left side) and TBs colored in blue corresponding to a low GB energy in the numerical twin microstructure (right side).

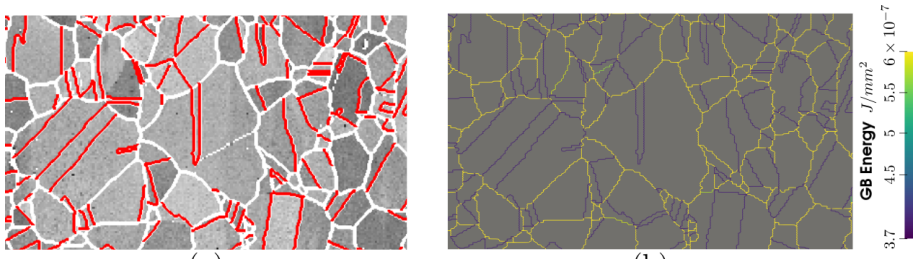

(a) (b)

Figure 4.19: Detail of the (a) EBSD band contrast map and (b) its numerical twin showing the GB Energy field. Twin boundaries depicted in red on the left image have low energy on the right image.

With the immersed data, one can obtain a close digital twin of the real microstructure with the initial GB distributions presented in Figure 4.20. The initial GB energy distribution (GBED) is shown in Figure 4.20b. With this particular distribution, several junctions will have a high anisotropy level, and as stated in [38, 185], one can expect different behaviours using the different formulations.

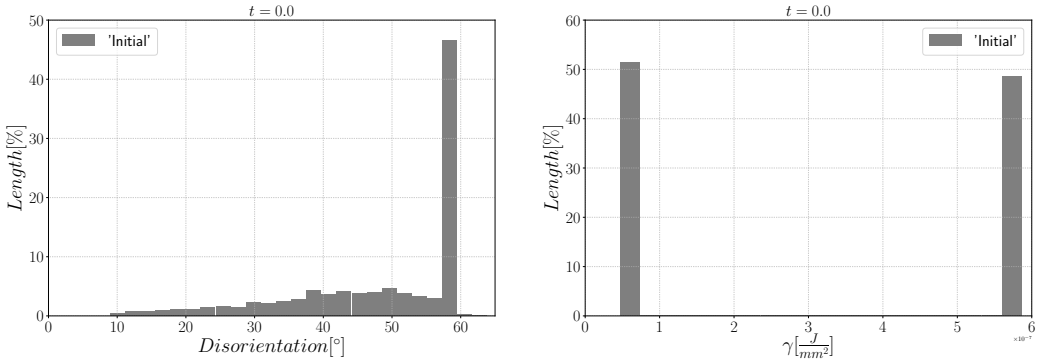

(a) DDF (b) GBED

Figure 4.20: Initial DDF and GBED of the initial immersed microstructure produced by the modified Read-Shockley equation.

As illustrated in Figure 4.21, the three simulations predict similar trends concerning the mean grain size and the grain number evolution. Comparatively to experimental EBSD data, these predictions are very good concerning the mean grain size prediction but all of them tend to predict, at the beginning, a faster disappearance of the small grains. Concerning the total energy, mean GB disorientation and mean GB energy evolutions, the Anisotropic formulation is closer to the EBSD data. This means that the Aniso formulation is more physical and promotes GBs with low GB energy.

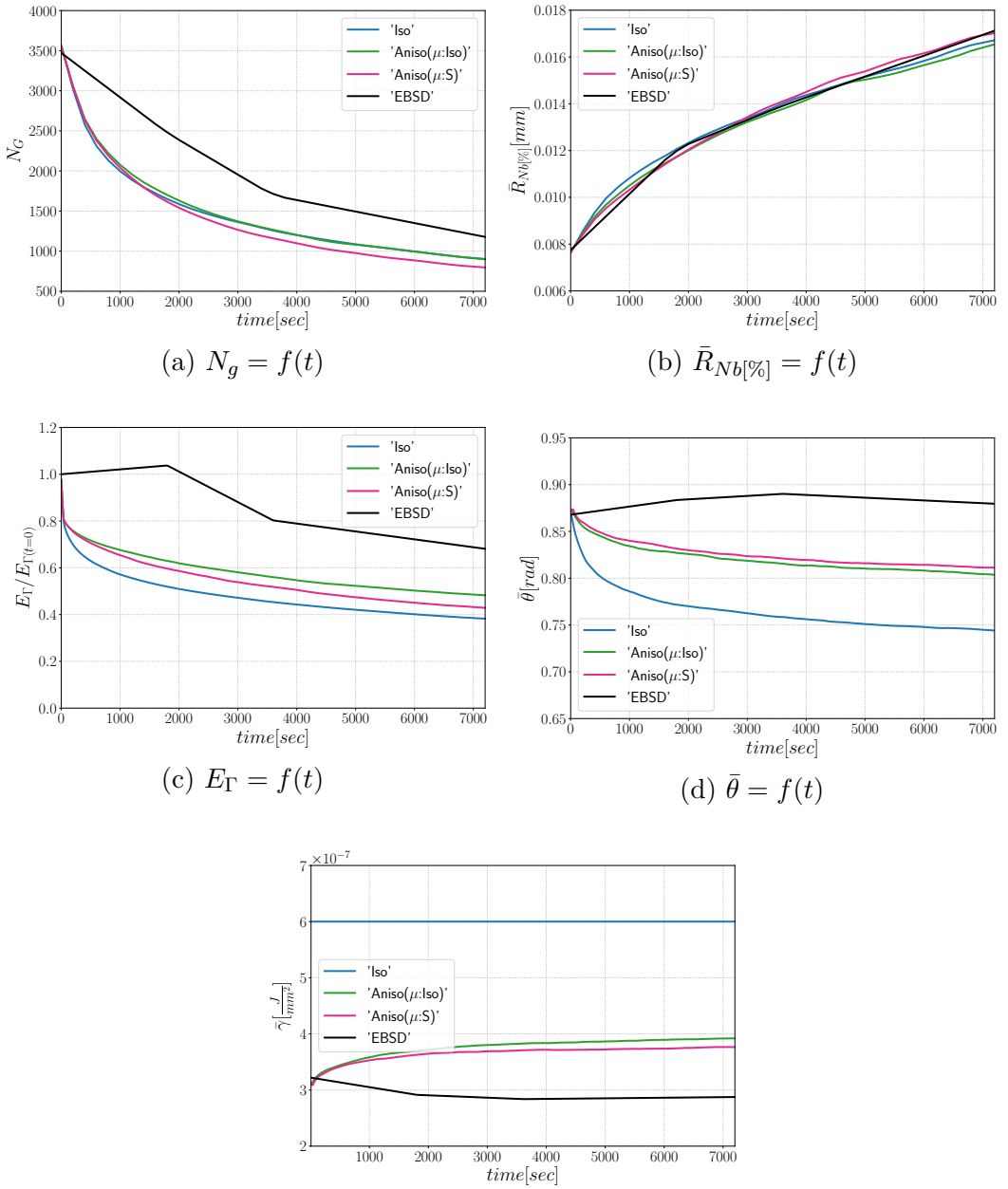

(a) $N_g = f(t)$

(b) $\bar{R}_{Nb[\%]} = f(t)$

(c) $E_\Gamma = f(t)$

(d) $\bar{\theta} = f(t)$

(e) $\bar{\gamma} = f(t)$

Figure 4.21: Mean values time evolution for the isotropic (Iso) formulation, anisotropic formulations with isotropic GB mobility (Aniso(μ:Iso)) and heterogeneous GB mobility (Aniso(μ:S)) and the experimental data (EBSD). Numerical results obtained from the initial microstructure shown in Figure 4.18.

Figure 4.22 illustrates the topology of grains at $t = 2h$. One can notice the higher quantity of GBs with low GB energy using the Anisotropic formulation and its similarity to the EBSD band contrast map even if one can notice from the EBSD data that the real microstructure contains more TBs that creates

small grains as reflected in the GSD in Figure 4.23. Another advantage of the Anisotropic formulation is the better reproduction of the DDF compared to the Iso formulation which contains a lower percentage of GBs with $\theta \approx \theta_{\Sigma 3}$ and tends to promote a Mackenzie-like DDF (see Figure 4.24). One can also see in Figures 4.22, 4.23 and 4.24 that the heterogeneous GB mobility improves the morphology of grain, the GSD and the DDF.

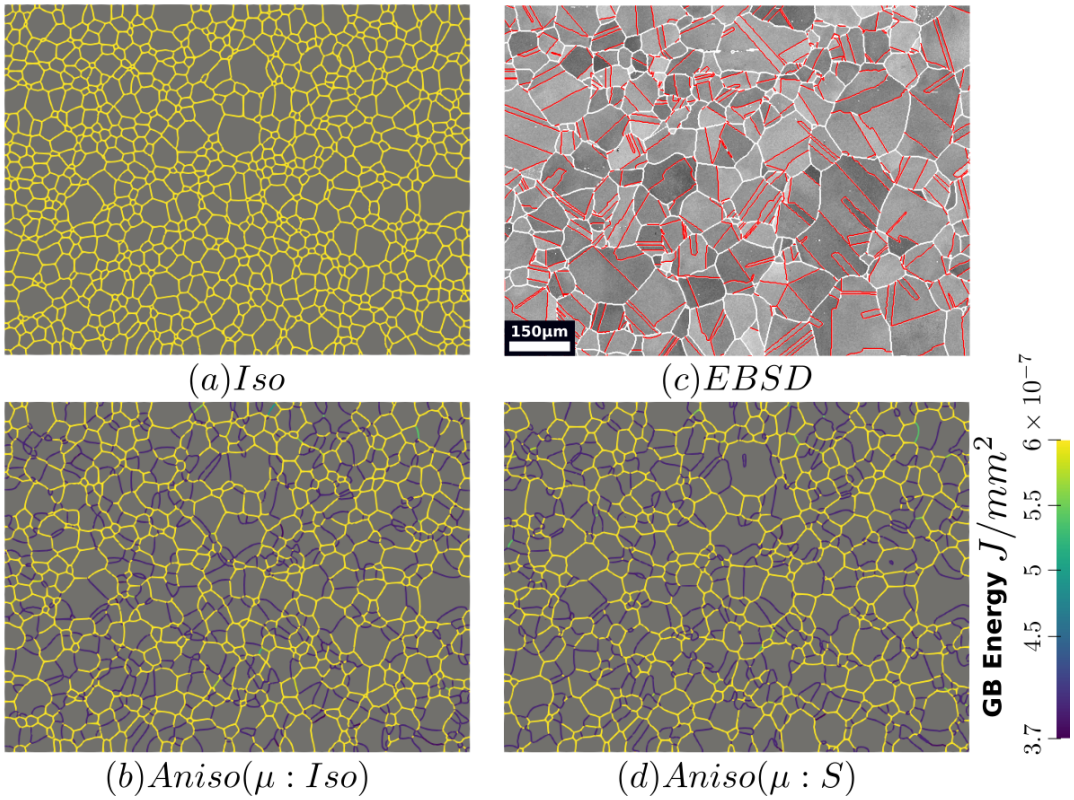

Figure 4.22: GB energy of the microstructures obtained numerically using the (a) isotropic formulation and the anisotropic formulations with (b) isotropic and (d) heterogeneous GB mobility and the experimental band contrast map at t=2h.

In this section it has been shown that the immersed data gives a better insight of the real microstructure evolution. In terms of mean values, there is small differences between the results from the Laguerre-Voronoï tessellation and the immersed microstructure. However, the GSD and DDF distributions are better reproduced for the immersed case when the anisotropic formalism is adopted. The heterogeneous GB mobility affects the grain topology, the GSD and the DDF due to its additional retarding effect. Regarding the GSD, the Aniso(μ:S) formulation can reproduce the peak at low values of grain size and the peak around $\theta_{\Sigma 3}$ for the DDF which are due to the TBs. Nevertheless, the behavior of TBs is still not perfectly reproduced by the proposed simulations, being the anisotropic formulation the one that seems more physical. In the next section this issue is addressed using the GB5DOF code which allows to define the GB

energy in terms of misorientation and GB inclination (in 2D) in order to better characterize the evolution of TBs.

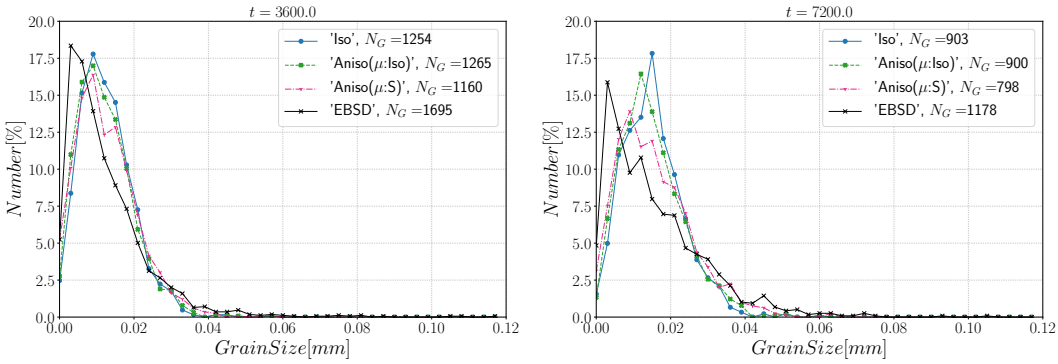

(a) $t = 1h$ (b) $t = 2h$

Figure 4.23: Grain Size Distributions obtained at (a) t=1h and (b) t=2h for the isotropic (Iso) formulation, anisotropic formulations with isotropic GB mobility (Aniso(μ:Iso)) and heterogeneous GB mobility (Aniso(μ:S)) and the experimental data (EBSD), N_G refers to the number. Numerical results obtained from the initial immersed microstructure shown in Figure 4.18 and the RS and Sigmoidal model to define GB energy and mobility.

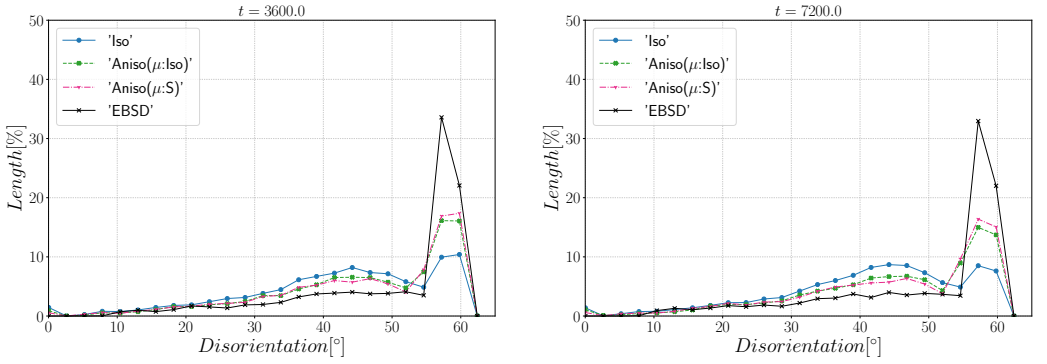

(a) $t = 1h$ (b) $t = 2h$

Figure 4.24: Disorientation Distribution obtained at (a) t=1h and (b) t=2h for the isotropic (Iso) formulation, anisotropic formulations with isotropic GB mobility (Aniso(μ:Iso)) and heterogeneous GB mobility (Aniso(μ:S)) and the experimental data (EBSD). The y-axis represents the GB length percentage. Numerical results obtained from the initial immersed microstructure shown in Figure 4.18 and the RS and Sigmoidal model to define GB energy and mobility.

4.5 Using anisotropic GB energy and heterogeneous GB mobility

4.5.1 Simulation results using immersed EBSD data

In this section, the immersed polycrystalline microstructure and the FE mesh presented in section 4.4 are used. Anisotropic GB energy values are defined using the GB5DOF code [34] and heterogeneous GB mobility are described using Equation 4.4. It means that the GB energy can vary with the GB misorientation and inclination even if the torque terms are neglected. Note that the GB inclination is measured in 2D and not 3D, in other words, the GB is supposed to be perpendicular to the EBSD map. The GB Energy of the microstructure and its GBED are shown in Figure 4.25. The initial microstructure is shown in Figure 4.25a, one can see that the maximum value of GB energy is set around $\gamma_{max} \approx 7 \times 10^{-7} J \cdot mm^{-2}$. As discussed in [34], incoherent $\Sigma 3$ TBs have a GB energy defined as $\gamma_{\Sigma 3} \approx 0.6 * \gamma_{max}$ meaning that the modified Read-Shockley model described by Equation 4.3 seems exaggerated. In Figure 4.25b the GBED is concentrated within the values $4 \times 10^{-7} J \cdot mm^{-2} \leq \gamma \leq 7 \times 10^{-7} J \cdot mm^{-2}$ which means that the level of heterogeneity is low and the different formulations are expected to promote similar trends as stated in [38]. The GB mobility was set to fit the evolution of the mean grain size, the maximal GB mobility for the Aniso(μ:Iso) and Aniso(μ:S) formulations are respectively set to $\mu_{max} = 0.0767\ mm^4 \cdot J^{-1} \cdot s^{-1}$ and $\mu_{max} = 0.1423\ mm^4 \cdot J^{-1} \cdot s^{-1}$. The difference between the μ_{max} values are generated by the higher values of GB energy produced by the GB5DOF code, note that with the RS model all the TBs are defined as coherent while the GB5DOF code can distinguish between a coherent twin boundaries and incoherent twin boundaries as pointed out in [32, 38].

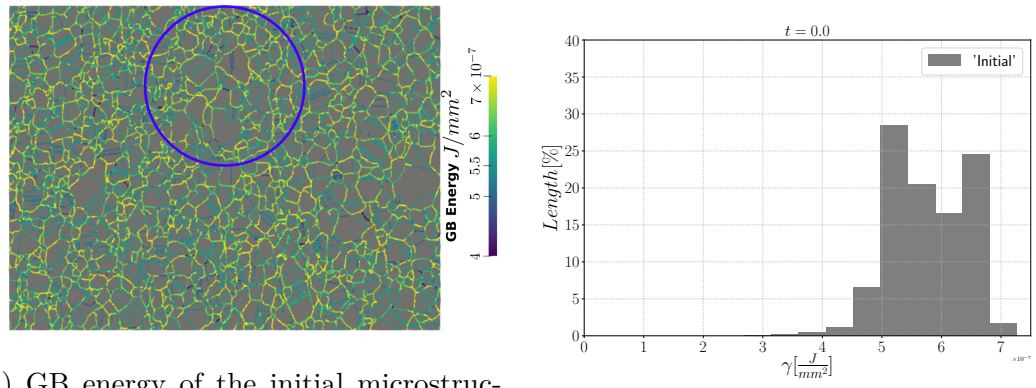

(a) GB energy of the initial microstructure

(b) Initial GBED

Figure 4.25: (a) GB energy field and (b) GBED of the initial immersed microstructure obtained using the GB5DOF code with the parameters $\epsilon_{RGB} = 0.763\ Jmm^{-2}$ and AlCu-parameter= 0. In (a) the blue circle shows a zone of interest with a twin boundary composed of a coherent and incoherent part, similar to the one shown in [38].

First the mean grain size evolution is well reproduced by the different simulations. The mean GB disorientation is not well represented by none of the formulations, the EBSD data show a stable value around 50° while all numerical results exhibit a decreasing trend. This effect is due to the TBs and illustrates the inability for the numerical formulations to preserve or generate them. Additionally, the DDF from both formulations are similar and do not correspond to the experimental DDF (see Figure 4.28). The similarity between the isotropic and anisotropic simulations is due to the low anisotropy level, that may be produced by the lack of information of the GB inclination (see Figure 4.29). As stated in [38], when the GBED is concentrated around a specific value, both formulations can present a similar trend. This is confirmed with Figure 4.30 where a zoom on the GB network is shown at four different times and one cannot see any obvious difference among the obtained microstructures with the three different simulations. The main difference of these results lay in the ability of the anisotropic formulation to keep more $\Sigma 3$ TBs when the sigmoid description of μ is used.

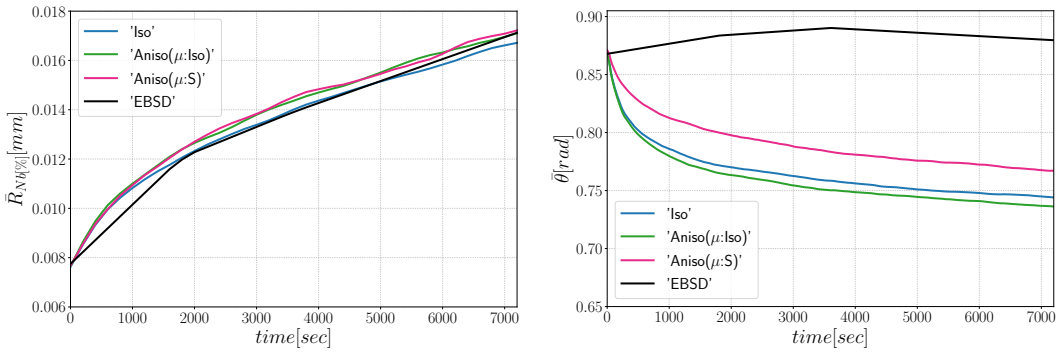

(a) $N_g = f(t)$ (b) $\bar{R}_{Nb[\%]} = f(t)$

Figure 4.26: Mean values time evolution for the isotropic (Iso) formulation, anisotropic formulations with isotropic GB mobility (Aniso(μ:Iso)) and heterogeneous GB mobility (Aniso(μ:S)) and the experimental data (EBSD): (a) number of grains, (b) average grain radius. Numerical results obtained from the initial immersed microstructure shown in Figure 4.25a and the GB5DOF code to define the GB energy.

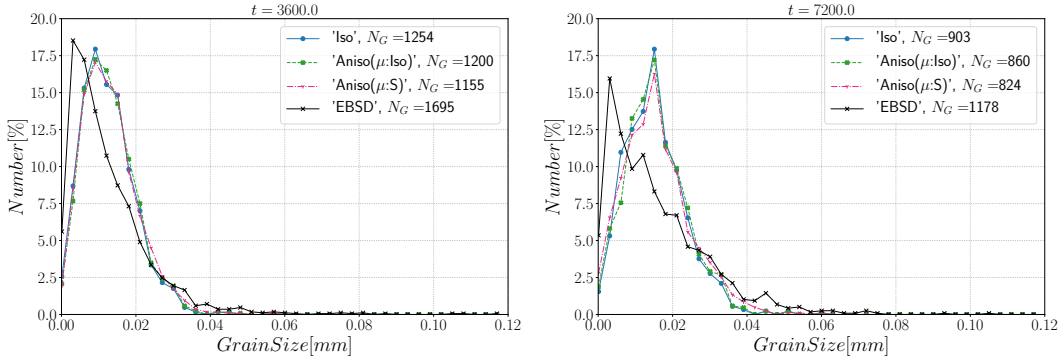

(a) $t = 1\ h$ (b) $t = 2\ h$

Figure 4.27: Grain Size Distributions obtained at (a) t=1h and (b) t=2h for the isotropic (Iso) formulation, anisotropic formulations with isotropic GB mobility (Aniso(μ:Iso)) and heterogeneous GB mobility (Aniso(μ:S)) and the experimental data (EBSD), N_G refers to the number. Initial immersed microstructure shown in Figure 4.25a and the GB5DOF code to define the GB energy.

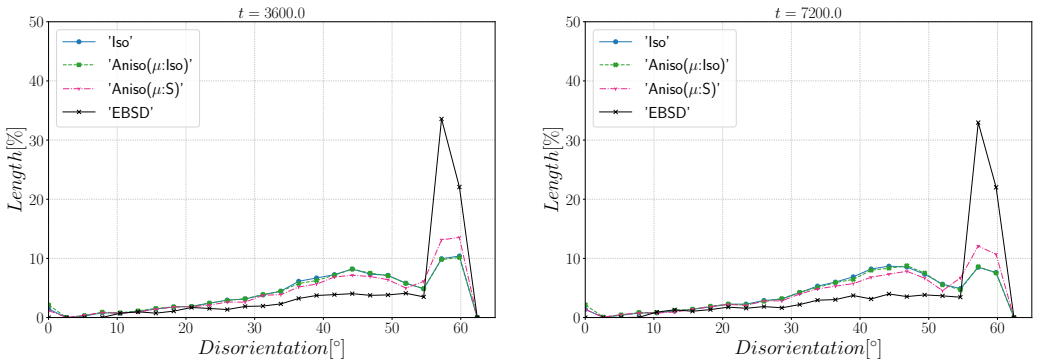

(a) $t = 1\ h$ (b) $t = 2\ h$

Figure 4.28: Disorientation Distribution obtained at (a) t=1h and (b) t=2h for the isotropic (Iso) formulation, anisotropic formulations with isotropic GB mobility (Aniso(μ:Iso)) and heterogeneous GB mobility (Aniso(μ:S)) and the experimental data (EBSD). The y-axis represents the GB length percentage. Initial immersed microstructure shown in Figure 4.25a and the GB5DOF code to define the GB energy.

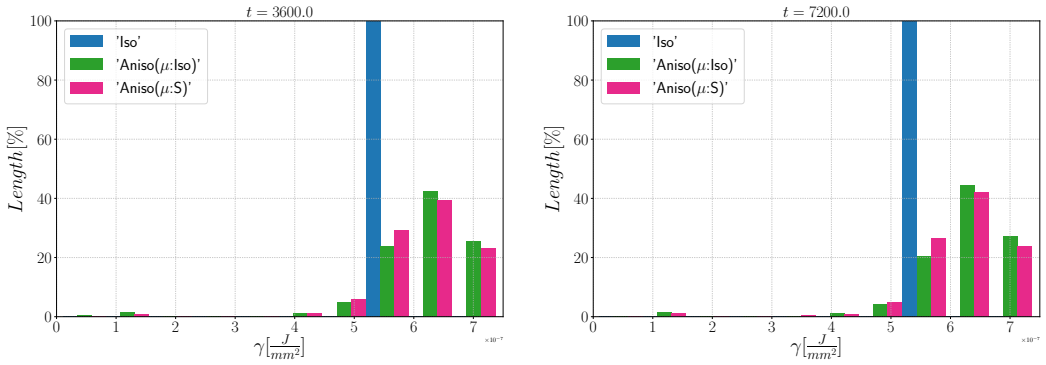

(a) $t = 1\ h$ (b) $t = 2\ h$

Figure 4.29: GBED obtained at (a) t=1h and (b) t=2h for the isotropic (Iso) formulation, anisotropic formulations with isotropic GB mobility (Aniso(μ:Iso)) and heterogeneous GB mobility (Aniso(μ:S)). The y-axis represents the GB length percentage. Initial immersed microstructure shown in Figure 4.25a and the GB5DOF code to define the GB energy.

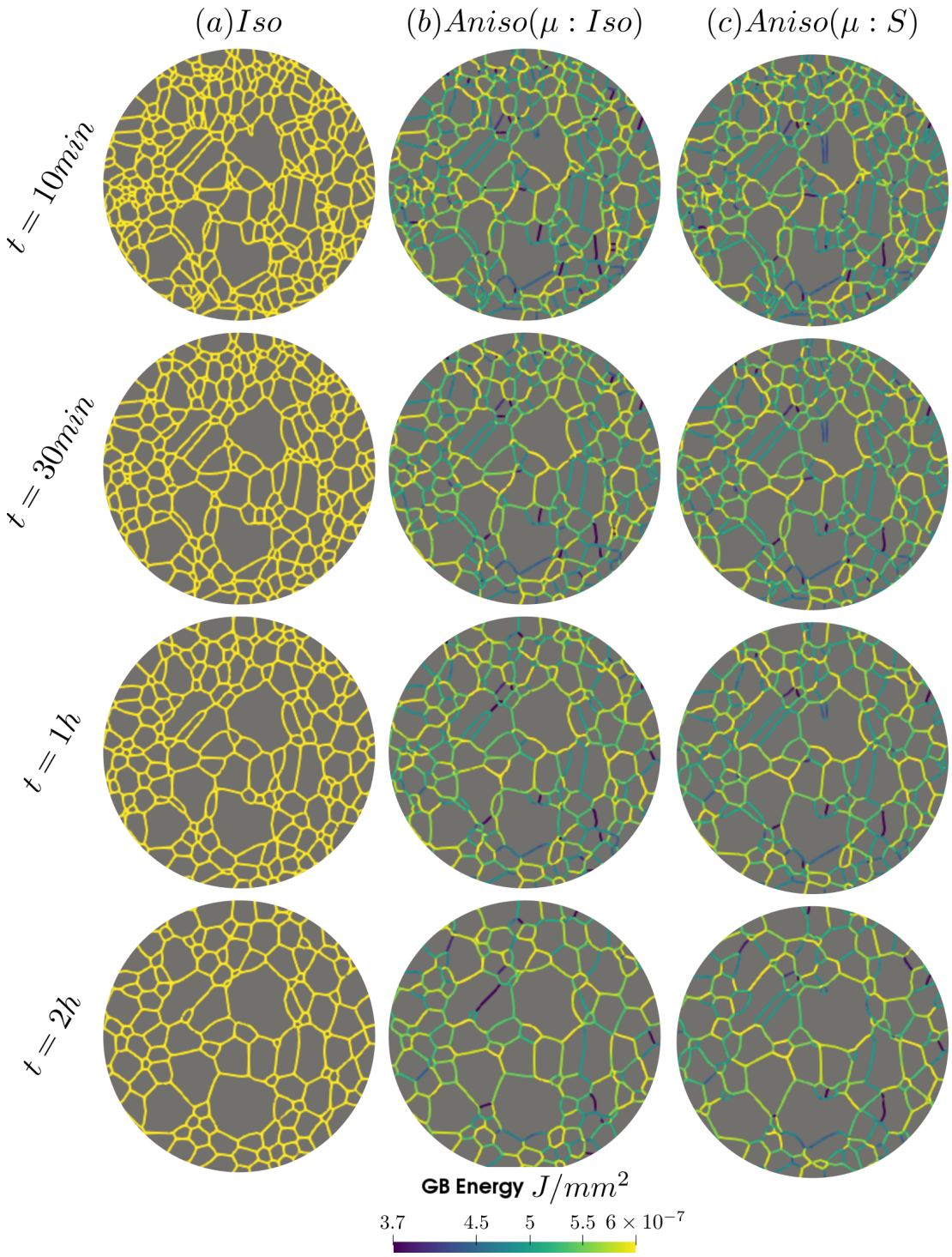

Figure 4.30: Microstructure evolution using the Isotropic formulation and Anisotropic formulation with isotropic and heterogeneous GB mobility at $t = 30min$, $1h$ and $2h$. The zone shown here is encircled in blue in Figure 4.25a.

4.5.2 Current state of the modeling of 3D anisotropic grain growth

A final question regarding the anisotropy of GB properties is still open: do the 3D description of GB properties can affect the microstructure evolution? Until now, most of the studies of GG in 3D have presented simulations of polycrystalline microstructures using different textures and a mathematical description of GB properties [137, 214–216] or using data bases of GB energy [217, 218]. The following conclusions are pointed out:

- The effect of the heterogeneity is stronger when the material is textured or the disorientation transition between LAGBs and HAGBs, θ_0, is high [215, 216, 218],
- The individual effect of GB energy and mobility is small on the GG [216].

Note that similar conclusions were presented in the first part of this work [38]. In [137, 214–216], GB properties are defined as heterogeneous and not as anisotropic. The inclination dependency can have an important impact, hence, a complete description of the GB properties is necessary, i.e. $\mu(M(\theta, \vec{a}), \vec{n})$ and $\gamma(M(\theta, \vec{a}), \vec{n})$, as well as 3D non-destructive in-situ characterization [92, 94–96] in order to obtain more realistic values of GB mobility must be considered as a crucial perspective concerning full-field modeling of GG.

In the simulations presented in this section, the GB inclination is simplified as it is projected in the observation plane. In other words, the description of the GB properties is simplified and only a slice of the GB energy is considered. For instance, Figure 4.31 shows the GB energy and mobility of a $\Sigma 3$ TB. One can see that the 3D surface of the TB properties have a complex geometry. On the other hand, the anisotropy of the GB mobility is simplified to a Sigmoidal model with a cusp at $\theta_{\Sigma 3}$. Unluckily, the GB mobility data is not available for the complete GB space and at different temperatures.

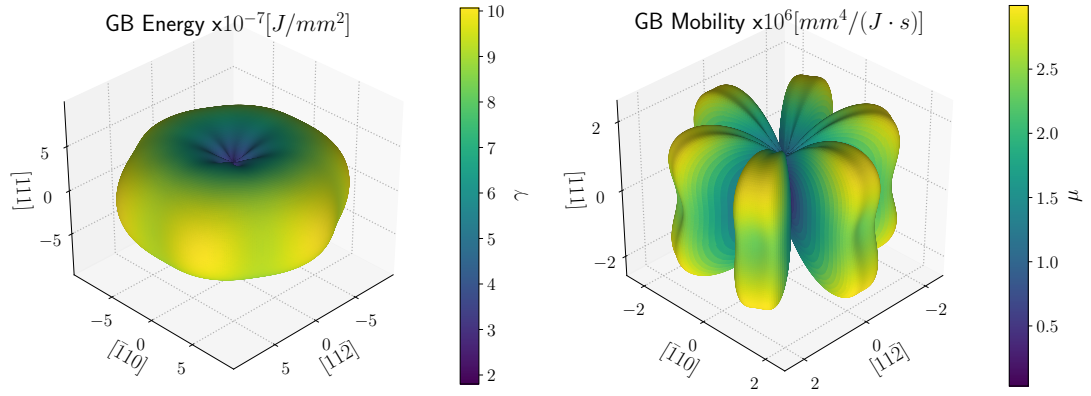

(a) $\gamma_{\Sigma 3}$ (b) $\mu_{\Sigma 3}$

Figure 4.31: (a) GB Energy and (b) Mobility of a Σ3 TB in Ni computed using the fits proposed in [104] of the atomistic simulation data in the study by Olmsted et al. [33, 90]. The minimum, maximum and average values of γ and μ are $\{1.803,\ 6.793,\ 10.064\}\ \times 10^{-7}\ J \cdot mm^{-2}$ and $\{0.032,\ 1.518,\ 2.995\}\ \times 10^{6}\ mm^4 \cdot J^{-1} \cdot s^{-1}$.

4.6 Conclusions

Different 2D FE-LS formulations to study GG of 316L stainless steel were compared. The isotropic formulation is able to reproduce, for statistically generated or immersed polycrystals, the average grain size and grain size distribution for a wide range of anisotropy levels.

The results obtained using representative Laguerre-Voronoï polycrystals show that the heterogeneous GB mobility values do not affect the response of the different formulations and that the anisotropic formulation is more physical being the only formulation that enables to promote GBs with low energy. However, the anisotropy level was largely underestimated because of the initial Mackenzie-like DDF which could not be controlled during the polycrystal generation.

Two additional cases were presented with a twin numerical microstructure obtained directly from EBSD data. The main advantage is that the initial DDF and topology are accurately defined. First, GB energy and mobility were defined using the modified Read-Shockley and sigmoidal models already tested for the virtual polycrystals. Then, the model was coupled with an anisotropic model of GB energy that takes into account the GB misorientation and inclination [34]. However, it is highlighted again that the GB inclination is not well defined as the GB is supposed to be perpendicular to the observation plane. The proposed RS model seemed to exaggerate the anisotropy level comparatively to the GB5DOF code. However, the predictions are clearly better with the proposed RS and sigmoid models associated to the anisotropic formulation while not allowing to be predictive concerning the DDF whatever the method choosen.

These results illustrate that the prediction of grain growth at the polycrystal scale can be ambiguous depending the aimed attributes and the available data. First of all, 3D simulations should be considered. Of course, this aspect is, firstly, essential to improve the representativy of the considered polycrystals but is also essential to describe correctly the γ dependence to the inclination. Indeed, the proposed 2D model/data context limits the actual use of the inclination as this parameter is described here with one degree of freedom and not in a 3D framework with 3D experimental data. This aspect can explain the low anisotropy level obtained using the GB5DOF code. Finally, this objective must also be correlated to the fact to integrate the torque effects, and so the GB stiffness tensor, in the simulations and analysis. It should be highlighted that this conclusion is common to all existing works of the state of the art involving anisotropic 2D GG simulations and 3D simulations were the inclination dependence, or torque terms, or both are not taken into account.

4.7 Résumé en Français du Chapitre 4

Différentes formulations 2D FE-LS permettant d'étudier la croissance des grains de l'acier 316L ont été comparées. La formulation isotrope est capable de reproduire, pour des polycristaux générés statistiquement ou immergés, la taille moyenne des grains et la distribution des grains pour un large intervalle de niveau d'anisotropie.

Des résultats obtenus à partir des polycristaux de type Laguerre-Voronoï, il est possible de conclure que les valeurs hétérogènes de la mobilité des joints de grains n'affectent pas le comportement des différentes formulations, et la formulation anisotrope est la plus physique. C'est en effet la seule formulation qui permet de favoriser les joints de grains de faible énergie. Cependant, le niveau d'anisotropie est en grande partie sous-estimé du fait que la distribution de désorientations initiales est de type Mackenzie; donnée qui ne peut être controlée durant la génération du polycristal à l'heure actuelle.

Deux cas supplémentaires ont été présentés, à partir d'une microstructure jumeau numérique des données EBSD. L'avantage principal est que la distribution de désorientation initiale et la topologie sont définies de manière fidèle. Dans le premier cas, l'énergie et la mobilité des joints de grains sont définies en utilisant les modèles modifiés de Read-Shockley et sigmoidal, déjà testés pour les polycristaux générés statistiquement. Enfin, le modèle est couplé à un modèle anisotrope de l'énergie des joints de grains prenant en compte la désorientation et l'inclinaison. Cela permet d'illustrer que le modèle RS proposé semble sur-évaluer le niveau d'anisotropie comparé au code GB5DOF. Cependant, les prédictions sont bien meilleures avec les modèles RS et sigmoidal proposés associés à la formulation anisotrope, tout en ne permettant pas de prédire efficacement la distribution de désorientation, comme pour toutes les autres méthodes étudiées.

Ces résultats illustrent l'ambiguité qui peut exister dans la notion des modèles prédictifs en croissance de grains. En effet, cette notion est dépendante des attributs que l'on cherche à prédire et des données à disposition.

Chapter 5

Conclusions and perspectives

5.1 Conclusions

One goal of this PhD work was to improve the definition of the GB mobility in a Finite Element Level-Set (FE-LS) framework for the modeling of grain growth and recrystallization. As such, the first chapter presents the basic concepts related to the grain boundaries (GB) and microstructures, and a brief review of the state of the art of GB mobility measurements. This bibliography led to the conclusion, and points out, that most of the GB mobility measurements are in fact GB reduced mobility measurements. This implies that the anisotropy effect of both GB energy and GB mobility are measured at the same time. The experimental estimations led to GB properties that depends on the disorientation, $\mu(\theta)$ and $\gamma(\theta)$, i.e., heterogeneous GB properties. Molecular dynamics (MD) data led to a more complete description of the GB properties as a function of misorientation and inclination, $\mu(M, \vec{n})$ and $\gamma(M, \vec{n})$, i.e., anisotropic GB properties in short time and space scales and also following the hypothesis done in these MD simulations. Thanks to the new description of GB properties three questions arise: How can we take into account the crystalline description of the GB? Can GB properties be described in 2D using a classical Read-Shockley and a Sigmoidal model? Is the effect of anisotropy stronger in 3D? The latter implying to carry out 3D simulations instead of 2D, thus using a better description of GB properties in the 5D GB space.

The first question was discussed in Chapter 2. First, a brief review of how different approaches take into account heterogeneity and anisotropy was presented. Second, a FE-LS framework is presented, as well as the mathematical description of GB dynamics and properties. Most of the existing mesoscopic approaches consider heterogeneous GB properties described by the disorientation. Regarding the effect of the misorientation and inclination, a couple of examples where MD data can be used as input of GB properties was described. Another option is to treat the effect of the inclination separately from the effect of the GB misorientation.

As the FE-LS framework has different variants, it was necessary to compare them and select the best formulation. As such, Chapter 3 was dedicated to

compare and improve the different existing formulations: Isotropic, Heterogeneous, Heterogeneous with Gradient, and Anisotropic. The numerical tools were tested using academic cases of triple junctions (three grains) and polycrystalline microstructures using heterogeneous (anisotropic) GB energy and heterogeneous GB mobility. The Isotropic and Anisotropic formulations were selected as the more suitable to model GB migration. The LS framework was then improved to take into account heterogeneous GB mobility.

The formulation was extended toward full anisotropy using heterogeneous GB mobility and anisotropic GB energy. To accomplish this, MD data of GB energy was included using the GB5DOF code. In Chapter 4, a comparison of experimental and numerical simulations using the Isotropic and Anisotropic formulation was presented. The improvements of the GB properties description showed a different behavior of twin boundaries. Also, it was shown that the effect of the GB mobility plays an important role on the morphology of grains, specifically where twin boundaries are involved. Note that in Chapters 3 and 4, the parameter describing the level of anisotropy was the GB energy distribution. When the level of anisotropy is low, the results between the Isotropic and Anisotropic formulations are similar. However, when the anisotropy level increases the results obtained by the two formulations are really different.

In Chapter 4, the Anisotropic formulation is depicted as more physical than the Isotropic formulation by reproducing the experimental results with more accuracy. However, in terms of GB disorientation, both formulations were not sufficiently accurate. Two models of GB energy were used, the first was a classic Read-Shockley (heterogeneous) model and the second an anisotropic model called GB5DOF. The predictions were better with the Read-Shockley model but both GB energy models does not predict the disorientation distribution function correctly.

In the appendix of this work, some perspectives concerning the improvement of the classical estimation of GB mobility using EBSD data are detailed. The methodology detailed in Appendix A.2 consist in:

- the dissociation of GB energy γ and GB mobility μ using an additional driving pressure (stored deformation energy),
- the tracking of GBs (instead of grains in precedent studies),
- to introduce a better description of the stored deformation energy using the geometrically necessary dislocation density.

However, it was also highlighted that the method presented must be improved to take into account the 3D description of GBs and the volumetric value of GND density instead of a surface value.

This work does not present a unequivocal answer to the anisotropic behavior of GB mobility. Instead, this work has contributed towards the full field modeling

of anisotropic grain growth and recrystallization. It has been shown that the classical isotropic FE-LS framework can be used for different cases with a narrow GB energy distribution, but the Anisotropic formulation is more physical and can take into account the torque terms (GB stiffness tensor). The role of GB mobility during grain growth has been shown using different definitions and it's now better understood in the context of full-field at the mesoscopic scale.

5.2 Perspectives

In order to move forward some supplemental issues must be addressed. As the research project finished new questions started to arise. One of them was about the correct description of GB energy. Do the GB mobility can be correctly studied using a simplified description of the GB energy? That's the main reason of the inclusion of MD data towards the GB5DOF code that can describe the GB energy in the 5D space. As this work was composed of both experimental and numerical techniques not all the questions were tackled due to time limits. Some problems were unexplored and should be presented as perspectives. A few of these propositions will be tackled in different future research projects of the MSR Team. The first perspective is the 3D data acquisition, estimation of GB properties and comparison with 3D numerical results. The second one is the introduction of the GB stiffness tensor or torque terms, this parameter may be take into account as it can, at some particular misorientation, introduce additional derivative values of the same order of magnitude that the GB energy. Finally, as it was shown in Chapter 4, the current framework cannot take into account the creation of annealing twins. Annealing twins can be included via the disconnection character of GBs that induce internal stresses. Some pre-results concerning the aforementioned perspectives are presented in detail in the following.

5.2.1 3D Immersion and GG simulations

Until now, most of the results presented in this text are in 2D. First, grain morphology is simplified. Second, the anisotropic nature of $\Gamma(\vec{n})$ and $\mu(\vec{n})$ is partially lost. Due to the lack of time, comparisons between real microstructures and simulation during heat treatments were not performed in 3D. The initial microstructure is obtained thanks to serial sectioning on a selected region of interest. Between every section an amount of material is removed from the surface and an image is collected (EBSD/EDS map or SE/BSE images).

A data treatment is necessary in order to link the 2D layers and reconstruct the 3D microstructure properly: alignment of the sections, post-processing filters and grain segmentation is performed with DREAM.3D [219]. Finally, 3D data is exported and immersed in our in-house FE code and one can perform simulations based on a real microstructure. Figure 5.1 shows the 3D microstructure and 2D layers at different positions. Note that TBs can be present in several 2D layers. Thanks to the 3D data one can study and analyze the behavior of TBs correctly.

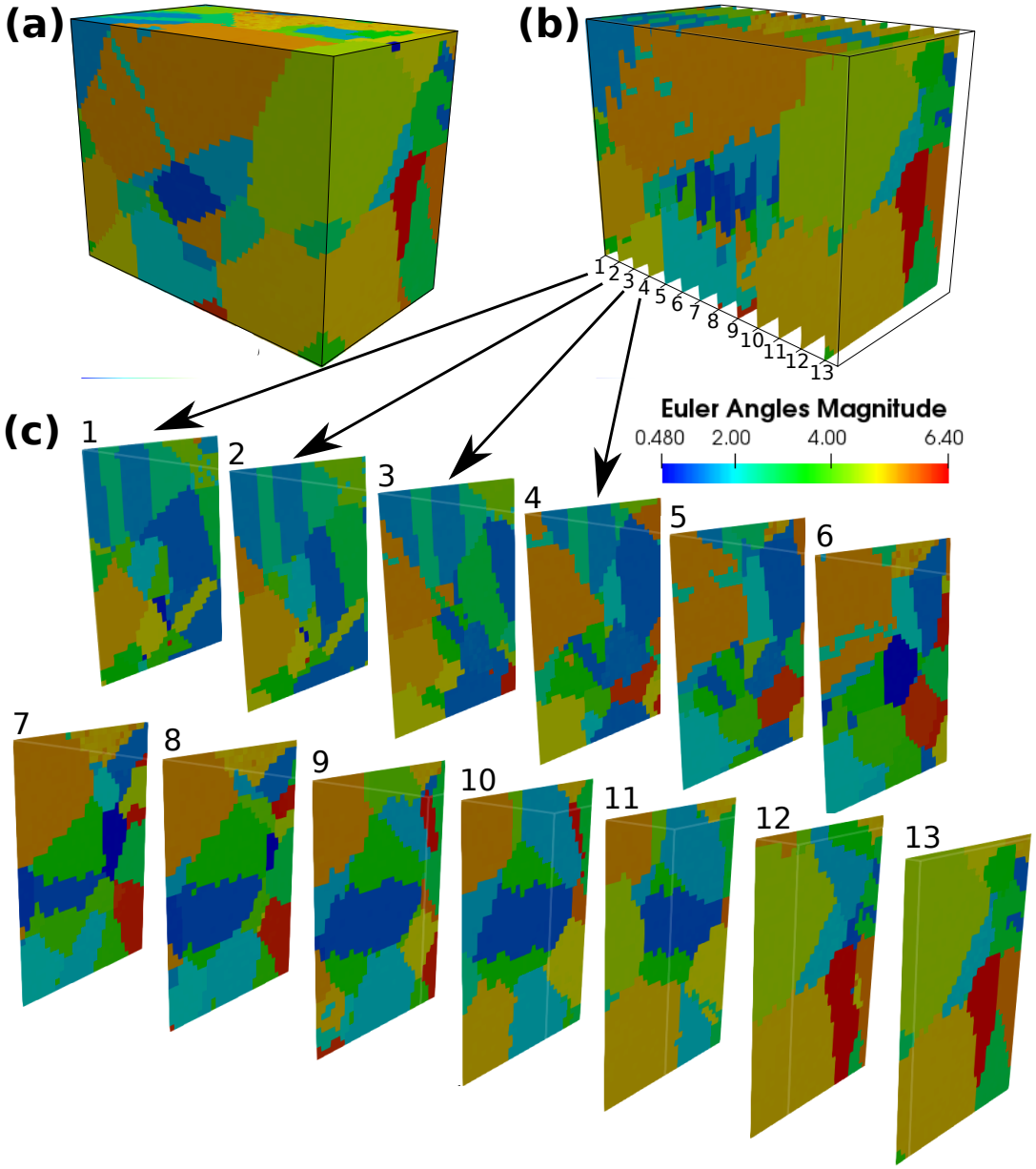

Figure 5.1: (a) 3D microstructure immersed from EBSD data. (b) Position and numbering of the slides shown in (c). (c) Slides from the 3D microstructure. The color represents the magnitude of the Euler angles vector. Material: Inconel 718. Domain: $25 \times 20 \times 14.5 \mu m$. Voxel size: $0.5 \times 0.5 \times 0.5 \mu m$. Data from Franco Jaime and Dr. Alexis Nicolay, Cemef, Mines ParisTech.

Figure 5.2 shows the φ_1 Euler angle of a 3D microstructure and the disorientation of two central grains composed of two TBs colored in red. A simulation of 60 seconds is performed using the Isotropic (Iso) and the Anisotropic formulations with Isotropic GB mobility (Aniso(μ:Iso)) and heterogeneous GB mobility (Aniso(μ:S)). The time step is fixed at $\Delta t = 1s$ and the domain is discretized

using an unstructured static tetrahedral mesh with a mesh size of $h = 0.5\mu m$.

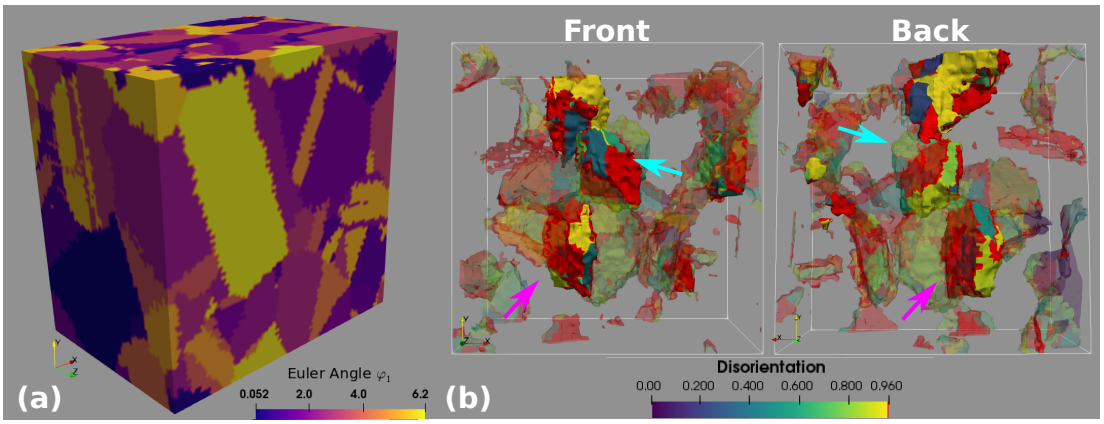

Figure 5.2: (a) Euler angle field φ_1 of 3D microstructure immersed from EBSD data. (b) Front and back view of two twin boundaries near the center of the volume. The color map is referring to the disorientation and the cyan and magenta arrows point out the two grains of interest. Material: Inconel 718. Domain: $40 \times 40 \times 27.5\mu m$. Voxel size: $0.5 \times 0.5 \times 0.5\mu m$. Data from Franco Jaime and Dr. Alexis Nicolay, Cemef, Mines ParisTech.

GB mobility and energy are respectively defined with a modified sigmoidal model (Equation 4.4) and the GB5DOF code. The maximal values are set to unitary values $\gamma_{max} = 1{\times}10^{-7} J/mm^2$ (Defined as ϵ_{RGB} in the GB5DOF code) and $\mu_{max} = 1mm^4/(Js)$. Figure 5.3 shows the DDF and GBED of the microstructure. In Figure 5.3a the peak around 60° is typical from Σ3 TBs and is also present in the DDF of a 2D microstructure in 316L (See Chapter 4).

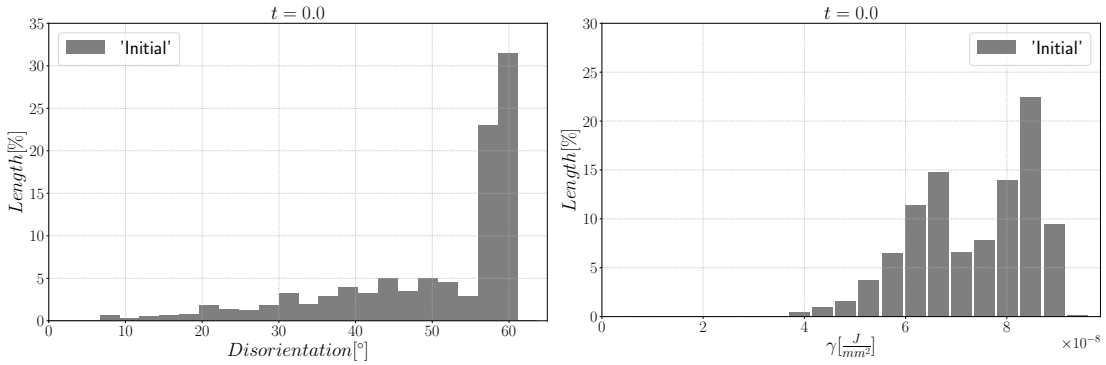

(a) DDF (b) GBED

Figure 5.3: Initial GB characteristics (a) disorientation distribution function and (b) GB energy distribution.

As in the 2D examples presented in Chapters 3 and 4, the Iso formulation is faster. Figure 5.4 shows the evolution of the number of grains and average

disorientation. The faster evolution of N_G obtained with the Iso formulation explains the faster minimization of the average disorientation and the total energy (Figure 5.4c). Figure 5.4d shows the total interfacial energy as a function of the total GB length. Note the linear behavior of the Iso formulation, this can be seen as a transition between efficient (above) and inefficient (below) energy minimization. In [35], a similar behavior is reported using an Anisotropic formulation without torque terms. Additionally, one can see the little difference between the Aniso(μ:Iso) and Aniso(μ:S) formulations. In Figures 5.5 and 5.6, the evolution of the TBs is shown. One can see that the difference between the Iso and Aniso(μ:Iso) is slight, similar to the 2D simulations.

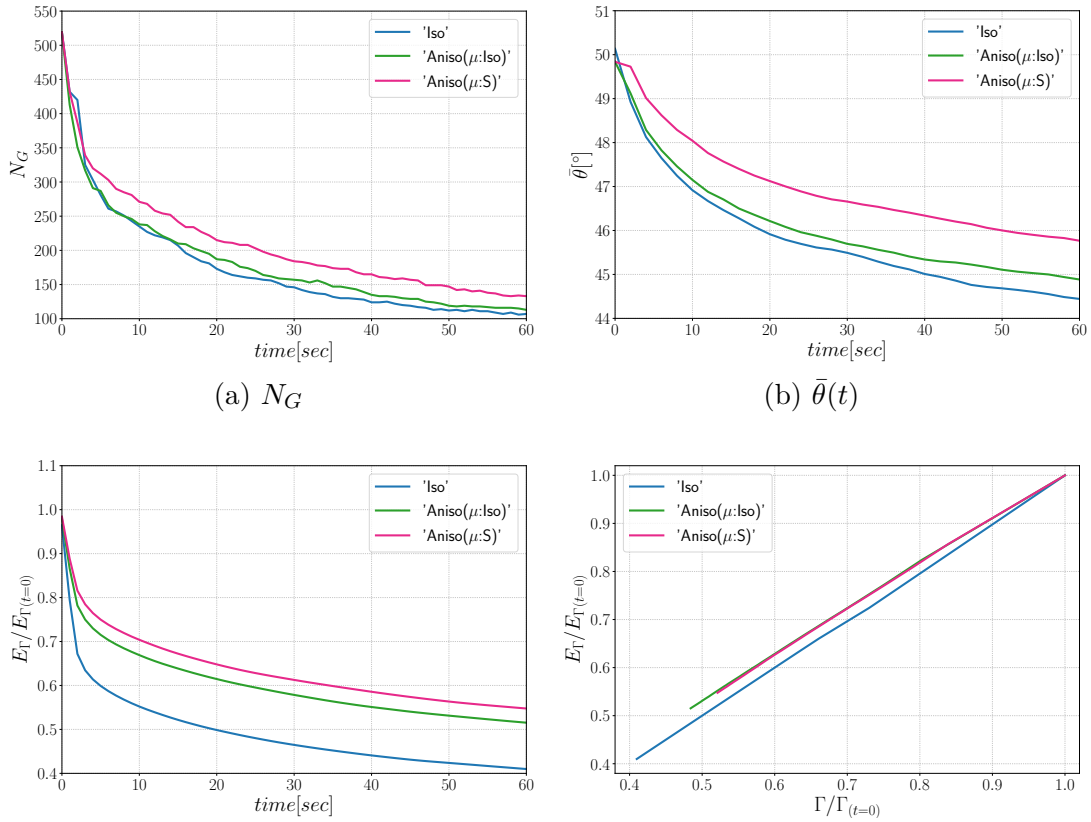

(a) N_G (b) $\bar{\theta}(t)$

(c) $E_\Gamma(t)/E_{\Gamma(t=0)}$ (d) $E_\Gamma/E_{\Gamma(t=0)}$ vs $\Gamma/\Gamma(t=0)$

Figure 5.4: Time series of 3D immersed simulations obtained using the Isotropic and Anisotropic formulations.

This study is in development and future simulations will be carried out using bigger volumes with a higher number of grains. In addition to the technical problems related to the characterization of bigger volumes, three additional items must be considered to understand GB movement in 3D:

- to estimate the GB reduced mobility $\mu\gamma$ using in-situ (sequential) heat treatments

- To introduce the effect of the GB stiffness tensor
- to dissociate the GB mobility from the GB energy thanks to an additional driving pressure by using a methodology similar to the one presented in the Appendix A.2.

A new project of the MSR Team is focused on the 3D characterization of microstructures. On the other hand, the basis of the integration of the GB stiffness tensor will be presented in the next section.

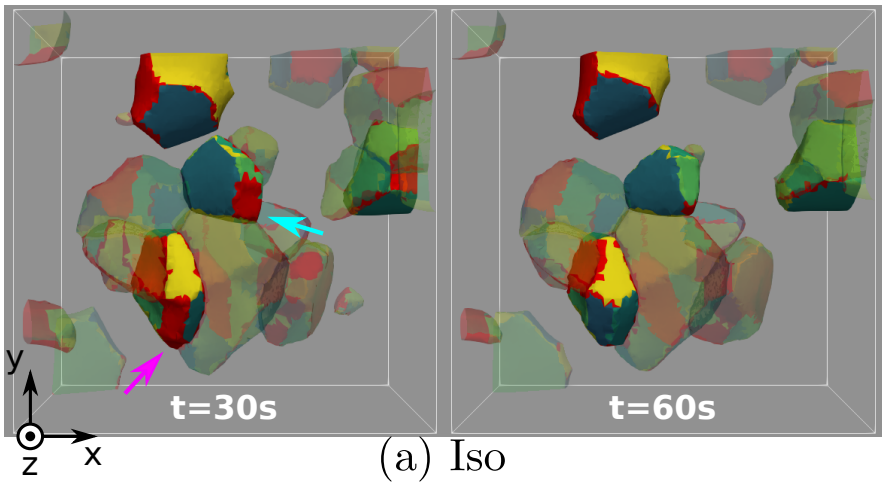

(a) Iso

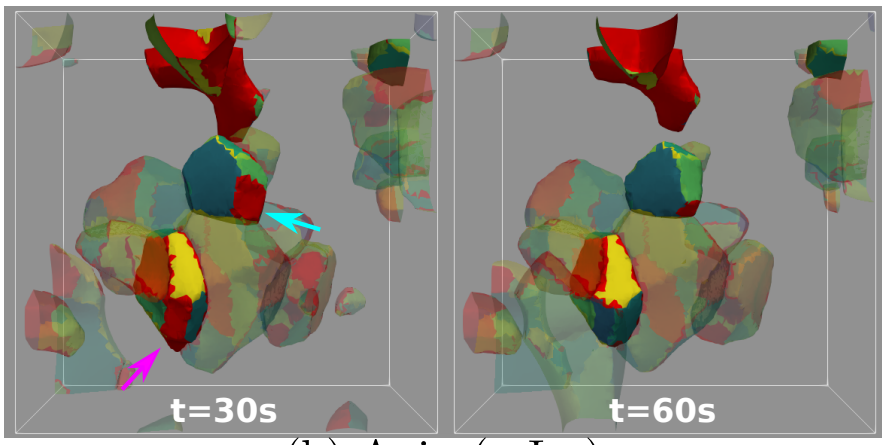

(b) Aniso(μ:Iso)

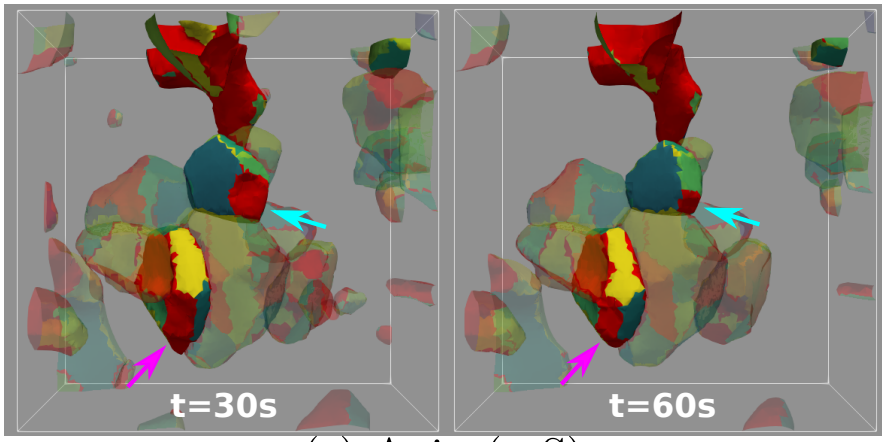

(c) Aniso(μ:S)

Figure 5.5: Grain evolution at different times, $t = \{30, 60\}s$. Front view. The two arrows point the same grains in Figure 5.2.

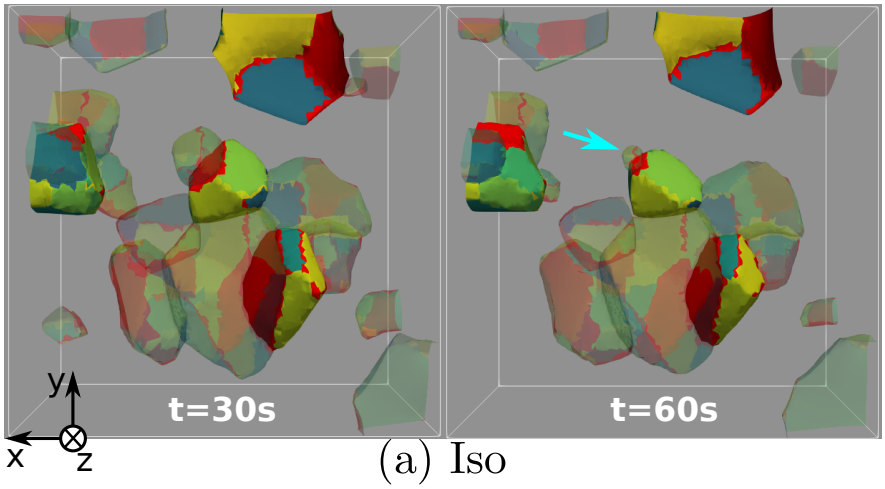

(a) Iso

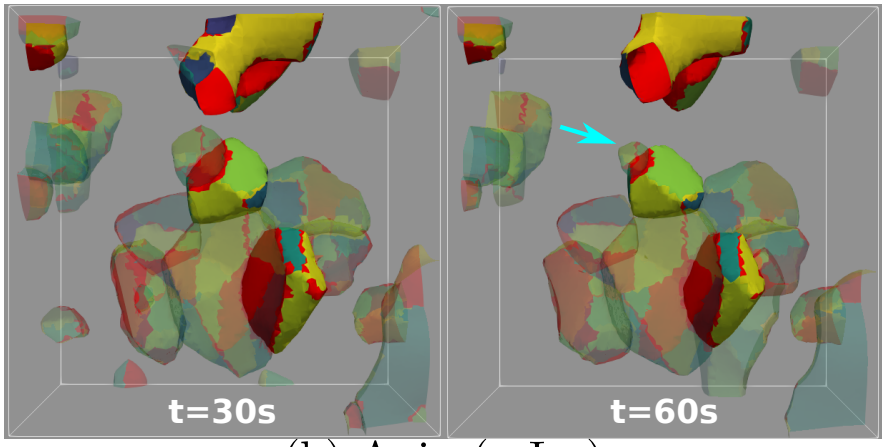

(b) Aniso(μ:Iso)

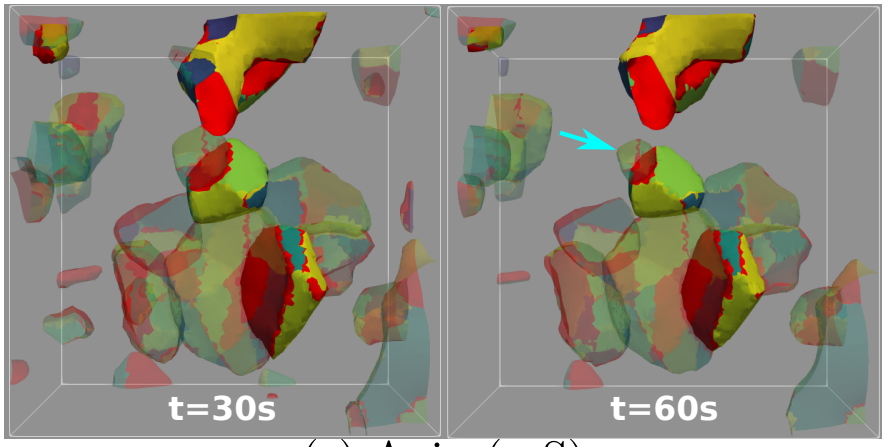

(c) Aniso(μ:S)

Figure 5.6: Grain evolution at different times, $t = \{30, 60\}s$. Back view. The arrow point the same grain in Figure 5.2.

5.2.2 Grain boundary stiffness tensor

GB stiffness tensor has been studied numerically using MD [104, 108–110, 220–222]. In [220], the authors pointed out that in some cases with high symmetry misorientation the minima of GB mobility can be canceled by a maximum value of the GB stiffness tensor $\Gamma(n)$ and vice versa. In [221], the authors studied the GB reduced mobility of a HL (half-loop) bicrystal, they found a linear relation between the GB velocity and curvature, and an Arrhenius behavior of the GB mobility but they computed average values of reduced mobility. Moreover, they couldn't dissociate the effect of the GB mobility anisotropy and GB stiffness tensor anisotropy from the average reduced mobility. Several question are still open regarding the effect of the GB stiffness tensor during GG and the impact over the actual knowledge of GB mobility. Additionally, for the author knowledge experiment research haven't been published about $\Gamma(n)$ that can confirm the hypothesis made in [220, 221].

Recent studies were carried out by Abdeljawad et al. in [104, 223], the GB stiffness tensor of $\Sigma 3$, $\Sigma 5$, $\Sigma 7$, $\Sigma 9$ and $\Sigma 11$ TBs in Ni is studied using a spherical grain. The work was based on the data coming from the works of Olmsted et al. [33, 90]. GB energy and mobility are fitted using Olmsted's database and the second derivative of γ, with respect to the inclination, is determined. The main observations obtained by the authors is that the anisotropy of the GB stiffness tensor is bigger than the anisotropy of GB energy for the aforementioned TBs and the GB stiffness tensor contribution can lead to faceted GBs.

The Anisotropic FE-LS formulation presented in chapter 2 has an intrinsic definition of the GB stiffness tensor. Combining the Anisotropic formulation [38, 134, 175] and the GB5DOF code to compute GB energy [34], the GB stiffness tensor could be studied for ideal cases such as TBs and more complex cases using polycrystalline microstructures. With the GB5DOF code, one can obtain the GB energy as a function of the grain boundary normal, Figure 5.7 shows the GB energy of the TBs $\Sigma 3$, $\Sigma 5$, $\Sigma 7$, $\Sigma 9$ and $\Sigma 11$. In this section we try to compute the GB stiffness tensor using the data obtained from the GB5DOF code.

The GB stiffness tensor is defined as:

$$\Gamma(\vec{n}) = \vec{\nabla}_{\vec{n}}\vec{\nabla}_{\vec{n}}\gamma + \gamma\mathbb{I}, \tag{5.1}$$

with

$$\vec{\nabla}_{\vec{n}}\gamma = \mathbb{P}\vec{\nabla}\gamma = (\mathbb{I} - \vec{n}\otimes\vec{n})\vec{\nabla}\gamma. \tag{5.2}$$

For a given misorientation M, the GB energy is defined as a function of the GB inclination $\gamma(\vec{n})$. In [104], the spherical coordinate system was preferred to define the term $\vec{\nabla}_{\vec{n}}\vec{\nabla}_{\vec{n}}\gamma$. Thus, $\vec{n}$ is defined in a unitary sphere using the polar θ_s and azimuthal ϕ_s angles with $\vec{n} = (cos(\phi_s)sin(\theta_s), sin(\phi_s)sin(\theta_s), cos(\theta_s))$ and $\gamma(\vec{n}) = \gamma(\theta_s, \phi_s)$. In that way, Equation 5.2 may be rewritten as

$$\vec{\nabla}_{\vec{n}}\gamma = \frac{\gamma_{\theta_s}}{R}\hat{\theta}_s + \frac{\gamma_{\phi_s}}{Rsin(\theta_s)}\hat{\phi}_s, \tag{5.3}$$

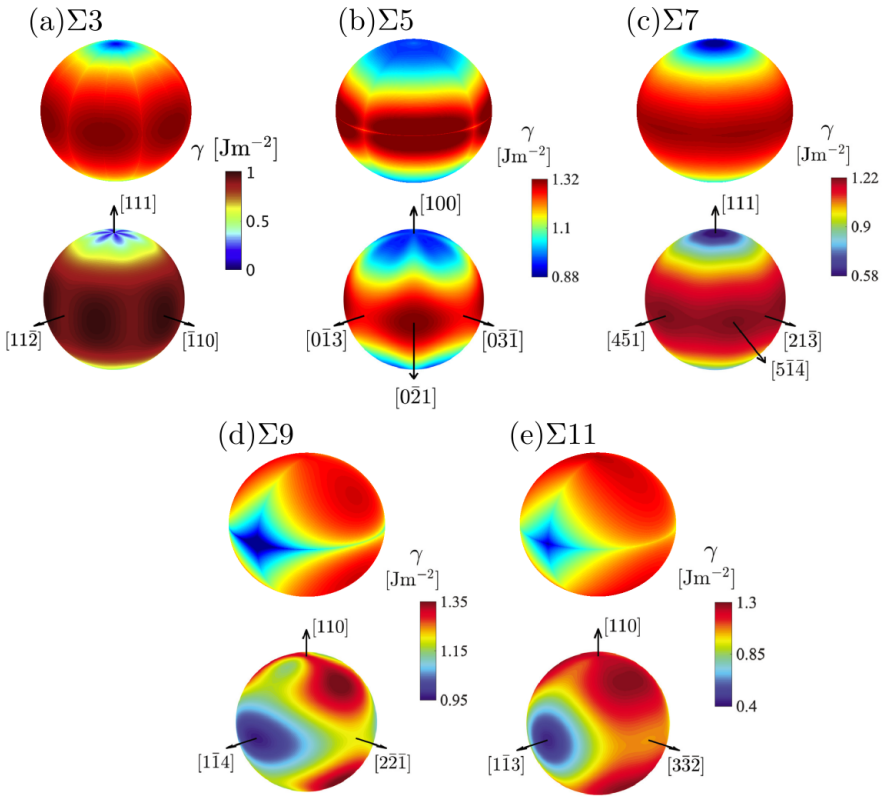

Figure 5.7: Grain boundary energy of the TBs Σ3, Σ5, Σ7, Σ9 and Σ11 obtained using the code GB5DOF. The top corresponds to the GB energy computed using the GB5DOF code and the bottom is the GB energy fitted by Abdeljawad et al. in [104, 223].

where $\gamma_{\theta_s} = \partial\gamma/\partial\theta_s$ and similar expressions for γ_{ϕ_s} or $\gamma_{\phi_s\theta_s}$. The relation of the second surface gradient is defined and the GB stiffness tensor is obtained using the spherical coordinate system [104]

$$\Gamma(\vec{n}) = \Gamma(\theta_s, \phi_s) = \begin{bmatrix} \gamma + \gamma_{\theta_s\theta_s} & \frac{1}{sin\theta_s}\gamma_{\theta_s\phi_s} - \frac{cos\theta_s}{sin^2\theta_s}\gamma_{\phi_s} \\ \frac{1}{sin\theta_s}\gamma_{\theta_s\phi_s} - \frac{cos\theta_s}{sin^2\theta_s}\gamma_{\phi_s} & \gamma + \frac{1}{sin^2\theta_s}\gamma_{\phi_s\phi_s} + \frac{cos\theta_s}{sin\theta_s}\gamma_{\theta_s} \end{bmatrix}, \quad (5.4)$$

after this parameterization, diagonalization of Γ leads to a simpler equation

$$\Gamma^*(\vec{n}) = \Gamma^*(\theta_s, \phi_s) = \begin{bmatrix} \lambda_1 & 0 \\ 0 & \lambda_2 \end{bmatrix} = A\Gamma(\vec{n})A^T, \quad (5.5)$$

being A the matrix of principal directions (eigenvectors) and $\lambda_{1,2}$ the eigenvalues defined as $\lambda_{1,2} = f(\theta_s, \phi_s) \pm g(\theta_s, \phi_s)$. The functions f and g are defined as

$$f(\theta_s, \phi_s) = \gamma + \frac{1}{2}\gamma_{\theta_s\theta_s} + \frac{1}{2}\frac{cos\theta_s}{sin\theta_s}\gamma_{\theta_s} + \frac{1}{2}\frac{1}{sin^2\theta_s}\gamma_{\phi_s\phi_s}, \quad (5.6)$$

and

$$g(\theta_s,\phi_s)=\frac{1}{2}\left[\left(\gamma_{\theta_s\theta_s}-\frac{1}{sin^2\theta_s}\gamma_{\phi_s\phi_s}-\frac{cos\theta_s}{sin\theta_s}\gamma_{\theta_s}\right)^2+\right.$$
$$\left.+4\left(\frac{1}{sin\theta_s}\gamma_{\theta_s\phi_s}-\frac{cos\theta_s}{sin^2\theta_s}\gamma_{\phi_s}\right)^2\right]^{1/2}. \quad (5.7)$$

In order to make easier the implementation, one can make the following assumptions: first, the energy varies smoothly. Second, the variations are allowed along the constant polar or azimuthal curves. Thus, the eigenvalues may be redefined as

$$\lambda_1=\gamma+\gamma_{\theta_s\theta_s}, \quad (5.8)$$

and

$$\lambda_2=\gamma+\gamma_{\phi_s\phi_s}. \quad (5.9)$$

Figures 5.8, 5.9 and 5.10 show some of the results obtained in [104]. Figure 5.8 shows the principal GB stiffness values of the Σ3 TB in a 3D spherical grain. One can see the abrupt changes of λ_1 and λ_2 and the symmetries which are different from the symmetry of μ and γ. The negative values represent instabilities and can be the origin of faceted GBs. Figure 5.9 shows the change of γ, λ_1 and λ_2 in 2D for a given value of polar and azimuthal angles. It is pointed out that the principal values of the GB stiffness tensor are more anisotropic (sensible to the inclination) than the GB energy itself.

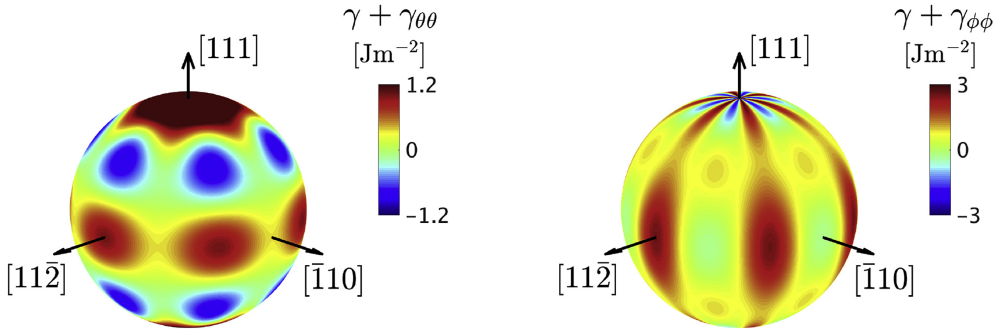

Figure 5.8: Plots of the of the principal stiffness values of the Σ3 TB in Ni. Figure from [104].

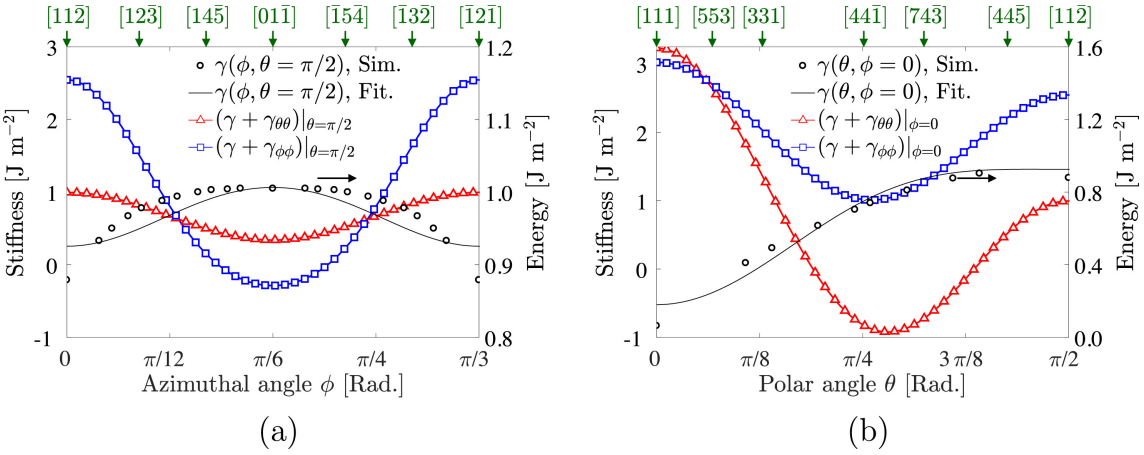

Figure 5.9: Plots of the principal stiffness values along (a) $\theta_s = \pi/2$ and (b) $\phi = 0$ of the $\Sigma 3$ TB in Ni. Figure from [104].

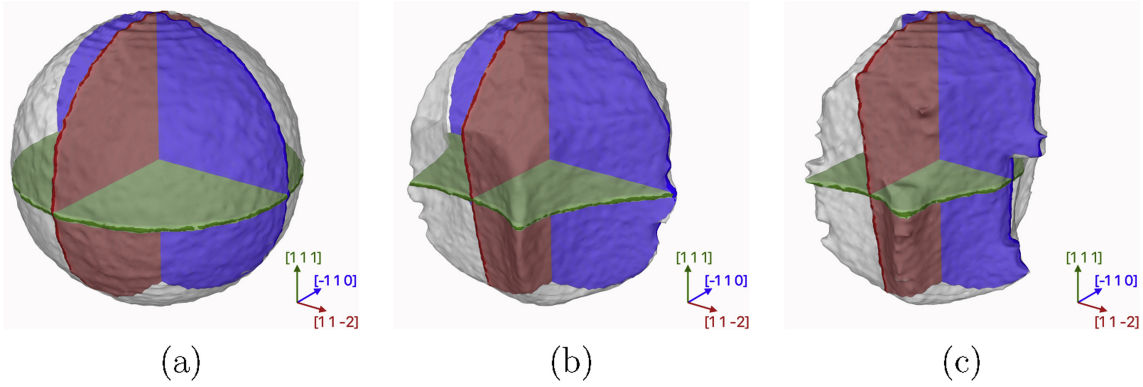

Figure 5.10: Evolution of the inner grain of the $\Sigma 3$ TB in Ni at (a) t=0, (b) t=0.1 ns and (c) t=6.1 ns using MD. (111) (green), ($\bar{1}$10) (blue), (11$\bar{2}$) (red) fiducial planes are included. The GB surface mesh is colored in gray. Figure from [104].

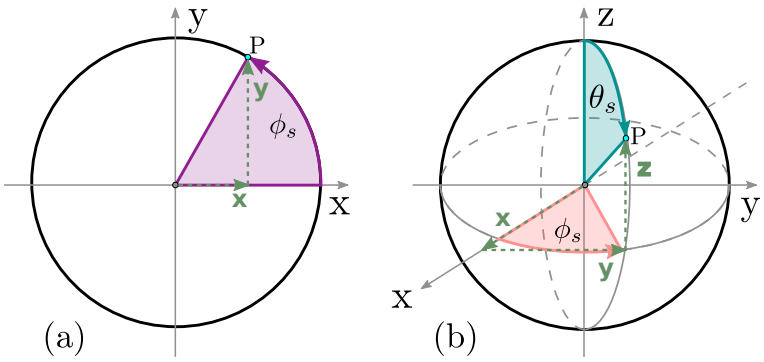

Figure 5.11: (a) Polar and (b) Spherical coordinates used in this section. In the spherical coordinates, θ_s and ϕ_s are the polar and azimuthal angles, respectively.

The evolution of the initial spherical grain is depicted in Figure 5.10 at $T = 500K \approx 0.3T_m$. One can see that after 0.1 ns, the GB is faceted and the interfaces along the [111] axis evolves slowly.

In order to study the effect of the GB stiffness tensor using the LS-FE framework, the coordinates must be changed from Spherical to Cartesian. Figure 5.11 illustrates, on a unitary sphere, the polar and spherical coordinates system used during the development of this section.

The GB stiffness tensor is constructed term by term. First, the surface gradient which is defined in Equation 5.2 must be redefined using Cartesian coordinates:

$$\vec{\nabla}_n\gamma = \begin{bmatrix} (1-x^2)\gamma_x - xy\gamma_y - xz\gamma_z \\ -xy\gamma_x + (1-y^2)\gamma_y - yz\gamma_z \\ -xz\gamma_x - yz\gamma_y + (1-z^2)\gamma_z \end{bmatrix}, \tag{5.10}$$

where $\gamma_y = \partial\gamma/\partial y$ is the first derivative.

The second surface gradient is defined as:

$$
\begin{aligned}
&\vec{\nabla}_n\vec{\nabla}_n\gamma = \\
&\quad -2x(1-x)\gamma_x + (1-x^2)^2\gamma_{xx} - 2xy(1-x^2)\gamma_{xy} - 2xz(1-x^2)\gamma_{xz} \\
&\quad -y(1-2x^2)\gamma_y + x^2y^2\gamma_{yy} + 2x^2yz\gamma_{yz} - z(1-2x^2)\gamma_z + x^2z^2\gamma_{zz}\boldsymbol{a^1a^1} \\
&\\
&\quad y(1-2x^2)\gamma_x - xy(1-x^2)\gamma_{xx} + (z^2+2x^2y^2)\gamma_{xy} - yz(1-2x^2)\gamma_{xz} \\
&\quad +2xy^2\gamma_y - xy(1-y^2)\gamma_{yy} - xz(1-2y^2)\gamma_{yz} + 2xyz\gamma_z + xyz^2\gamma_{zz}\boldsymbol{a^1a^2} \\
&\\
&\quad -z(1-2x^2)\gamma_x - xz(1-x^2)\gamma_{xx} - yz(1-2x^2)\gamma_{xy} + (y^2+2x^2z^2)\gamma_{xz} \\
&\quad 2xyz\gamma_y + xy^2z\gamma_{yy} - xy(1-2z^2)\gamma_{yz} + 2xz^2\gamma_z - xz(1-z^2)\gamma_{zz}\boldsymbol{a^1a^3} \\
&\\
&\quad 2x^2y\gamma_x - xy(1-x^2)\gamma_{xx} + (z^2+2x^2y^2)\gamma_{xy} - yz(1-2x^2)\gamma_{xz} \\
&\quad -x(1-2y^2)\gamma_y - xy(1-y^2)\gamma_{yy} - xz(1-2y^2)\gamma_{yz} + 2xyz\gamma_z + xyz^2\gamma_{zz}\boldsymbol{a^2a^1} \\
&\\
&\quad -x(1-2y^2)\gamma_x + x^2y^2\gamma_{xx} - 2xy(1-y^2)\gamma_{xy} + 2xy^2z\gamma_{xz} \\
&\quad -2y(1-y^2)\gamma_y + (1-y^2)^2\gamma_{yy} - 2yz(1-y^2)\gamma_{yz} - z(1-2y^2)\gamma_z + y^2z^2\gamma_{zz}\boldsymbol{a^2a^2} \\
&\\
&\quad 2xyz\gamma_x + x^2yz\gamma_{xx} - xz(1-2y^2)\gamma_{xy} - xy(1-2z^2)\gamma_{xz} \\
&\quad -z(1-2y^2)\gamma_y - yz(1-y^2)\gamma_{yy} + (x^2+2y^2z^2)\gamma_{yz} + 2yz^2\gamma_z - yz(1-z^2)\gamma_{zz}\boldsymbol{a^2a^3} \\
&\\
&\quad 2x^2z\gamma_x - xz(1-x^2)\gamma_{xx} - yz(1-2x^2)\gamma_{xy} + (2x^2z^2+y^2)\gamma_{xz} \\
&\quad 2xyz\gamma_y + xy^2z\gamma_{yy} - xy(1-2z^2)\gamma_{yz} - x(1-2z^2)\gamma_z - xz(1-z^2)\gamma_{zz}\boldsymbol{a^3a^1} \\
&\\
&\quad 2xyz\gamma_x + x^2yz\gamma_{xx} - xz(1-2y^2)\gamma_{xy} - xy(1-2z^2)\gamma_{xz} \\
&\quad 2y^2z\gamma_y - yz(1-y^2)\gamma_{yy} + (2y^2z^2+x^2)\gamma_{yz} - y(1-2z^2)\gamma_z - yz(1-z^2)\gamma_{zz}\boldsymbol{a^3a^2} \\
&\\
&\quad -x(1-2z^2)\gamma_x + x^2z^2\gamma_{xx} + 2xyz^2\gamma_{xy} - 2xz(1-z^2)\gamma_{xz} \\
&\quad -y(1-2z^2)\gamma_y + y^2z^2\gamma_{yy} - 2yz(1-z^2)\gamma_{yz} - 2z(1-z^2)\gamma_z + (1-z^2)^2\gamma_{zz}\boldsymbol{a^3a^3}
\end{aligned}
\tag{5.11}
$$

where $\boldsymbol{a^1} = \hat{x}$, $\boldsymbol{a^2} = \hat{y}$ and $\boldsymbol{a^3} = \hat{z}$ denote the matrix components and the terms with two subscripts as γ_{xx} denote second derivatives.

Hence, the GB stiffness tensor may be redefined as:

$$
\begin{aligned}
\Gamma(\vec{n}) = \Gamma(x,y,z) = \\
&\gamma - 2x(1-x)\gamma_x + (1-x^2)^2\gamma_{xx} - 2xy(1-x^2)\gamma_{xy} - 2xz(1-x^2)\gamma_{xz} \\
&-y(1-2x^2)\gamma_y + x^2y^2\gamma_{yy} + 2x^2yz\gamma_{yz} - z(1-2x^2)\gamma_z + x^2z^2\gamma_{zz}\boldsymbol{a^1a^1} \\
\\
&y(1-2x^2)\gamma_x - xy(1-x^2)\gamma_{xx} + (z^2+2x^2y^2)\gamma_{xy} - yz(1-2x^2)\gamma_{xz} \\
&+2xy^2\gamma_y - xy(1-y^2)\gamma_{yy} - xz(1-2y^2)\gamma_{yz} + 2xyz\gamma_z + xyz^2\gamma_{zz}\boldsymbol{a^1a^2} \\
\\
&-z(1-2x^2)\gamma_x - xz(1-x^2)\gamma_{xx} - yz(1-2x^2)\gamma_{xy} + (y^2+2x^2z^2)\gamma_{xz} \\
&2xyz\gamma_y + xy^2z\gamma_{yy} - xy(1-2z^2)\gamma_{yz} + 2xz^2\gamma_z - xz(1-z^2)\gamma_{zz}\boldsymbol{a^1a^3} \\
\\
&2x^2y\gamma_x - xy(1-x^2)\gamma_{xx} + (z^2+2x^2y^2)\gamma_{xy} - yz(1-2x^2)\gamma_{xz} \\
&-x(1-2y^2)\gamma_y - xy(1-y^2)\gamma_{yy} - xz(1-2y^2)\gamma_{yz} + 2xyz\gamma_z + xyz^2\gamma_{zz}\boldsymbol{a^2a^1} \\
\\
&\gamma - x(1-2y^2)\gamma_x + x^2y^2\gamma_{xx} - 2xy(1-y^2)\gamma_{xy} + 2xy^2z\gamma_{xz} \\
&-2y(1-y^2)\gamma_y + (1-y^2)^2\gamma_{yy} - 2yz(1-y^2)\gamma_{yz} - z(1-2y^2)\gamma_z + y^2z^2\gamma_{zz}\boldsymbol{a^2a^2} \\
\\
&2xyz\gamma_x + x^2yz\gamma_{xx} - xz(1-2y^2)\gamma_{xy} - xy(1-2z^2)\gamma_{xz} \\
&-z(1-2y^2)\gamma_y - yz(1-y^2)\gamma_{yy} + (x^2+2y^2z^2)\gamma_{yz} + 2yz^2\gamma_z - yz(1-z^2)\gamma_{zz}\boldsymbol{a^2a^3} \\
\\
&2x^2z\gamma_x - xz(1-x^2)\gamma_{xx} - yz(1-2x^2)\gamma_{xy} + (2x^2z^2+y^2)\gamma_{xz} \\
&2xyz\gamma_y + xy^2z\gamma_{yy} - xy(1-2z^2)\gamma_{yz} - x(1-2z^2)\gamma_z - xz(1-z^2)\gamma_{zz}\boldsymbol{a^3a^1} \\
\\
&2xyz\gamma_x + x^2yz\gamma_{xx} - xz(1-2y^2)\gamma_{xy} - xy(1-2z^2)\gamma_{xz} \\
&2y^2z\gamma_y - yz(1-y^2)\gamma_{yy} + (2y^2z^2+x^2)\gamma_{yz} - y(1-2z^2)\gamma_z - yz(1-z^2)\gamma_{zz}\boldsymbol{a^3a^2} \\
\\
&\gamma - x(1-2z^2)\gamma_x + x^2z^2\gamma_{xx} + 2xyz^2\gamma_{xy} - 2xz(1-z^2)\gamma_{xz} \\
&-y(1-2z^2)\gamma_y + y^2z^2\gamma_{yy} - 2yz(1-z^2)\gamma_{yz} - 2z(1-z^2)\gamma_z + (1-z^2)^2\gamma_{zz}\boldsymbol{a^3a^3}
\end{aligned}
\tag{5.12}
$$

In practical terms, the GB stiffness tensor can be constructed as follows:

1. Compute $\vec{\nabla}\gamma$ $(\gamma_{,i})$
2. Compute $\mathbb{P}\vec{\nabla}\gamma$ $(\mathbb{P}_{ji}\gamma_{,i})$
3. Construct and compute $\vec{\nabla}\mathbb{P}\vec{\nabla}\gamma$ $((\mathbb{P}_{ji}\gamma_{,i})_{,k})$
4. Compute $\mathbb{P}\vec{\nabla}\mathbb{P}\vec{\nabla}\gamma$ $(\mathbb{P}_{lk}(\mathbb{P}_{ji}\gamma_{,i})_{,k})$
5. Compute $\Gamma = \mathbb{I}\gamma + \mathbb{P}\vec{\nabla}\mathbb{P}\vec{\nabla}\gamma$ $(\Gamma_{lj} = \mathbb{I}_{lj}\gamma + \mathbb{P}_{lk}(\mathbb{P}_{ji}\gamma_{,i})_{,k})$

In [104], the authors used the following functions of GB mobility and energy of the TB Σ3 fitted from atomistic data

$$\gamma_{\Sigma 3} = 681.8 - 355.6cos(2\theta) - 70.3cos(4\theta) - 30.2cos(6\phi) \\ - 17cos(6\phi)cos(2\theta) - 27.3cos(6\phi)cos(4\theta) - 1.1cos(12\phi), \quad (5.13)$$

$$\mu_{\Sigma 3} = 1.527 - 0.535cos(2\theta) - 0.361cos(4\theta) - 0.976cos(6\phi) \\ + 0.41cos(6\phi)cos(2\theta) + 0.359cos(6\phi)cos(4\theta) - 0.392cos(12\phi). \quad (5.14)$$

The 3D plots of the GB mobility and energy are shown in Figure 5.12. One can see that both GB properties have different symmetries and cusps. The anisotropy of the GB mobility is stronger for this particular case.

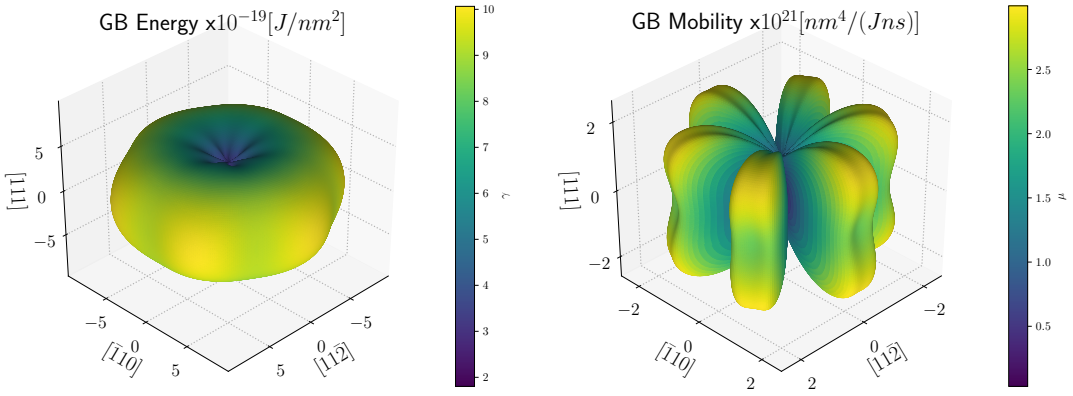

(a) (b)

Figure 5.12: GB Energy and Mobility of a Σ3 TB in Ni computed using Equations 5.13 and 5.14.

The GB reduced mobility and the product $\mu\Gamma$ are shown in Figure 5.13 using a constant GB mobility (Isotropic) and Figure 5.14 using the anisotropic GB mobility defined in Equation 5.14. The main difference between $\mu\gamma$ and $\mu\Gamma$ is the magnitude. The GB stiffness tensor has a bigger magnitude which is produced by its non-diagonal components.

The simulations were performed using the Het and Aniso formulations with isotropic and anisotropic GB mobility. The initial microstructure is composed of an initial spherical grain with initial radius $R = 20.35nm$ centered inside a domain of $50nm \times 50nm \times 50nm$ [104]. The geometry is discretized with a non-structured static mesh with a size of $h = 1nm$ and the time step is fixed at $\Delta t = 0.0005ns$. This geometry is adequate to study the effect of the GB stiffness tensor because the 3D anisotropy of the GB is taken into account.

Figures 5.13 and 5.14 show the initial GB reduced mobility and the initial magnitude of $\mu\Gamma$ which is computed as $\mu(\Gamma_{11}^2 + \Gamma_{12}^2 + \Gamma_{13}^2 + \Gamma_{21}^2 + \Gamma_{22}^2 + \Gamma_{23}^2\Gamma_{31}^2 + \Gamma_{32}^2 + \Gamma_{33}^2)^{0.5}$. For the case shown in Figure 5.13 the GB mobility is isotropic and

is set to an average value $\mu = 1.518 \times 10^{21}\ nm^4/(J \cdot ns)$. And for the case shown in Figure 5.14, the GB mobility is computed using Equation 5.14.

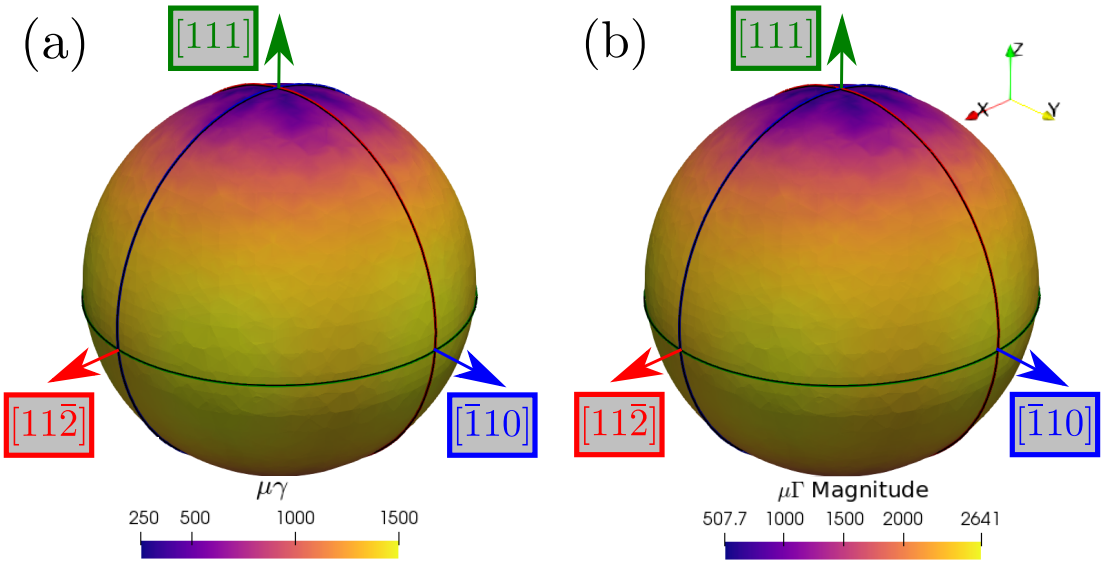

Figure 5.13: (a) Initial GB reduced mobility (nm^2/ns) used for the Het(μ:Iso) and Aniso(μ:Iso) formulations. (b) Initial $\mu\Gamma$ tensor magnitude (nm^2/ns) used for the Aniso5(μ:Iso) formulation. The black lines represent the XY, YZ and XZ planes.

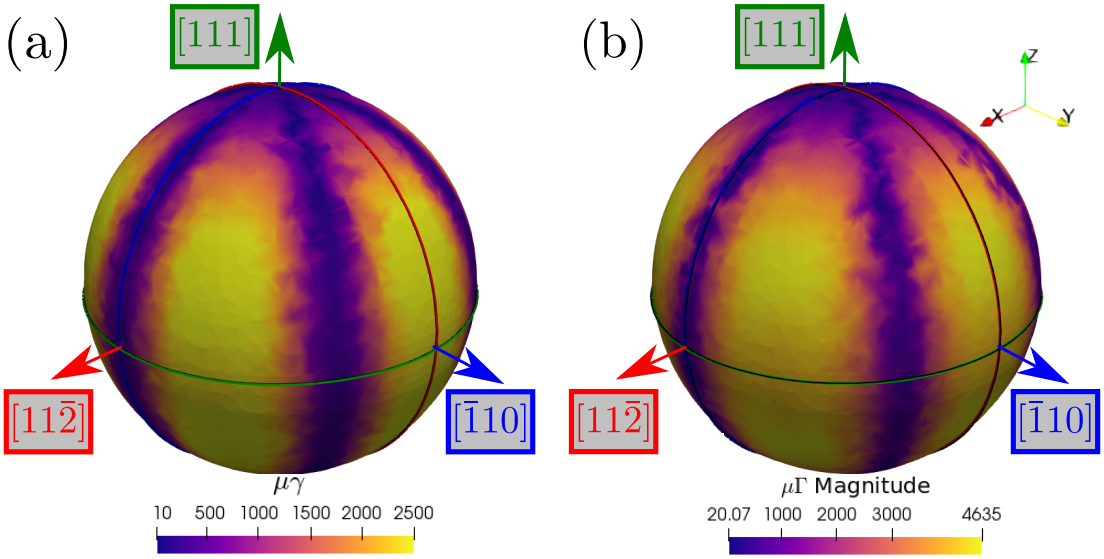

Figure 5.14: (a) Initial GB reduced mobility (nm^2/ns) used for the Het($\mu(\theta_s,\phi_s)$) and Aniso($\mu(\theta_s,\phi_s)$) formulations. (b) Initial $\mu\Gamma$ tensor magnitude (nm^2/ns) used for the Aniso5($\mu(\theta_s,\phi_s)$) formulation. The black lines represent the XY, YZ and XZ planes.

The evolution of the spherical grain is shown in Figure 5.16 using the isotropic

GB mobility and Figure 5.17 using the anisotropic GB mobility. Note there is no a noticeable difference in the GB morphology using the three formulations. The main change is produced by the definition of the GB mobility. The case with the isotropic GB mobility produces a ellipsoid-like grain, while the case with the anisotropic GB mobility generates a grain with an hexagonal profile in the XY plane that follows the symmetry of GB mobility, see Figure 5.15.

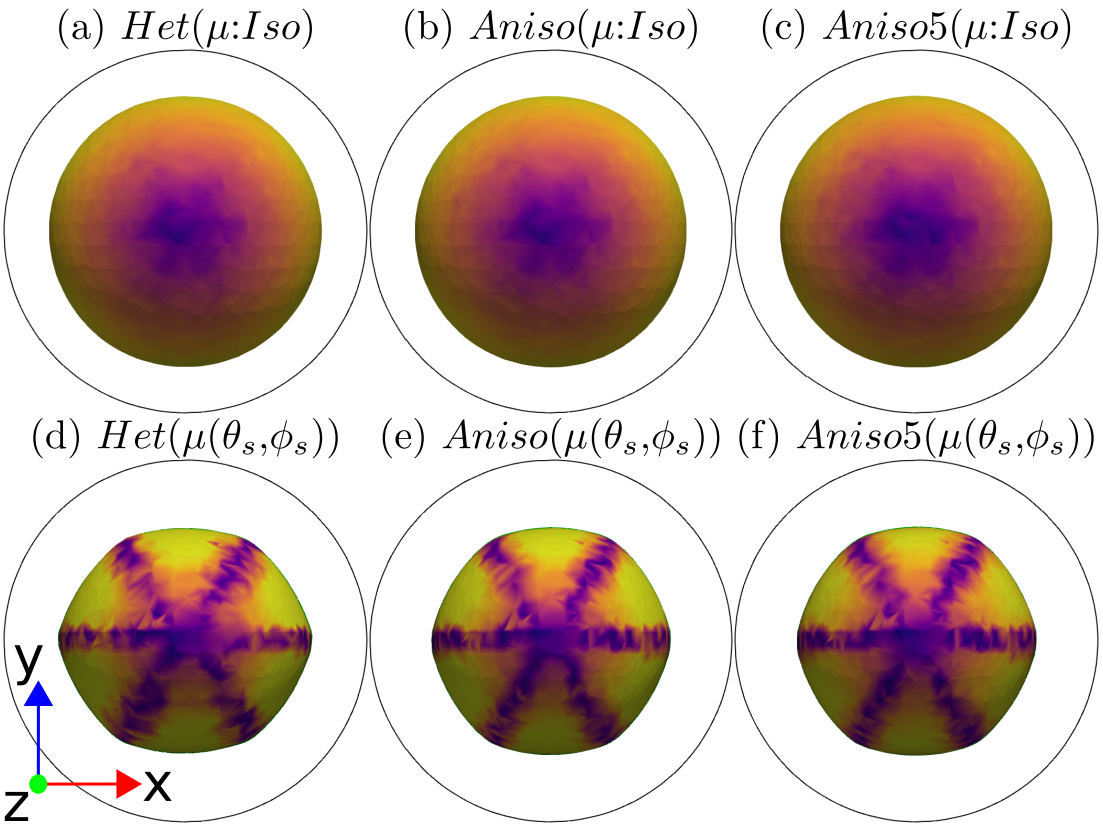

Figure 5.15: Top view (XY plane) of the grain at $t = 0.03\ ns$ obtained with the three formulations, and isotropic (top) and anisotropic (bottom) GB mobility. The black circle represents the initial radius of the grain in the XY plane.

The study of the GB stiffness tensor is relatively new, the first article that propose a clear way to study the tensor was published in 2018 [104] and a second one was published by the same group of authors in 2021 [223]. The introduction of the GB stiffness tensor in a mesoscopic framework needs more data concerning the GB mobility and energy as a function of the normal as well as the introduction of the disconnection nature of GBs. First ideas concerning a disconnection-based LS framework are detailed in the next section.

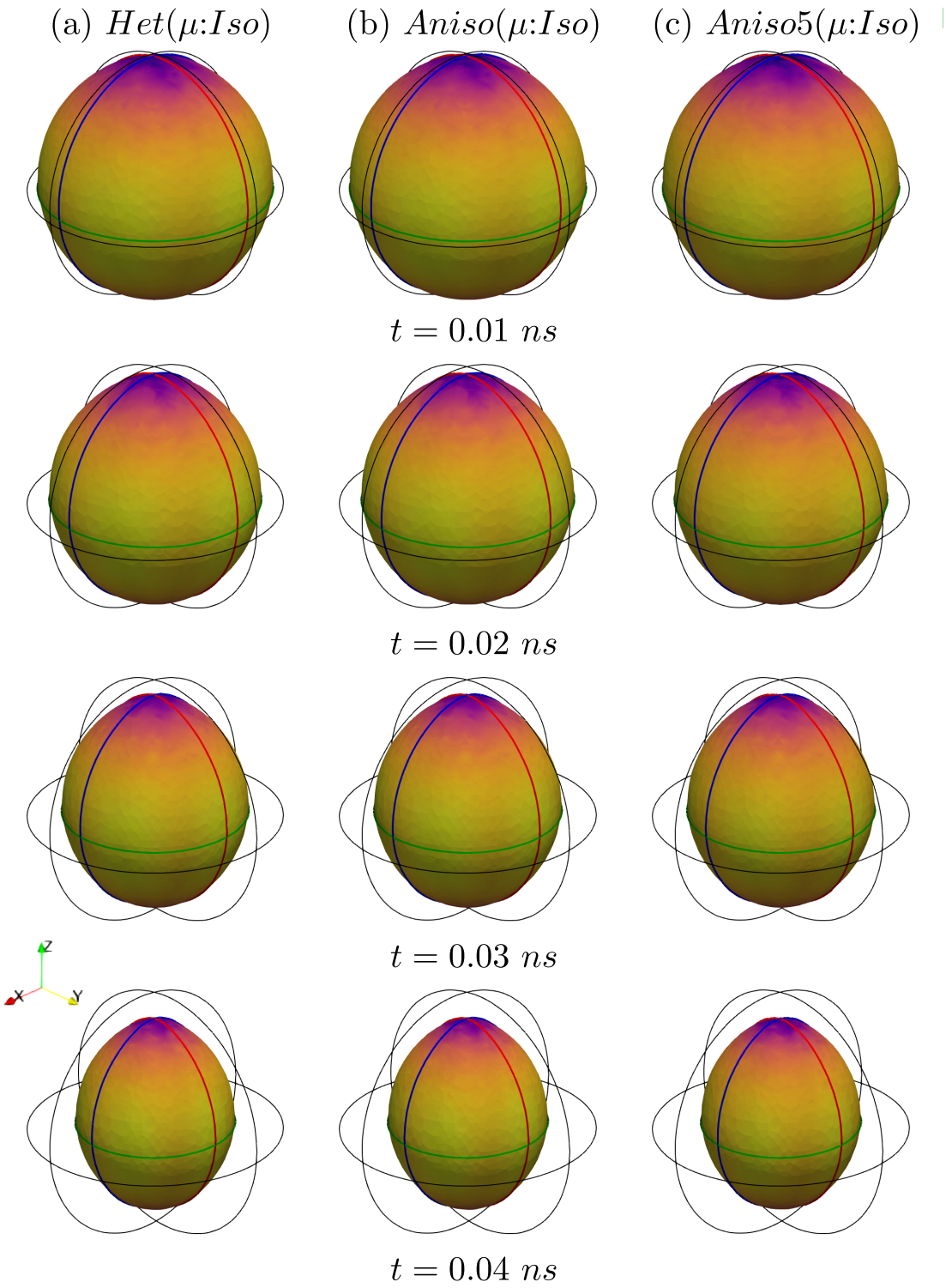

Figure 5.16: Evolution of the GB using the (a) Het(μ:Iso), (b) Aniso(μ:Iso) and (c) Aniso5(μ:Iso) formulations at $t = 0.01$, 0.02, 0.03, 0.04 ns using an isotropic GB mobility. The colorbar is the same as in Figure 5.13. The black lines represent the initial grain in the XY, YZ and XZ planes.

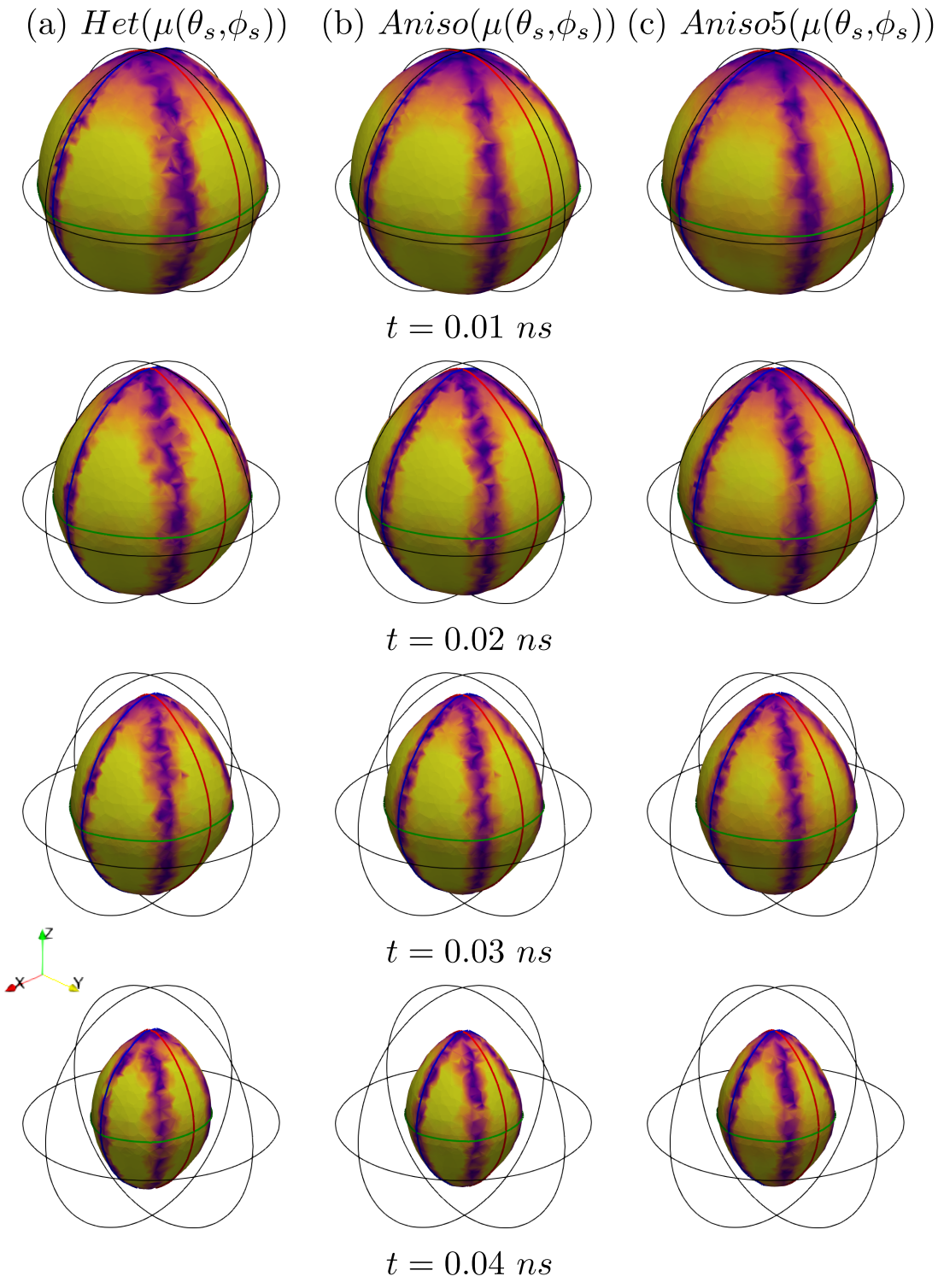

Figure 5.17: Evolution of the GB using the (a) Het($\mu(\theta_s,\phi_s)$), (b) Aniso($\mu(\theta_s,\phi_s)$) and (c) Aniso5($\mu(\theta_s,\phi_s)$) formulations at t =0.01, 0.02, 0.03, 0.04 ns using an anisotropic GB mobility. The colorbar is the same as in Figure 5.14. The black lines represent the initial grain in the XY, YZ and XZ planes.

5.2.3 LS Disconnection-based approach

Another ingredient that one can add to the FE-LS formulation is the disconnection character of the GB. The Anisotropic FE-LS formulation may be redefined as:

$$v_i = \left(\mathbb{P}_{kj}\gamma_{,j}n_k - \Gamma_{mn}\mathbb{K}_{mn} + \tau\Lambda\right)\mu n_i, \tag{5.15}$$

where $\tau = \tau_{disc} + \tau_{ext}$ is the shear stress composed of the external shear stress τ_{ext} and the stress generated by the disconnections along the interface τ_{disc}, and Λ describes the shear coupling. The driving pressure generated by $v_i^d = \mu\tau\Lambda n_i$ can change the profile of the interfaces and generate a stepped interface. The driving force produced by disconnections is defined as [181]:

$$P^d = \tau\Lambda, \tag{5.16}$$

with

$$\Lambda \equiv \beta^{(2)} - \beta^{(1)} = \frac{b^{(2)}}{h^{(2)}} - \frac{b^{(1)}}{h^{(1)}}, \tag{5.17}$$

where $\beta^{(m)}$ is the shear-coupling factor and $m = 1, 2$ represent the x and y axis, also called interface references. The stress generated by the disconnections is defined as:

$$\tau_{disc}(s) = \beta^{(1)} I_\Sigma^{(1)}(s) + \beta^{(2)} I_\Sigma^{(2)}(s), \tag{5.18}$$

where

$$I_\Sigma^{(m)}(s) = \frac{G}{2\pi(1-\nu)} \int_\Sigma \left\{ \left(\frac{dx_n}{ds}\right)_{s=s_0} \frac{x_m(s) - x_m(s_0)}{\varrho_a^2} \times \left[1 - \frac{2(x_n(s) - x_n(s_0))^2}{\varrho_a^2}\right] \right\} ds_0, \tag{5.19}$$

$(m, n) \in \{(1, 2), (2, 1)\}$, $\varrho_a^2 \equiv [x_1(s) - x_1(s_0)]^2 + [x_2(s) - x_2(s_0)]^2 + a^2$, and G, ν and a are respectively the shear modulus, Poisson ratio and a parameter related to the disconnection core size [181,224]. In the finite element mesh the stress is computed in the set of points around the zero iso-value of the level set function $x_i \in \Sigma_{\phi\pm\delta}$ describing the GB, $\tau_{disc}(s) \equiv \tau_{disc}(x_i)$ using the following equation [181]:

$$\tau_{disc}(x_i) = \sum_{x_j \in \Sigma} \left[\Delta S \beta^{(1)} \frac{dx_2}{ds}(x_j) \tau^{(1)}(x_i, x_j) + \beta^{(2)} \frac{dx_1}{ds}(x_i) \tau^{(2)}(x_i, x_j) \right], \tag{5.20}$$

with

$$\tau^{(m)}(x_i, x_j) = \frac{G}{2\pi(1-\nu)} \frac{x_m(x_i) - x_m(x_j)}{\varrho_a^2(x_i, x_j)} \left[1 - \frac{2(x_n(x_i) - x_n(x_j))^2}{\varrho_a^2(x_i, x_j)}\right], \tag{5.21}$$

and

$$\varrho_a^2(x_i, x_j) = [x_1(x_i) - x_1(x_j)]^2 + [x_2(x_i) - x_2(x_j)]^2 + a^2, \tag{5.22}$$

$(m, n) = (1, 2)$ or $(2, 1)$, $dx_j/ds = (x^j_{i+1} - x^j_{i-1})(\Delta S)$, $\Delta S = (|x_{i+1} - x_i| + |x_i - x_{i-1}|)^{0.5}$.

Due to a lack of time, the aforementioned equations were not tested in our FE-LS framework. Two important questions may be studied: what is the effect of the temperature on β and how can it be studied experimentally? Do the driving force $P^d = \tau\Lambda$ have an important effect in the context of hot metal forming? These studies are relatively new in the state of the art and we need more data to answer to these questions. Although, it has been shown that the effect of disconnections can highly affect the shape of GBs [181], and there is an infinite set of disconnections modes (b,h) that describes an interface; but at high temperatures, one can describe the kinetics of a GB using a statistical average of the contribution of all the activated modes [128].

5.3 Résumé en Français du Chapitre 5

Outre un résumé des principaux résultats exposés dans les chapitres précédents, ce chapitre a permis de décrire différentes perspectives immédiates de ce travail et différents résultats préliminaires ont été détaillés.

Ces perspectives concernent une discussion 3D des modèles développés, l'introduction du tenseur de rigidité dans l'ensemble des discussions et l'intérêt ou non à introduire le concept de disconnections dans nos approches LS lorsque des prédictions à l'échelle mésoscopique et dans un contexte de mise en forme à chaud sont visées.

Bibliography

[1] A. Rollett, G. S. Rohrer, and J. Humphreys. *Recrystallization and Related Annealing Phenomena*. Elsevier, 2017. (Cited on pages 3, 24, 27, 30, 33, 34, 35, 38, 39, 42, 44, and 45.)

[2] L. Zhang, J. Han, Y. Xiang, and D. J. Srolovitz. Equation of motion for a grain boundary. *Phys. Rev. Lett.*, 119:246101, Dec 2017. (Cited on pages 3, 35, 66, and 70.)

[3] Q. Zhu, G. Cao, J. Wang, C. Deng, J. Li, Z. Zhang, and S. X. Mao. In situ atomistic observation of disconnection-mediated grain boundary migration. *Nature communications*, 10(1):1–8, 2019. (Cited on pages 3 and 70.)

[4] C. S. Smith. Introduction to grains, phases, and interfaces—an interpretation of microstructure. *Transactions of the American Institute of Mining and Metallurgical Engineers*, 175(2):15–51, 1948. (Cited on page 3.)

[5] S. Kohara, M. N. Parthasarathi, and P. A. Beck. Anisotropy of boundary mobility. *Journal of Applied Physics*, 29(7):1125–1126, 1958. (Cited on pages 3 and 42.)

[6] M. Wang, J. Dake, S. S., D. Molodov, and C. Krill III. Reverse engineering the kinetics of grain growth in Al-based polycrystals by microstructural mapping in 4D. In *40th Risø International Symposium on Materials Science*, 2019. (Cited on pages 3 and 70.)

[7] H. Garcke, B. Nestler, and B. Stoth. A multiphase field concept: numerical simulations of moving phase boundaries and multiple junctions. *SIAM Journal on Applied Mathematics*, 60(1):295–315, 1999. (Cited on pages 4, 55, and 76.)

[8] E. Miyoshi and T. Takaki. Multi-phase-field study of the effects of anisotropic grain-boundary properties on polycrystalline grain growth. *Journal of Crystal Growth*, 474:160–165, 2017. (Cited on pages 4, 55, 62, 70, and 97.)

[9] N. Moelans, F. Wendler, and B. Nestler. Comparative study of two phase-field models for grain growth. *Computational Materials Science*, 46(2):479–490, 2009. (Cited on pages 4 and 55.)

[10] J. Gao and R. Thompson. Real time-temperature models for monte carlo simulations of normal grain growth. *Acta materialia*, 44(11):4565–4570, 1996. (Cited on pages 4 and 55.)

[11] M. Upmanyu, G. N. Hassold, A. Kazaryan, E. A. Holm, Y. Wang, B. Patton, and D. J. Srolovitz. Boundary mobility and energy anisotropy effects on microstructural evolution during grain growth. *Interface Science*, 10(2):201–216, 2002. (Cited on pages 4, 55, and 56.)

[12] P. W. Hoffrogge and L. A. Barrales-Mora. Grain-resolved kinetics and rotation during grain growth of nanocrystalline aluminium by molecular dynamics. *Computational Materials Science*, 128:207–222, 2017. (Cited on pages 4, 49, and 50.)

[13] S. Sakout, D. Weisz-Patrault, and A. Ehrlacher. Energetic upscaling strategy for grain growth. i: Fast mesoscopic model based on dissipation. *Acta Materialia*, 196:261–279, 2020. (Cited on pages 4, 55, and 70.)

[14] L. A. Barrales Mora. 2D vertex modeling for the simulation of grain growth and related phenomena. *Mathematics and Computers in Simulation*, 80(7):1411–1427, 2010. (Cited on pages 4, 55, 59, and 60.)

[15] F. Wakai, N. Enomoto, and H. Ogawa. Three-dimensional microstructural evolution in ideal grain growth—general statistics. *Acta Materialia*, 48(6):1297–1311, 2000. (Cited on pages 4 and 55.)

[16] S. Florez, M. Shakoor, T. Toulorge, and M. Bernacki. A new finite element strategy to simulate microstructural evolutions. *Computational Materials Science*, 172:109335, 2020. (Cited on pages 4 and 55.)

[17] S. Florez, K. Alvarado, D. P. Muñoz, and M. Bernacki. A novel highly efficient lagrangian model for massively multidomain simulation applied to microstructural evolutions. *Computer Methods in Applied Mechanics and Engineering*, 367:113107, 2020. (Cited on pages 4, 55, 59, and 60.)

[18] M. Bernacki, R. E. Logé, and T. Coupez. Level set framework for the finite-element modeling of recrystallization and grain growth in polycrystalline materials. *Scripta Materialia*, 64(6):525–528, 2011. (Cited on pages 4, 55, 63, 64, and 120.)

[19] C. Mießen, M. Liesenjohann, L. Barrales-Mora, L. Shvindlerman, and G. Gottstein. An advanced level set approach to grain growth–accounting for grain boundary anisotropy and finite triple junction mobility. *Acta Materialia*, 99:39–48, 2015. (Cited on pages 4, 55, and 63.)

[20] J. Fausty, N. Bozzolo, and M. Bernacki. A 2D level set finite element grain coarsening study with heterogeneous grain boundary energies. *Applied*

Mathematical Modelling, 78:505 – 518, 2020. (Cited on pages 4, 55, 65, 73, 94, and 120.)

[21] M. Anderson, D. Srolovitz, G. Grest, and P. Sahni. Computer simulation of grain growth—i. kinetics. *Acta metallurgica*, 32(5):783–791, 1984. (Cited on pages 4, 55, and 56.)

[22] E. A. Lazar, J. K. Mason, R. D. MacPherson, and D. J. Srolovitz. A more accurate three-dimensional grain growth algorithm. *Acta Materialia*, 59(17):6837–6847, 2011. (Cited on pages 4 and 55.)

[23] A. Rollett, D. J. Srolovitz, and M. Anderson. Simulation and theory of abnormal grain growth—anisotropic grain boundary energies and mobilities. *Acta metallurgica*, 37(4):1227–1240, 1989. (Cited on pages 4 and 55.)

[24] N. M. Hwang. Simulation of the effect of anisotropic grain boundary mobility and energy on abnormal grain growth. *Journal of materials science*, 33(23):5625–5629, 1998. (Cited on pages 4 and 55.)

[25] J. Fausty, N. Bozzolo, D. P. Muñoz, and M. Bernacki. A novel level-set finite element formulation for grain growth with heterogeneous grain boundary energies. *Materials & Design*, 160:578–590, 2018. (Cited on pages 4, 55, 64, 65, 73, 74, 78, 86, and 88.)

[26] D. Zöllner and I. Zlotnikov. Texture Controlled Grain Growth in Thin Films Studied by 3D Potts Model. *Advanced Theory and Simulations*, 2(8):1900064, 2019. (Cited on pages 4 and 55.)

[27] E. Miyoshi and T. Takaki. Validation of a novel higher-order multi-phase-field model for grain-growth simulations using anisotropic grain-boundary properties. *Computational Materials Science*, 112:44–51, 2016. (Cited on pages 4 and 55.)

[28] K. Chang and H. Chang. Effect of grain boundary energy anisotropy in 2D and 3D grain growth process. *Results in Physics*, 12:1262–1268, 2019. (Cited on pages 4, 55, and 70.)

[29] E. Miyoshi, T. Takaki, M. Ohno, and Y. Shibuta. Accuracy evaluation of phase-field models for grain growth simulation with anisotropic grain boundary properties. *ISIJ International*, pages ISIJINT–2019, 2019. (Cited on pages 4, 55, and 86.)

[30] E. A. Holm, G. N. Hassold, and M. A. Miodownik. On misorientation distribution evolution during anisotropic grain growth. *Acta Materialia*, 49(15):2981–2991, 2001. (Cited on pages 4, 55, 70, 95, and 129.)

[31] A. Kazaryan, Y. Wang, S. Dregia, and B. Patton. Grain growth in anisotropic systems: comparison of effects of energy and mobility. *Acta Materialia*, 50(10):2491–2502, 2002. (Cited on pages 4, 55, and 62.)

[32] H. Hallberg and V. V. Bulatov. Modeling of grain growth under fully anisotropic grain boundary energy. *Modeling and Simulation in Materials Science and Engineering*, 27(4):045002, 2019. (Cited on pages 4, 55, 64, 70, 106, 107, 109, and 140.)

[33] D. L. Olmsted, S. M. Foiles, and E. A. Holm. Survey of computed grain boundary properties in face-centered cubic metals: I. grain boundary energy. *Acta Materialia*, 57(13):3694–3703, 2009. (Cited on pages 4, 106, 146, and 158.)

[34] V. V. Bulatov, B. W. Reed, and M. Kumar. Grain boundary energy function for fcc metals. *Acta Materialia*, 65:161–175, 2014. (Cited on pages 4, 25, 50, 64, 75, 106, 107, 119, 140, 146, and 158.)

[35] S. Florez, K. Alvarado, B. Murgas, N. Bozzolo, D. Chatain, C. E. Krill, M. Wang, G. S. Rohrer, and M. Bernacki. Statistical behaviour of interfaces subjected to curvature flow and torque effects applied to microstructural evolutions. *Acta Materialia*, page 117459, 2021. (Cited on pages 4, 154, and 212.)

[36] M. Upmanyu, R. Smith, and D. J. Srolovitz. Atomistic simulation of curvature driven grain boundary migration. *Interface science*, 6(1):41–58, 1998. (Cited on page 4.)

[37] K. Barmak, E. Eggeling, D. Kinderlehrer, R. Sharp, S. Ta'asan, A. Rollett, and K. Coffey. Grain growth and the puzzle of its stagnation in thin films: The curious tale of a tail and an ear. *Progress in Materials Science*, 58(7):987–1055, 2013. (Cited on page 4.)

[38] B. Murgas, S. Florez, N. Bozzolo, J. Fausty, and M. Bernacki. Comparative study and limits of different level-set formulations for the modeling of anisotropic grain growth. *Materials*, 14(14), 2021. (Cited on pages 5, 73, 115, 120, 126, 128, 129, 130, 136, 140, 141, 145, and 158.)

[39] J. R. Weertman. Hall-petch strengthening in nanocrystalline metals. *Materials Science and Engineering: A*, 166(1-2):161–167, 1993. (Cited on page 15.)

[40] C. S. Barrett. *Structure of metals*. McGraw-Hill Book Company, Inc.; New York, 1943. (Cited on page 16.)

[41] A. Bravais. Les systemes formes par des pointes distribues regulierement sur un plan ou dans l'espace. *J. Ecole. Polytech.*, pages 1–128, 1850. (Cited on page 16.)

[42] F. C. Frank. On miller–bravais indices and four-dimensional vectors. *Acta Crystallographica*, 18(5):862–866, 1965. (Cited on page 16.)

[43] C. R. Catlow. An introduction to disorder in solids. In *Defects and disorder in crystalline and amorphous solids*. NATO Advanced Study Institute Series, Series C, 1994. (Cited on page 16.)

[44] C. Jiang, N. Swaminathan, J. Deng, D. Morgan, and I. Szlufarska. Effect of grain boundary stresses on sink strength. *Materials Research Letters*, 2(2):100–106, 2014. (Cited on page 16.)

[45] S. Chakraborty and S. Ghosh. A concurrent atomistic-crystal plasticity multiscale model for crack propagation in crystalline metallic materials. *Computer Methods in Applied Mechanics and Engineering*, 379:113748, 2021. (Cited on page 16.)

[46] X. Zhou, J. R. Mianroodi, A. K. da Silva, T. Koenig, G. Thompson, P. Shanthraj, D. Ponge, B. Gault, B. Svendsen, and D. Raabe. The hidden structure dependence of the chemical life of dislocations. *Science Advances*, 7(16):eabf0563, 2021. (Cited on pages 16 and 17.)

[47] P. Gehlen. *Interatomic potentials and simulation of lattice defects*. Springer Science & Business Media, 2012. (Cited on page 16.)

[48] X. Zhou, J. R. Mianroodi, A. Kwiatkowski da Silva, T. Koenig, G. B. Thompson, P. Shanthraj, D. Ponge, B. Gault, B. Svendsen, and D. Raabe. The hidden structure dependence of the chemical life of dislocations. *Science Advances*, 7(16), 2021. (Cited on page 16.)

[49] N. Yamanaka, S. Sakane, and T. Takaki. Multi-phase-field lattice boltzmann model for polycrystalline equiaxed solidification with motion. *Computational Materials Science*, 197:110658, 2021. (Cited on page 18.)

[50] A. Morawiec. *Orientations and rotations*. Springer, 2003. (Cited on pages 18, 20, 23, and 24.)

[51] P. Neumann. Representation of orientations of symmetrical objects by rodrigues vectors. *Textures and Microstructures*, 14:53–58, 1991. (Cited on page 23.)

[52] G. Gottstein and L. S. Shvindlerman. Grain boundary migration in metals. crc series in materials science and technology, 1999. (Cited on pages 24, 25, 26, 29, 30, 31, and 195.)

[53] R. W. Balluffi, S. Allen, and W. C. Carter. *Kinetics of materials*. John Wiley & Sons, 2005. (Cited on pages 25, 26, and 44.)

[54] A. P. Sutton and R. W. Balluffi. *Interfaces in Crystalline Materials*. Clarendon Press, Oxford, 2006. (Cited on pages 25, 42, and 51.)

[55] Y. Huang and F. J. Humphreys. Measurements of grain boundary mobility during recrystallization of a single-phase aluminium alloy. *Acta Materialia*, 47(7):2259–2268, 1999. (Cited on pages 31, 32, 36, 40, and 217.)

[56] Y. Huang, F. J. Humphreys, and M. Ferry. The annealing behaviour of deformed cube-oriented aluminium single crystals. *Acta Materialia*, 48(10):2543–2556, 2000. (Cited on pages 31, 37, 38, and 41.)

[57] Y. Huang and F. J. Humphreys. The effect of solutes on grain boundary mobility during recrystallization and grain growth in some single-phase aluminium alloys. *Materials Chemistry and Physics*, 132(1):166–174, 2012. (Cited on pages 31, 32, and 217.)

[58] E. R. Homer, E. A. Holm, S. M. Foiles, and D. L. Olmsted. Trends in grain boundary mobility: survey of motion mechanisms. *Jom*, 66(1):114–120, 2014. (Cited on pages 31, 46, 49, 51, and 68.)

[59] R. Viswanathan and C. L. Bauer. Kinetics of grain boundary migration in copper bicrystals with [001] rotation axes. *Acta Metallurgica*, 21(8):1099–1109, 1973. (Cited on pages 31, 36, 37, and 42.)

[60] D. W. Demianczuk and K. T. Aust. Effect of solute and orientation on the mobility of near-coincidence tilt boundaries in high-purity aluminum. *Acta Metallurgica*, 23(10):1149–1162, 1975. (Cited on page 31.)

[61] E. L. Maksimova, L. S. Shvindlerman, and B. B. Straumal. Transformation of Σ17 special tilt boundaries to general boundaries in tin. *Acta Metallurgica*, 36(6):1573–1583, 1988. (Cited on pages 31, 32, 38, and 39.)

[62] G. Gottstein and L. S. Shvindlerman. On the true dependence of grain boundary migration rate on driving force. *Scripta metallurgica et materialia*, 27(11):1521–1526, 1992. (Cited on page 31.)

[63] G. Gottstein and L. S. Shvindlerman. On the orientation dependence of grain boundary migration. *Scripta metallurgica et materialia*, 27(11):1515–1520, 1992. (Cited on page 31.)

[64] G. Gottstein, D. A. Molodov, L. S. Shvindlerman, D. J. Srolovitz, and M. Winning. Grain boundary migration: misorientation dependence. *Current Opinion in Solid State and Materials Science*, 5(1):9–14, 2001. (Cited on page 31.)

[65] M. Winning, G. Gottstein, and L. S. Shvindlerman. On the mechanisms of grain boundary migration. *Acta Materialia*, 50(2):353–363, 2002. (Cited on pages 31, 34, and 35.)

[66] V. A. Ivanov. On kinetics and thermodynamics of high angle grain boundaries in aluminum: Experimental study on grain boundary properties in

bi-and tricrystals. Technical report, Fakultät für Georessourcen und Materialtechnik, 2006. (Cited on page 31.)

[67] R. C. Sun and C. L. Bauer. Tilt boundary migration in NaCl bicrystals. *Acta Metallurgica*, 18(6):639–647, 1970. (Cited on pages 32, 36, and 37.)

[68] Y. Huang and F. J. Humphreys. Subgrain growth and low angle boundary mobility in aluminium crystals of orientation {110}<001>. *Acta materialia*, 48(8):2017–2030, 2000. (Cited on pages 32, 36, and 37.)

[69] W. T. Read and W. Shockley. Dislocation models of crystal grain boundaries. *Physical Review*, 78(3):275–289, 1950. Cited By :1247. (Cited on pages 32, 56, 92, 119, and 128.)

[70] R. Ørsund and E. Nes. Subgrain growth during annealing of heavily deformed metals. *Scripta Metallurgica*, 23(7):1187–1192, 1989. (Cited on page 34.)

[71] D. W. Bainbridge, H. L. Choh, and E. H. Edwards. Recent observations on the motion of small angle dislocation boundaries. *Acta metallurgica*, 2(2):322–333, 1954. (Cited on pages 33 and 35.)

[72] M. Winning, G. Gottstein, and L. S. Shvindlerman. Stress induced grain boundary motion. *Acta materialia*, 49(2):211–219, 2001. (Cited on pages 33, 34, and 35.)

[73] M. Winning, G. Gottstein, and L. S. Shvindlerman. Migration of grain boundaries under the influence of an external shear stress. *Materials Science and Engineering: A*, 317(1-2):17–20, 2001. (Cited on pages 33 and 34.)

[74] D. A. Molodov, V. A. Ivanov, and G. Gottstein. Low angle tilt boundary migration coupled to shear deformation. *Acta materialia*, 55(5):1843–1848, 2007. (Cited on pages 33 and 34.)

[75] T. Gorkaya, D. A. Molodov, and G. Gottstein. Stress-driven migration of symmetrical <100> tilt grain boundaries in al bicrystals. *Acta Materialia*, 57(18):5396–5405, 2009. (Cited on pages 33 and 34.)

[76] M. Ferry and F. J. Humphreys. Discontinuous subgrain growth in deformed and annealed {110} < 001 > aluminium single crystals. *Acta Materialia*, 44(4):1293–1308, 1996. (Cited on page 37.)

[77] F. J. Humphreys. A unified theory of recovery, recrystallization and grain growth, based on the stability and growth of cellular microstructures—i. the basic model. *Acta Materialia*, 45(10):4231–4240, 1997. (Cited on pages 37, 92, 119, and 128.)

[78] J. W. Rutter and K. T. Aust. Migration of <100> tilt grain boundaries in high purity lead. *Acta Metallurgica*, 13(3):181–186, 1965. (Cited on pages 38, 39, 44, and 45.)

[79] C. H. V. Kopetskii, V. G. Sursaeva, and L. S. Shvindlerman. The activationless movement of grain boundaries in zinc. *Fiz. Tverd. Tela*, 21(2):401–405, 1979. (Cited on page 38.)

[80] M. L. Kronberg and F. H. Wilson. Secondary recrystallization in copper. *JOM*, 1(8):501–514, 1949. (Cited on page 40.)

[81] D. A. Molodov, U. Czubayko, G. Gottstein, and L. S. Shvindlerman. Mobility of <111> tilt grain boundaries in the vicinity of the special misorientation Σ=7 in bicrystals of pure aluminum. *Scripta Metallurgica et Materialia;(United States)*, 32(4), 1995. (Cited on page 41.)

[82] E. M. Fridman, C. V. Kopesky, and L. S. Shvindlerman. Effects of orientation and concentration factors on migration of individual grain boundaries in aluminum. *Zeitschrift fur Metallkunde*, 66(9):533–539, 1975. (Cited on pages 41, 44, and 45.)

[83] M. G. Ardakani and F. J. Humphreys. The annealing behaviour of deformed particle-containing aluminium single crystals. *Acta metallurgica et materialia*, 42(3):763–780, 1994. (Cited on page 42.)

[84] C. Frois and M. O. Dimitrov. Influence de quelques eléments d'addition sur la recristallisation de l'aluminium très pur. In *Annales de Chimie*, volume 1, pages 113–128, 1966. (Cited on page 43.)

[85] W. Grünwald and F. Haessner. Thermisch aktivierte korngrenzenwanderung in gewalzten goldeinkristallen unter dem einfluss gelöster fremdatome. *Acta Metallurgica*, 18(2):217–224, 1970. (Cited on page 44.)

[86] P. Gordon and R. A. Vandermeer. Mechanism of boundary migration in recrystallization. *Transactions of the metallurgical society of AIME*, 224(5):917, 1962. (Cited on page 44.)

[87] K. T. Aust and J. W. Rutter. Grain boundary migration in high-purity lead and dilute lead-tin alloys. *Transactions of the American Institute of Mining and Metallurgical Engineers*, 215(1):119–127, 1959. (Cited on page 45.)

[88] K. T. Aust and J. W. Rutter. Temperature dependence of grain migration in high-purity lead containing small additions of tin. *Transactions of the American Institute of Mining and Metallurgical Engineers*, 215(5):820–831, 1959. (Cited on page 45.)

[89] K. G. Janssens, D. Olmsted, E. A. Holm, S. M. Foiles, S. J. Plimpton, and P. M. Derlet. Computing the mobility of grain boundaries. *Nature materials*, 5(2):124–127, 2006. (Cited on pages 46 and 49.)

[90] D. L. Olmsted, E. A. Holm, and S. M. Foiles. Survey of computed grain boundary properties in face-centered cubic metals—ii: Grain boundary mobility. *Acta materialia*, 57(13):3704–3713, 2009. (Cited on pages 46, 49, 50, 51, 146, and 158.)

[91] J. L. Priedeman, D. L. Olmsted, and E. R. Homer. The role of crystallography and the mechanisms associated with migration of incoherent twin grain boundaries. *Acta Materialia*, 131:553–563, 2017. (Cited on pages 46 and 49.)

[92] J. Zhang, S. O. Poulsen, J. W. Gibbs, P. W. Voorhees, and H. F. Poulsen. Determining material parameters using phase-field simulations and experiments. *Acta Materialia*, 129:229–238, 2017. (Cited on pages 46, 47, and 145.)

[93] J. Zhang, W. Ludwig, Y. Zhang, H. H. B. Sørensen, D. J. Rowenhorst, A. Yamanaka, P. W. Voorhees, and H. F. Poulsen. Grain boundary mobilities in polycrystals. *Acta Materialia*, 191:211–220, 2020. (Cited on pages 46, 47, and 48.)

[94] D. Juul Jensen and Y. Zhang. Impact of 3D/4D methods on the understanding of recrystallization. *Current Opinion in Solid State and Materials Science*, 24(2):100821, 2020. (Cited on pages 46 and 145.)

[95] H. Fang, D. Juul Jensen, and Y. Zhang. Improved grain mapping by laboratory X-ray diffraction contrast tomography. *IUCrJ*, 8(4):559–573, Jul 2021. (Cited on pages 46 and 145.)

[96] M. Wang. *Reverse engineering the kinetics of grain growth in Al-based polycrystals by microstructural mapping in 4D*. PhD thesis, Universität Ulm, 2022. (Cited on pages 46, 47, and 145.)

[97] H. F. Poulsen, S. F. Nielsen, E. M. Lauridsen, S. Schmidt, R. Suter, U. Lienert, L. Margulies, T. Lorentzen, and D. Juul Jensen. Three-dimensional maps of grain boundaries and the stress state of individual grains in polycrystals and powders. *Journal of applied crystallography*, 34(6):751–756, 2001. (Cited on page 46.)

[98] B. Gault, A. Chiaramonti, O. Cojocaru-Mirédin, P. Stender, R. Dubosq, C. Freysoldt, S. K. Makineni, T. Li, M. Moody, and J. M. Cairney. Atom probe tomography. *Nature Reviews Methods Primers*, 1(1):1–30, 2021. (Cited on page 46.)

[99] M. Sitko, K. Banaś, and L. Madej. Scaling scientific cellular automata microstructure evolution model of static recrystallization toward practical industrial calculations. *Materials*, 14(15), 2021. (Cited on page 46.)

[100] J. W. Cahn and J. E. Hilliard. Free energy of a nonuniform system. i. interfacial free energy. *The Journal of chemical physics*, 28(2):258–267, 1958. (Cited on pages 47 and 61.)

[101] S. Fukuhara, K. M. Bal, E. C. Neyts, and Y. Shibuta. Accelerated molecular dynamics simulation of large systems with parallel collective variable-driven hyperdynamics. *Computational Materials Science*, 177:109581, 2020. (Cited on pages 49 and 51.)

[102] S. Plimpton. Fast parallel algorithms for short-range molecular dynamics. *Journal of Computational Physics*, 117(1):1–19, 1995. (Cited on page 49.)

[103] Z. Trautt and Y. Mishin. Grain boundary migration and grain rotation studied by molecular dynamics. *Acta Materialia*, 60(5):2407–2424, 2012. (Cited on page 49.)

[104] F. Abdeljawad, S. M. Foiles, A. P. Moore, A. R. Hinkle, C. M. Barr, N. M. Heckman, K. Hattar, and B. L. Boyce. The role of the interface stiffness tensor on grain boundary dynamics. *Acta Materialia*, 158:440–453, 2018. (Cited on pages 49, 50, 66, 146, 158, 159, 160, 161, 165, 167, and 196.)

[105] M. Upmanyu, D. J. Srolovitz, L. S. Shvindlerman, and G. Gottstein. Misorientation dependence of intrinsic grain boundary mobility: simulation and experiment. *Acta materialia*, 47(14):3901–3914, 1999. (Cited on page 49.)

[106] I. Toda-Caraballo, P. Bristowe, and C. Capdevila. A molecular dynamics study of grain boundary free energies, migration mechanisms and mobilities in a bcc Fe–20Cr alloy. *Acta Materialia*, 60(3):1116–1128, 2012. (Cited on page 49.)

[107] B. Schönfelder, D. Wolf, S. Phillpot, and M. Furtkamp. Molecular-dynamics method for the simulation of grain-boundary migration. *Interface Science*, 5(4):245–262, 1997. (Cited on page 49.)

[108] H. Zhang, M. Mendelev, and D. Srolovitz. Computer simulation of the elastically driven migration of a flat grain boundary. *Acta Materialia*, 52(9):2569–2576, 2004. (Cited on pages 49 and 158.)

[109] S. M. Foiles and J. Hoyt. Computation of grain boundary stiffness and mobility from boundary fluctuations. *Acta Materialia*, 54(12):3351–3357, 2006. (Cited on pages 49 and 158.)

[110] A. Karma, Z. T. Trautt, and Y. Mishin. Relationship between equilibrium fluctuations and shear-coupled motion of grain boundaries. *Phys. Rev. Lett.*, 109:095501, Aug 2012. (Cited on pages 49 and 158.)

[111] S. Ratanaphan, R. Sarochawikasit, N. Kumanuvong, S. Hayakawa, H. Beladi, G. S. Rohrer, and T. Okita. Atomistic simulations of grain boundary

energies in austenitic steel. *Journal of Materials Science*, 54(7):5570–5583, 2019. (Cited on pages 49, 128, and 213.)

[112] R. B. Godiksen, Z. T. Trautt, M. Upmanyu, J. Schiøtz, D. J. Jensen, and S. Schmidt. Simulations of boundary migration during recrystallization using molecular dynamics. *Acta Materialia*, 55(18):6383–6391, 2007. (Cited on page 49.)

[113] R. Aguirre, S. Abdullah, X. Zhou, and D. Zubia. Molecular dynamics calculations of grain boundary mobility in CdTe. *Nanomaterials*, 9(4), 2019. (Cited on page 49.)

[114] S. L. Thomas, C. Wei, J. Han, Y. Xiang, and D. J. Srolovitz. Disconnection description of triple-junction motion. *Proceedings of the National Academy of Sciences*, 116(18):8756–8765, 2019. (Cited on pages 49, 50, and 66.)

[115] A. Sutton, E. Banks, and A. Warwick. The five-dimensional parameter space of grain boundaries. *Proceedings of the Royal Society A: Mathematical, Physical and Engineering Sciences*, 471(2181):20150442, 2015. (Cited on pages 50 and 106.)

[116] A. Morawiec. Misorientation-angle distribution of randomly oriented symmetric objects. *Journal of applied crystallography*, 28(3):289–293, 1995. (Cited on pages 50 and 106.)

[117] J. W. Cahn and J. E. Taylor. Metrics, measures, and parametrizations for grain boundaries: a dialog. *Journal of materials science*, 41(23):7669–7674, 2006. (Cited on pages 50 and 106.)

[118] A. Morawiec. Models of uniformity for grain boundary distributions. *Journal of Applied Crystallography*, 42(5):783–792, 2009. (Cited on pages 50 and 106.)

[119] S. Patala and C. A. Schuh. Symmetries in the representation of grain boundary-plane distributions. *Philosophical Magazine*, 93(5):524–573, 2013. (Cited on pages 50 and 106.)

[120] E. R. Homer, S. Patala, and J. L. Priedeman. Grain boundary plane orientation fundamental zones and structure-property relationships. *Scientific reports*, 5(1):1–13, 2015. (Cited on pages 50 and 106.)

[121] D. L. Olmsted. A new class of metrics for the macroscopic crystallographic space of grain boundaries. *Acta Materialia*, 57(9):2793–2799, 2009. (Cited on pages 50 and 106.)

[122] B. Schönfelder, G. Gottstein, and L. Shvindlerman. Comparative study of grain-boundary migration and grain-boundary self-diffusion of [001] twist-grain boundaries in copper by atomistic simulations. *Acta Materialia*, 53(6):1597–1609, 2005. (Cited on page 51.)

[123] K. Chen, J. Han, S. L. Thomas, and D. J. Srolovitz. Grain boundary shear coupling is not a grain boundary property. *Acta Materialia*, 167:241–247, 2019. (Cited on page 51.)

[124] J. Hirth. Dislocations, steps and disconnections at interfaces. *Journal of Physics and Chemistry of Solids*, 55(10):985–989, 1994. (Cited on page 51.)

[125] J. Hirth and R. Pond. Steps, dislocations and disconnections as interface defects relating to structure and phase transformations. *Acta Materialia*, 44(12):4749–4763, 1996. (Cited on page 51.)

[126] J. Hirth, J. Wang, and C. Tomé. Disconnections and other defects associated with twin interfaces. *Progress in Materials Science*, 83:417–471, 2016. (Cited on page 51.)

[127] J. Han, S. L. Thomas, and D. J. Srolovitz. Grain-boundary kinetics: A unified approach. *Progress in Materials Science*, 98:386–476, 2018. (Cited on pages 51, 66, and 70.)

[128] K. Chen, J. Han, X. Pan, and D. J. Srolovitz. The grain boundary mobility tensor. *Proceedings of the National Academy of Sciences*, 117(9):4533–4538, 2020. (Cited on pages 51, 66, 67, 68, 69, and 171.)

[129] K. Chang, C. E. K. III, Q. Du, and L.-Q. Chen. Evaluating microstructural parameters of three-dimensional grains generated by phase-field simulation or other voxel-based techniques. *Modelling and Simulation in Materials Science and Engineering*, 20(7):075009, sep 2012. (Cited on page 55.)

[130] L. Sieradzki and L. Madej. A perceptive comparison of the cellular automata and monte carlo techniques in application to static recrystallization modeling in polycrystalline materials. *Computational Materials Science*, 67:156–173, 2013. (Cited on page 55.)

[131] K. Chang, L.-Q. Chen, C. E. Krill, and N. Moelans. Effect of strong nonuniformity in grain boundary energy on 3-D grain growth behavior: A phase-field simulation study. *Computational Materials Science*, 127:67–77, 2017. (Cited on pages 55 and 62.)

[132] I. Basu, M. Chen, M. Loeck, T. Al-Samman, and D. Molodov. Determination of grain boundary mobility during recrystallization by statistical evaluation of electron backscatter diffraction measurements. *Materials Characterization*, 117:99–112, 2016. (Cited on pages 55 and 57.)

[133] M. Sitko, Q. Chao, J. Wang, K. Perzynski, K. Muszka, and L. Madej. A parallel version of the cellular automata static recrystallization model dedicated for high performance computing platforms – development and verification. *Computational Materials Science*, 172:109283, 2020. (Cited on pages 55 and 57.)

[134] J. Fausty, B. Murgas, S. Florez, N. Bozzolo, and M. Bernacki. A new analytical test case for anisotropic grain growth problems. *Applied Mathematical Modelling*, 93:28–52, 2021. (Cited on pages 55, 56, 65, 66, 73, 74, and 158.)

[135] S. Florez, J. Fausty, K. Alvarado, B. Murgas, and M. Bernacki. A 2D front-tracking lagrangian model for the modeling of anisotropic grain growth. *Materials*, 14(15), 2021. (Cited on pages 56 and 59.)

[136] G. Grest, D. Srolovitz, and M. Anderson. Computer simulation of grain growth—iv. anisotropic grain boundary energies. *Acta Metallurgica*, 33(3):509–520, 1985. (Cited on page 56.)

[137] E. Fjeldberg and K. Marthinsen. A 3D monte carlo study of the effect of grain boundary anisotropy and particles on the size distribution of grains after recrystallisation and grain growth. *Computational Materials Science*, 48(2):267–281, 2010. (Cited on pages 56 and 145.)

[138] H. Hesselbarth and I. Göbel. Simulation of recrystallization by cellular automata. *Acta Metallurgica et Materialia*, 39(9):2135–2143, 1991. (Cited on page 57.)

[139] Y. Liu, T. Baudin, and R. Penelle. Simulation of normal grain growth by cellular automata. *Scripta Materialia*, 34(11), 6 1996. (Cited on page 57.)

[140] D. Raabe. Introduction of a scalable three-dimensional cellular automaton with a probabilistic switching rule for the discrete mesoscale simulation of recrystallization phenomena. *Philosophical Magazine A*, 79(10):2339–2358, 1999. (Cited on page 57.)

[141] D. Weaire and J. P. Kermode. Computer simulation of a two-dimensional soap froth. *Philosophical Magazine B*, 48(3):245–259, 1983. (Cited on page 58.)

[142] A. Soares, A. Ferro, and M. Fortes. Computer simulation of grain growth in a bidimensional polycrystal. *Scripta Metallurgica*, 19(12):1491–1496, 1985. (Cited on page 58.)

[143] K. Kawasaki, T. Nagai, and K. Nakashima. Vertex models for two-dimensional grain growth. *Philosophical Magazine B*, 60(3):399–421, 1989. (Cited on page 58.)

[144] U. Czubayko, V. Sursaeva, G. Gottstein, and L. Shvindlerman. Influence of triple junctions on grain boundary motion. *Acta Materialia*, 46(16):5863–5871, 1998. (Cited on page 59.)

[145] M. Upmanyu, D. J. Srolovitz, L. Shvindlerman, and G. Gottstein. Triple junction mobility: A molecular dynamics study. *Interface Science*, 7(3):307–319, 1999. (Cited on page 59.)

[146] D. Weygand, Y. Bréchet, and J. Lépinoux. Influence of a reduced mobility of triple points on grain growth in two dimensions. *Acta Materialia*, 46(18):6559–6564, 1998. (Cited on page 59.)

[147] D. Weygand, Y. Bréchet, and J. Lépinoux. Reduced mobility of triple nodes and lines on grain growth in two and three dimensions. *Interface Science*, 7(3):285–295, 1999. (Cited on page 59.)

[148] S. Florez, K. Alvarado, and M. Bernacki. A new front-tracking lagrangian model for the modeling of dynamic and post-dynamic recrystallization. *Modelling and Simulation in Materials Science and Engineering*, 29(3):035004, 2021. (Cited on page 59.)

[149] K. Piękoś, J. Tarasiuk, K. Wierzbanowski, and B. Bacroix. Stochastic vertex model of recrystallization. *Computational Materials Science*, 42(1):36–42, 2008. (Cited on page 60.)

[150] L.-Q. Chen. Phase-field models for microstructure evolution. *Annual review of materials research*, 32(1):113–140, 2002. (Cited on page 61.)

[151] J. B. Collins and H. Levine. Diffuse interface model of diffusion-limited crystal growth. *Physical Review B*, 31(9):6119, 1985. (Cited on page 61.)

[152] J. Langer. Models of pattern formation in first-order phase transitions. In *Directions in Condensed Matter Physics: Memorial Volume in Honor of Shang-Keng Ma*, pages 165–186. World Scientific, 1986. (Cited on page 61.)

[153] J. W. Cahn. On spinodal decomposition. *Acta Metallurgica*, 9(9):795–801, 1961. (Cited on page 61.)

[154] S. M. Allen and J. W. Cahn. A microscopic theory for antiphase boundary motion and its application to antiphase domain coarsening. *Acta Metallurgica*, 27(6):1085–1095, 1979. (Cited on page 61.)

[155] L.-Q. Chen and W. Yang. Computer simulation of the domain dynamics of a quenched system with a large number of nonconserved order parameters: The grain-growth kinetics. *Phys. Rev. B*, 50:15752–15756, Dec 1994. (Cited on page 61.)

[156] D. Fan and L.-Q. Chen. Diffusion-controlled grain growth in two-phase solids. *Acta Materialia*, 45(8):3297–3310, 1997. (Cited on page 61.)

[157] D. Fan and L.-Q. Chen. Computer simulation of grain growth using a continuum field model. *Acta Materialia*, 45(2):611–622, 1997. (Cited on page 61.)

[158] I. Steinbach, F. Pezzolla, B. Nestler, M. Seeßelberg, R. Prieler, G. Schmitz, and J. Rezende. A phase field concept for multiphase systems. *Physica D: Nonlinear Phenomena*, 94(3):135–147, 1996. (Cited on page 62.)

[159] J. Eiken, B. Böttger, and I. Steinbach. Multiphase-field approach for multicomponent alloys with extrapolation scheme for numerical application. *Phys. Rev. E*, 73:066122, Jun 2006. (Cited on page 62.)

[160] G. I. Tóth, T. Pusztai, and L. Gránásy. Consistent multiphase-field theory for interface driven multidomain dynamics. *Phys. Rev. B*, 92:184105, Nov 2015. (Cited on page 62.)

[161] E. Miyoshi, T. Takaki, M. Ohno, and Y. Shibuta. Accuracy evaluation of phase-field models for grain growth simulation with anisotropic grain boundary properties. *Isij International*, 60(1):160–167, 2020. (Cited on page 62.)

[162] J. Eiken. Discussion of the accuracy of the multi-phase-field approach to simulate grain growth with anisotropic grain boundary properties. *ISIJ International*, 60(8):1832–1834, 2020. (Cited on pages 62 and 86.)

[163] N. Moelans, B. Blanpain, and P. Wollants. Quantitative analysis of grain boundary properties in a generalized phase field model for grain growth in anisotropic systems. *Physical Review B*, 78(2):024113, 2008. (Cited on page 62.)

[164] S. Osher and J. A. Sethian. Fronts Propagating with Curvature Dependent Speed: Algorithms Based on Hamilton-Jacobi Formulations. *Journal of Computational Physics*, 79:12–49, 1988. (Cited on page 62.)

[165] B. Merriman, J. K. Bence, and S. J. Osher. Motion of multiple junctions: A level set approach, 1994. (Cited on pages 62 and 63.)

[166] H. Zhao, T. Chan, B. Merriman, and S. Osher. A variational level set approach to multiphase motion. *Journal of Computational Physics*, 127:179–195, 1996. (Cited on page 62.)

[167] M. Bernacki, Y. Chastel, T. Coupez, and R. E. Logé. Level set framework for the numerical modelling of primary recrystallization in polycrystalline materials. *Scripta Materialia*, 58(12):1129–1132, 2008. (Cited on pages 62 and 73.)

[168] M. Bernacki, R. E. Logé, and T. Coupez. Level set framework for the finite-element modelling of recrystallization and grain growth in polycrystalline materials. *Scripta Materialia*, 64(6):525–528, 2011. (Cited on pages 62, 63, and 73.)

[169] B. Scholtes, M. Shakoor, A. Settefrati, P.-O. Bouchard, N. Bozzolo, and M. Bernacki. New finite element developments for the full field modeling of microstructural evolutions using the level-set method. *Computational Materials Science*, 109:388–398, 2015. (Cited on pages 63, 64, and 73.)

[170] M. Shakoor, B. Scholtes, P.-O. Bouchard, and M. Bernacki. An efficient and parallel level set reinitialization method – Application to micromechanics and microstructural evolutions. *Applied Mathematical Modelling*, 39(23-24):7291–7302, 2015. (Cited on page 63.)

[171] B. Scholtes, R. Boulais-Sinou, A. Settefrati, D. Pino Muñoz, I. Poitrault, A. Montouchet, N. Bozzolo, and M. Bernacki. 3D level set modeling of static recrystallization considering stored energy fields. *Computational Materials Science*, 122:57–71, sep 2016. (Cited on page 63.)

[172] J. Cahn. Stability, microstructural evolution, grain growth, and coarsening in a two-dimensional two-phase microstructure. *Acta metallurgica et materialia*, 39(10):2189–2199, 1991. (Cited on pages 64, 96, 98, and 99.)

[173] A. Cruz-Fabiano, R. Logé, and M. Bernacki. Assessment of simplified 2D grain growth models from numerical experiments based on a level set framework. *Computational Materials Science*, 92:305 – 312, 2014. (Cited on pages 64, 93, 125, 128, and 130.)

[174] L. Maire. *Full field and mean field modeling of dynamic and post-dynamic recrystallization in 3D – Application to 304L steel*. Theses, Université Paris sciences et lettres, Nov. 2018. (Cited on pages 64 and 73.)

[175] J. Fausty. *Towards the full field modeling and simulation of annealing twins using a Finite Element Level Set method*. Theses, Université Paris sciences et lettres, Jan. 2020. (Cited on pages 65, 66, 120, and 158.)

[176] D. Du, H. Zhang, and D. J. Srolovitz. Properties and determination of the interface stiffness. *Acta Materialia*, 55(2):467–471, 2007. (Cited on page 66.)

[177] C. Wei, L. Zhang, J. Han, D. J. Srolovitz, and Y. Xiang. Grain boundary triple junction dynamics: A continuum disconnection model. *SIAM Journal on Applied Mathematics*, 80(3):1101–1122, 2020. (Cited on page 66.)

[178] B. Runnels and V. Agrawal. Phase field disconnections: A continuum method for disconnection-mediated grain boundary motion. *Scripta Materialia*, 186:6–10, 2020. (Cited on pages 66 and 68.)

[179] L. Zhang, J. Han, D. J. Srolovitz, and Y. Xiang. Equation of motion for grain boundaries in polycrystals. *npj Computational Materials*, 7(1):1–8, 2021. (Cited on pages 66 and 70.)

[180] J. Han, D. J. Srolovitz, and M. Salvalaglio. Disconnection-mediated migration of interfaces in microstructures: I. continuum model. *Acta Materialia*, page 117178, 2021. (Cited on pages 66, 68, and 69.)

[181] M. Salvalaglio, D. J. Srolovitz, and J. Han. Disconnection-mediated migration of interfaces in microstructures: II. diffuse interface simulations. *Acta Materialia*, page 117463, 2021. (Cited on pages 66, 68, 170, and 171.)

[182] M. Gokuli and B. Runnels. Multiphase field modeling of grain boundary migration mediated by emergent disconnections. *Acta Materialia*, 217:117149, 2021. (Cited on pages 66 and 68.)

[183] A. F. Voter. Introduction to the kinetic monte carlo method. In *Radiation effects in solids*, pages 1–23. Springer, 2007. (Cited on page 70.)

[184] M. Prieto-Depedro, I. Martin-Bragado, and J. Segurado. An atomistically informed kinetic monte carlo model of grain boundary motion coupled to shear deformation. *International Journal of Plasticity*, 68:98–110, 2015. (Cited on page 70.)

[185] M. Elsey, S. Esedoglu, and P. Smereka. Simulations of anisotropic grain growth: Efficient algorithms and misorientation distributions. *Acta Materialia*, 61(6):2033–2043, apr 2013. (Cited on pages 70, 95, 105, 115, 129, and 136.)

[186] M. Bernacki, H. Resk, T. Coupez, and R. E. Logé. Finite element model of primary recrystallization in polycrystalline aggregates using a level set framework. *Modelling and Simulation in Materials Science and Engineering*, 17(6), 2009. (Cited on pages 73, 75, 76, 86, and 126.)

[187] A. N. Brooks and T. J. Hughes. Streamline upwind/petrov-galerkin formulations for convection dominated flows with particular emphasis on the incompressible navier-stokes equations. *Computer Methods in Applied Mechanics and Engineering*, 32(1):199 – 259, 1982. (Cited on page 75.)

[188] E. Roux, M. Bernacki, and P. Bouchard. A level-set and anisotropic adaptive remeshing strategy for the modeling of void growth under large plastic strain. *Computational Materials Science*, 68:32–46, 2013. (Cited on pages 75, 76, 86, and 126.)

[189] P. De Micheli, L. Maire, D. Cardinaux, C. Moussa, N. Bozzolo, and M. Bernacki. DIGIMU®: Full field recrystallization simulations for optimization of multi-pass processes. In *AIP Conference Proceedings*, volume 2113, page 040014. AIP Publishing LLC, 2019. (Cited on page 75.)

[190] J. Cahn and D. Hoffman. A vector thermodynamics for anisotropic surfaces—II. curved and faceted surfaces. *Acta Metallurgica*, 22(10):1205–1214, 1974. (Cited on page 76.)

[191] C. Herring. Surface tension as a motivation for sintering. In *Fundamental Contributions to the Continuum Theory of Evolving Phase Interfaces in Solids*, pages 33–69. Springer, 1999. (Cited on pages 77 and 106.)

[192] M. Shakoor, M. Bernacki, and P.-O. Bouchard. A new body-fitted immersed volume method for the modeling of ductile fracture at the microscale: Analysis of void clusters and stress state effects on coalescence. *Engineering Fracture Mechanics*, 147:398–417, 2015. (Cited on page 86.)

[193] K. Hitti, P. Laure, T. Coupez, L. Silva, and M. Bernacki. Precise generation of complex statistical Representative Volume Elements (RVEs) in a finite element context. *Computational Materials Science*, 61:224–238, 2012. (Cited on pages 91, 111, 119, and 126.)

[194] K. Hitti and M. Bernacki. Optimized dropping and rolling (odr) method for packing of poly-disperse spheres. *Applied Mathematical Modelling*, 37(8):5715–5722, 2013. (Cited on pages 91, 111, and 126.)

[195] J. Mackenzie. Second paper on statistics associated with the random disorientation of cubes. *Biometrika*, 45(1-2):229–240, 1958. (Cited on page 93.)

[196] K. Chang and N. Moelans. Effect of grain boundary energy anisotropy on highly textured grain structures studied by phase-field simulations. *Acta materialia*, 64:443–454, 2014. (Cited on pages 95, 98, and 129.)

[197] J. Gruber, H. Miller, T. Hoffmann, G. Rohrer, and A. Rollett. Misorientation texture development during grain growth. part i: Simulation and experiment. *Acta Materialia*, 57(20):6102–6112, 2009. (Cited on pages 95 and 129.)

[198] E. Holm, D. J. Srolovitz, and J. Cahn. Microstructural evolution in two-dimensional two-phase polycrystals. *Acta metallurgica et materialia*, 41(4):1119–1136, 1993. (Cited on pages 98 and 99.)

[199] T. Francis, I. Chesser, S. Singh, E. A. Holm, and M. De Graef. A geodesic octonion metric for grain boundaries. *Acta Materialia*, 166:135–147, 2019. (Cited on page 106.)

[200] I. Chesser, T. Francis, M. De Graef, and E. Holm. Learning the grain boundary manifold: tools for visualizing and fitting grain boundary properties. *Acta Materialia*, 195:209–218, 2020. (Cited on page 106.)

[201] I. Chesser and E. Holm. Understanding the anomalous thermal behavior of $\Sigma 3$ grain boundaries in a variety of fcc metals. *Scripta Materialia*, 157:19 – 23, 2018. (Cited on page 106.)

[202] H. Garcke, B. Stoth, and B. Nestler. Anisotropy in multi-phase systems: a phase field approach. *Interfaces and Free Boundaries*, 1(2):175–198, 1999. (Cited on page 106.)

[203] J. Brown and N. Ghoniem. Structure and motion of junctions between coherent and incoherent twin boundaries in copper. *Acta Materialia*, 57(15):4454–4462, 2009. (Cited on page 107.)

[204] B. Murgas, B. Flipon, N. Bozzolo, and M. Bernacki. Level-set modeling of grain growth in 316L stainless steel under different assumptions regarding grain boundary properties. *arXiv [cond-mat.mtrl-sci]*, arXiv:2202.04930v2, 2022. (Cited on page 119.)

[205] S. Nishikawa and S. Kikuchi. Diffraction of cathode rays by calcite. *Nature*, 122(3080):726–726, 1928. (Cited on page 121.)

[206] A. Winkelmann, G. Cios, T. Tokarski, G. Nolze, R. Hielscher, and T. Kozieł. Ebsd orientation analysis based on experimental kikuchi reference patterns. *Acta Materialia*, 188:376–385, 2020. (Cited on page 121.)

[207] F. Bachmann, R. Hielscher, and H. Schaeben. Grain detection from 2d and 3d ebsd data—specification of the mtex algorithm. *Ultramicroscopy*, 111(12):1720–1733, 2011. (Cited on pages 121 and 213.)

[208] K. Alvarado, I. Janeiro, S. Florez, B. Flipon, J.-M. Franchet, D. Locq, C. Dumont, N. Bozzolo, and M. Bernacki. Dissolution of the primary γ' precipitates and grain growth during solution treatment of three nickel base superalloys. *Metals*, 11(12):1921, 2021. (Cited on page 125.)

[209] J. Burke and D. Turnbull. Recrystallization and grain growth. *Progress in Metal Physics*, 3:220–292, 1952. (Cited on page 125.)

[210] A. Agnoli, N. Bozzolo, R. Logé, J.-M. Franchet, J. Laigo, and M. Bernacki. Development of a level set methodology to simulate grain growth in the presence of real secondary phase particles and stored energy–application to a nickel-base superalloy. *Computational Materials Science*, 89:233–241, 2014. (Cited on pages 125 and 130.)

[211] L. Maire, B. Scholtes, C. Moussa, D. Pino Muñoz, N. Bozzolo, and M. Bernacki. Improvement of 3-D mean field models for pure grain growth based on full field simulations. *Journal of Materials Science*, 51(24):10970–10981, 2016. (Cited on pages 125 and 130.)

[212] K. Alvarado, S. Florez, B. Flipon, N. Bozzolo, and M. Bernacki. A level set approach to simulate grain growth with an evolving population of second phase particles. *Modelling and Simulation in Materials Science and Engineering*, 29(3):035009, 2021. (Cited on pages 125 and 130.)

[213] X. Tu, A. Shahba, J. Shen, and S. Ghosh. Microstructure and property based statistically equivalent rves for polycrystalline-polyphase aluminum alloys. *International Journal of Plasticity*, 115:268–292, 2019. (Cited on page 132.)

[214] K. Chang and H. Chang. Effect of grain boundary energy anisotropy in 2d and 3d grain growth process. *Results in Physics*, 12:1262–1268, 2019. (Cited on page 145.)

[215] Y.-H. Song, M.-T. Wang, J. Ni, J.-F. Jin, and Y.-P. Zong. Effect of grain boundary energy anisotropy on grain growth in ZK60 alloy using a 3D phase-field modeling. *Chinese Physics B*, 29(12):128201, 2020. (Cited on page 145.)

[216] E. Miyoshi, T. Takaki, S. Sakane, M. Ohno, Y. Shibuta, and T. Aoki. Large-scale phase-field study of anisotropic grain growth: Effects of misorientation-dependent grain boundary energy and mobility. *Computational Materials Science*, 186:109992, 2021. (Cited on page 145.)

[217] H.-K. Kim, W.-S. Ko, H.-J. Lee, S. G. Kim, and B.-J. Lee. An identification scheme of grain boundaries and construction of a grain boundary energy database. *Scripta Materialia*, 64(12):1152–1155, 2011. (Cited on page 145.)

[218] H.-K. Kim, S. G. Kim, W. Dong, I. Steinbach, and B.-J. Lee. Phase-field modeling for 3D grain growth based on a grain boundary energy database. *Modelling and Simulation in Materials Science and Engineering*, 22(3):034004, 2014. (Cited on page 145.)

[219] M. A. Groeber and M. A. Jackson. DREAM. 3D: a digital representation environment for the analysis of microstructure in 3D. *Integrating materials and manufacturing innovation*, 3(1):56–72, 2014. (Cited on page 151.)

[220] A. Lobkovsky, A. Karma, M. Mendelev, M. Haataja, and D. Srolovitz. Grain shape, grain boundary mobility and the herring relation. *Acta Materialia*, 52(2):285–292, 2004. (Cited on page 158.)

[221] H. Zhang, M. Upmanyu, and D. Srolovitz. Curvature driven grain boundary migration in aluminum: molecular dynamics simulations. *Acta Materialia*, 53(1):79–86, 2005. (Cited on page 158.)

[222] Y. Mishin, M. Asta, and J. Li. Atomistic modeling of interfaces and their impact on microstructure and properties. *Acta Materialia*, 58(4):1117–1151, 2010. (Cited on page 158.)

[223] R. D. Moore, T. Beecroft, G. S. Rohrer, C. M. Barr, E. R. Homer, K. Hattar, B. L. Boyce, and F. Abdeljawad. The grain boundary stiffness and its impact on equilibrium shapes and boundary migration: Analysis of the Σ5, 7, 9, and 11 boundaries in ni. *Acta Materialia*, page 117220, 2021. (Cited on pages 158, 159, 167, and 196.)

[224] W. Cai, A. Arsenlis, C. R. Weinberger, and V. V. Bulatov. A non-singular continuum theory of dislocations. *Journal of the Mechanics and Physics of Solids*, 54(3):561–587, 2006. (Cited on page 170.)

[225] J. Dutra, F. Siciliano Jr, and A. Padilha. Interaction between second-phase particle dissolution and abnormal grain growth in an austenitic stainless steel. *Materials Research*, 5:379–384, 2002. (Cited on pages 207 and 217.)

[226] D. Samantaray, A. Chaudhuri, U. Borah, A. Bhaduri, and P. Dutta. Role of grain boundary ferrite layer in dynamic recrystallization of semi-solid processed type 304L austenitic stainless steel. *Materials Letters*, 179:65–68, 2016. (Cited on pages 207 and 217.)

[227] A. Seret, C. Moussa, M. Bernacki, J. Signorelli, and N. Bozzolo. Estimation of geometrically necessary dislocation density from filtered ebsd data by a local linear adaptation of smoothing splines. *Journal of Applied Crystallography*, 52(3), 2019. (Cited on page 207.)

[228] Y. Jin, B. Lin, M. Bernacki, G. Rohrer, A. Rollett, and N. Bozzolo. Annealing twin development during recrystallization and grain growth in pure nickel. *Materials Science and Engineering: A*, 597:295–303, 2014. (Cited on page 208.)

[229] N. Bozzolo and M. Bernacki. Viewpoint on the formation and evolution of annealing twins during thermomechanical processing of fcc metals and alloys. *Metallurgical and Materials Transactions A*, 51(6):2665–2684, 2020. (Cited on page 208.)

[230] L. Gavard. *Recristallisation dynamique d'aciers inoxydables austenitiques de haute purete*. PhD thesis, Grenoble INPG, 2001. (Cited on page 213.)

[231] T. Ruggles and D. Fullwood. Estimations of bulk geometrically necessary dislocation density using high resolution ebsd. *Ultramicroscopy*, 133:8–15, 2013. (Cited on page 213.)

[232] W. Pantleon. Resolving the geometrically necessary dislocation content by conventional electron backscattering diffraction. *Scripta Materialia*, 58(11):994–997, 2008. (Cited on page 213.)

[233] J. Schindelin, I. Arganda-Carreras, E. Frise, V. Kaynig, M. Longair, T. Pietzsch, S. Preibisch, C. Rueden, S. Saalfeld, B. Schmid, et al. Fiji: an open-source platform for biological-image analysis. *Nature methods*, 9(7):676–682, 2012. (Cited on page 214.)

[234] D. G. Lowe. Distinctive image features from scale-invariant keypoints. *International journal of computer vision*, 60(2):91–110, 2004. (Cited on page 214.)

Appendix A

Appendix

A.1 Analytical case of the Quarter Loop bicrystal model

Figure A.1 shows a diagram of the QL technique, where the velocity of the GB tip at $x = 0$ (magenta dot) is called v_t. After a transitory phase, the GB profile keeps its shape.

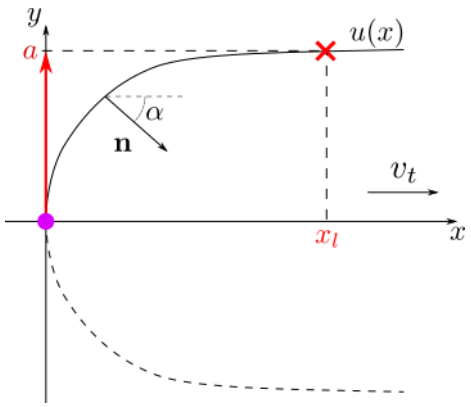

Figure A.1: Diagram of the QL geometry. a is the QL width, v_t the tip velocity, (x, y) the GB profile coordinates attached to the tip of the QL profile, α the GB inclination measured with respect to the x-axis and n the GB normal.

In [52], the exhibit proposed an analytical solution for the tip velocity and the interface profile of the QL under three boundary conditions:

$$\begin{aligned} &y(0) = 0, \\ &y(\infty) = a, \\ &y'(0) = \infty. \end{aligned} \tag{A.1}$$

where $y' = dy/dx$ is the first derivative with respect to x. The evolution of the interface is measured experimentally at $x = 0$. Its velocity and profile are

respectively defined as

$$v_t = \frac{1}{a}\int_0^{\alpha_{max}} \mu\gamma d\alpha = \frac{\gamma}{a}\frac{\mu\pi}{2}, \tag{A.2}$$

and

$$y = \frac{a}{\pi} arccos\left(exp\left(\frac{-\pi x}{a}\right)\right), \tag{A.3}$$

where $\alpha_{max} = 90°$.

In other words, inserting Equation 1.32 into Equation A.2 the measured average mobility is defined as $\bar{\mu} = \mu\pi/2$. This measurement does not capture the anisotropic nature of GBs, thus, the system can be reproduced using the Isotropic FE-LS formulation. A dimensionless example is shown in Figure A.2, the HL width is set to $a = 0.2$ and GB mobility is set to $\mu = 0.1273$. One can see the little difference between the evolution of the analytical profile and the numerical result.

These techniques were presented very early and revealed the dependence of the GB reduced mobility on the misorientation. However, the anisotropy of the GB properties is neglected and average values of GB reduced mobility are measured. Hence, the anisotropy of the GB mobility may be compensated by the anisotropy of the GB stiffness tensor ($\gamma\mathbb{I} + \vec{\nabla}_{\vec{n}}\vec{\nabla}_{\vec{n}}\gamma$). However, the GB stiffness tensor is only known for a few twin boundaries (TBs) [104, 223] and it must be known for a more general set of GBs.

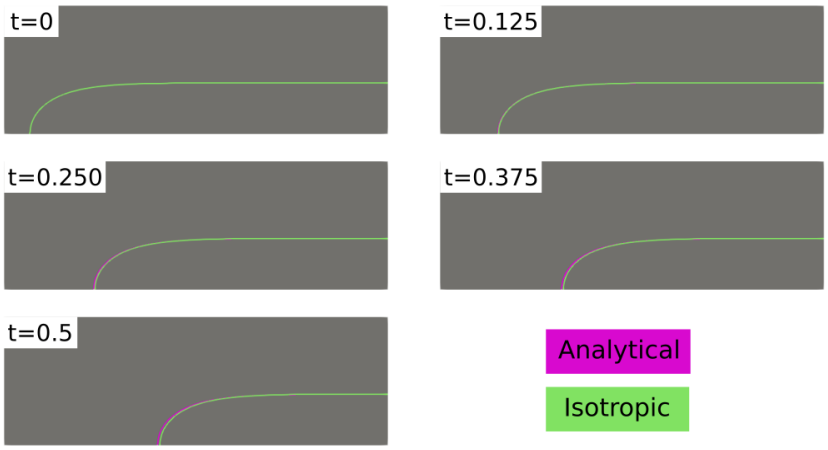

Figure A.2: Comparison of the interface between the isotropic FE-LS formulation and the analytical model of the QL technique at $t = \{0, 0.125, 0.25, 0.375, 0.5\}$. The domain is set to 1.5×0.5, the non-structured isotropic mesh size is set to $h = 0.003$, the time step is set to $\Delta t = 2.5 \times 10^{-4}$. The QL width is $a = 0.2$ and the numerical GB mobility is $\mu = \dfrac{2\bar{\mu}}{\pi}$.

A.2 GB mobility estimation from the growth of recrystallized grains in a polycrystalline deformed matrix

As GB mobility is difficult to dissociate from the GB energy in capillarity driven grain growth experiments, an alternative methodology was investigated and preliminary results are presented here. It is based on the classical GB motion equation $v = \mu P$ but the mobility is separated thanks to the additional driving pressure associated with stored energy (dislocations stored during plastic deformation).

Section A.2.1 presents the material, specimen preparation, compression tests and the way sequential annealing has been conducted. The evolution of the mean values and distributions of quantities such as grain size, GB energy and total interfacial energy are presented in section A.2.2. The methodology to compute the normal velocity v_n and the driving pressure P, and the sequential annealing experiments are presented in section A.2.3. The section ends with conclusions and remarks about possible improvements for such experiments in section A.2.4.

A.2.1 Materials and methods

Austenitic 304L Stainless steel

Stainless steels are widely used for their good corrosion resistance thanks to their high chromium content. Depending on the chemical composition and the thermomechanical path they can be composed of different phases: martensite, ferrite, austenite, or a combination of them. 304L used in this study is an austenitic stainless steel used in different applications such as automotive, aerospace or nuclear industry. The chemical composition of the 304L steel is reported in Table A.1.

Table A.1: Chemical composition (wt %) of the 304L stainless steel used in this study.

Elem. wt %	**C**	**Mn**	**P**	**S**	**Si**	**Cr**	**Ni**	**N**	**Fe**
Min						17.8	7.9		Bal.
Measured	0.023	1.92	0.028	0.003	0.28	18.0	8.0	0.09	Bal.
Max	0.035	2.04	0.055	0.035	0.8	20.2	10.7	0.11	Bal.

The material was provided by the ArcelorMittal company, together with the actual composition indicated as the "measured" one in Table A.1. It was hot rolled, solution annealed at T=1055°C and water quenched. The initial microstructure is mainly composed of the austenitic phase but with secondary ferritic phase corresponding to a fcc and bcc crystalline structure, respectively. The ferrite phase found in the as received state is remnant from the hot rolling (shown by blue rectangles in Figure A.3).

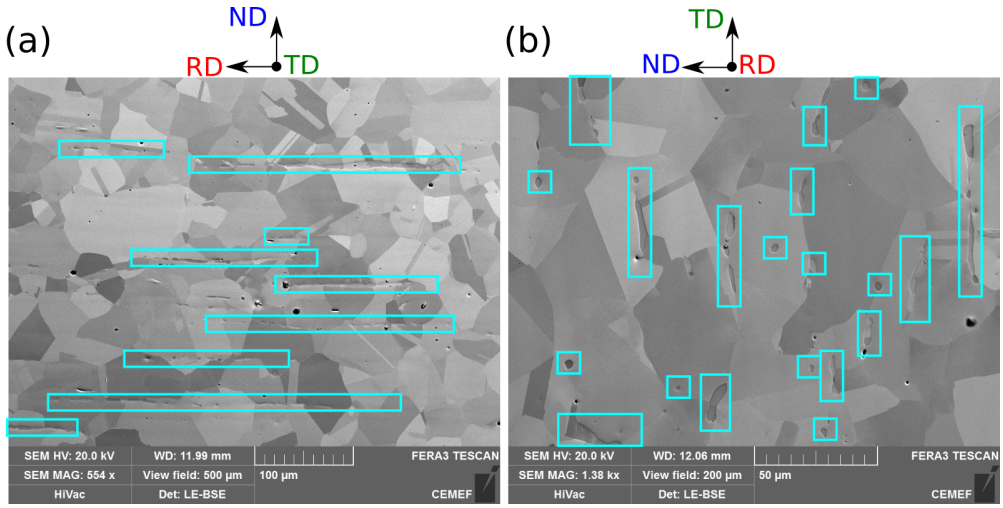

Figure A.3: BSE images of the as received microstructure of the 304L stainless steel. Blue rectangles show ferrite strings as appearing in two different planes perpendicular to (a) TD and (b) RD directions. The RD, ND and TD directions are the rolling, normal and transverse directions of the hot rolling process, respectively.

Compression test

Hot deformation was performed on cylindrical samples with diameter of 8.5 mm and height of 12 mm and in a compression machine MTS Landmark 370-25. A schematic representation of the machine is shown in Figure A.4. Compression is performed by controlling the displacement of the upper tool while the bottom tool is fixed. The tools are made of Udimet 720 (Nickel based superalloy) with silicon nitride (Si_3N_4) insert at the tool extremity. Molybdenum disulphide powder is added on the bottom and top of the samples to reduce friction and sticking with the ceramic inserts. The machine is equipped with a furnace. Temperature is controlled with 2 thermocouples (TC1 and TC2 on Figure A.4) at the upper and lower tools.

The thermomechanical path that followed the sample is shown in Figure A.5a. When the furnace reaches the desired temperature ($1000°C$), the sample is inserted and is maintained during 30 minutes before compression to homogenize temperature inside the sample. Since the as-received state has undergone solution annealing at $1055°C$, this holding for 30 min at $1000°C$ is not expected to make the microstructure evolve. After compression, the furnace slides up and the sample is pushed manually into water. The time between the end of deformation and the quenching is measured to 1.1 second based on video recording.

As the strain and strain rate fields are heterogeneous inside the sample, the compression test was simulated using the Forge® finite element software in order to get to know about the local thermomechanical conditions at the center of the sample where the microstructure will be analized (Figure A.5b).

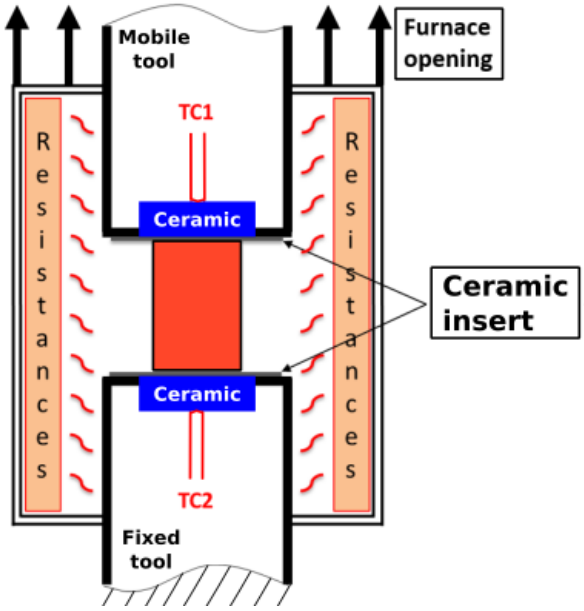

Figure A.4: Scheme of the compression machine and mobile furnace.

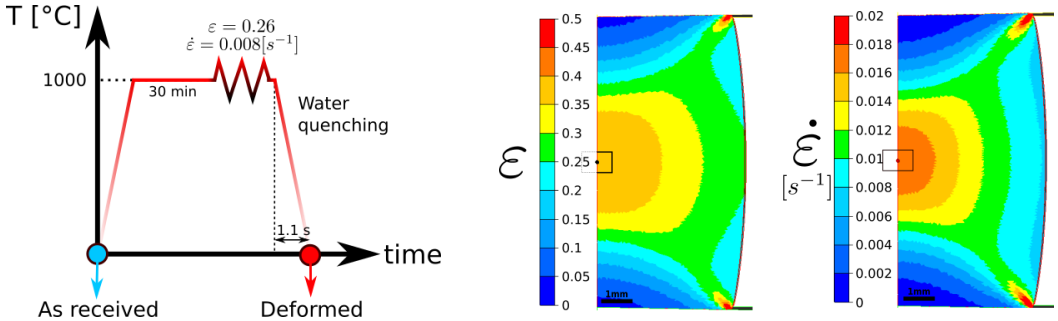

Figure A.5: (a) Thermomechanical path applied to the samples in order to obtain the initial state (Deformed) for the sequential annealing series. (b) Finite element simulations performed on a cylindrical sample at $1000°C$ and $\dot{\varepsilon} = 0.008\ s^{-1}$ up to $\varepsilon = 0.26$ (macroscopic values). The numerical fields represent the equivalent strain and strain rate at the end of the deformation. The square in figure (b) represents the EBSD map.

For the applied macroscopic strain $\varepsilon = 0.26$, the local equivalent strain at the center of the sample (where microstructure will be analyzed) is $\varepsilon \approx 0.37$ and is relatively homogeneous over a few mm wide (see Figure A.5b). As it will be shown later, under this deformation condition, dynamic recrystallization was initiated but not completed at the center of the sample.

Sample preparation and sequential annealing

The extraction of the samples for the sequential annealing series from the deformed material was carried out carefully to ensure its repeatability in terms of position and thus of deformation levels, Figure A.6a shows the steps of the sample preparation. A rectangular cuboid was extracted from one half of the barrel-like deformed sample. The face near the center was polished following the steps listed in Table A.2. The sample was cut using a wire saw. The final dimension of the samples is 4 $mm \times 5\ mm \times 250\ \mu m$.

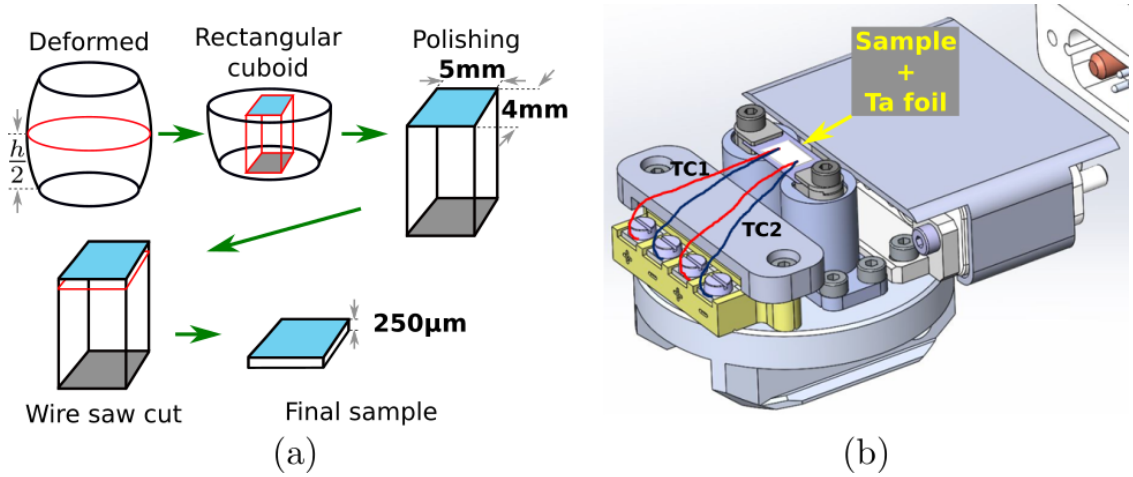

Figure A.6: (a) Steps followed to prepare the samples. (b) Sample welded to the Ta foil mounted onto the heating stage.

Table A.2: Polishing procedure applied to the 304L stainless steel samples. Plate and tower rate are the parameter of the used automatic polisher.

Abrasive	**time [s]**	**Plate [rpm]**	**Tower [rpm]**	**Force [dN]**
320 SiC paper	60	250	150	2.5
600 SiC paper	60	250	150	2.5
1200 SiC paper	60	250	150	2.5
2400 SiC paper	60	150	100	1
HSV - 3µm Diamond solution 0.12mL/8s	120	150	100	2
electrolytic polishing	30s	30V	Electrolyte A2 (Struers)	

The samples were welded onto a Tantalum foil (30 µm thick). Then, the two thermocouples are welded to the sample in order to control the temperature and evaluate its gradient through the sample. The assembly is then mounted onto a stage (Figure A.6b) that will be moved between the heat treatment chamber

and the SEM chamber at every heat treatment step (Figure A.7). In the heat treatment chamber the stage is connected to a power supply and the Tantalum foil is heated by Joule effect.

The microscope is a TESCAN FERA 3 Field Emission Gun Scanning Electron Microscope (FEGSEM), equipped with several analytical devices, among which the C-nano EBSD detector from the Oxford company that has been used in this work.

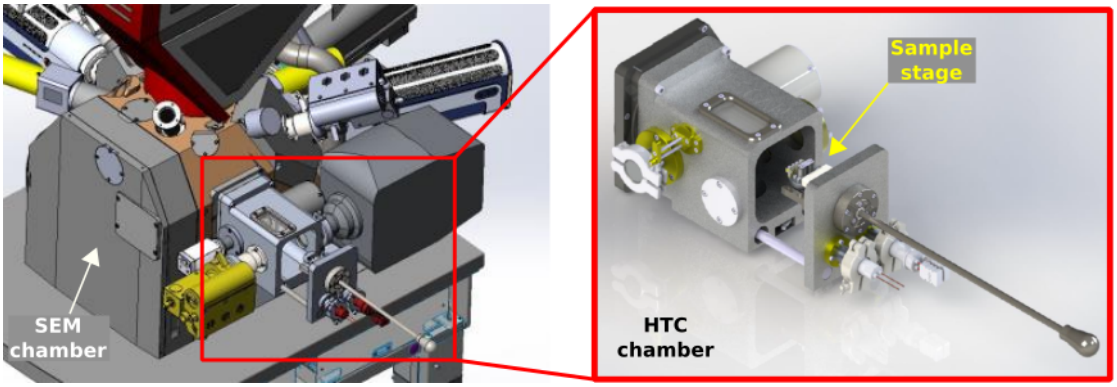

Figure A.7: View of the in-house heat treatment chamber mounted on the FERA3 SEM chamber.

The in-situ test consists in a series of short interrupted heat treatments (Figure A.8a) followed by fast cooling and transfer to the SEM chamber for analyzing the region of interest by EBSD. Temperature regulation is performed with a PID control using the signal from one of the thermocouples. In the real in-situ heat treatment shown on Figure A.8b one can see that the regulated thermocouple (TC2) follows the setpoint temperature. However, the thermocouple TC1 provides a temperature value that is about 70°C higher than the regulation thermocouple. This difference may be due to the slight difference of thickness in the sample or bad contact between the thermocouple and the sample. The zone of interest has been chosen close to the regulation thermocouple. The aim of this experiment is not to establish the temperature dependence of recrystallization kinetics but to evaluate the possibility of assessing relevant information regarding the GB mobility. In this attempt, there is thus an uncertainty about the exact temperature undergone by the sample, which could be fixed in further experiments if these first trials are successful.

After the heat treatment is finished the sample is transferred to the SEM chamber and EBSD is performed on the exact same area measured before. This process is repeated several times until recrystallization significantly progressed.

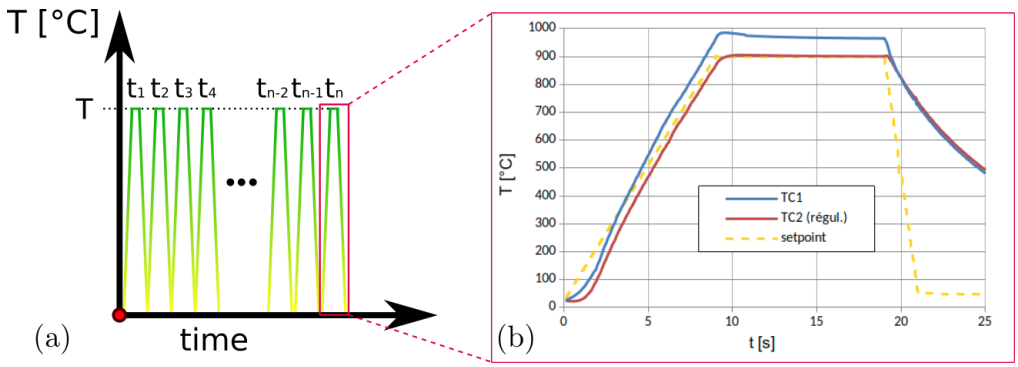

Figure A.8: (a) Schema of the heat treatments series, T is the heat treatment temperature and t_i the time of each heat treatment step. (b) A real annealing step performed with a target temperature of 900°C for 5 seconds, the blue, red and yellow lines are the temperature of the thermocouples (TC1 and TC2 shown in Figure A.6) and the set point, respectively.

Furthermore, the Ta foil can undergo distortions due to the cooling and heating cycles. This can change the initial orientation of the samples with respect to the laboratory coordinate system, which induces distortions in the EBSD maps which then do not coincide exactly.

Microstructure of the as-received state and of the initial deformed sample used for the sequential annealing experiment

Microstructures were analyzed at the center of the sample where the strain and strain rate are relatively homogeneous (see Figure A.5b). The EBSD maps presented in this section have a size of 0.984 mm×0.739 mm and were acquired with a constant step size of 1 µm.

Figure A.9 show the IPF-Z orientation and Kernel Average Misorientation (KAM) maps of the as-received and after hot-compression and quenching microstructures. The KAM represents the average of the misorientation angles θ_{ij} between a point i and its first and second neighbors ($n = 2$ in Equation A.4, see Figure A.9e). Given that this parameter varies as the geometrical necessary dislocation (GND) density, small recrystallized grains can be recognized owing to their low grain average KAM (GAKAM) value. The GAKAM is the average value of KAM values of the N points within a grain (Equation A.5). In Figure A.9d, recrystallized grains have a GAKAM below 0.35°. Figure A.10 shows the difference between the as-received and deformed materials, the main changes are the decrease of GBs at $\theta = 60°$ (which mostly correspond to annealing twin boundaries (TB) which are present in the as-received state and have been modified during deformation) in the disorientation distribution and the increase of the GAKAM.

$$KAM_i = \frac{1}{n}\sum_{j=1}^{n}\theta_{ij} \tag{A.4}$$

$$GAKAM = \frac{1}{N}\sum_{k=1}^{N}\frac{1}{n}\sum_{j=1}^{n}\theta_{ij}. \tag{A.5}$$

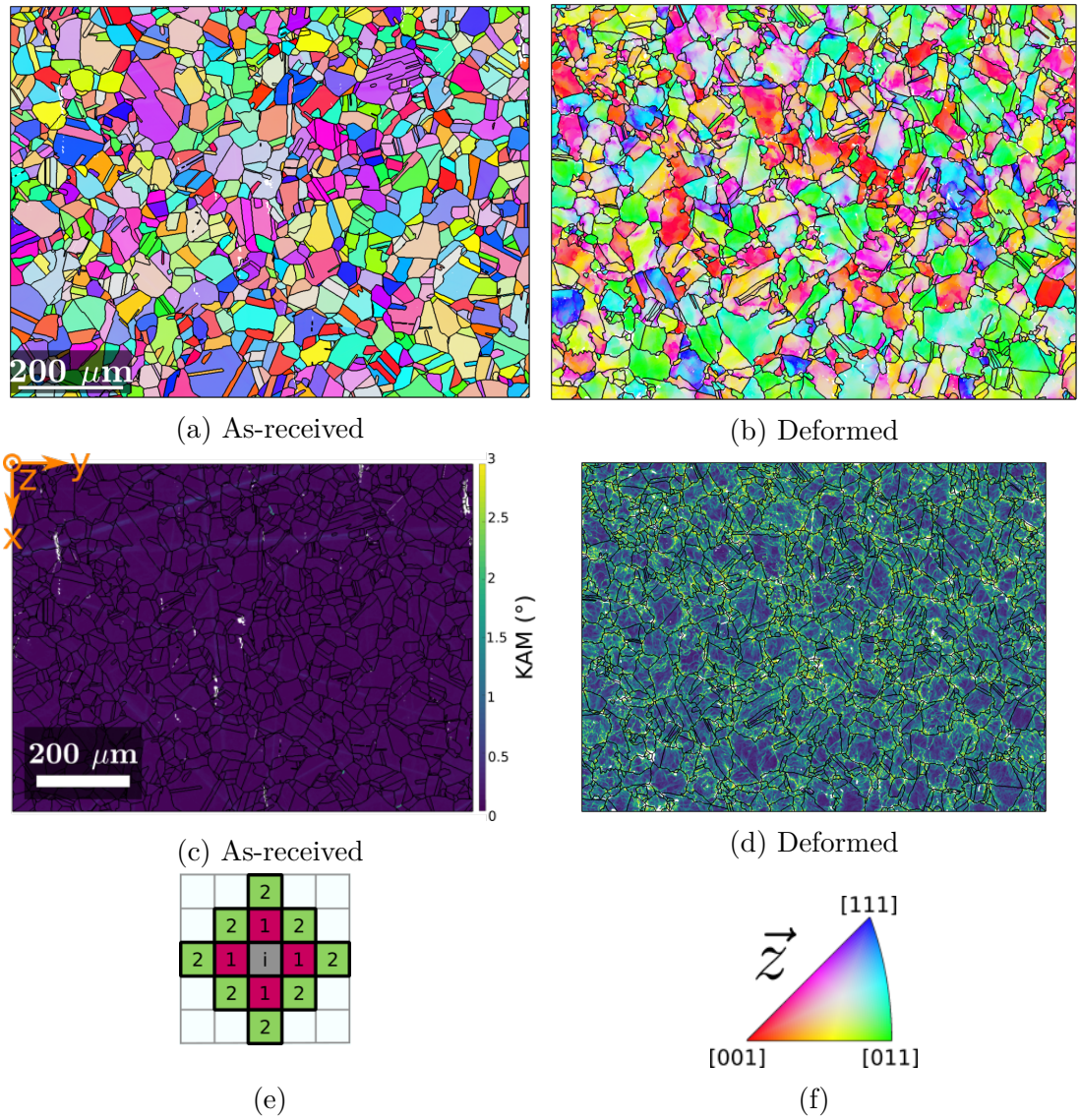

(a) As-received (b) Deformed

(c) As-received (d) Deformed

(e) (f)

Figure A.9: Orientation map obtained by EBSD on the (a) as-received and (b) deformed states. KAM map of the microstructure of the (c) as-received sample and (d) deformed sample. The compression is performed in the Z direction perpendicular to the scanned section. The same color coding is used during this chapter unless it is specified. (e) First and second order neighbors considered to compute the KAM. (f) Standard triangle used to color the orientation maps IPF-Z (indicating which crystallographic direction is lying parallel to the direction perpendicular to the scanned section).

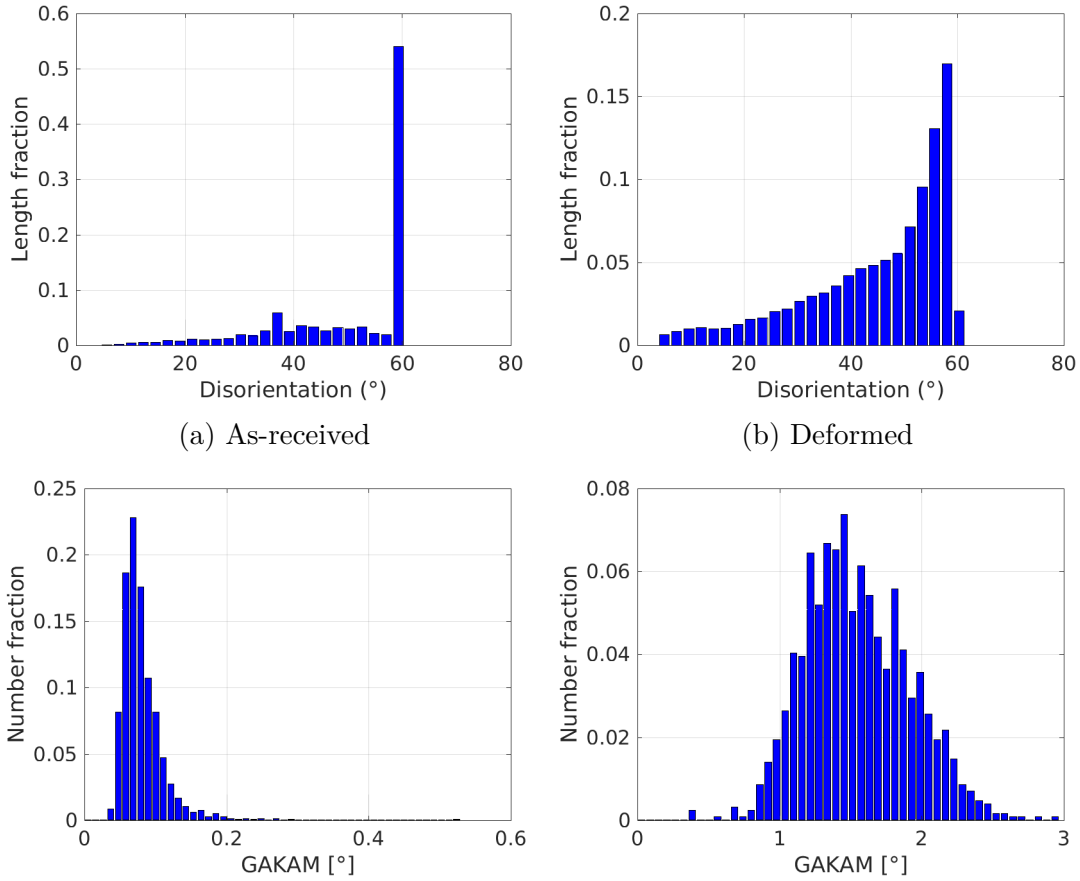

(a) As-received

(b) Deformed

(c) GAKAM As-received

(d) GAKAM Deformed

Figure A.10: (a,c) GB disorientation distribution and (c,d) GAKAM distribution obtained from the EBSD maps of Figures A.9(a,c) of the as-received, and Figures A.9(b,d) of the deformed states.

A.2.2 Microstructure evolution

Two heat treatment series were perfomed, one at 900°C and the other at 950°C, starting from distinct samples that have undergone the same thermomechanical path decribed above. Figures A.11 and A.12 show the evolution of the microstructures. From these two series, it is clear that recrystallization proceeds faster at higher temperatures, as expected.

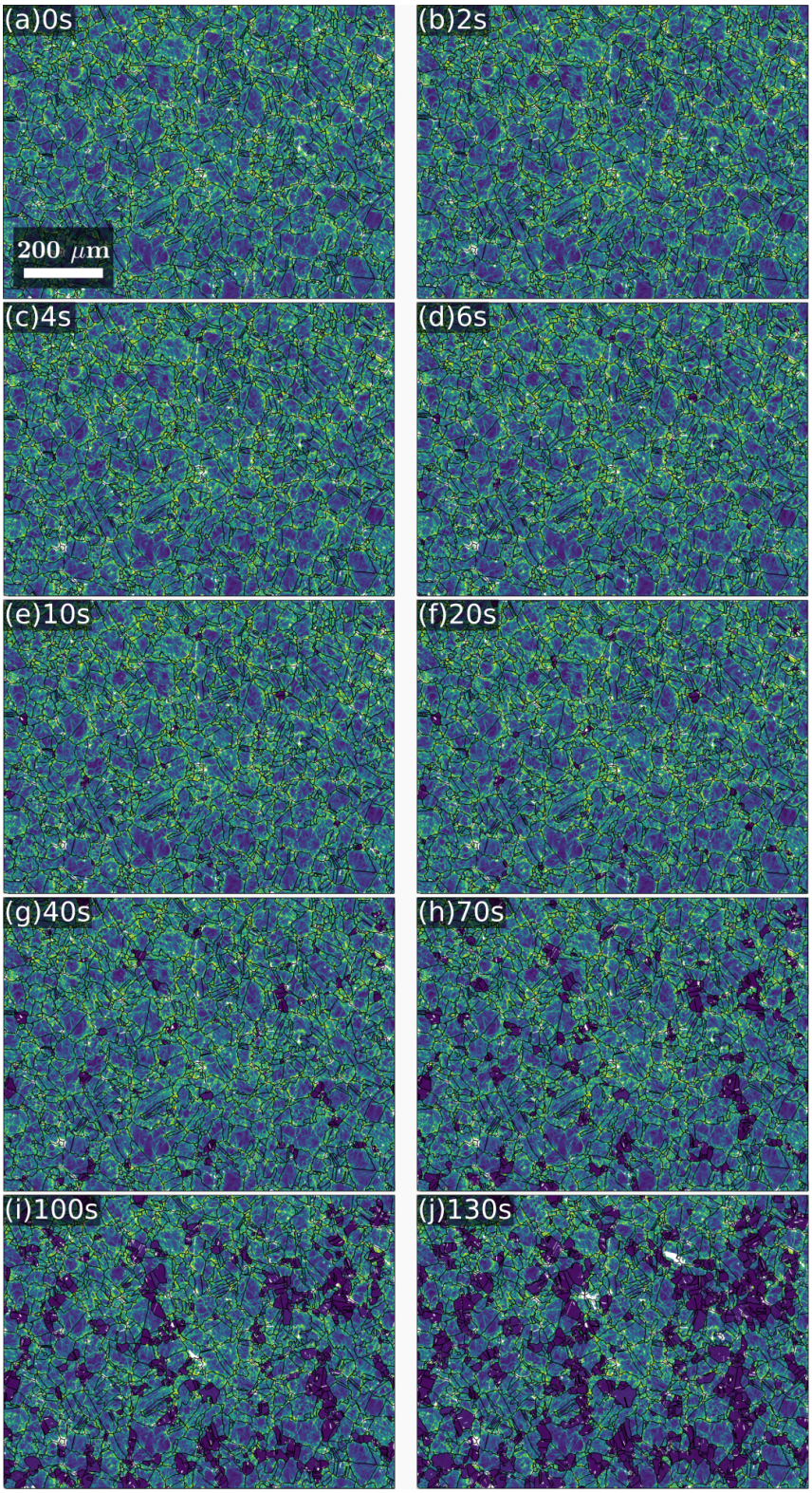

Figure A.11: Microstructure of the 304L stainless submitted to sequential annealing at a target temperature of 900°C. The KAM map is shown at t=0 (Deformed), 2, 4, 6, 10, 20, 40, 70, 100, 130s (cumulative time). GBs ($\theta > 5°$) of the nuclei and deformed grains are depicted in black.

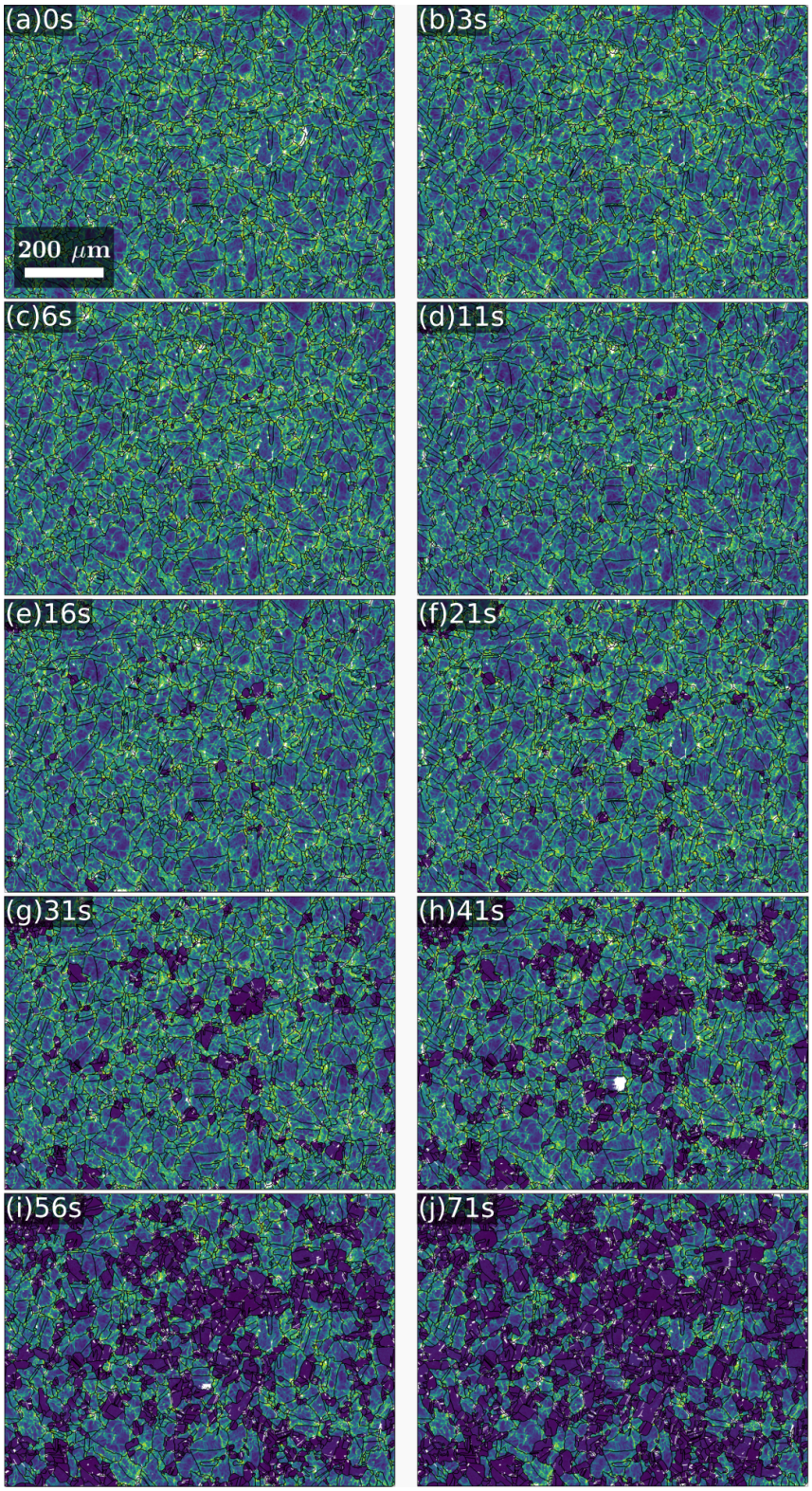

Figure A.12: Microstructure of the 304L stainless submitted to sequential annealing at a target temperature of 950°C. The KAM map is shown at t=0 (Deformed), 3, 6, 11, 16, 21, 31, 41, 56, 71s (cumulative time). GBs ($\theta > 5°$) of the nuclei and deformed grains are depicted in black.

Two other important aspects of the microstructure evolution must be pointed out: First, the KAM does not decrease during the heat treatments within the deformed grains. Second, the GBs between deformed grains remain static. The static behavior of the deformed grains may be due to the ferritic phase which block their evolution [225, 226]. This was confirmed by carrying out heat treatment tests of the as-received material at 1000°C without any evolution of the grains, see Figure A.13. Thus, tracking the growth of the recrystallized grains is simpler because they are the only grains that evolve. On the other hand, one should keep in mind that the ferritic phase can also interrupt the growth of the recrystallized grains.

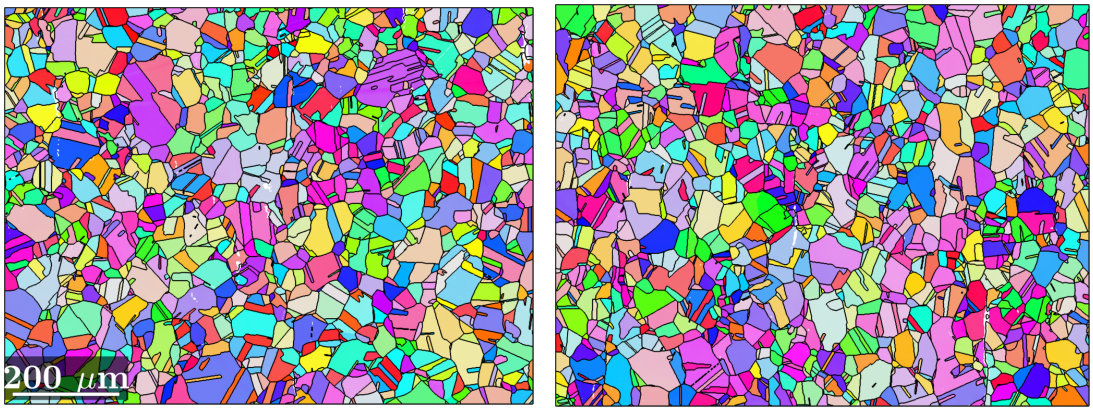

(a) As-received (b) 1 h

Figure A.13: Orientation map (IPF-Z) of 304L of the (a) as-received sample and (b) after 1 hour at 1000°C.

Figure A.14 shows the recrystallized fraction (Rx-Fraction[%]), the stored energy related to the GND density (E_Ω), the mean GB disorientation and the twin boundary length fraction (TB-Fraction[%]). The recrystallized fraction is computed using the following equations:

$$Rx - Fraction[\%] = \frac{S_{RX}}{S_\Omega} * 100, \tag{A.6}$$

where S_{RX} is the surface of the recrystallized grains, S_Ω the surface of the austenite phase and the recrystallized grains are identified based on a GAKAM value threshold (GAKAM<0.35°). The stored energy is approximated as:

$$E_\Omega = \tau \sum_{pixels} \rho_{GND}, \tag{A.7}$$

where $\sum_{pixels}$ is a sum in all the austenite pixels, τ is the energy per unit dislocation line and ρ_{GND} is the GND density which is calculated using the method proposed in [227]. This force is underestimated because the statistically stored dislocations are neglected. Finally, TBs are recognized thanks to their misorientation axis <111> ±5° and disorientation $\theta = 60° \pm 5°$, and the TB length

fraction is computed as:

$$TB - Fraction[\%] = \frac{L_{TB}}{L_{\Gamma}} * 100, \tag{A.8}$$

where L_{TB} is the length of TBs and L_{Γ} is the length of all GBs. In Figure A.14, the faster evolution of recrystallized grains at higher temperature is represented by a faster decrease of the stored energy. An increase in the average GB disorientation is also observed as recrystallization progresses, which is mostly associated with higher TB length fraction as annealing twins form as the ReX grain develop [228, 229].

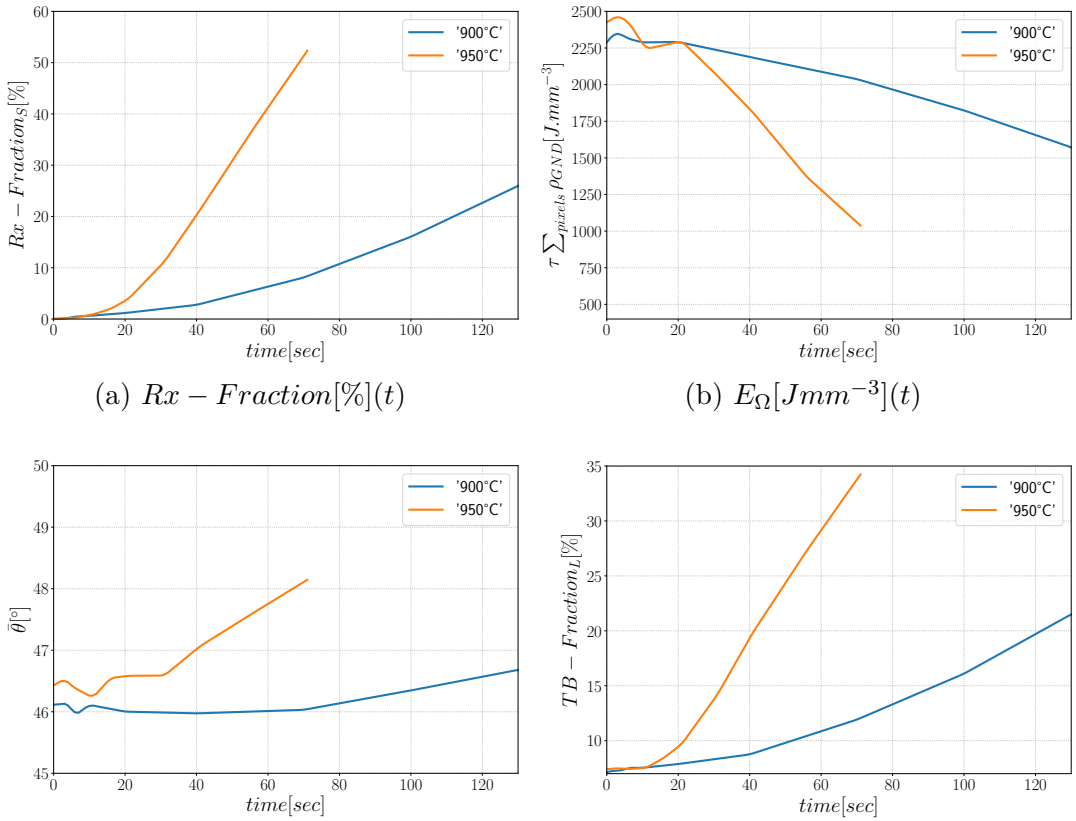

(a) $Rx - Fraction[\%](t)$ (b) $E_{\Omega}[Jmm^{-3}](t)$

(c) $\bar{\theta}[°](t)$ (d) $TB - Fraction[\%](t)$

Figure A.14: Mean values time evolution of the areas analyzed during the sequential annealing series at targeted temperatures of 900°C and 950°C. (a) Recrystallized area fraction. (b) Estimated stored energy. (c) Mean GB disorientation. (d) Twin boundary length fraction.

A.2.3 Rough GB Mobility estimation using the classical velocity equation

Zones around the growing recrystallized grains were selected to accelerate the computation and see the GB movement clearly. Figure A.15 shows a scheme of the zone selection, the recrystallized grain is identified and the area is selected such that the surrounding grains are captured. The example shown is from the initial microstructure mapped for the test at 900°C. The zone of interest is on the bottom left in Figure A.15b and the movement of this recrystallized grain is shown at $t = 0s$ and $t = 190s$ in Figure A.15c.

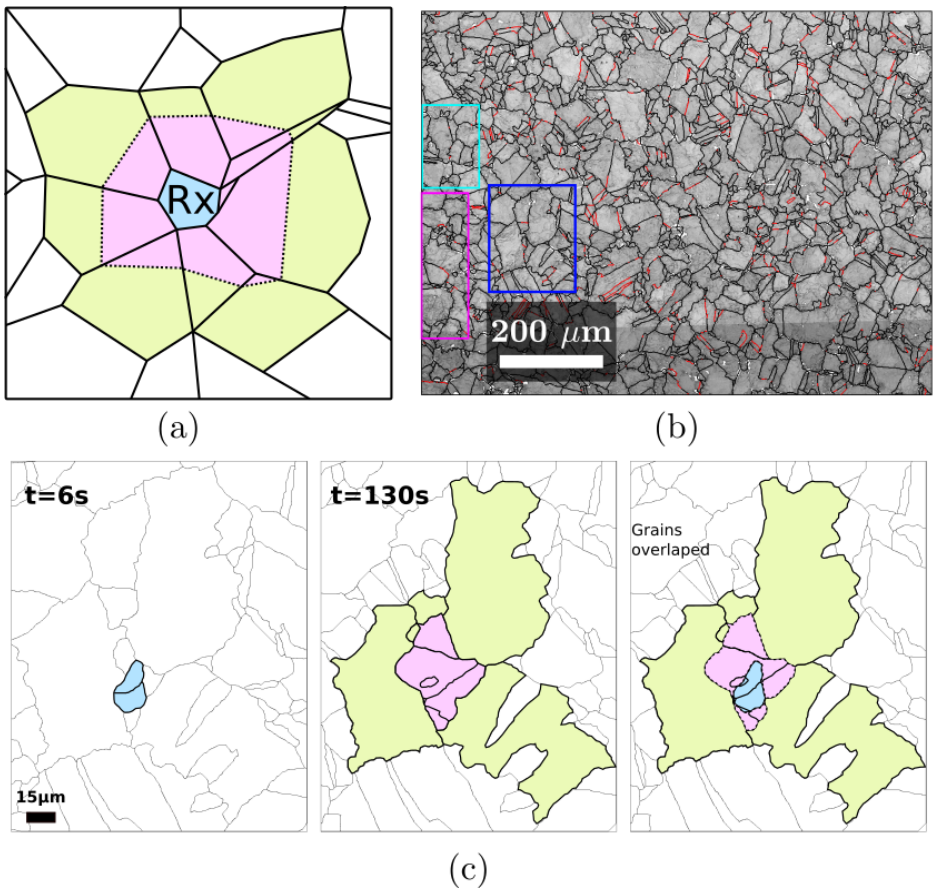

Figure A.15: (a) Scheme of the zone surrounding a recrystallized grain (blue) that grows during the heat treatment (pink) and the grains around the grain of interest (yellow) at the end of the test. (b) Initial microstructure mapped along the sequential annealing series at T=900°C with three zones of interest in magenta (Figure A.16), cyan (Figure A.17) and blue (Figure A.18). (c) The blue zone is shown at t=6s with the initial grain colored in blue, at t=130s the blue grain grows and is colored in pink, the blue and pink are overlapped to show the same diagram in (a).

Within a grain, GBs can have different behaviors: they can be immobile, fast

moving, slow moving or have mixed behavior along the GB. The behavior of a grain boundary may be due to its nature, to the interaction with intermetallics or carbide particles or to the nucleation of TBs. Hence, not all the boundaries of a given recrystallized grain can be used to compute a GB mobility value. 11 grains were studied. In Figure A.16, the magenta arrow points a GB that evolved smoothly and will be used to explain how the GB mobility has been estimated.

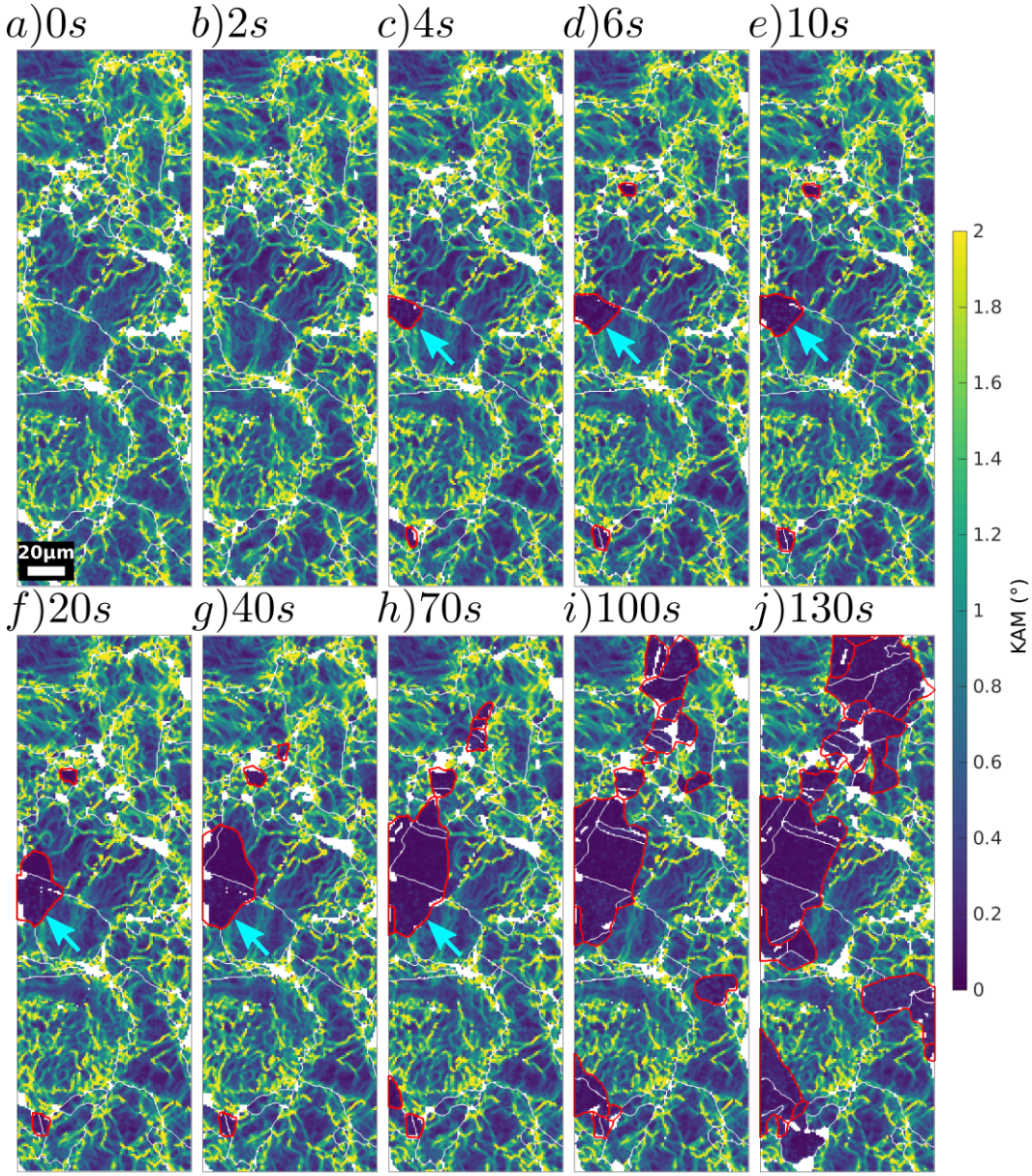

Figure A.16: KAM maps of the samples submitted to sequential annealing at 900°C in the magenta zone depicted in Figure A.15. The cyan arrow shows the interface that will be used to explain the methodology adopted to compute the GB mobility. The white zones are ferrite strings.

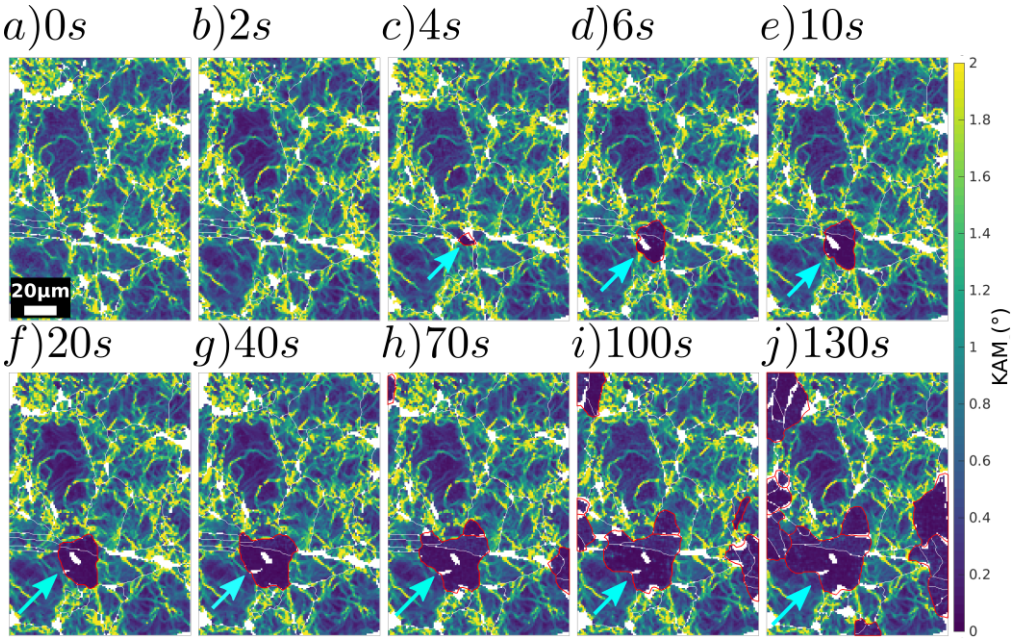

Figure A.17: KAM maps of the samples submitted to sequential annealing at 900°C in the cyan zone depicted in Figure A.15. The cyan arrow shows the GB shown in Figure A.20. The white zones are ferrite strings.

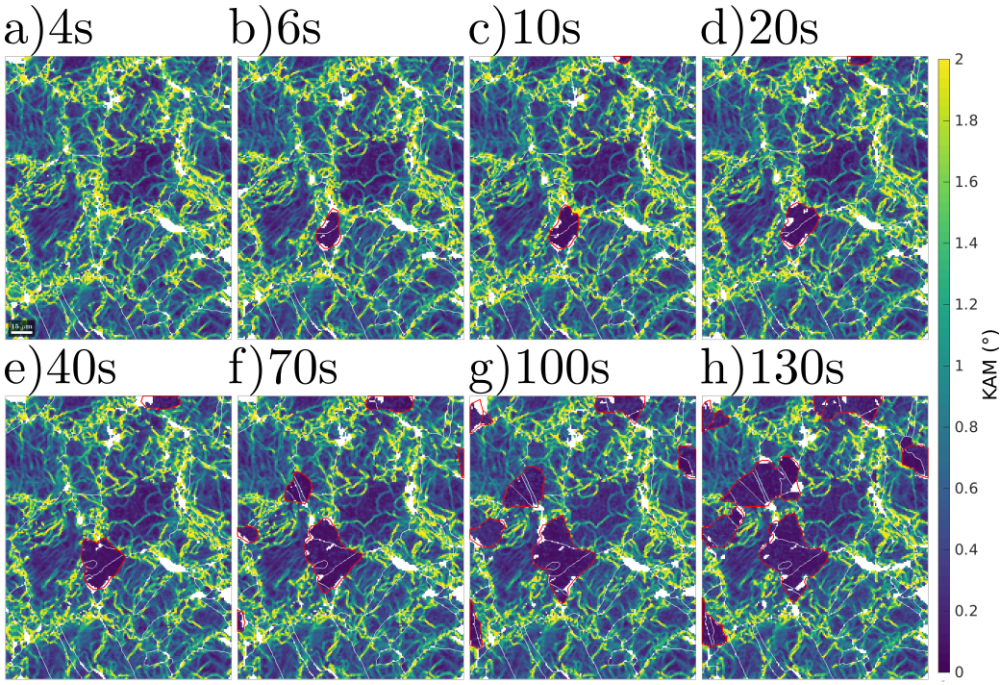

Figure A.18: KAM maps of the samples submitted to sequential annealing at 900°C in the blue zone depicted in Figure A.15. The white zones are ferrite strings.

Due to the presence of energy stored during hot deformation, the GB motion equation may be redefined as:

$$\vec{v} = \mu(P_c + P_e)\vec{n}, \tag{A.9}$$

the driving pressures associated with capillarity effects and with stored energy difference across the boundary are defined as $P_c = -\gamma\kappa$ and $P_e = [\![E]\!] = \tau[\![\rho]\!]$ (Equation 1.27), respectively. Theoretically, it is possible to compute GB mobility from equation A.9 if the geometry $(\vec{n}, \kappa)$, the position (x, y) and the orientation $(\rho(O_i))$ are known. If the aforementioned data are known, one can approximate the GB mobility using the following equation:

$$\mu = \frac{v_n}{P_c + P_e} = \frac{v_n}{\pm\gamma\kappa \pm \tau[\![\rho]\!]}, \tag{A.10}$$

with v_n the normal velocity and the $\pm$ sign is used because both driving forces can act in either directions. EBSD performed on 2D sections provides an estimate for the dislocation density, but the inclination of the GB below the section plane is unknown, so that the normal to the boundary and its 3D curvature are undetermined. One must therefore make here the strong assumption that the GB are perpendicular to the section plane to proceed further with a rough approximation of the GB mobility. In addition, one must keep in mind that the estimated dislocation density is actually an underestimated value, since only the contribution of GNDs is accessible by EBSD. Moreover, torque terms can have an impact on Equations A.10 and A.11 near the multiple junctions [35], which are neglected here. Dealing with the growth of recrystallized grains, the stored energy provides a driving force that makes the GB move further to make the recrystallized grain grows and consumes the deformed matrix. Because of the stored energy consumption, the recrystallized grains often develop concave shapes. In this configuration, the capillarity effects opposes that of GB movement, therefore must then be seen as braking force.

Hence in this configuration, Equation A.10 may be approximated as:

$$\mu = \frac{v_n}{\tau[\![\rho]\!] \pm \gamma/R}, \tag{A.11}$$

with R the equivalent radius of the GB segment.

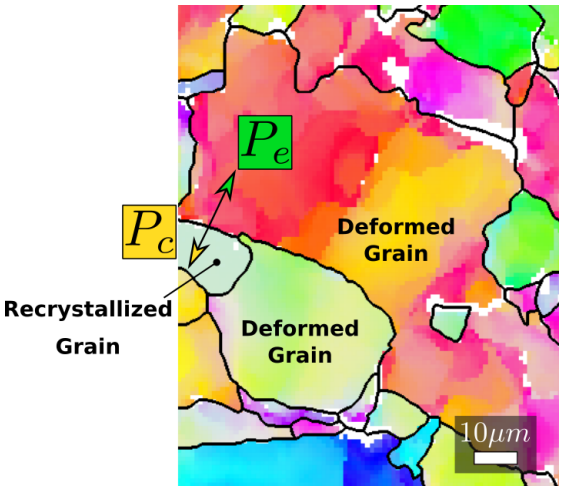

Figure A.19: Driving pressures of a GB from a recrystallized grain surrounded by deformed grains.

Post processing was conducted using the MTEX toolbox in a Matlab environment [207]. First, capillarity pressure is computed directly using a constant GB energy $\gamma = 6 \times 10^{-7}[J/mm]$ [111] and the radius R is obtained directly from MTEX. Second, stored energy $P_e = \tau[\![\rho]\!]$ is estimated using a dislocation line energy set to $\tau = Gb^2 = 4.97 \times 10^{-12}$ $[J/mm]$ typical for a stainless steel [230]. The dislocation density is simplified to the contribution of the geometrically necessary dislocations as $[\![\rho]\!] \approx [\![\rho_{GND}]\!]$. ρ_{GND} is calculated through the relation $\rho_{GND} = \frac{3.6}{b}||\alpha||_1$ [231], with $||\alpha||_1 = \sum_i \sum_j |\alpha_{ij}|$ defined as the entry wise one norm of the dislocation density tensor, $\bar{\bar{\alpha}} = \bar{\bar{\kappa}}_{el}^T - trace(\bar{\bar{\kappa}}_{el}) \cdot \mathbb{I}$ and the elastic curvature tensor $\bar{\bar{\kappa}}_{el} = \bar{\bar{\nabla}} M_{i,i'}$ [232]. Here raw EBSD data was used. With standard EBSD techniques, just 2D data is measured and the Nye tensor is incomplete, thus the scaling factor 3.6 is used to correct the contribution of the unknown terms [231]. Finally, for practical purposes the stored energy is defined with ρ_{GAGND} the grain average of ρ_{GND}:

$$P_e = [\![E]\!] \approx \tau[\![\rho_{GAGND}]\!]. \tag{A.12}$$

where $[\![\rho_{GAGND}]\!]$ is the jump of ρ_{GAGND} around the segment.

The velocity of the GB is approximated from its position using a backward difference scheme

$$v_n^i \approx \frac{\bar{d}_{GB}}{\Delta t} = \frac{x^i - x^{i-1}}{\Delta t} \tag{A.13}$$

where $\bar{d}_{GB}$ is the average displacement of the GB in the normal direction measured at the sample surface, this relation is simple and its accuracy theoretically depends on the time and EBSD step. In practice, it also depends on the quality of the aligment of the successive EBSD maps. Figure A.20(a) shows the evolution of the GB pointed by the cyan arrow in Figure A.16. One can see that along a GB the interface does not evolve uniformly, so $\bar{d}_{GB}$ is computed manually in different

zones along the GB and averaged. Moreover, carbides and ferrite strings can pin the interfaces and the evolution along one GB can drastically vary as shown in Figure A.20(b). The computation of $\bar{d}_{GB}$ presents another problem, one can notice the overlap between GBs in Figure A.20. The origin of the deformation of the Tantalum foil after the heating-cooling cycles which ends up with distortions in the EBSD maps after the required tilt corrections. This is corrected using a Fiji [233] plugin that align image stacks based on the article of D. Lowe [234]: Linear Stack Alignment with SIFT. This plugin uses the common points of the large microstructures shown in Figures A.11 and A.12 to realign the shift and distortion among every EBSD map.

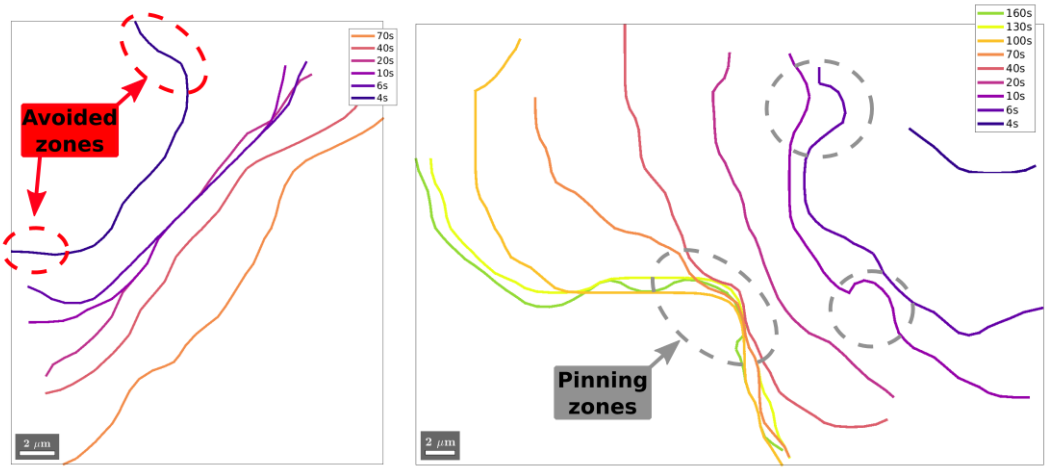

Figure A.20: (a) Evolution of the GB pointed out in Figure A.16 from the heat treatment at 900°C and t=4, 6, 10, 20, 40 and 70 s. (b) Evolution of the GB pointed out in Figure A.17 from the heat treatment at 900°C and t=4, 6, 10, 20, 40, 70, 100, 130 and 160 s.

Finally, GB mobility is computed using Equation A.11. Figure A.21 shows the estimated driving pressure, GND density, GB velocity and GB mobility of the GB shown in Figure A.20a. One can see that P_e, even though it is underestimated by considering only the contribution of GNDs, is much higher than P_c (Figure A.21a) and ρ_{GAGND} values of both the recrystallized grain and of the deformed grain remain almost constant (Figure A.21b). Note that in Figure A.20a, the GB displacement between $t = 4s$ and $6s$ is important, hence the GB velocity (mobility) presents an abrupt peak proportional to the displacement of the GB. Also, the GB is blocked in the middle from $t = 6s$ and $20s$, but it evolves in the bottom extremity. Thus, GB mobility estimated for this particular GB is the average of the stable points, i.e., $\mu \approx 0.05\ mm^4 J^{-1} s^{-1}$, see Figure A.21d. The retarding effect is caused by the appearing annealing twins. Indeed, one can see in Figure A.16, that both extremities of the GB are stopped while the annealing twins appeared.

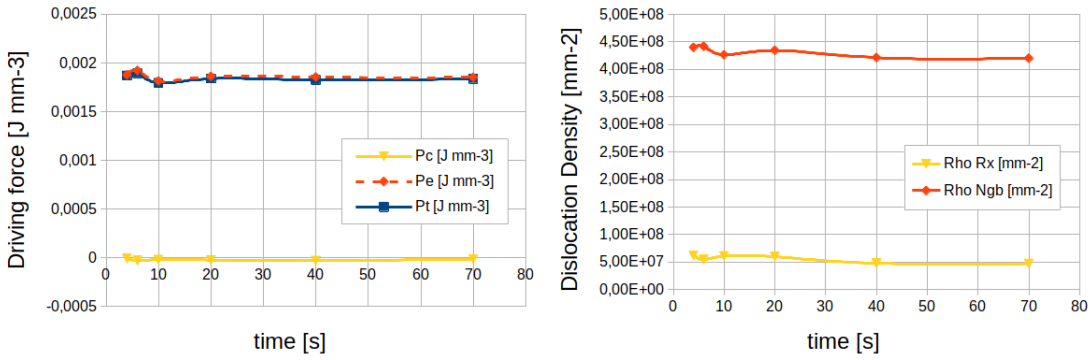

(a) $P_t(t)$, $P_e(t)$ and $P_c(t)$ (b) $\rho_{GAGND}(t)$

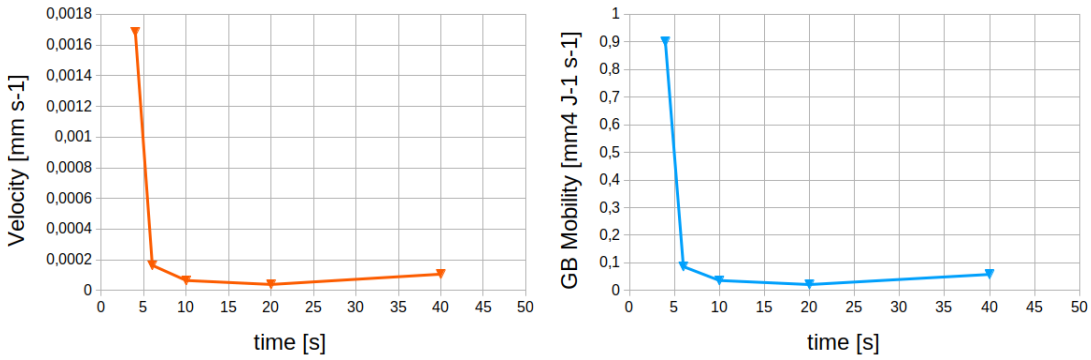

(c) $v_n(t)$ (d) $\mu(t)$

Figure A.21: (a) Evolution of the estimated driving pressures (Total, capillarity and stored energy jump), (b) the grain average geometrically necessary dislocation density ρ_{GAGND} of the recrystallized grain (Rx) and the adjacent deformed grain (Ngb), (c) GB velocity, and (d) GB mobility of the GB shown in Figure A.20(a) and A.16

The boundary of Figure A.20b does not show a similar stagnation in its motion all along the boundary, but clearly shows the effect of grain boundary pinning by second phase particles. This boundary has met two particles at 6 and 10 seconds, which could be crossed, and another one at 70 seconds where it remains hanged on. In such situation, the migration distance has been measured along moving segments, and the GB mobility value tends to $\mu \rightarrow 0.05\ mm^4 J^{-1} s^{-1}$ as seen in Figure A.22.

This analysis was repeated for 34 GBs in different zones. The relation between the GB mobility and the GB misorientation is shown in Figures A.23a and A.23b. Figure A.23a shows the GB mobility seems to be higher at intermediate disorientation values ($\theta = 30 - 50°$). Figure A.23b shows that the effect of the angular deviation from the <111> axis ($\omega_{<111>}$) where the GB mobility seems to be higher at $900°C$ when the misorientation axis is close to <111> but there is no clear trend at $950°C$. As expected, the GB mobility found at 950°C is higher but the number of studied GBs are lower.

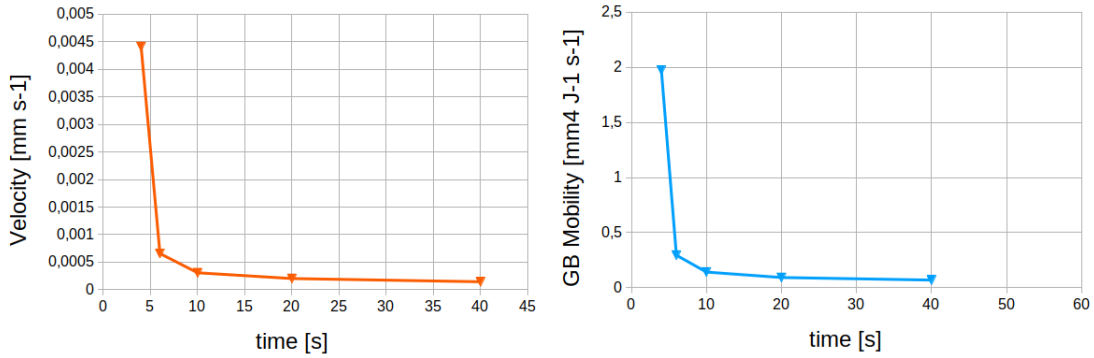

(a) $v_n(t)$ $\frac{mm}{s}$ (b) $\mu(t)$ $\frac{mm^4}{Js}$

Figure A.22: (a) Evolution of the driving pressures (Total, capillarity and stored energy), (b) the grain average geometrically necessary dislocation density ρ_{GAGND} of the recrystallized grain (Rx) and the adjacent deformed grain (Ngb), (c) GB velocity, and (d) GB mobility of the GB shown in Figure A.20(b) and A.17

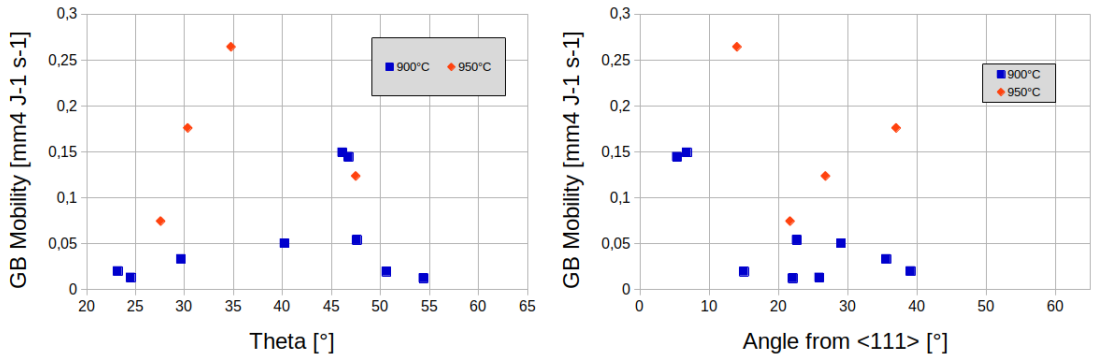

(a) $\bar{\mu}(\theta)$ (b) $\bar{\mu}(\omega_{<111>})$

Figure A.23: GB mobility as a function of (a) disorientation and (b) angular deviation of the misorientation axis from the axis <111>.

This attempt of measuring GB velocity and mobility by performing sequential annealing series and following the development of recrystallized grains has confirmed several difficulties and issues. Future experiments may be performed using single-phase materials with low propency to form twins thus tracking GBs may be easier. The following major issues should be pointed out as well. GBs traces can be tracked during the sequential heat treatments (with an accuracy that could be improved with better distortion correction of the aligned EBSD maps) but the GB inclination cannot be assessed from 2D sections leading to wrong values of GB velocity since the normal velocity is required. On the other hand, the estimation of the dislocation density is over simplified, i.e., $[\![\rho]\!] \approx [\![\rho_{GND}]\!]$ being another source of error in the estimation of the GB mobility.

A.2.4 Discussion

In this chapter several methodologies have been presented to estimate (an apparent) GB mobility. The main conclusion is that there is no ideal way to estimate GB mobility. One may consider multiple time and length scales combining approaches from molecular dynamics to experimental results. In the literature, GB mobility has been computed using molecular dynamics allowing to quantify GB stiffness tensor which is worth noticing, but the time scale limit is still present and long term effects are neglected. Moreover, MD simulations remain simulations with some numerical choices. 3D measurements offer the great advantage of allowing the mobility tensor to be estimated and to assess the real movement of GBs in 3D, but the behavior of the GB mobility is difficult to exhibit using such data.

An attempt to estimate GB mobility is presented in this section but suffers from some limitations inherent to 2D section observations. Sequential annealing experiments were carried out on deformed samples using a SEM equipped with a heat treatment chamber. The peculiarity of these experiments is that they started from a hot-deformed microstructure: the initial samples presented a few small recrystallized grains and the estimation of GB mobility is performed by analyzing the migration of their GBs under the driving pressure dominated by the difference in dislocation densities on both sides of the moving boundaries. Residual ferrite phase present in the as-received 304L partially blocked the evolution of the microstructure during GG [225, 226].

One perspective of this work will be to perform equivalent analysis in 3D in order to gain a better understanding of the mechanisms and kinetics of GB motion. Especially, the peak between $\theta = 30$ and $50°$ that was also found in [55, 57]. Also, these experiments may be carried out in simpler microstructures at different temperatures in order to avoid the effect of second phases particles.

RÉSUMÉ

La relation entre procédé de fabrication, microstructure, propriétés et performance des matériaux relève d'un grand intérêt pour l'industrie de mise en forme des métaux. Cette relation est à l'origine d'une nouvelle branche de la science des matériaux appelée ingénierie des joints de grains, qui vise à obtenir des propriétés spécifiques des matériaux métalliques grâce au contrôle de la distribution des types de joints de grains. Les procédés de fabrication des métaux peuvent être modélisés à une échelle mésoscopique grâce à l'utilisation d'outils numériques décrivant l'évolution des joints de grains. L'approche Level-Set (LS), dans un contexte de formulation éléments finis (EF), est un outil puissant permettant de reproduire les traitements thermodynamiques industriels où de grandes déformations peuvent avoir lieu.

Ce travail visait à améliorer une formulation EF-LS en y introduisant des modèles plus précis concernant la description de l'énergie des joints de grains et de leur mobilité. L'objectif principal étant de construire des modèles encore plus prédictifs en croissance de grains et recristallisation. Des cas applicatifs sur un acier austénitique ont été considérés. Lorsque des joints de grains spéciaux ou des sous-joints sont étudiés, ils est en effet nécessaire d'améliorer les modèles décrivant les propriétés des joints de grains. Ces améliorations ont été intégrées dans différents formulations EF-LS grâce à l'ajout de termes dans le champ de vitesse et leur prise en compte, parfois complexe, dans les formulations faibles. La formulation dite anisotrope, testée sur des simulations de cas analytiques de jonctions triples et sur des microstructures polycristallines, s'est confirmée être la formulation la plus physique. Néanmoins, il convient de noter que la connaissance actuelle des données et des modèles de propriétés des joints de grains souffre toujours du manque de données expérimentales pertinentes et précises. La description complète des propriétés des joints de grains nécessite une analyse spatiale tridimensionnelle de la microstructure, ainsi qu'une évolution temporelle dans les conditions thermomécaniques données, ce qui reste impossible à réaliser avec les techniques les plus récentes.

En se basant donc sur des données expérimentales partielles obtenues durant ce travail de thèse, sur des données issues de calculs pré-existants en dynamique moléculaire, et sur des simulations EF-LS réalisés sur des jonctions multiples et des polycristaux de plusieurs milliers de grains, il a été mis en évidence que la formulation Anisotrope est la plus physiquement pertinente parmi les formulations proposées pendant ce travail. Cependant, il a également été mis en évidence que la formulation isotrope peut être utilisée pour des niveaux faibles d'hétérogénéité ou d'anisotropie avec une précision équivalente aux prédictions du modèle anisotrope. Les développements réalisés permettent aussi aujourd'hui de considérer, dans le formalisme LS, des macles cohérentes et incohérentes, isolées ou intégrées à une microstructure polycristalline.

MOTS CLÉS

Eléments Finis, Level-set, Joint des grains, Mobilité, Énergie, Anisotropie, Hétérogénéié.

ABSTRACT

The relation among process, microstructure, properties, and performance of materials is of great interest to the metal forming industries. The microstructure-properties relationship has opened an exciting branch of materials science called Grain Boundary Engineering: control the grain boundary character distribution to promote specific materials properties. The manufacturing processes of metallic materials can be modeled at the mesoscopic scale using numerical tools that describe the evolution of grain boundaries. The Level-Set (LS) approach, in the context of Finite Element (FE) formulations, remains a powerful tool that allows mimicking industrial thermomechanical treatments where large deformation can take place.

This work aims to improve the FE-LS framework by including enriched grain boundary energy and mobility models and to apply this enriched framework to the simulation of grain growth and recrystallization in a single phase austenitic steel. Accounting for the heterogeneity or the anisotropy of GB properties is necessary if special boundaries or subgrains have to be considered. The improvement of the GB property models was incorporated in different FE-LS formulations using additional terms in the existing kinetic framework. Noteworthily, the current knowledge of GB property data and models still suffers from the lack of relevant and accurate experimental data. The complete description of GB properties calls for high spatial three-dimensional microstructure analysis, and for temporal evolution under given thermomechanical conditions, which remains unattainable with the state-of-the-art techniques.

Based on partial experimental data acquired in this work, existing molecular dynamics data, triple junction test cases and polycrystalline simulations, it was confirmed that the Anisotropic formulation was the most physical formulation. Nevertheless, when low levels of heterogeneity/anisotropy are involved in the considered microstructure, the isotropic formulation can be used safely in grain growth and recrystallization simulations. Finally, the new proposed numerical framework is shown to be able to model coherent and incoherent twin boundaries individually or immersed in a polycrystalline microstructure.

KEYWORDS

Finite Elements, Level-set, Grain Boundary, Mobility, Energy, Anisotropy, Heterogeneity.